Mathematical Aspects of Extreme Water Waves

(with Dutch and Indonesian summaries)

Wiskundige Aspecten van Extreme Watergolven

(met Nederlandse en Indonesische samenvattingen)

Applied Analysis and Mathematical Physics

Dutch Technology Foundation

Maritime Research Institute Netherlands

Dutch Research School for Fluid Mechanics

The research described in this thesis was undertaken at the Department of Applied Mathematics, Faculty of Electrical Engineering, Mathematics, and Computer Science (EWI), University of Twente (UT), Enschede, The Netherlands. The research was supported by the Dutch Organization for Scientific Research (NWO), subdivision Applied Sciences the Dutch Technology Foundation (STW) under the project TWI–5374 'Prediction and Generation of Deterministic Extreme Waves in Hydrodynamic Laboratories'.

2000 Mathematics Subject Classification:
76B15, 74J15, 74J30, 35Q55, 35Q53, 37K05, 37K40, 81U30, 76-05.

2006 Physics and Astronomy Classification Scheme:
46.40.Cd, 47.35.Bb, 47.54.Bd, 05.45.Yv, 47.10.ab, 52.35.Mw, 47.54.De.

Printed in the Netherlands.
This thesis is printed on acid-free paper by Wöhrmann Print Service, Zutphen.
Typeset using LaTeX 2_ε.
Cover design using *Scribus* by Lars Pesch and Natanael Karjanto.
Background picture on back cover: The Great Wave off Kanagawa by Katsushika Hokusai.

ISBN 90-365-2431-8

MATHEMATICAL ASPECTS

OF

EXTREME WATER WAVES

DISSERTATION

to obtain
the doctor's degree at the University of Twente,
on the authority of the rector magnificus,
Prof. Dr. W. H. M. Zijm,
on account of the decision of the graduation committee,
to be publicly defended
on Friday December 1, 2006 at 15.00

by

Natanael Karjanto
born on April 1, 1979
in Bandung, West Java, Indonesia

This thesis has been approved by the promotor
Prof. Dr. E. W. C. van Groesen

and the assistant promotor
Dr. Andonowati.

To my parents
Zakaria and Linda Karjanto
(許金瑞、陳玉林)
and my sister Ferli Tiani

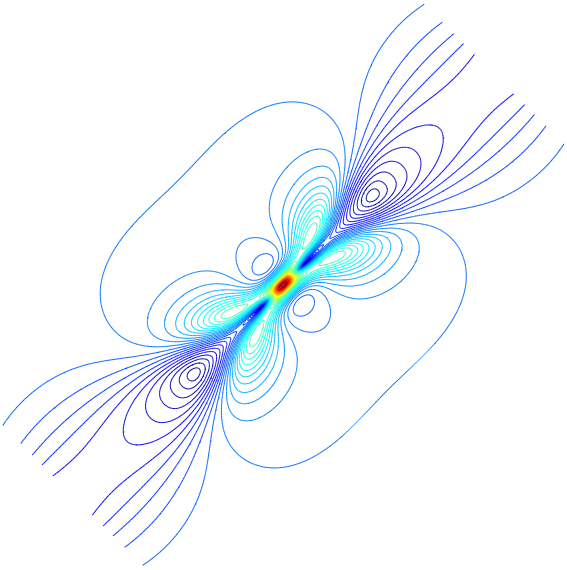

"But I, Jehovah, am your God,
the One stirring up the sea
that its waves may be boisterous.
Jehovah of armies is his name."
— Isaiah 51:15

Composition of the Graduation Committee

Chairperson and Secretary:

Prof. Dr. A. J. Mouthaan	University of Twente, The Netherlands

Promotor:

Prof. Dr. E. W. C van Groesen	University of Twente, Applied Mathematics

Assistant Promotor:

Dr. Andonowati	University of Twente, Applied Mathematics and Bandung Institute of Technology, Indonesia

Members:

Prof. Dr. C. Kharif	University of Aix Marseille, France
Prof. Dr. R. H. M. Huijsmans	MARIN, Wageningen, The Netherlands
Prof. Dr. A. E. Mynett	WL|Delft Hydraulics, The Netherlands
Prof. Dr. M. A. Peletier	Eindhoven University of Technology, The Netherlands
Dr. O. Bokhove	University of Twente, Applied Mathematics
Prof. Dr. S. A. van Gils	University of Twente, Applied Mathematics

Acknowledgement

Thank you for your interest and taking time to read my PhD thesis. Although only my name is displayed in the front cover of this thesis, no doubt many have contributed to the success of this project, resulting into this thesis. In the following paragraphs, I would like to express my sincere gratitude to many individuals and organizations for their generous helps so that I am able to complete my academic work and to experience a memorable study period.

The financial support from STW during this project, travel fund to attend conferences and printing this thesis is greatly appreciated. An excellent opportunity to conduct the experiments on extreme wave generation at the high-speed basin of MARIN is very much esteemed. Annual *Burgersdag*, PhD courses and PhD outings organized by J. M. Burgerscentrum, as well as travel support to attend the *Rogue Waves 2004* conference in Brest, France are highly regarded. The financial support during my research visit in Bandung, Indonesia from the European-Union Jakarta is highly valued. The accommodation support from the International Centre for Mechanical Sciences during a summer school in Udine, Italy is appraised. The travel support to attend the workshop in Stability and Instability of Nonlinear Waves and the conference of Nonlinear Waves and Coherent Structure in Seattle, Washington from the Society for Industrial and Applied Mathematics, the National Science Foundation and the Pacific Institute for the Mathematical Sciences is also appreciated.

For the foremost, I am indebted to Professor E. (Brenny) van Groesen, my promotor and my daily supervisor, for granting me a privilege to be involved in the combined master-doctoral program at his chair. He has inculcated a critical attitude toward mathematical and physical problems. His patience and perseverance has helped me significantly to improve my analytical, writing and oral skills. Above all, I thank him for reading and correcting my manuscripts meticulously, as well as improving the *samenvatting* of this thesis. I express my sincere grateful to Dr. Andonowati, my assistant promotor and also my undergraduate supervisor. She introduced me to the theory of water wave and opened up an opportunity to study abroad. I also thank her for the hospitality during my research visit in her laboratory at the Center for Mathematical Modelling and Simulation during summer period of 2004.

I thank Professor Christian Kharif who comes all the way from Marseille, France to be a member of my graduation committee. His complement about the content of this thesis is very encouraging. I thank Professor René Huijsmans from Delft who formerly was in MARIN and Professor Arthur Mynett from Delft Hydraulic for the fruitful input every semester during the project meeting and their willingness to be members of my graduation committee. I thank Professor Mark Peletier from Eindhoven for some good remarks. I thank other committee members from our Mathematical Physics and Computational Mechanics (MPCM) group: Dr. Onno Bokhove for many corrections of my thesis draft and Professor Stephan van Gils for useful input in the theory of stability analysis.

Many friends and colleagues in the MPCM group have shown a great help to my academic life at campus. I thank my undergraduate friend and former office mate Hadi Susanto for countless discussions on mathematics and faith, academic advices and his hospitality during my visit to Lumajang, East Java. *Matur nuwun!* I thank A. (Sena) Sopaheluwakan for many conversations, advices and helps with regard to *Maple*, *Matlab* and other computer related stuffs, not to forget in improving the Indonesian summary of this thesis. *Hatur nuhun!* I thank

Lars Pesch for improving my academic portfolio, helping with LaTeX and introducing me to *Scribus* for designing my thesis cover. *Danke schön!* I thank Sander Rhebergen for sharing an office together, helping in translating many Dutch documents and many stories about Africa. I also thank to my other cooperative office mates: Henk and Tim. I certainly enjoy many conversations during lunch time and other occasions with the group members: Fedderik, Chris Klaij, Arek, Davit, Pablo, Alyona, Remco, Marieke, Sanne, J. (Vita) Sudirham, Milan, Jaqueline, Lie, Ivan, Mike, Joris, Dom, Vijay, Yan, Manfred, Bernard and Bob. I thank Gerard Jeurnink for involving me in educational activities as his teaching assistant. I thank Gert Klopman for research discussions from the practical application, designing experiments, and water wave theory from different perspective. I appreciate tireless works from Marielle Plekenpol and Diana Dalenoord in handling administrative duties, organizing nice group outings and giving me opportunity to write some articles in *Ideaal!* I thank those who help me in translating my thesis summary into Dutch: Lars, Sander, Fedderik, Gerard , Henk, Marieke, and smoothing out by Brenny. I also thank Xu Yan for helping to insert the Chinese character of my parents' name. Certainly I will not forget former members of the group: Frits van Beckum, Debby Lanser, Kiran Hiremath (North Carolina), Helena Margaretha (for a privilege of *paranymph*), Monika Polner, Agus Suryanto, Edy Cahyono, Imelda van de Voorde (for helping in *Finite Element* homeworks, *hartelijk dank!*), Willem Visser, Christa van der Meer, Sandra Kamphuis, Renske Westerhof, Pearu Peterson (Estonia) and J. Kojo Ansong (Alberta, Canada).

I thank Johan Simonetti and Michel ten Bulte for their help in providing nice desk and good chairs to work conveniently. I thank Henri Holtkamp and Ewout Bakker for solving computer related problems. I thank Muharini and Marwan for many discussions on the theory of extreme water waves. I thank Tan Wooi Nee for the hospitality during my visit to Kajang, Malaysia. I thank Diah Chaerani for the hospitality and advices during my visit in Delft. I would like to thank members of the Indonesian Students Association in Enschede as well as Indonesian Applied Mathematical Society in the Netherlands for many nice conversations: Sri Nurdiati (for hospitality in Enschede and in Bogor and countless useful counsels), Henri Uranus, Irwan Endrayanto, Eko Purnomo, Jamari, Agung Julius, Agoes Moelja, Salman, Dadan Darmana and Jenny Ngo (for helping to improve my bike-repairing skills).

I would like to acknowledge members of the Christian Congregation of Jehovah's Witnesses in Enschede for providing service in English to sustain my spiritual life. I thank Rudi and Naomi van der Moolen, Alexander and Daniela Gathier, Joop and Annie Buitenhuis, Axel and Barbara Senf, Jerry Sadler, Bas and Monique van Aken, Albert and Coby Herbeke, Michael Nwani and Marlisa ten Have, Munyaburanga, Kaba, Sikazwe, Sabaya, Nkrumah and Robinson for nice meetings, working together in field service, transportation to the assemblies and to help in moving. Former members will never be forgotten: Anene, Dragstra, Ntela, do Santos (Angola), family van der Nent, Johnson, Losi (Canada), Jalink, family Oindo (Kenya), Chiuco (The Philippines), Sichivula, Chali and Sinyemba (Zambia), Søndergard (Denmark), Mensah, Afriyie, and Amoah (Ghana). I also thank the Enschede Oosterveld congregation for the friendship and organizing wholesome activities: Chin Yee Mooi, Brenda Vaartjes and family Kruidhof. I thank Tjeerd for the tutorial on *Adobe Illustrator*. I thank you all for your noblest *agape* love. May Jehovah God continue to shower blessings upon you.

Last but not least, I thank my loving parents and my dear younger sister for supporting me through prayer, as a continuous function that will never vanish to time indefinite.

Natanael Karjanto, Enschede, November 6, 2006.

Contents

List of Figures

Abbreviations and Acronyms

AAF	amplitude amplification factor
BBC	British Broadcasting Corporation
	bottom boundary condition
BVP	boundary value problem
CMq	Chu-Mei quotient
DFSBC	dynamic free surface boundary condition
DO	Dingemans-Otta
DS	Davey-Stewartson
IVP	initial value problem
IFREMER	*Institut français de recherche pour l'exploitation de la mer*
	(French Research Institute for Exploitation of the Sea)
KdV	Korteweg-de Vries
KFSBC	kinematic free surface boundary condition
KWMBC	kinematic wavemaker boundary condition
LDR	linear dispersion relation
MARIN	Maritime Research Institute Netherlands
MI	modulational instability
mKdV	modified Korteweg-de Vries
MTA	maximum temporal amplitude
NDR	nonlinear dispersion relation
NLS	nonlinear Schrödinger
PV	principal value
RHS	right-hand side
SFB	Soliton on Finite Background

Symbols and Notations

Notation	Description	Page
a, $a(x,t)$	wave amplitude; real-valued amplitude	6, 18
$a_n(\xi)$	amplitude spectrum, complex Fourier coefficient	57
approx	subscript indicates an approximation of a quantity	22
$A_0(\xi)$	plane wave solution of the NLS equation	24
A_j, $j = 1, 2$	SFB_1 and SFB_2, respectively	84
$A(\xi, \tau)$	complex amplitude of a wave group;	15
	exact solutions of the NLS equation	46
$A^*(\xi, \tau)$	complex conjugate of A	17
$\bar{A}$(x,t)	A in the physical variables	18
$\mathcal{A}(A)$	action functional of a function A	28
$A_{\mathrm{TC}}(\xi, \tau)$	complex amplitude of trichromatic waves	74
α_j, $j =$ 1–4	coefficients of the potential function $V(F)$	55
$\alpha_S(\xi)$	position dependent constant of integration	17
$\alpha_T(\tau)$	time dependent constant of integration	20
b_j, $j = -1, 0, 1$	coefficients of trichromatic waves	74
$B(\xi, \tau)$	complex amplitude of 2^{nd}-order double harmonic wave	16
	perturbation function to the plane wave solution	24
B_j, $j = 1, 2$	complex coefficient of the perturbation function B	24
β, β_0	dispersion coefficient of the NLS equation	17
c	nonlinear coefficient of the KdV type of equation	16
c c	complex conjugate of the preceding term(s)	13
crit	subscript denotes critical value	22
Crit	an optimization of a constrained variational problem	43
$C(\xi, \tau)$	complex amplitude of 2^{nd}-order nonharmonic wave	16
C_n	conserved quantities correspond to the NLS equation	29
$\mathbb{C}$	the set of complex numbers	24

Notation	Description	Page
des	subscript denotes design parameter	102
δ	variational or Fréchet derivative	28
δ_0	convergence criterium	101
E	dynamic energy, spectrum energy	40, 58
ϵ	small positive parameter	15
$\eta(x,t)$	surface wave field, wave elevation	15
$\eta_{\mathrm{c}}(x,t)$	complexification of η	70
$f(z)$	geometry of the wavemaker	138
$\hat{f}(\omega)$	spectrum or Fourier transform of a function $f(t)$	26
$F(\xi,\tau)$	complex amplitude of waves on finite background	37
F_j, $j=1,2$	SFB_j without the plane wave, $F_j = A_j/A_0$	84
g	gravitational acceleration	61
$G(\xi,\tau)$	real-valued displaced amplitude	37
γ, γ_0	nonlinear coefficient of the NLS equation	17
h	water depth	4
H	Hamiltonian	28
H_j, $j=1,2$	the denominator of F_j+1	84
$\bar{H}$	transformed Hamiltonian	39
$\mathcal{H}$	Hamiltonian density; Hilbert transform	28, 70
I	a value of an integral	71
k_0, $k(x,t)$	wavenumber; local wavenumber	6, 18
$K(\omega)$	inverse of $\Omega(k)$; differential operator	13
$K_{\mathrm{res}}(\omega)$	residue terms of $K(\omega)$	15
$K_{\mathrm{res}}(-i\partial_\tau)$	differential operator corresponds to K_{res}	15
L, $\mathcal{L}$	Lagrangian, Lagrangian density	28
$\mathcal{L}$	linear operator	136
λ	wavelength; Lagrange multiplier	4, 43
$\max_t$	maximum over time of the surface elevation η	50
M	maximum amplitude at the extreme position	102
μ, $\tilde{\mu}$	a parameter in the Ma solution	61

Notation	Description	Page
N	number of waves in one modulation period	102
$N(x)$	number of waves of a signal in a certain interval	71
$\mathbb{N}$	the set of natural numbers	140
$\mathbb{N}_0$	the set of nonnegative whole numbers	128
ν, $\tilde{\nu}$	(normalized) modulation frequency	25, 44
$\mathcal{O}$	order of a quantity	15
ω_0, $\omega(x,t)$	wave frequency; local frequency	13, 18
$\Omega(k)$, $\Omega(-i\partial_x)$	linear dispersion relation; differential operator	13
P_j, $j=1,2$	the real part of the numerator of F_j+1	84
ϕ, $\phi(x,t)$	(reduced) real-valued phase	18
$\phi_n(\xi)$	phase spectrum	58
$\Phi(x,t)$	$\theta(x,t)+\phi(x,t)$, real-valued phase	18
$\phi(\xi,\tau)$	displaced phase	37
$\phi(\xi)$	time independent displaced phase	41
$\phi(x,z,t)$	velocity potential function	138
Q_j, $j=1,2$	the imaginary part of the numerator of F_j+1	84
ref	subscript denotes reference of a quantity	110
res	subscript denotes residue of a quantity	15
$2r_0$	plane wave amplitude, asymptotic amplitude	25
R	coefficient of wave groups superposition	16
R_{nm}	coefficient of $e^{im\theta}$ with order ϵ^n	16
$\mathbb{R}$	the set of real numbers	16
ρ, $\tilde{\rho}$	a quantity that depends on μ	61
s; s_0, s_M	wave steepness; initial, extremal steepness	102
$S(t)$	wavemaker motion	138
σ, $\tilde{\sigma}$	(normalized) growth rate	25
σ_j, $j=1,2$	two growth rates in SFB_2	85
t	time in physical variable	15
T_c	carrier wave period, $T_\mathrm{c}=2\pi/\omega_0$	102
T	modulation period, $T=2\pi/\nu$	49

Notation	Description	Page
τ	time in a moving frame of reference	15
θ_j, $j = 1, 2$	phase of the complex coefficients B_j, $j = 1, 2$	25
$\theta(x, t)$	$k_0 x - \omega_0 t$, phase of monochromatic wave	16
$\mathbf{u}$	velocity vector defined by potential function ϕ	138
$V(F)$, $V(G, \phi)$	potential function, potential energy	40
$W(G, \phi)$	normalized potential energy	39
x	position in physical variable	15
ξ	position in a moving frame of reference	15
$\Xi(z, t)$	wavemaker position	138
$\mathbb{Z}$	the set of whole numbers	57
$\mathbb{Z} \setminus \mathbb{N}$	the set of non positive whole numbers	128
$\zeta(\tau)$	special functions related to breather solutions	43

Chapter 1

Introduction

1.1 Background and motivation

1.1.1 Extreme wave events in the oceans

We start to quote parts of a few reports about the occurrences of extreme waves in the oceans.

- *"In late 1942, carrying 15,000 U.S. soldiers bound for England, the Queen Mary hit a storm about 700 miles off the coast of Scotland. Without warning amid the tumult, a single, mountainous wave struck the ocean liner, rolling it over and washing water across its upper decks. Luckily, the ship managed to right itself and continue on its voyage." —**Science News Online**, 23 November 1996.*
- *"In the past 30 years, hundreds of ships have gone down in mysterious circumstances, taking thousands of lives with them. Naval architects now believe that a large number of these were sunk by rogue waves." —Monsters of the deep, **New Scientists** Magazine issue 2297, 30 June 2001.*
- *"Since 1990, 20 vessels have been struck by waves off the South African coast that defy the linear model's predictions. And on New Year's Day, 1995 a wave of 26m was measured hitting the Draupner oil rig in the North Sea off Norway." —**BBC Horizon** Television programme, 14 November 2002.*
- *"They are known as 'rogue waves'–the towering walls of water that, some experts suspect, sink tens of ships every year." —**Nature**, volume **430**, 29 July 2004, page 492.*
- *"During the last two decades, more than 200 super-tankers-ships over 200 meters (656 feet) long–have sunk beneath the waves. Rogue waves are thought to be the cause for many of these disasters, perhaps by flooding the main hold of these giant container ships. . . . Offshore oil rigs also get hit by rogue waves. Radar reports from the North Sea's Gorm oil field show 466 rogue-wave encounters in the last 12 years."*

— "Monster" waves surprisingly common, satellites show, ***National Geographic*** *news, 10 August 2004.*

- *"Over the last two decades more than 200 super-carriers–cargo ships over 200 m long–have been lost at sea. Eyewitness reports suggest many were sunk by high and violent walls of water that rose up out of calm seas." —****BBC News Report*** *on Wave Research, 21 August 2004.*
- *"Bad weather has sunk more than 200 supertankers and container ships during the past 20 years, and researchers believe that monster 10-story-tall ocean waves are often the culprit." —Surf's Up-Way Up,* ***Scientific American****, October 2004, volume* ***291****, issue 4, page 38.*
- *"Stories told by seamen about walls of water as high as 10-story buildings, waves that could destroy even big cargo ships, were treated as legends and myths. But these waves do exist. ... Over two hundred ships have been their victims in the past two decades. In the North Atlantic alone, between 1995 and 1999, 27 big vessels foundered after being hit by freak waves." —****Janson*** *Television programme, 28 December 2004.*

These reports show that extreme waves are dangerous to merchant ships, offshore platforms, naval fleets, and other sea-going marine structures. We will take a closer look at the characteristics of these waves.

1.1.2 Possible causes of extreme waves

As reported above, 'extreme waves' are unusually very large waves which appear unexpectedly even under relatively calm conditions in the open ocean. They are also known as 'freak waves', 'rogue waves', 'giant waves', 'monster waves', 'steep wave events', 'gargantuan waves', 'abnormal waves', 'exceptional waves', or 'cape rollers'. The wave height can reach 30 meters or more from crest to trough. They are so large that they can overwhelm and sink even the sturdiest ships. However, extreme waves can also occur in bad weather conditions when the average wave height is high and possibly several big waves come together to create a monster. See Figure 1.1 as an example. Extreme waves are defined as waves larger than 2.2 times the significant wave height [Dean, 1990]. In this context, the significant wave height is defined as the average height of the highest one third of the waves in a long sample.

The precise causes of extreme waves are still being investigated and scientists try to find out these possible causes. These possible causes can be an internal one, which occurs in homogeneous situations, or an external one, which occurs in nonhomogeneous situations, or a combination of both causes. Internal causes for extreme waves are wave focussing and nonlinear instability. Wave focussing may occur in the deep ocean, when unstable waves self-focus in bad weather conditions, creating extreme waves. Nonlinear processes may cause waves of different amplitudes and wavelengths to interact with each other and form large waves. Since the chance to generate extreme waves can be very small, many sailors claim that they seldom occur, for instance once in every 10,000 years. This suggests to study the extreme waves from a statistical probability

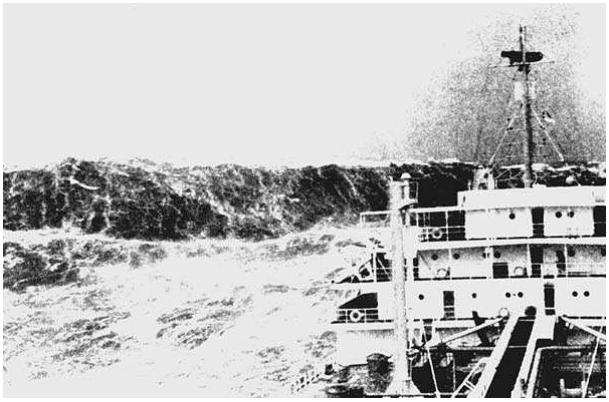

Figure 1.1: One photograph showing an extreme wave in Biscayne Bay, Florida, reproduced from *Mariners Weather Log*, volume **38** no 4.

point of view. However, the latest data from satellites suggest that they take place more frequently. This is also supported by an examination of five years of wave measurements made in the South Atlantic Ocean [Liu and Pinho, 2004].

External causes for extreme waves are due to geometric shape of coasts and the bathymetry* of a sea, interaction of wind forces and currents, and by storm systems of low pressure such as typhoons or hurricanes. An example of the geometric shape is the coast of Norway where a shallow sea bottom focusses into one spot, creating extreme waves. Examples of wind-current interaction occur in the south-eastern coast of South Africa when wind pushes against a strong Agulhas current flowing southward, within or near the Gulf Stream in the North Atlantic, in the south of Japan that enjoys the warm Kuroshio current and the notorious seas off Cape Horn in South America. Examples of extreme waves caused by storms are typhoons in certain areas of Pacific Ocean and hurricane Ivan in the Gulf of Mexico. The latter one is recently reported in *Science* magazine [Wang et al., 2005].

Extreme waves should not be confused with tsunamis. The latter waves are series of travelling waves of extremely long length and period and are caused by a sudden displacement of large volume of water. Usually, tsunamis are generated by disturbances associated with earthquakes occurring below the ocean floor, volcanic eruptions, landslides or even oceanic meteor impacts. The height of the waves in the open ocean is very small, a couple of meters at most, so they pass under ships and boats undetected. The height is growing as they reach shallow waters. Their length from one crest to the next, can be up to 200 km long, and they travel in the deep ocean at speeds around 700 km/hr. Compared to tsunamis, extreme waves have very short wavelengths, less than 2000 m. Therefore, in the open ocean, tsunamis are shallow-water waves and

*the underwater equivalent of topography

extreme waves are deep-water waves. A wave is considered deep-water if $\lambda/h < 2$ and shallow-water if $\lambda/h > 2$, where λ is the wavelength and h is the water depth. In Chapter 6, we will report about experiments in a wave tank where the wavelength is $\lambda = 4.4$ m and the water depth $h = 3.55$ m, so $\lambda/h \approx 1.24$. Even though these waves are considered as intermediate water waves, in the wave basin they are already quite 'extreme' since it is based on the theoretical model of extreme wave evolution.

1.1.3 Current research on extreme waves

The term 'freak waves' itself is apparently already introduced as early as the 1960's by [Draper, 1965]. Much research has been done since then to study and to predict the occurrence of extreme waves. Observation of extreme wave events using satellites images of the ocean surfaces has been done by the European Space Agency. One of its project is called *MaxWave*, devoted to observe, to model, and eventually to forecast the occurrence of extreme waves [Dankert et al., 2003; Rosenthal, 2005]. Another project is called *WaveAtlas*, which uses the images to create a worldwide atlas of extreme wave events.

Theoretical studies of extreme waves can be divided into a deterministic approach and a statistical approach. In the deterministic approach, scientists use mathematical models to describe the evolution of extreme waves. For example, the nonlinear Schrödinger (NLS) equation, also known as the cubic Schrödinger equation, has been proposed as early as 1970's to model extreme waves [Smith, 1976]. In his paper the author apparently uses the term 'giant waves'. Further in 2000, [Osborne et al., 2000] study the dynamical behaviour of extreme waves in deep-water waves using solutions of the NLS equation in $1+1$ or (x,t) and $2+1$ or (x,y,t) dimensions. Using the inverse scattering technique, they present and discuss analytical solutions of $1+1$ NLS, in which one of the solutions is known as the Soliton on Finite Background (SFB). For $2+1$ NLS, they demonstrate numerical simulations of the equation and show the existence of unstable modes which can take the form of large amplitude extreme waves. More about the analytical and spectral study of extreme wave properties of exact solutions of the NLS equation that describe the nonlinear evolution of deep-water waves is given in [Osborne, 2001]. Apart from the NLS equation, some scientists use the Korteweg-de Vries (KdV) equation for extreme wave modelling [Kharif et al., 2000; Pelinovsky et al., 2000; Kokorina and Pelinovsky, 2002; Pelinovsky et al., 2004]. A computation of modulated wave trains using a fully nonlinear inviscid irrotational flow model in a spatially periodic domain and its comparison with the NLS equation to produce extreme wave events is given in [Henderson et al., 1999].

The statistical approach to study extreme waves phenomena is related to probabilistic aspects at random locations. A study of extreme wave generation in a random oceanic sea state characterized by the Joint North Wave Project spectrum can be found in [Onorato et al., 2001]. A study of extreme waves in the context of a statistical or stochastic approach in the connection with nonlinear four-wave interactions is given in [Janssen, 2003]. Statistics of weakly nonlinear high random waves with a deriva-

tion of new analytical models for the prediction of nonlinear extreme waves by means of the theory of quasideterminism of Boccoti [Boccotti, 2000] is published recently [Fedele and Arena, 2005]. The statistical study of sea waves started as early as 1950's with particular attention to properties of wave groups in Gaussian noise. Studies of the extreme waves based on the 'New Year wave' recorded at Draupner platform in the North Sea are given for instance in [Walker et al., 2004; Gibson et al., 2005; Haver, 2005]. A focusing mechanism to produce extreme waves at random locations when ocean swell traverses an area of random current is shown by [White and Fornberg, 1998]. Recently, an overview of extreme waves formation in the context of a statistical event from Longuett-Higgins and the refraction model from White and Fornberg is given in [Heller, 2005]. A review of the physical mechanisms of the extreme waves phenomena including both deterministic and statistical approaches is given by [Kharif and Pelinovsky, 2003; Olagnon and Prevosto, 2005; Grimshaw and Saut, 2005].

1.1.4 Extreme wave modelling in a hydrodynamic laboratory

The mechanisms of extreme wave generation have become an issue of interest in many projects and research topics. Maritime Research Institute Netherlands (MARIN) aims to generate and study large waves in one wave basin of its laboratory. Eventually, MARIN will use these large waves to test ships, offshore platforms and other floating structures in the wave basin. For extreme wave generation in a hydrodynamic laboratory, we are interested in the deterministic aspects instead of the random ones. Extreme wave generation in the entire contents of this thesis will always be deterministic. It means that we try to generate the desired extreme wave at a certain location in the wave tank. This is done by prescribing an initial signal as input to the wavemaker, for which the wave signal is found from a mathematical model for extreme wave evolution. More details about how the experiments are conducted can be found in Chapter 6.

In this thesis, we will concentrate on the study of a solution of a mathematical model that describe the evolution of extreme wave events. To study theoretical aspects of extreme wave characteristics, we choose the 'spatial' NLS equation as a mathematical model to our problem. This type of NLS equation is suitable for the signalling problem, when we give an initial signal to the wavemaker and the model predicts the propagation in space. This is different from the 'temporal' NLS equation, for which, given an initial condition, the model predicts the evolution in time. Furthermore, we have selected one family of exact solutions of the spatial NLS equation that describe extreme wave events in a wave tank. This family of exact solution is known as the SFB. More information on the NLS equation will be given in Chapter 2 and more properties of the SFB are presented in Chapter 3.

The choice to study the SFB family in great detail is motivated by the fact that the asymptotic behaviour of this solution at the far field describes (the envelope of) a modulated wave. This modulated surface wave is a solution of the linear equation obtained from a perturbation analysis of the plane wave solution of the NLS equation. According to the linear theory, this plane wave solution is unstable under a long mod-

ulation, and the exponential growth is known as the linear 'modulational instability', or 'sideband instability', or 'Benjamin-Feir instability' [Benjamin and Feir, 1967]. This type of instability is observed not only in water waves but also in many fields of wave propagation in nonlinear media. Therefore, in order to describe a complete evolution of a modulated wave signal in the wave tank, we choose the SFB as a nonlinear extension of the linear modulational instability into the nonlinear regime. The relation between modulational instability and the SFB solution of the NLS equation is explained in Subsection 3.3.2 of Chapter 3. See also [Akhmediev and Korneev, 1986].

Additionally, we use the maximum temporal amplitude (MTA) of the SFB for application in wave generation. The MTA is introduced in the field of nonlinear optics [Andonowati and Van Groesen, 2003], but it has also applications in water waves. It is defined at each position as the maximum over time of a wave field. From this definition, the MTA describes the largest wave amplitude that can appear at a certain position. It can also be interpreted as a stationary envelope of the wave group envelope. In a wave tank, the MTA has a meaningful interpretation, namely the highest points on the wall wetted after a long time of evolution. An explicit expression can be found for the MTA corresponding to the SFB. This is exceptional since an explicit expression for the MTA is not easily obtained from the mathematical model that describes the nonlinear dynamical evolution of a wave.

In our application, the MTA is a very useful tool for designing a strategy of extreme wave generation. Using the MTA, we are able to determine the signal input for the wavemaker that produces an extreme wave signal at the desired position. A plot of the MTA gives information about the extreme position, which is the position where the envelope of a wave signal is at its largest value. Hence, to produce this extreme wave signal at a particular position in the laboratory, the details of the initial modulated wave signal depend on the MTA plot. Therefore, it is important to know in advance the properties and the characteristics of the SFB wave signal, also to avoid breaking before the wave reaches the extreme position. This breaking criterium is determined by the wave steepness $a\,k \geq 0.443$, where a is the wave amplitude and k is the wavenumber. A plot of the MTA together with the spatial evolution and its envelope of the SFB is given in Figure 1.2. More information of the MTA of the SFB is found in Chapter 3; and its application to wave generation is found in Chapter 6.

We see in Figure 1.2 that waves of moderate amplitude at the left propagate downstream to form wave groups. These wave groups increase in amplitude as they propagate and reach a maximal wave height at the extreme position $x = 0$ for a specified time. We observe that close to $x = 0$, the wave groups increase in amplitude faster within the same distance than when they are far away at the left. This is due to the nonlinear effect of the Benjamin-Feir instability. At a distance sufficiently far from the extreme position, the effect is only linear due to the exponential behaviour of this instability. After reaching the maximum wave height, the wave groups decrease in amplitude and return to a modulated monochromatic wave at the right with a phase shift

compared to the monochromatic wave at the right. The MTA has a space symmetry property with respect $x = 0$.

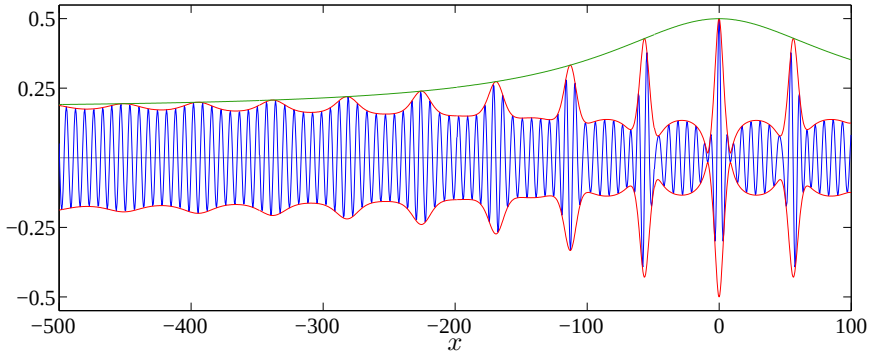

Figure 1.2: Shown is a plot of a wave field, its envelope and MTA related to a characteristic member of the SFB family. At a specified time, the plot shows horizontally the distance from the position of maximal wave height at $x = 0$. The distance and the vertical elevation are measured in meters, and the waves are on a layer of water depth of 5 m.

The NLS equation is not the only mathematical model that scientists have studied for this problem. Note that several authors prefer the modified NLS equation and other higher order NLS equations as mathematical models to describe extreme waves [Trulsen and Dysthe, 1997; Trulsen and Stansberg, 2001]. In this thesis we will concentrate on the NLS equation instead of the higher order equations, since the NLS equation has as advantage that it possesses exact solutions that the higher orders equations do not have. Studying these families of exact solutions is very insightful from a theoretical point of view and useful from a practical point of view for an initial stage of study in extreme wave generation.

1.2 Outline of the thesis

This thesis is divided into seven chapters; the rest of the thesis is briefly summarized as follows.

Chapter 2. In this chapter we review known mathematical descriptions for surface wave evolution. We are interested in a nonlinear and dispersive wave equation that describes extreme wave phenomena. In particular, we choose the nonlinear (cubic) Schrödinger (NLS) equation of the spatial type instead of the temporal one since it is more suitable to model our wave evolution in a wave tank. We derive the spatial NLS equation from a KdV type equation with exact dispersion relation for water wave potential flow using the multiple scale method. We also derive the corresponding phase-amplitude equations using the polar representation of the complex amplitude and introduce the Chu-Mei quotient from the nonlinear dispersion relation. Furthermore,

we compare the approximate dispersion of both the temporal and the spatial NLS equations. It is found that the spatial type approximates the dispersion relation better than the temporal one for increasing carrier wavenumber and is exact for the deep-water case. We derive the modulational instability corresponding to the NLS equation and we show that both plane-wave and single-soliton solutions of the NLS equation are coherent state solutions. We also present a formulation of the NLS equation from a variational principle that will be used in Chapter 3.

Chapter 3. In this chapter we derive properties of waves on finite background. These are exact solutions of the NLS equation. There are three special types of waves on finite background, also known as breather type of solutions, that have been proposed as models of extreme waves [Dysthe and Trulsen, 1999]. They are the Soliton on Finite Background (SFB), also known as the Akhmediev solution, the Ma breather, and the rational solution, also known as the Peregrine solution. We will concentrate on the SFB solution since it is a good model for extreme wave generation, that is practically to generate, while the Ma solution is impossible and the rational solution is difficult to generate in practice. The reason are as follows. The SFB wave signal can be generated with a moderate amplitude at the wavemaker. The Ma wave signal has necessarily the maximal amplitude already at the wavemaker. The rational wave signal is still possible to generate in principle, but it has infinite modulation period.

To study these waves on finite background, we will introduce a novel transformation to the displaced phase-amplitude variables with respect to a background of the monochromatic plane wave solution in the context of the NLS equation. The transformation of the displaced-phase is restricted to be time independent. The change of phase with positions physically corresponds to a change of the wavelength of the carrier wave of a wave group. This turns out to be the only driving force responsible for the nonlinear amplitude amplification toward extreme wave events. Remarkably, the assumption that the displaced-phase is time independent leads to the breather solutions of the NLS equation mentioned above. A particulary extensive study is devoted to the SFB solution. This solution is the unstable modulated plane-wave solution of the NLS equation, has amplitude amplification up to maximum factor of 3 and is a very good candidate for extreme wave generation. The contents of this chapter are partly based on the papers by [Andonowati et al., 2006; Van Groesen et al., 2006].

Chapter 4. This chapter is motivated to study in detail one physical property of the SFB, namely phase singularity and wavefront dislocation. This phenomenon occurs at singular points of a wave field where the amplitude vanishes. We discuss it in a more general setting for surface wave fields. The phenomenon is purely linear. We introduce the Chu-Mei quotient from the (nonlinear) dispersion relation for wave groups as a result of the nonlinear transformation to phase-amplitude variables. We observe that the unboundedness of this quotient is responsible for the appearance of wavefront dislocation. The study of physical property of the SFB and the accompanying phenomena of phase singularity and wavefront dislocation have not been discussed in

the literature. The connection of the Chu-Mei quotient and wavefront dislocation also seems to be novel in the context of wave dislocation theory.

Chapter 5. This chapter deals, just as Chapter 3, with special solutions of the NLS equation. We now study a family of higher order solutions of the NLS equation that also describe modulational instability, namely SFB_2. Similar to SFB, now denoted as SFB_1, this class of solutions describes to the waves on finite background. Indices 1 and 2 refer to the number of initial sideband pairs in the spectrum domain. For a special choice of parameters, solutions from SFB_2 can have an amplitude amplification up to a factor of 5. Furthermore, SFB_2 solutions can also show wavefront dislocation and phase singularity.

Chapter 6. This chapter deals with experiments on extreme wave generation that have been conducted at high speed basin of MARIN. The experiments are designed by Gert Klopman, Andonowati and Natanael Karjanto. We try to investigate both qualitative and quantitative comparisons between the theoretical and the experimental signals. This kind of comparisons is novel and part of the work has not been reported elsewhere in the literature. It should be noted that all experimental results show amplitude increase, non-breaking waves according to the Benjamin-Feir instability of the SFB solution of the NLS equation. We also observe that both the carrier wave frequency and the modulation period are conserved during the propagation in the wave basin. A significant difference is that the experimental wave signal does not preserve the symmetry structure as the theoretical SFB does.

The dynamic evolution in the Argand diagram (complex plane) gives an understanding of the qualitative comparison between the experimental signal and a perturbed SFB signal. This comparison explains why the experimental signals have two phase singularities at two different positions and the extreme position is located in between. We also explore the concept and properties of the MTA in relation with the experimental design. We compare quantitatively the sensitivity of the MTA and its extreme position toward parameter changes and variations in a model parameter. We discover that the extreme position depends sensitively toward these changes. For SFB parameters, the extreme position is more sensitive toward the changes in the asymptotic amplitude rather than the maximum amplitude. For NLS parameters, it is essential to use an accurate value of the nonlinear coefficient for the extreme position to occur at the desired location. The investigation of these parameters using the MTA curves in the context of extreme wave generation is new and useful for understanding the experiments.

Chapter 7. We present the highlights that this thesis has contributed. We end this thesis with some conclusions on the extreme wave modelling. Furthermore, we give some recommendations on possible future research directions.

References

[Akhmediev and Korneev, 1986] N. N. Akhmediev and V. I. Korneev. Modulation instability and periodic solution of the nonlinear Schrödinger equation. *Theor. Math. Phys.* **69**: 1089–1092, 1986. Translated from *Teor. Mat. Fiz. (USSR)* **69**(2): 189–194, 1986.

[Andonowati and Van Groesen, 2003] Andonowati and E. van Groesen. Optical pulse deformation in second order nonlinear media. *J. Nonlinear Opt. Phys. Mat.* **12**(2): 221–234, 2003.

[Andonowati et al., 2006] Andonowati, N. Karjanto, and E. van Groesen. Extreme wave phenomena in down-stream running modulated waves. *Appl. Math. Modelling*, article in press, corrected proof, available online 27 June 2006.

[Benjamin and Feir, 1967] T. B. Benjamin and J. E. Feir. The disintegration of wave trains in deep water. *J. Fluid Mech.* **27**: 417–430, 1967.

[Boccotti, 2000] P. Boccotti. *Wave Mechanics for Ocean Engineering*, Elsevier Science, New York, 2000.

[Dankert et al., 2003] H. Dankert, J. Horstmann, S. Lehner and W. Rosenthal. Detection of wave groups in SAR images and radar image sequences. *IEEE Trans. Geosci. Remote Sens.* **41**(6): 1437–1446, 2003.

[Dean, 1990] R. G. Dean. Freak waves: a possible explanation. In A. Tørum and O. T. Gudmestad, editors, *Water Wave Kinematics*, pp 609–612, Kluwer Academic Publishers, Amsterdam, 1990.

[Draper, 1965] L. Draper. 'Freak' ocean waves. *Marine Observer*, **35**: 193–195, 1965.

[Dysthe and Trulsen, 1999] K. B. Dysthe and K. Trulsen. Note on breather type solutions of the NLS as models for freak-waves. *Phys. Scripta* **T82**: 48–52, 1999.

[Fedele and Arena, 2005] F. Fedele and F. Arena. Weakly nonlinear statistics of high random waves. *Phys. Fluids* **17**:026601, 2005.

[Gibson et al., 2005] R. Gibson, C. Swan, P. Tromans, L. Vanderscuren. Wave crest statistics calculated using a fully nonlinear spectral response surface method. In M. Olagnon and M. Prevosto, editors, *Rogue Waves 2004*. Proceedings of a workshop in Brest, France (October 20–22, 2004), 10 pp, 2005.

[Grimshaw and Saut, 2005] R. Grimshaw and J.-C. Saut, organizers. *Rogue Waves 2005*. Proceedings of a workshop in Edinburgh, United Kingdom (December 12–15, 2005), 2005. `http://www.icms.org.uk/meetings/2005/roguewaves/index.html`

[Haver, 2005] S. Haver. A possible freak wave event measured at the Draupner jacket January 1, 1995. In M. Olagnon and M. Prevosto, editors, *Rogue Waves 2004*. Proceedings of a workshop in Brest, France (October 20–22, 2004), 8 pp, 2005.

[Heller, 2005] E. Heller. Freak waves: just bad luck, or avoidable? *Europhysics News* **36**(5): 159–162, 2005.

[Henderson et al., 1999] K. L. Henderson, D. H. Peregrine and J. W. Dold. Unsteady water wave modulations: fully nonlinear solutions and comparison with the nonlinear Schrödinger equation. *Wave Motion* **29**: 341–461, 1999.

[Janssen, 2003] P. A. E. M. Janssen. Nonlinear four-wave interactions and freak waves. *J. Phys. Ocean.* **33**: 863–884, 2003.

[Kharif et al., 2000] C. Kharif, E. Pelinovsky and T. Talipova. Formation de vagues géantes en eau peu profonde. *C. R. Acad. Sci. Paris, Séerie II b, Mécanique des fluides*, **328**(11): 801–807, 2000.

[Kharif and Pelinovsky, 2003] C. Kharif and E. Pelinovsky. Physical mechanisms of the rogue wave phenomenon. *Eur. J. Mech. B: Fluids* **22**: 603–634, 2003.

[Liu and Pinho, 2004] P. C. Liu and U. F. Pinho. Freak waves–more frequent than rare! *Annal. Geophys.* **22**: 1839–1842, 2004.

[Olagnon and Prevosto, 2005] M. Olagnon and M. Prevosto, editors. *Rogue Waves 2004*. Proceedings of a workshop in Brest, France (October 20–22, 2004), 308 pp, 2005.

[Onorato et al., 2001] M. Onorato, A. R. Osborne, M. Serio and S. Bertone. Freak waves in random oceanic sea states. *Phys. Rev. Lett.* **86**: 5831–5834, 2001.

[Osborne et al., 2000] A. R. Osborne, M. Onorato, and M. Serio. The nonlinear dynamics of rogue waves and holes in deep-water gravity wave trains. *Phys. Lett. A* **275**: 386–393, 2000.

[Osborne, 2001] A. R. Osborne. The random and deterministic dynamics of 'rogue waves' in unidirectional, deep-water wave trains. *Mar. Struct.* **14**: 275–293, 2001.

[Kokorina and Pelinovsky, 2002] A. Kokorina and E. Pelinovsky. The applicability of the Korteweg-de Vries equation for description of the statistics of freak waves. *J. Korean Soc. Coastal and Ocean Eng.* **14**(4): 308–318, 2002.

[Pelinovsky et al., 2000] E. Pelinovsky, T. Talipova and C. Kharif. Nonlinear-dispersive mechanism of the freak wave formation in shallow water. *Physica D* **147**: 83–94, 2000.

[Pelinovsky et al., 2004] E. Pelinovsky, T. Talipova, M. Ruderman, and R. Erdelyi. Freak waves described by the modified Kortewegde Vries equation. *Izvestia, Russian Academy of Engineering Sciences*, *Applied Mathematics and Mechanics Series*, **6**: 3–16, 2004.

[Rosenthal, 2005] W. Rosenthal. Result of the MaxWave project. In *Proceedings of the 14th 'Aha Huliko'a Hawaiian Winter Workshop Rogue Waves*, University of Hawaii, January 25–28, 2005

[Smith, 1976] R. Smith. Giant waves. *J. Fluid Mech.* **77**: 417–431, 1976.

[Trulsen and Dysthe, 1997] K. Tappert and K. B. Dysthe. Freak waves–a three-dimensional wave simulation. In *Proceedings of the Twenty-First (1996) Symposium on Naval Hydrodynamics*, Trondheim, Norway, June 2428, pp 550–558, 1997.

[Trulsen and Stansberg, 2001] K. Trulsen and C. T. Stansberg. Spatial evolution of water surface waves: numerical simulation and experiment of bichromatic waves. In *Proceedings of the Eleventh (2001) International Offshore and Polar Engineering Conference*, Stavanger, Norway, June 17–22, pp 71–77, 2001.

[Van Groesen et al., 2006] E. van Groesen, Andonowati and N. Karjanto. Displaced phase-amplitude variables for waves on finite background. *Phys. Lett. A* **354**: 312–319, 2006.

[Walker et al., 2004] D. A. G. Walker, P. H. Taylor and R. E. Taylor. The shape of large surface waves on the open sea and the Draupner New Year wave. *Appl. Ocean Res.* **26**: 73–83, 2004.

[Wang et al., 2005] D. W. Wang, D. A. Mitchell, W. J. Teague, E. Jarosz and M. S. Hulbert. Extreme waves under hurricane Ivan. *Science* **309**: 896, 5 August 2005.

[White and Fornberg, 1998] B. S. White and B. Fornberg. On the chance of freak waves at sea. *J. Fluid Mech.*, **355**: 113–138, 1998.

Chapter 2

Mathematics of water waves

2.1 Introduction

In this chapter we present the mathematical description of surface water waves. The theory of water waves has a long history since the time of Isaac Newton (1643-1727). For an overview on the origins and the development of water wave theory, the readers are encouraged to consult [Craik, 2004] and [Craik, 2005] for a thorough examination of Stokes' papers and letters concerning water waves as well as on how Stokes built on the earlier foundations to establish a definite theory of linear and weakly nonlinear waves.

We are interested in nonlinear and dispersive wave equations that describe extreme wave phenomena. In fact, the context of wave evolution in this thesis is meant to be the dispersive type of wave motion. Potential flow is considered with no shear or vertical components. Another class of wave motion is the hyperbolic type, since it is formulated mathematically in terms of hyperbolic differential equations. A formal definition of dispersive waves is given in [Whitham, 1974]. Elementary solutions for linear problems are given as $\eta(x,t) = Ae^{i(kx-\omega t)} + \text{c c}$, where c c denotes the complex conjugate of the preceding term; the wavenumber k and the frequency ω are related by the 'linear dispersion relation' $\omega = \Omega(k)$. Dispersive means that this function has to be real, the group velocity $\Omega'(k)$ is not constant, which means that the wave velocity depends on the wavelength. Since the linear dispersion relation for surface water waves is given by $\Omega(k) = k\sqrt{(\tanh k)/k}$, this function is invertible and we will write $k = K(\omega)$, where $K = \Omega^{-1}$ is the inverse. The last representation is used more often in the signalling problem while the former one is used more often in the initial value problem. However, in this thesis we will use both representations interchangeably.

One example of a nonlinear dispersive wave equation is the Korteweg-de Vries (KdV) equation. The readers who are interested to the historical essays on the KdV equation can consult [Miles, 1981; Drazin and Johnson, 1989; Bullough and Caudrey,

1995]. For narrow-banded spectrum of wave groups, the nonlinear Schrödinger (NLS) equation can be derived from the KdV equation. Although both the KdV and the NLS equations are two of many mathematical models describing wave evolution, there is a significant difference. The KdV equation describes the waves themselves (the elevation of the water surface) while the NLS equation describes the envelope of wave groups. 'Wave groups', sometimes also called 'wave packets', are localized groups of waves which travel with the group velocity and naturally occur when the waves are dispersive and have small deviation of an averaged wavelength. Hence, a wave group is composed by a superposition of a collection of waves with frequencies centered around one value.

In the following sections, we will consider various properties of the NLS equation. This chapter is organized as follows. Section 2.2 starts with linear dispersive wave equations, and the approximative description of wave groups. Section 2.3 continues with nonlinear dispersive wave equations. This section explains the relationship between the KdV and the NLS equation. Both spatial and temporal NLS equation are derived in this section, together with the corresponding phase-amplitude equations. Section 2.4 deals with the quality of the dispersion in the NLS equation describes the linear modulational (Benjamin-Feir) instability, and resumes the simplest coherent states of the equation. Section 2.5 presents the NLS equation from a different perspective, namely from the variational formulation that will be used extensively in Chapter 3.

2.2 Linear dispersive wave equation

For a linear dispersive wave equation, it is possible to write the general solution in the Fourier transform representation. Let a linear wave problem be specified by the evolution equation:

$$\partial_t \eta + i\Omega(-i\partial_x)\eta = 0. \tag{2.1}$$

Then the general solution $\eta(x,t)$ is given in the Fourier representation:

$$\eta(x,t) = \frac{1}{2\pi}\int_{-\infty}^{\infty} F(\omega) e^{i(kx-\omega t)} d\omega, \tag{2.2}$$

where k and ω are related by the linear dispersion relation. For a signalling problem, $F(\omega)$ is the Fourier transform of the initial signal $\eta(0,t)$, given as

$$F(\omega) = \int_{-\infty}^{\infty} \eta(0,t) e^{i\omega t} dt. \tag{2.3}$$

The wavenumber k and the frequency ω are related by the linear dispersion relation $\omega = \Omega(k)$ or $k = K(\omega)$, where $K = \Omega^{-1}$. From the fact that $k = K[\Omega(k)]$, the relations between its derivatives can be found explicitly:

$$K'(\omega_0) = \frac{1}{\Omega'(k_0)} \qquad \text{and} \qquad K''(\omega_0) = -\frac{\Omega''(k_0)}{[\Omega'(k_0)]^3}. \tag{2.4}$$

Under the assumption that $F(\omega)$ is narrow-banded spectrum around ω_0, i.e. vanishingly small outside a small interval around ω_0, we write the dispersion relation in its Taylor expansion around ω_0:

$$k = K(\omega) = \sum_{n=0}^{\infty} \frac{1}{n!} K^{(n)}(\omega_0)(\omega-\omega_0)^n = k_0 + K'(\omega_0)(\omega-\omega_0) + \frac{1}{2!}K''(\omega_0)(\omega-\omega_0)^2 + \dots. \tag{2.5}$$

Therefore, we can write $\eta(x,t) = A(\xi,\tau)e^{i(k_0 x - \omega_0 t)}$, where A is the corresponding complex-valued amplitude of the wave group

$$A(\xi,\tau) = \frac{1}{2\pi}\int_{-\infty}^{\infty} F(\omega_0+\nu)e^{-i(\tau - K_{\text{res}}(\omega)/\nu^2\xi)}d\nu, \tag{2.6}$$

where $\nu = \omega - \omega_0 = \mathcal{O}(\epsilon)$, ϵ is a small positive parameter, $\xi = \nu^2 x$, $\tau = \nu(t - K'(\omega_0)x)$ and

$$K_{\text{res}}(\omega) = K(\omega) - [k_0 - K'(\omega_0)\nu] = \left(\frac{1}{2!}K''(\omega_0) + \frac{1}{3!}K'''(\omega_0)\nu + \dots\right)\nu^2. \tag{2.7}$$

From the complex-amplitude representation (2.6), it follows that ν is associated with the differential operator $-i\partial_\tau$, and so $\nu^2 = -\partial_\tau^2$. Thus, the complex-valued amplitude A satisfies:

$$\partial_\xi A + iK_{\text{res}}(-i\partial_\tau)A = 0. \tag{2.8}$$

For narrow-banded spectrum, the equation (2.8) reduces to an approximate equation, the so-called 'linear Schrödinger' equation, by approximating K_{res} by its lowest order term:

$$\partial_\xi A + i\beta\partial_\tau^2 A = 0, \tag{2.9}$$

where the dispersion coefficient $\beta = \frac{1}{2}K''(\omega_0) = -\frac{1}{2}\frac{\Omega''(k_0)}{[\Omega'(k_0)]^3}$. In the next section we will see that a cubic term is added to equation (2.9) when the governing wave equation contains nonlinear terms.

2.3 Nonlinear dispersive wave equation

In this section we study the KdV-NLS relationship. We also derive the complex amplitude equation from the KdV equation with exact dispersion relation. Depending on the scaling in variables, we obtain either the spatial or the temporal NLS equation.

2.3.1 The KdV-NLS relationship

The relation between the KdV equation and the NLS equation has been known for many years. The NLS equation describing the slow modulation of a harmonic wave moving over a surface of a two dimensional channel is derived using the multiple scale

method in [Johnson, 1976, 1997]. An analysis of the connection between the NLS and KdV periodic inverse scattering methods for wave packets is given in [Tracy et al., 1988, 1991]. Moreover, the derivation from the KdV type of equation with exact dispersion relation is given in [Van Groesen, 1998; Cahyono, 2002]. Another reference of the derivation through perturbation theory can also be found in [Boyd and Chen, 2001]. In addition, the latter authors also give a discussion on the KdV-induced long wave pole in the nonlinear coefficient of the NLS equation, resonance effects and numerical illustrations. We will review again the latter derivation in this chapter and give special emphasis to the spatial NLS equation.

2.3.2 Derivation of the spatial NLS equation

In this subsection we derive the spatial NLS equation using the 'multiple time scale' method [Kevorkian, 1961; Nayfeh, 1973]. The KdV type of equation with exact dispersion relation is given by

$$\partial_t \eta + i\Omega(-i\partial_x)\eta + c\,\eta\partial_x\eta = 0, \qquad c \in \mathbb{R} \tag{2.10}$$

where c is the coefficient in front of the nonlinear term in the KdV equation and contributes to the coefficient in front of the nonlinear term in the NLS equation as we will see; Ω is used for both the differential operator and the dispersion relation. We consider the residue of an approximation up to the third order to find the corresponding complex-amplitude equation. An expression for wave groups consisting of a superposition of a first-order harmonic, a second-order double harmonic and a second-order non-harmonic long wave is given by

$$\eta(x,t) = \epsilon A(\xi,\tau)e^{i\theta} + \epsilon^2[B(\xi,\tau)e^{2i\theta} + C(\xi,\tau)] + \mathrm{c\,c}, \tag{2.11}$$

where ϵ is a small positive parameter as used commonly in perturbation theory, $\theta = k_0 x - \omega_0 t$ and c c means the complex conjugate of the preceding terms. The variables ξ and τ are related to the physical variables x and t by:

$$\xi = \epsilon^2 x \qquad \text{and} \qquad \tau = \epsilon(t - x/\Omega'(k_0)). \tag{2.12}$$

The complex amplitudes A, B, and C are allowed to vary slowly in the frame of reference. Substituting this Ansatz into the KdV equation (2.10) will result in an expression of the following form

$$R = \sum_{n,m} \epsilon^n R_{nm} e^{im\theta} + \mathrm{c\,c}, \tag{2.13}$$

where $n \geq 1$, $m \geq 0$, and where the coefficients R_{nm} contain expressions in A, B, and C and their derivatives. In order to satisfy the KdV equation (2.10), all coefficients of R have to vanish. The first order coefficients simply vanish: $R_{1m} = 0$, $m \geq 0$ when k_0 and ω_0 are related by the linear dispersion relation. The second order coefficients read

$$R_{20} = 0; \qquad R_{21} = 0; \qquad R_{2m} = 0, \quad m \geq 3; \tag{2.14}$$

$$R_{22} = i([\Omega(2k_0) - 2\omega_0]B + c\,k_0 A^2). \tag{2.15}$$

Vanishing of R_{22} expresses B as function of A:

$$B(\xi,\tau) = \frac{c\,k_0 A^2(\xi,\tau)}{2\omega_0 - \Omega(2k_0)}. \tag{2.16}$$

The third order coefficients read:

$$R_{30} = \left(1 - \frac{\Omega'(0)}{\Omega'(k_0)}\right)\partial_\tau C - \frac{1}{2}\frac{c}{\Omega'(k_0)}\partial_\tau |A|^2 \tag{2.17}$$

$$R_{31} = \Omega'(k_0)\partial_\xi A - \frac{1}{2}i\frac{\Omega''(k_0)}{[\Omega'(k_0)]^2}\partial_\tau^2 A + i\,ck_0(A^*B + AC + AC^*) \tag{2.18}$$

$$R_{32} = -\frac{1}{\Omega'(k_0)}\left(\Omega'(2k_0)\partial_\tau B + \frac{1}{2}c\partial_\tau A^2\right) \tag{2.19}$$

$$R_{33} = 3ik_0 c\,AB. \tag{2.20}$$

Vanishing of R_{30} expresses $C(\xi,\tau)$ as function of $A(\xi,\tau)$ and a ξ-dependent constant of integration $\alpha_S(\xi)$ for all θ:

$$C(\xi,\tau) = \frac{1}{2}\frac{c\,|A(\xi,\tau)|^2}{\Omega'(k_0) - \Omega'(0)} + \alpha_S(\xi). \tag{2.21}$$

To prevent resonance, R_{31} has to vanish which leads to the dynamic evolution equation for A:

$$\partial_\xi A + i\beta\partial_\tau^2 A + i\gamma|A|^2 A + \frac{2ik_0 c}{\Omega'(k_0)}\mathrm{Re}(\alpha_S)A = 0. \tag{2.22}$$

This equation is originally derived for the unidirectional wave propagation, in which the wave groups propagate over an uneven bottom and under the condition that reflection can be neglected. Since we consider the depth to be constant, we have $\mathrm{Re}[\alpha_S(\xi)] = 0$ and both β and γ are constants [Dingemans, 1997; Dingemans and Otta, 2001]. To get rid of the term $\mathrm{Re}[\alpha_S(\xi)]$, we can also apply the 'gauge transformation' by multiplying the evolution equation by $e^{\frac{2ik_0 c}{\Omega'(k_0)}\int \mathrm{Re}[\alpha_S(\xi)]d\xi}$, see also [Mei, 1983]. Consequently, the new complex amplitude $\tilde{A}(\xi,\tau) = e^{\frac{2ik_0 c}{\Omega'(k_0)}\int \mathrm{Re}[\alpha_S(\xi)]d\xi}A(\xi,\tau)$ now satisfies the spatial NLS equation, which after dropping the tilde reads:

$$\partial_\xi A + i\beta\partial_\tau^2 A + i\gamma|A|^2 A = 0. \tag{2.23}$$

Here the dispersion coefficient β and the nonlinear coefficient γ are respectively given as follows:

$$\beta = \beta(k_0) = -\frac{1}{2}\frac{\Omega''(k_0)}{[\Omega'(k_0)]^3} \tag{2.24}$$

$$\gamma = \gamma(k_0, c^2) = \frac{k_0 c^2}{\Omega'(k_0)}\left(\frac{1}{\Omega'(k_0) - \Omega'(0)} + \frac{k_0}{2\omega_0 - \Omega(2k_0)}\right). \tag{2.25}$$

We observe that the nonlinear coefficient γ depends quadratically on the nonlinear coefficient of the KdV equation c. Note also that applying the gauge transformation affects this nonlinear coefficient. In Chapter 6, we will see that different values of γ in the design experiments gives large changes to the extreme position. For $\gamma = 0$, neglecting nonlinear effects, we see that the linear Schrödinger equation (2.9) is recovered. The spatial NLS equation (2.23) is the appropriate equation for the signalling problem that we consider in this thesis.

2.3.3 Phase-amplitude equations for the spatial NLS equation

Let the complex amplitude A be written in its original physical variables as $\bar{A}(x,t) = \epsilon A(\xi,\tau)$, with transformation of variables relation as in (2.12). Then the NLS equation in the physical variables is expressed as:

$$\partial_x \bar{A} + \frac{1}{\Omega'(k_0)}\partial_t \bar{A} + i\beta\partial_t^2 \bar{A} + i\gamma|\bar{A}|^2\bar{A} = 0. \tag{2.26}$$

Now let this complex amplitude $\bar{A}$ be written in its polar form with the real-valued amplitude $a(x,t)$ and the real-valued phase $\phi(x,t)$, $\bar{A}(x,t) = a(x,t)e^{i\phi(x,t)}$. Then the phase-amplitude equations are obtained by substituting it into the NLS equation (2.26). This transformation is nonlinear and is also called 'Madelung's transformation' [Sulem and Sulem, 1999], referring to Madelung's paper in 1926 on quantum theory. After the substitution, we remove the factor $e^{i\phi}$ and collect the real and the imaginary terms. Vanishing of both the real and the imaginary parts leads to the following coupled phase-amplitude equations in the original physical variables:

$$\begin{cases} \partial_x a + \dfrac{\partial_t a}{\Omega'(k_0)} - \beta\left(a\partial_t^2\phi + 2\partial_t a\partial_t\phi\right) & = 0 \\ \partial_x\phi + \dfrac{\partial_t\phi}{\Omega'(k_0)} + \beta\left(\dfrac{\partial_t^2 a}{a} - (\partial_t\phi)^2\right) + \gamma a^2 & = 0. \end{cases} \tag{2.27}$$

Let us define the local wavenumber k and the local frequency ω as follows:

$$k(x,t) = k_0 + \partial_x\phi \qquad \omega(x,t) = \omega_0 - \partial_t\phi. \tag{2.28}$$

Writing the expressions in terms of local wavenumber and local frequency, we can write the phase-amplitude equations in a simpler way.

The amplitude equation is the first equation of the phase-amplitude equations (2.27). After expressing $\partial_t\phi$ in terms of the local frequency and multiplying the equation with a, it can be written as:

$$\frac{1}{2}\partial_x(a^2) + \frac{1}{2}\partial_t\left([K'(\omega_0) + K''(\omega_0)(\omega-\omega_0)]a^2\right) = 0. \tag{2.29}$$

Now the amplitude equation is known as the 'energy equation'. For the accuracy up to $\mathcal{O}(\nu^2)$, where $\nu = \omega - \omega_0$ as in page 15, this equation is written as:

$$\partial_x(a^2) + \partial_t[K'(\omega)a^2] = 0, \tag{2.30}$$

which equation describes the conservation of energy.

The phase equation is the second equation of the phase-amplitude equations (2.27). Similarly, we express $\partial_x\phi$ and $\partial_t\phi$ in terms of the local wavenumber and the local frequency. We obtain the following relation:

$$\left[k_0 + K'(\omega_0)(\omega-\omega_0) + \frac{1}{2}K''(\omega_0)(\omega-\omega_0)^2\right] - k = \beta\frac{\partial_t^2 a}{a} + \gamma\, a^2. \tag{2.31}$$

This equation can now be written as the nonlinear dispersion relation. For the accuracy up to $\mathcal{O}(\nu^2)$, it is given by:

$$K(\omega) - k = \beta\frac{\partial_t^2 a}{a} + \gamma\, a^2. \tag{2.32}$$

This expression describes the relation between the local wavenumber and the local frequency in the dispersion plane. Note that in general the right hand side of (2.32) does not vanish, and hence (k,ω) does not satisfy the linear dispersion relation. The ratio of the second derivative of a with respect of t and the real amplitude a itself is called the 'Chu-Mei quotient'. Chu and Mei introduced this term for the first time when they derived the modulation equations of Whitham's theory for slowly varying Stokes waves [Chu and Mei, 1970, 1971]. Some authors call this quotient the 'Fornberg-Whitham term' [Infeld and Rowlands, 1990], referring to [Fornberg and Whitham, 1978].

Note that the Chu-Mei quotient is an immediate consequence of the nonlinear transformation $A \longmapsto (a,\phi)$ and it is not of the nonlinearity of the evolution equation. Indeed, for the linear Schrödinger equation ($\gamma = 0$), we find that

$$K(\omega) - k = \beta\frac{\partial_t^2 a}{a}, \tag{2.33}$$

which right hand side vanishes for constant amplitudes, i.e., for a monochromatic mode. We will see further in Chapter 4 that the unboundedness of Chu-Mei quotient at the vanishing amplitude is responsible for the occurrence of wavefront dislocation.

2.3.4 Derivation of the temporal NLS equation

The same method of multiple scales can also be applied to derive the temporal NLS equation from the KdV equation with exact dispersion relation [Van Groesen, 1998; Cahyono, 2002]. A significant difference is the choice of variables in the moving frame of reference, which now becomes $\xi = \epsilon(x - \Omega'(k_0)t)$ and $\tau = \epsilon^2 t$. The first and the second order coefficients are the same as in the spatial case. The third order coefficients read:

$$R_{30} = [\Omega'(0) - \Omega'(k_0)]\partial_\xi C + \frac{1}{2}c\,\partial_\xi|A|^2; \tag{2.34}$$

$$R_{31} = \partial_\tau A - \frac{1}{2}i\Omega''(k_0)\partial_\xi^2 A + i\,ck_0(A^*B + AC + AC^*). \tag{2.35}$$

Vanishing of R_{30} expresses C as a function of A and a τ-dependent constant of integration α_T, given as follows:

$$C(\xi,\tau) = \frac{1}{2}\frac{c\,|A(\xi,\tau)|^2}{\Omega'(k_0)-\Omega'(0)} + \alpha_T(\tau) \tag{2.36}$$

To prevent resonance, R_{31} has to vanish which leads to an evolution equation for A:

$$\partial_\tau A + i\beta_0\partial_\xi^2 A + i\gamma_0|A|^2A + 2ik_0c\,\mathrm{Re}[\alpha_T(\tau)]A = 0. \tag{2.37}$$

A similar assumption of unidirectional wave propagation, applying the 'gauge transformation' by multiplying the evolution equation by $e^{2ik_0c\int \mathrm{Re}[\alpha_T(\tau)]d\tau}$, we obtain the temporal NLS equation for A:

$$\partial_\tau A + i\beta_0\partial_\xi^2 A + i\gamma_0|A|^2A = 0, \tag{2.38}$$

where

$$\beta_0 = \beta\,[\Omega'(k_0)]^3 = -\frac{1}{2}\Omega''(k_0) \tag{2.39}$$

$$\gamma_0 = \gamma\,\Omega'(k_0) = k_0c^2\left(\frac{1}{\Omega'(k_0)-\Omega'(0)} + \frac{k_0}{2\omega_0-\Omega(2k_0)}\right). \tag{2.40}$$

The temporal NLS equation is appropriate for the initial value problem, for example wave evolution in the oceans, including the dynamics of extreme waves [Osborne et al., 2000; Onorato et al., 2001].

2.3.5 Phase-amplitude equations for the temporal NLS equation

A similar procedure as in Subsection 2.3.3 gives the phase-amplitude equations for the temporal NLS equation. The 'energy equation' is given by

$$\partial_t(a^2) + \partial_x[\Omega'(k)a^2] = 0. \tag{2.41}$$

The 'nonlinear dispersion relation' is given as follows:

$$\omega - \Omega(k) = \beta_0\frac{\partial_x^2 a}{a} + \gamma_0 a^2. \tag{2.42}$$

2.4 On the NLS equation as a dispersive wave equation

The temporal NLS equation (2.38) is a nonlinear generalization of the linear equation $\partial_\tau A + i\beta_0\partial_\xi^2 A = 0$. This linear equation is known as a Schrödinger equation for

the quantum mechanical probability amplitude of a particle (like an electron) moving through a region of uniform potential. Therefore, it is natural to call equation (2.38) the nonlinear Schrödinger (NLS) equation, in this case, the temporal NLS equation. The NLS equation is also known as the 'cubic Schrödinger' equation, since the nonlinearity is of order three. Together with the KdV equation and the sine-Gordon equation, the NLS equation belongs to the classical soliton equations. Each one of these three and many more completely integrable equations possesses solutions with soliton properties. Readers interested in an overview of the classical soliton equations and the history of solitons may consult [Scott, 2003, 2005]. A formal definition of soliton is a solitary wave solution of a wave equation which asymptotically preserves its shape and velocity upon collision with other solitary waves [Scott et al., 1973]. Although the term was originally applied only to solitary waves of the KdV equation, it is often used in a wider context without formal definition or verification of collision property.

As mentioned before, the NLS equation describes the evolution of the envelope of a wave field and finds many applications. In hydrodynamics of nonlinear envelope waves, see e.g. [Benney and Newell, 1967; Newell, 1974; Whitham, 1974; Yuen and Lake, 1982], in nonlinear optics, see e.g. [Kelley, 1965; Talanov, 1965; Karpman and Kruskal, 1969; Hasegawa and Tappert, 1973], in nonlinear acoustics [Tappert and Varma, 1970], in plasma physics, see e.g. [Taniuti and Washimi, 1968; Ichikawa et al., 1972; Zakharov, 1972], and so forth. The NLS equation and its two-dimensional extension were originally derived for deep-water waves via a spectral method by [Zakharov, 1968]. Further, [Hasimoto and Ono, 1972] and [Davey, 1972] derived the NLS equation for finite depth independently using multiple scale methods. In addition, [Yuen and Lake, 1975] derived it using the averaged Lagrangian formulation from Whitham's theory. Moreover, a heuristic derivation of the NLS equation has been given by several authors [Kadomtsev and Karpman, 1971; Karpman, 1975; Jeffrey and Kawahara, 1982; Dingemans, 1997; Dingemans and Otta, 2001]. A similar derivation of the spatial NLS equation can be found in [Djordjević and Redekopp, 1978], but under an assumption of slowly varying bottom. The NLS equation is also a special case of the complex Ginzburg-Landau equation [Ginzburg and Landau, 1950; Van Saarloos and Hohenberg, 1992; Goldman and Sirovich, 1994]. Specifically, we select the spatial type of the NLS equation instead of the temporal one since it is more suitable to model our wave evolution in a wave tank. A perspective from the variational formulation point of view will be presented below.

2.4.1 Approximate dispersion of the NLS equation

The linear dispersion relation of surface water waves for finite depth is given by $\omega = \sqrt{gk\,\tanh(kh)}$. In normalized quantities, it is given by $\omega = \Omega(k) = k\sqrt{\tanh k/k}$. The NLS equation is derived under the assumption of narrow-banded spectrum. In this subsection, we will compare the approximate dispersion corresponding to both the temporal and the spatial NLS equations. Let (k_0, ω_0) be the wavenumber and the frequency of a carrier wave of a wave group that satisfy the linear dispersion relation.

We write the linear dispersion relation and its inverse in a Taylor series expansion around k_0 and ω_0, respectively:

$$\omega = \omega_0 + \Omega'(k_0)(k-k_0) + \frac{1}{2}\Omega''(k_0)(k-k_0)^2 + \ldots \tag{2.43}$$

$$k = k_0 + \frac{1}{\Omega'(k_0)}(\omega-\omega_0) - \frac{1}{2}\frac{\Omega''(k_0)}{[\Omega'(k_0)]^3}(\omega-\omega_0)^2 + \ldots. \tag{2.44}$$

Let us denote the approximation up to and including quadratic terms above as $\Omega_{\text{approx}}(k)$ and $K_{\text{approx}}(\omega)$, respectively. Figure 2.1 shows the plots of the linear dispersion relation and its two approximations for different values of k_0 and finite water depth. We observe that for $k_0 \to 0$, both approximations are good but $\Omega_{\text{approx}}(k)$ approximates better the linear dispersion relation than $K_{\text{approx}}(\omega)$ for $k < k_0$. But for $k_0 \to \infty$, $K_{\text{approx}}(\omega)$ approximates better than $\Omega_{\text{approx}}(k)$. This implies that the spatial NLS equation is a better approximation than the temporal NLS equation for a mathematical model of surface envelope water wave evolution.

For the case of deep water, the linear dispersion relation becomes $\Omega_{\text{deep}}(k) = \sqrt{k}$ and its inverse becomes $K_{\text{deep}}(\omega) = \omega^2$. The spatial NLS equation approximates better than the temporal NLS equation for deep-water waves since the former is exact* but the latter one is not, $K_{\text{approx,deep}}(\omega) = \omega^2 = K_{\text{deep}}(\omega)$, but $\Omega_{\text{deep}} = \sqrt{k} \neq \Omega_{\text{approx,deep}}(k)$.

2.4.2 Modulational instability

Based on the value of the coefficients β and γ, there are two types of the NLS equation. For $\beta\gamma > 0$, it is called the 'focusing' type, or NLS(+) type. For $\beta\gamma < 0$, it is called the 'defocusing' type, or NLS(−) type. For the above NLS equation, since $\beta > 0$ for $k > 0$, the focusing type equation occurs for $\gamma > 0$. Positive values of γ are found for sufficiently small wavelength: $k > k_{\text{crit}}$. The value of the critical wavenumber is given by $k_{\text{crit}} = 1.363$ when the NLS equation is most accurately derived from the fully nonlinear water wave equation [Benjamin, 1967]. When the NLS equation is derived from the KdV equation with exact dispersion relation, the critical value is found as $k_{\text{crit}} = 1.146$ [Van Groesen, 1998]. The stability of a monochromatic wave depends on the wavenumber k: for $k < k_{\text{crit}}$ it is stable and for $k > k_{\text{crit}}$ it is unstable. The analysis of stability for finite depth is given by [Benjamin, 1967] and the same result is obtained independently using an average Lagrangian approach by [Whitham, 1967], which is well explained in Whitham's book [Whitham, 1974].

As we will see in this section, a plane wave solution of the focusing type of the NLS equation shows modulational instability if $k > k_{\text{crit}}$. On the other hand, a plane wave solution with $k < k_{\text{crit}}$ is stable and therefore it is not so interesting to discuss in the context of modulational instability. However, this type of the NLS equation and one family of solutions the so-called 'dark solitons' received special attentions from researchers in the field of nonlinear optics [Kivshar and Luther-Davies, 1998].

*Observation by Gert Klopman, 2006.

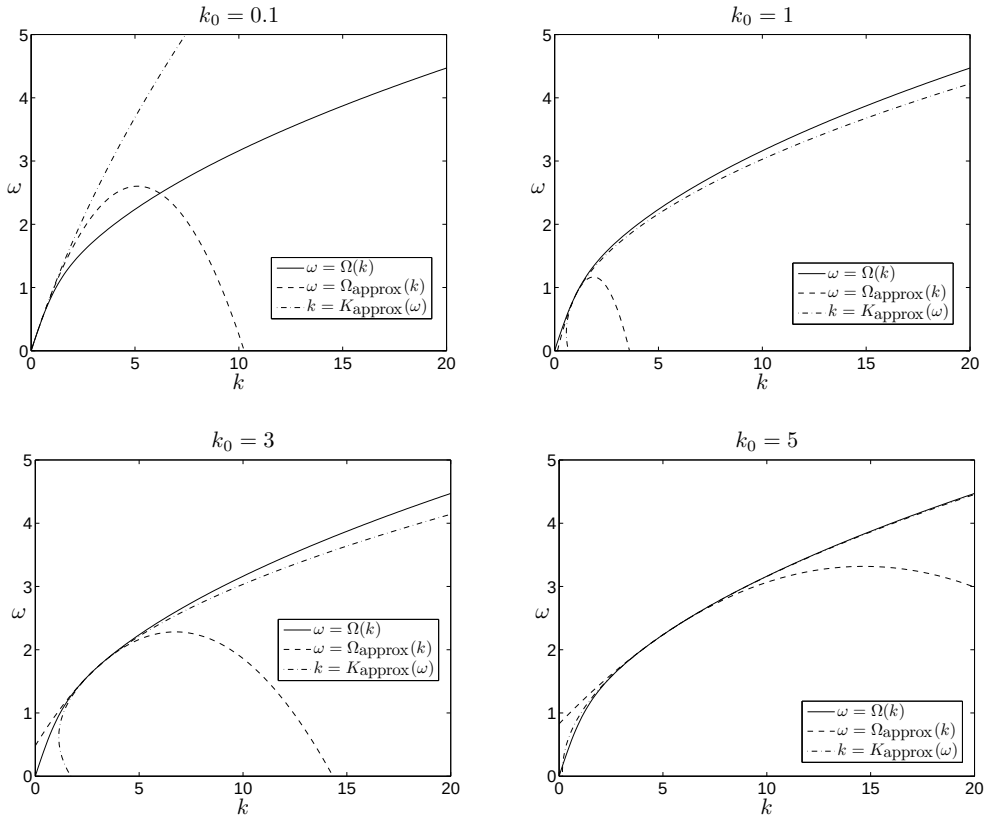

Figure 2.1: Plots of the linear dispersion relation $\Omega(k)$, its quadratic approximation $\Omega_{\text{approx}}(k)$ and the quadratic approximation of its inverse $K_{\text{approx}}(\omega)$ for different values of k_0. In all cases, the water depth is finite.

In the context of this thesis, 'modulational instability', also called 'sideband instability', is defined as the process of growth in space of the plane wave solution of the NLS equation as a result of a small modulation in a monochromatic wave signal. In the context of water waves, the modulational instability is also known as the 'Benjamin-Feir instability' since [Benjamin and Feir, 1967] investigated the phenomenon of wave trains in deep water. The same independent result is also observed in nonlinear liquids [Bespalov and Talanov, 1966]. Apparently the term 'modulational instability' is mentioned for the first time by [Taniuti and Washimi, 1968]. Furthermore, the instability of weakly nonlinear waves in dispersive media has been investigated by [**?**Lighthill, 1967; Benjamin, 1967; Ostrovsky, 1967; Whitham, 1967; Zakharov, 1967]. Much other research later on shows that modulational instability is observed in almost

any field of wave propagation in nonlinear media [Dodd et al., 1982; Newell, 1985; L'vov, 1994; Remoissenet, 1999]. For nonlinear optics, we refer to [Agrawal, 1995; Hasegawa and Kodama, 1995].

The references given in this paragraph refer to the temporal NLS equation. The long time behaviour of the modulational instability of the NLS equation is investigated in [Janssen, 1981]. The results are in qualitative agreement with experimental findings of [Lake et al., 1977] and the numerical computation of [Yuen and Ferguson, 1978a,b]. Their works show that unstable modulations grow to a maximum limit and then subside. The energy is transferred from the primary wave to the sidebands for a certain period of time, and is then recollected back into the primary wave mode. The long time evolution of an unstable wave train leads to a series of modulation-demodulation cycles in the absence of viscosity, known as the Fermi-Pasta-Ulam recurrence phenomenon [Fermi et al., 1955]. An alternative treatment of the Benjamin-Feir instability mechanism of the two-dimensional Stokes waves on deep water was given by [Stuart and DiPrima, 1978]. Recently, [Segur et al., 2005] show that any amount of a certain type of dissipation stabilizes the Benjamin-Feir instability for waves with narrow bandwidth and moderate amplitude. On the other hand, [Bridges and Dias, 2004] show that there is an overlooked mechanism whereby the addition of dissipation leads to an enhancement of the Benjamin-Feir instability.

In the following, we derive the modulational instability based on the NLS equation. This stability analysis can be found also in several books [Debnath, 1994; Dingemans, 1997]. For the readers who are interested in the history of T. B. Benjamin and his contributions to nonlinear wave theory, it is suggested to check a recent overview in [Hunt, 2005].

Let us first introduce the simplest nontrivial solution of the NLS equation, called the 'plane wave' solution. We discuss further this solution in the following subsection. Explicitly it is given by:

$$A = A_0(\xi) = r_0 e^{-i\gamma r_0^2 \xi}. \tag{2.45}$$

To investigate the stability of the plane wave solution of the NLS equation, substitute $A(\xi,\tau) = A_0(\xi)[1 + \epsilon B(\xi,\tau)]$ into the NLS equation (2.23). The corresponding linearized equation reads

$$\partial_\xi B + i\beta\partial_\tau^2 B + i\gamma r_0^2 (B + B^*) = 0. \tag{2.46}$$

Substituting an Ansatz $B(\xi,\tau) = B_1 e^{(\sigma\xi + i\nu\tau)} + B_2 e^{(\sigma^*\xi - i\nu\tau)}$, $\quad B_1,\ B_2 \in \mathbb{C}$ into the linear equation, we get a set of two equations:

$$\begin{pmatrix} [\sigma - i(\beta\nu^2 - \gamma r_0^2)] & i\gamma r_0^2 \\ -i\gamma r_0^2 & [\sigma + i(\beta\nu^2 - \gamma r_0^2)] \end{pmatrix} \begin{pmatrix} B_1 \\ B_2^* \end{pmatrix} = \begin{pmatrix} 0 \\ 0 \end{pmatrix}. \tag{2.47}$$

Requiring the determinant of the matrix above to be zero, we have the condition $\sigma^2 = 2\beta\gamma r_0^2 \nu^2 - \nu^4$. The coefficient σ is real for sufficiently small ν, and is then the growth rate of the instability. The growth rate $\sigma > 0$ is given by $\sigma = \nu\sqrt{2\beta\gamma r_0^2 - \beta^2\nu^2}$.

Defining a normalized modulation frequency $\tilde{\nu}$ by $\nu = r_0\sqrt{\frac{\gamma}{\beta}}\tilde{\nu}$, the growth rate σ becomes $\sigma = \gamma r_0^2\tilde{\sigma}$, with $\tilde{\sigma} = \tilde{\nu}\sqrt{2-\tilde{\nu}^2}$. Note that for instability, the normalized modulation frequency has to be in the instability interval $0 < \tilde{\nu} < \sqrt{2}$.

For the above two equations for B_1 and B_2 (2.47), we obtain $B_1/B_2^* = (\tilde{\nu}^2 - 1) - i\tilde{\sigma}$. Taking the modulus of this ratio, we have $|B_1/B_2^*| = 1$. Since $|B_2| = |B_2^*|$, we have also $|B_1| = |B_2|$. Therefore we write $B_j = |B_j|e^{i\theta_j}$, $j = 1, 2$, and we have the phase relation as follows:

$$e^{i(\theta_1+\theta_2)} = (\tilde{\nu}^2 - 1) - i\tilde{\sigma}. \tag{2.48}$$

The solution A now reads

$$A(\xi,\tau) = A_0(\xi)\left[1 + \epsilon|B_1|e^{\sigma\xi}\left(e^{i\theta_1}e^{i\nu\tau} + e^{-i\nu\tau}e^{i\theta_2}\right)\right]. \tag{2.49}$$

We see that for $\xi \to \infty$, this solution grows exponentially in space. This is the linear instability of the Benjamin-Feir modulated wave signal. Because of nonlinear effects from the cubic term nature that have been ignored in the analysis above, this growth is bounded. In the following chapter, we will see that a fully nonlinear extension of the Benjamin-Feir instability can be found, and is given by the Soliton on Finite Background (SFB) and the rational solution for a very long modulation wavelength (when the modulation frequency $\nu \to 0$).

2.4.3 Coherent state solutions

The NLS equation (2.23) has a number of exact solutions. The simplest nontrivial solution is the 'plane wave' or the 'continuous wave' (cw) solution. It does not depend on the temporal variable τ and is given by (2.45), where r_0 is the plane wave amplitude. The corresponding physical wave field given in the lowest order term according to (2.11) is given by

$$\eta(x,t) = 2r_0\cos\left[(k_0 - \gamma r_0^2)x - \omega_0 t\right] \tag{2.50}$$

and it travels with the phase velocity of $\omega_0/(k_0 - \gamma r_0^2)$. Since $\gamma > 0$, this wave travels faster compared to a simple monochromatic wave that travels with phase velocity ω_0/k_0. Note that the velocity is determined by the nonlinear dispersion relation, in agreement with (2.32). In addition, the wave has a constant amplitude $2r_0$. Figure 2.2(a) shows a time signal and its envelope corresponding to the plane wave solution at $x = 0$.

Another simple solution of the NLS equation is the 'one soliton', or 'single soliton', or 'bright soliton' solution. It can be found by the inverse scattering technique [Zakharov and Shabat, 1972; Zakharov, 1972], but also much simpler by seeking a travelling-wave solution that decays at infinity. An explicit expression is given by

$$A(\xi,\tau) = A_0(\xi)\sqrt{2}\,\mathrm{sech}\left(r_0\sqrt{\frac{\gamma}{\beta}}\tau\right), \tag{2.51}$$

where A_0 is the plane wave solution as given above. This solution represents a solitary (envelope) wave, briefly called 'envelope soliton'. The corresponding physical wave field of the single soliton for the lowest order term is given by:

$$\eta(x,t) = 2r_0\sqrt{2}\ \mathrm{sech}\left(r_0\sqrt{\frac{\gamma}{\beta}}\,[t - x/\Omega'(k_0)]\right)\ \cos\left[(k_0 - \gamma r_0^2)x - \omega_0 t\right]. \qquad (2.52)$$

Different from the wave field corresponding to the plane wave solution (2.50) that has a constant amplitude, this wave field of the single soliton has amplitude that depends on time, is localized around $t = x/\Omega'(k_0)$ and vanishes for $t \to \pm\infty$. The wave signal propagates in a nonlinear medium without spreading due to the balance of the wave dispersion and the nonlinearity of the system. Figure 2.2(b) shows a time signal and its envelope of the single soliton solution at $x = 0$. Higher order solutions, N-soliton solutions, can be constructed using the inverse scattering method of [Zakharov and Shabat, 1972], see also [Drazin and Johnson, 1989].

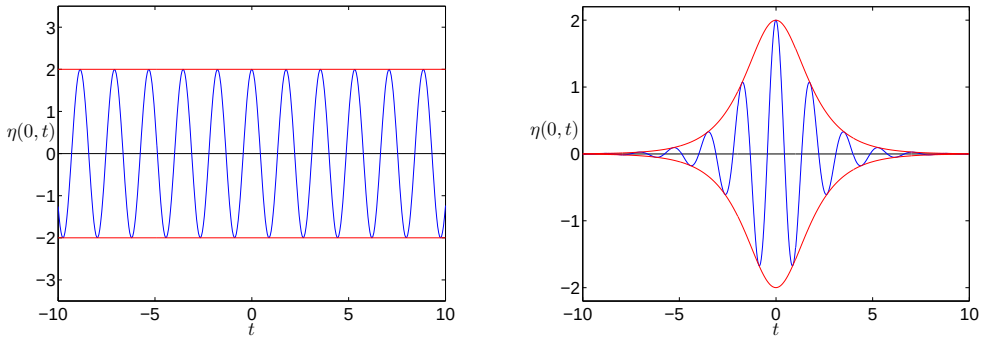

Figure 2.2: Plots of the wave signal and the envelope of (a) the plane wave solution and (b) the single soliton solution of the NLS equation. The plots are given for normalized parameters $r_0 = \beta = \gamma = 1$.

We now remark that both these solutions have a coherent state character. Coherent state means that all Fourier components have the same phase. Generally speaking, if we write a function $f(t)$ with its Fourier transform $\hat{f}(\omega)$ as $f(t) = \int \hat{f}(\omega)e^{i\omega t}\,d\omega = \int \left|\hat{f}(\omega)\right| e^{i\vartheta(\omega)}e^{i\omega t}\,d\omega$, we will have that the phase $\vartheta(\omega)$ depends nonlinearly on ω, since for $f(\omega) \in \mathbb{C}$. If this phase is constant (and then necessarily 0 mod π if f is real), the function $f(t)$ is called 'coherent'. In particular it means that a real function f has maximal (or minimal) value at $t = 0$, since then all Fourier modes contribute optimally. The function $f(t)$ is coherent if $\vartheta(\omega) \equiv \vartheta_0$ for all $\omega \in \mathbb{R}$.

In order to explore more about the coherent state, we study the evolution of the spectrum of the solutions in the frequency domain. The spectrum $\hat{A}(\xi,\omega)$ of a complex

amplitude function $A(\xi,\tau)$ is obtained by applying the Fourier transform with respect to the time variable τ, as follows:

$$\hat{A}(\xi,\omega) = \int_{-\infty}^{\infty} A(\xi,\tau) e^{-i\omega\tau} d\tau. \tag{2.53}$$

Moreover, since the spectrum is a complex-valued function, it can be written in the polar coordinate as $\hat{A}(\xi,\omega) = |\hat{A}(\xi,\omega)|e^{i\vartheta(\xi,\omega)}$, where $|\hat{A}(\xi,\omega)|^2$ is called the 'power spectrum' and $\vartheta(\xi,\omega)$ is called the 'phase spectrum'.

The Fourier transform of the plane wave is given by $\hat{A}_0(\xi,\omega) = A_0(\xi)\,\delta(\omega)$, where $\delta(\omega)$ is the Dirac's delta function. Furthermore, the Fourier transform of the single soliton is given by:

$$\hat{A}(\xi,\omega) = 4\alpha\sqrt{2}A_0(\xi) \sum_{m=0}^{\infty} (-1)^m \frac{(2m+1)}{\alpha^2(2m+1)^2 + \omega^2}, \tag{2.54}$$

where $\alpha = r_0\sqrt{\gamma/\beta}$. See Appendix A on page 125 for the derivation of this expression. Since both spectra have the same phase for all ω, both the plane wave and the single soliton solutions have a coherent state characteristic. Figure 2.3 shows the power spectrum for the plane wave and the single soliton solutions. We will see in the next chapter that other solutions of the NLS equation, in particular the SFB, are not coherent.

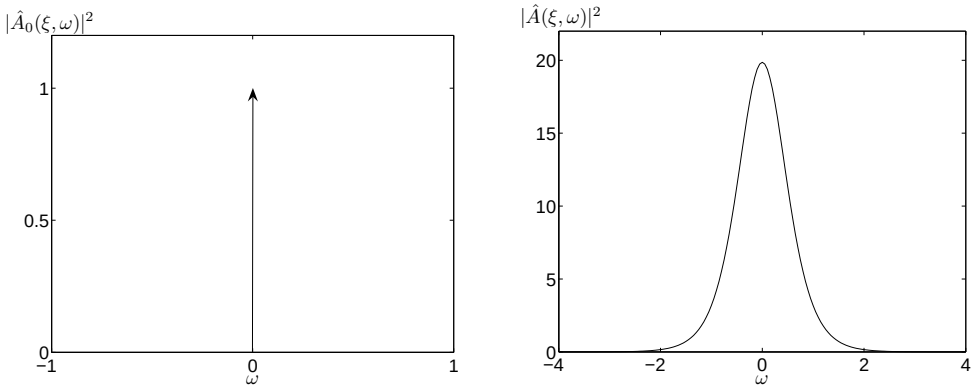

Figure 2.3: The power spectrum plots for (a) the plane wave and (b) the single soliton solutions for normalized parameters $r_0 = \beta = \gamma = 1$.

2.5 Variational formulation and conserved quantities of the NLS equation

In this section, we discuss the variational formulation of the NLS equation that we will use in Chapter 3. We present the Lagrangian and Hamiltonian structures corresponding to the NLS equation [Sulem and Sulem, 1999].

Let A denote a smooth solution of the NLS equation

$$\partial_\xi A + i\beta\partial_\tau^2 A + i\gamma|A|^2 A = 0. \tag{2.55}$$

A Lagrangian density $\mathcal{L}$ associated to the NLS equation can be written in terms of A and is given as follows:

$$\mathcal{L}(A) = \frac{1}{4}i(A^*\partial_\xi A - A\partial_\xi A^*) + \frac{1}{2}\beta|\partial_\tau A|^2 - \frac{1}{4}\gamma|A|^4. \tag{2.56}$$

Then the action functional $\mathcal{A}$ is such that any solution A of the NLS equation is a critical point of the corresponding action functional:

$$\mathcal{A}(A) = \int_{\xi_0}^{\xi_1}\int_{-\infty}^{\infty} \mathcal{L}\, d\tau\, d\xi. \tag{2.57}$$

Indeed, the Euler-Lagrange equation is given by:

$$\frac{\partial\mathcal{L}}{\partial A} = \frac{\partial}{\partial\tau}\left(\frac{\partial\mathcal{L}}{\partial A_\tau}\right) + \frac{\partial}{\partial\xi}\left(\frac{\partial\mathcal{L}}{\partial A_\xi}\right), \tag{2.58}$$

and this equation leads to the NLS equation.

A Hamiltonian structure is derived from the existence of a Lagrangian. The Hamiltonian density $\mathcal{H}$ corresponds to the NLS equation is given by

$$\mathcal{H}(A) = \frac{1}{4}i(A^*\partial_\xi A - A\partial_\xi A^*) - \mathcal{L}(A) \tag{2.59}$$

$$= -\frac{1}{2}\beta|\partial_\tau A|^2 + \frac{1}{4}\gamma|A|^4. \tag{2.60}$$

The Hamiltonian H is given by:

$$H(A) = \int_{-\infty}^{\infty} \mathcal{H}(\mathcal{A})\, d\tau. \tag{2.61}$$

The Hamilton equation in the complex form is given by:

$$i\partial_\xi A = \delta H(A), \tag{2.62}$$

where the right-hand side is the variational or Fréchet derivative. This is the canonical form of the NLS equation since the right-hand side of the term reads $\delta H(A) = \beta\partial_\tau^2 A +$

$\gamma|A|^2A$. Thus, both the Euler-Lagrange and the Hamilton equations lead to the NLS equation.

Conservation laws are a common feature of mathematical physics, where they describe the conservation of fundamental physical quantities. It is well-known that conservation laws for many systems arise from variational principles that are invariant under transformations which belong to a continuous group. A conservation law then follows from the application of Noether's theorem to the Lagrangian density. The NLS equation is a dynamical system with an infinite number of degrees of freedom and corresponds to an infinite-dimensional Hamiltonian system. It is integrable and as a consequence it has an infinite number of conserved quantities [Zakharov, 1972]. These quantities have the form of an integral with respect to τ of a polynomial expression in terms of the function $A(\xi,\tau)$ and its derivatives with respect to τ. The conserved quantities are given in the form [Lamb, 1980]:

$$(2i)^n C_n = \int_{-\infty}^{\infty} f_n(\tau)\, d\tau, \qquad n \geq 1, \tag{2.63}$$

where

$$f_0 = 0, \qquad f_1 = \frac{1}{2}\gamma|A|^2 \tag{2.64}$$

$$f_{n+1} = A\frac{d}{d\tau}\left(\frac{f_n}{A}\right) + \sum_{j+k=n} f_j f_k. \tag{2.65}$$

The first three conservation integrals have a simple physical meaning. The lowest order conserved quantity is called as the 'wave energy', 'mass', 'wave action', 'plasmon number', or 'wave power' in optics. It is given as

$$C_1 = \int_{-\infty}^{\infty} |A|^2\, d\tau. \tag{2.66}$$

The second order conserved quantity is called the '(linear) momentum' and the explicit expression is given by:

$$C_2 = \int_{-\infty}^{\infty} i(A\partial_\tau A^* - A^*\partial_\tau A)\, d\tau. \tag{2.67}$$

The third order conserved quantity C_3 is precisely the 'Hamiltonian' (2.61) introduced above.

References

[Agrawal, 1995] G. P. Agrawal. *Nonlinear Fiber Optics*. Academic Press, New York, 1995.

[Andonowati et al., 2005] Andonowati, N. Karjanto, and E. van Groesen. Extreme wave phenomena in down-stream running modulated waves. *Appl. Math. Modelling*, article in press, corrected proof, available online 27 June 2006.

[Benjamin, 1967] T. B. Benjamin. Instability of periodic wave trains in nonlinear dispersive systems. *Proc. R. Soc. London A* **229**(1456): 59–75, 1967.

[Benjamin and Feir, 1967] T. B. Benjamin and J. E. Feir. The disintegration of wave trains in deep water. *J. Fluid Mech.* **27**: 417–430, 1967.

[Benney and Newell, 1967] D. J. Benney and A. C. Newell. The propagation of nonlinear wave envelopes *J. Math. Phys.* **46**: 133–139, 1967.

[Bespalov and Talanov, 1966] V. I. Bespalov and V. I. Talanov. On the filament structure of a light beam in nonlinear liquids. *JETP Lett.* **3**: 307–312, 1966. Translated from *Zh. Eksperim. i Teor. Fiz.-Pis'ma Redakt.* **3**: 471–476, 1966.

[Boyd and Chen, 2001] J. P. Boyd and G.-Y. Chen. Weakly nonlinear wavepackets in the Korteweg-de Vries equation: the KdV/NLS connection. *Math. Comput Simuluation* **55**: 317–328, 2001.

[Bridges and Dias, 2004] T. J. Bridges and F. Dias. On the enhancement of the Benjamin-Feir instability due to dissipation. Under consideration for publication in *J. Fluid Mech.*, 2004.

[Bullough and Caudrey, 1995] R. K. Bulllough and P. J. Caudrey. Solitons and the Korteweg-de Vries equation: Integrable systems in 1834-1995. *Acta Appl. Math. (Acta Applicandae Mathematicae)* **39**: 193–228, 1995.

[Cahyono, 2002] E. Cahyono. *Analytical Wave Codes for Predicting Surface Waves in a Laboratory Basin*. Ph.D. thesis, Department of Applied Mathematics, University of Twente, The Netherlands, 2002.

[Chu and Mei, 1970] V. H. Chu and C. C. Mei. On slowly-varying Stokes waves. *J. Fluid Mech.* **41**: 873–87, 1970.

[Chu and Mei, 1971] V. H. Chu and C. C. Mei. The nonlinear evolution of Stokes waves in deep water. *J. Fluid Mech.* **42**: 337–351, 1971.

[Craik, 2004] A. D. D. Craik. The origin of water wave theory. *Annu. Rev. Fluid Mech.* **36**: 1–28, 2004.

[Craik, 2005] A. D. D. Craik. George Gabriel Stokes on water wave theory. *Annu. Rev. Fluid Mech.* **37**: 23–42, 2005.

[Davey, 1972] A. Davey. The propagation of a weak nonlinear wave. *J. Fluid Mech.* **53**: 769–781, 1972.

[Debnath, 1994] L. Debnath. *Nonlinear Water Waves*. Academic Press, San Diego, 1994.

[Dingemans, 1997] M. W. Dingemans. *Water Wave Propagation over Uneven Bottoms*. World Scientific, Singapore, 1997.

[Dingemans and Otta, 2001] M. W. Dingemans and A. K. Otta. *Nonlinear Modulation of Water Waves*. In P. L.-F. Liu, editor, volume **7** of *Advances in Coastal and Ocean Engineering*, World Scientific, Singapore, 2001.

[Djordjević and Redekopp, 1978] V. D. Djordjević and L. G. Redekopp. On the development of packets of surface gravity waves moving over an uneven bottom. *J. Appl. Math. Phys. (ZAMP)* **29**: 950–962, 1978.

[Dodd et al., 1982] R. K. Dodd, J. C. Eilbeck, J. D. Gibbon and H. C. Morris. *Solitons and Nonlinear Wave Equations*. Academic Press, 1982.

[Drazin and Johnson, 1989] P. G. Drazin and R. S. Johnson. *Solitons: an introduction*. Cambridge University Press, Cambridge, 1989.

[Fermi et al., 1955] E. Fermi, J. Pasta and S. M. Ulam. Studies of nonlinear problem. Los Alamos Scientific Laboratory Report No. LA-1940, 1955. Reprinted in A. C. Newell, editor, *Nonlinear Wave Motion*, volume **15** of AMS Lectures in Applied Mathematics, pp 143–156, 1974.

[Fornberg and Whitham, 1978] B. Fornberg and G. B. Whitham. A numerical and theoretical study of certain nonlinear wave phenomena. *Phil. Trans. R. Soc. London. A, Math. Phys. Sci.*, **289**: 373–404, 1978.

[Ginzburg and Landau, 1950] V. L. Ginzburg and L. D. Landau. On the theory of superconductivity. *Zh. Eksp. Teor. Fiz.* (USSR), **20**: 1064–1082 1950. English translation in L.D. Landau. *Men of Physics*, edited by D. ter Haar, volume **1**, Pergamon Press, Oxford, pp 138–167, 1965.

[Goldman and Sirovich, 1994] D. Goldman and L. Sirovich. The one dimensional complex Ginzburg-Landau equation in the low dissipation limit. *Nonlinearity*, **7**: 417–439, 1994.

[Hasegawa and Kodama, 1995] A. Hasegawa and Y. Kodama. *Solitons in Optical Communications*, volume **7** of *Oxford Series in Optical and Imaging Sciences*. Clarendon Press, Oxford, 1995.

[Hasegawa and Tappert, 1973] A. Hasegawa and F. D. Tappert. Transmission of stationary nonlinear optical pulses in dispersive dielectric fibres. I. Anomalous dispersion. II. Normal dispersion. *Appl. Phys. Lett.* **23**: 142–144, 171–172, 1973.

[Hasimoto and Ono, 1972] H. Hasimoto and H. Ono. Nonlinear modulation of gravity waves. *J. Phys. Soc. Japan* **33**: 805–811, 1972.

[Hunt, 2005] J. C. R. Hunt. Nonlinear and wave theory contributions of T. Brooke Benjamin (1929-1995). *Annu. Rev. Fluid Mech.* **38**: 1–25, 2005.

[Ichikawa et al., 1972] Y. H. Ichikawa, T. Imamura, and T. Taniuti. Nonlinear wave modulation in collisionless plasma. *J. Phys. Soc. Japan* **33**: 189–197, 1972.

[Infeld and Rowlands, 1990] E. Infeld and G. Rowlands. *Nonlinear Waves, Solitons, and Chaos*, Cambridge University Press, 1990.

[Janssen, 1981] P. A. E. M. Janssen. Modulational instability and the Fermi-Pasta-Ulam recurrence. *Phys. Fluids* **24**(1): 23–26, 1981.

[Jeffrey and Kawahara, 1982] A. Jeffrey and T. Kawahara. *Asymptotic Methods in Nonlinear Wave Theory*. Applicable Mathematics Series, Pitman, Boston, 1982.

[Johnson, 1976] R. S. Johnson. On the modulation of water waves on shear flows. *Proc. R. Soc. London. Ser. A* **347**(1651): 537–546, 1976.

[Johnson, 1997] R. S. Johnson. *A modern introduction to the mathematical theory of water waves*, volume **18** of *Cambridge Texts in Applied Mathematics*, Cambridge University Press, Cambridge, 1997.

[Kadomtsev and Karpman, 1971] B. B. Kadomtsev and V. I. Karpman. Nonlinear waves. *Sov. Phys. Uspekhi*, **14**(1): 40–60, 1971. Translated from *Usp. Fiz. Nauk* **103**: 193–232, 1971.

[Karpman and Kruskal, 1969] V. I. Karpman and E. M. Kruskal. Modulated waves in a nonlinear dispersive media. *Sov. Phys. JETP*, **28**: 277–281, 1969.

[Karpman, 1975] V. I. Karpman. *Nonlinear Waves in Dispersive Media*. Pergamon Press, Oxford, 1975.

[Kelley, 1965] P. L. Kelley. Self-focusing of optic beams. *Phys. Rev. Lett.* **15**: 1005–1008, 1965.

[Kevorkian, 1961] J. K. Kevorkian. *The Uniformly Valid Asymtotic Approximations to the Solutions of Certain Nonlinear Ordinary Differential Equations*. PhD thesis, California Institute of Technology, 1961.

[Kivshar and Luther-Davies, 1998] Y. S. Kivshar and B. Luther-Davies. Dark optical solitons: Physics and applications. *Phys. Reports* **298**: 81–197, 1998.

[Lake et al., 1977] B. M. Lake, H. C. Yuen, H. Rundgaldier and W. E. Ferguson. Nonlinear deep water waves: Theory and experiment, Part 2, Evolution of a continous wave train. *J. Fluid Mech.* **83**: 49–74, 1977.

[Lamb, 1980] G. L. Lamb, Jr. *Elements of Soliton Theory*, John Wiley & Sons, New York, 1980.

[Lighthill, 1965] M. J. Lighthill. Contributions to the theory of waves in nonlinear dispersive systems. *Journal of the Institute of Mathematics and Its Applications (J. Inst. Math. Applics.)* **1**: 269–306, 1965.

[Lighthill, 1967] M. J. Lighthill. Special cases treated by Whitham theory. *Proc. R. Soc. London. Ser. A* **299**(1456): 28–53, 1967.

[L'vov, 1994] V. S. L'vov. *Wave Turbulence Under Parametric Excitation–Applications to Magnets*. In V. E. Zakharov, series editor, *Springer Series in Nonlinear Dynamics*. Springer-Verlag, Berlin, 1994.

[Mei, 1983] C. C. Mei. *The Applied Dynamics of Ocean Surface Waves*. John Wiley & Sons, New York, 1983.

[Miles, 1981] J. W. Miles. The Korteweg–de Vries equation: a historical essay. *J. Fluid Mech.* **106**: 131–147, 1981.

[Nayfeh, 1973] A. H. Nayfeh. *Perturbation Methods*, Wiley-Interscience, New York, 1973.

[Newell, 1974] A. C. Newell. Envelope equations. In A. C. Newell, editor, *Nonlinear Wave Motion*, volume **15** of *Lectures in Applied Mathematics*. American Mathematical Society, 1974.

[Newell, 1985] A. C. Newell. *Solitons in Mathematical Physics*, volume **48** of *Regional Conference Series in Applied Mathematics*. Society for Industrial and Applied Mathematics, 1985.

[Onorato et al., 2001] M. Onorato, A. R. Osborne, M. Serio and S. Bertone. Freak waves in random oceanic sea states. *Phys. Rev. Lett.* **86**: 5831–5834, 2001.

[Osborne et al., 2000] A. R. Osborne, M. Onorato, and M. Serio. The nonlinear dynamics of rogue waves and holes in deep-water gravity wave trains. *Phys. Lett. A* **275**: 386–393, 2000.

[Ostrovsky, 1967] L. A. Ostrovsky. Propagation of wave packets and space-time self-focusing in a nonlinear medium. *Sov. Phys. JETP* **24**: 797–800, 1967.

[Remoissenet, 1999] M. Remoissenet. *Waves Called Solitons: Concepts and Experiments*. Springer, third edition, 1999.

[Segur et al., 2005] H. Segur, D. Henderson, J. Carter, J. Hammack, C.-M. Li, D. Pheiff and K. Socha. Stabilizing the Benjamin-Feir instability. *J. Fluid Mech.* **539**: 229–271, 2005.

[Scott et al., 1973] A. C. Scott, F. Y. H. Chu and D. W. McLaughlin. The soliton: a new concept in applied science *Proc. IEEE* **61**(10): 1443–1483, 1973.

[Scott, 2003] A. C. Scott. *Nonlinear Science–Emergence and Dynamics of Coherent Structures*. Oxford University Press, second edition, 2003.

[Scott, 2005] A. C. Scott. Solitons, a brief history. In A. C. Scott, editor, *Encyclopedia of Nonlinear Science*. Routledge Taylof & Francis Group, New York, 2005.

[Stuart and DiPrima, 1978] J. T. Stuart and R. C. DiPrima. The Eckhaus and Benjamin-Feir resonance mechanisms. *Proc. R. Soc. London A* **362**(1708): 27–41, 1978.

[Sulem and Sulem, 1999] C. Sulem and P.-L. Sulem. *The Nonlinear Schrödinger Equation—Self-Focusing and Wave Collapse*, volume **139** of *Applied Mathematical Sciences*, Springer-Verlag, New York, 1999.

[Talanov, 1965] V. I. Talanov. Self focusing of wave beams in nonlinear media. *JETP Lett.* **2**: 138–141, 1965. Translated from *Pis'ma Zh. Eksp. Teor. Fiz.* **2**: 223–236, 1965.

[Taniuti and Washimi, 1968] T. Taniuti and H. Washimi. Self-trapping and instability of hydromagnetics waves along the magnetic field in a cold plasma. *Phys. Rev. Lett.* **21**: 209–212, 1968.

[Tappert and Varma, 1970] F. Tappert and C. M. Varma. Asymptotic theory of self-trapping of heat pulses in solids. *Phys. Rev. Lett.* **25**: 1108–1111, 1970.

[Tracy et al., 1988] E. R. Tracy, J. W. Larson, A. R. Osbrone and L. Bergamasco. On the nonlinear Schrödinger limit of the Korteweg-de Vries equation. *Physica D* **32**(1): 83–106, 1988.

[Tracy et al., 1991] E. R. Tracy, J. W. Larson, A. R. Osbrone and L. Bergamasco. The relationship between the spectral theories for the periodic Korteweg-de Vries and nonlinear Schrödinger equations. In A. R. Osborne, editor, *Nonlinear Topics of Ocean Physics*, Fermi Summer School, Course LIX, pp. 769–825, North-Holland, Amsterdam, 1991.

[Van Groesen, 1998] E. van Groesen. Wave groups in uni-directional surface-wave model. *J. Engng. Math.* **34**(1–2): 215–226, 1998.

[Van Groesen and Andonowati, 2006] E. van Groesen and Andonowati. Finite energy wave signals of extremal amplitude in the spatial NLS-dynamics. *Phys. Lett. A* **357**: 86–91, 2006.

[Van Saarloos and Hohenberg, 1992] W. van Saarloos and P. C. Hohenberg. Fronts, pulses, sources and sinks in generalized complex Ginzburg-Landau equations. *Physica D* **56**: 303–367, 1992.

[Whitham, 1967] G. B. Whitham. Nonlinear dispersion of water waves. *J. Fluid Mech.* **27**(2): 399–412, 1967.

[Whitham, 1974] G. B. Whitham. *Linear and Nonlinear Waves*. John Wiley & Sons, New York, 1974.

[Yuen and Ferguson, 1978a] H. C. Yuen and W. E. Ferguson, Jr. Relationship between Benjamin-Feir instability and recurrence in the nonlinear Schrödinger equation. *Phys. Fluids* **21**(8): 1275–1278, 1978.

[Yuen and Ferguson, 1978b] H. C. Yuen and W. E. Ferguson, Jr. Fermi-Pasta-Ulam recurrence in the two-space dimensional nonlinear Schrödinger equation. *Phys. Fluids* **21**(11): 2116–2118, 1978.

[Yuen and Lake, 1975] H. C. Yuen and B. M. Lake. Nonlinear deep water waves: Theory and experiment. *Phys. Fluids* **18**: 956–960, 1975.

[Yuen and Lake, 1982] H. C. Yuen and B. M. Lake. Nonlinear dynamics of deep-water gravity waves. *Adv. Appl. Mech.* **22**: 67–229, 1982.

[Zakharov, 1967] V. E. Zakharov. The wave stability in nonlinear media. *Sov. Phys. JETP* **24**: 455–459, 1967.

[Zakharov, 1968] V. E. Zakharov. Stability of periodic waves of finite amplitude on the surface of a deep fluid. *J. Appl. Mech. Tech. Phys.* **9**: 190–194, 1968. Translated from *Zh. Prikl. Mekh. Tekh. Fiz.* **9**(2): 86–94, 1968.

[Zakharov and Shabat, 1972] V. E. Zakharov and A. B Shabat. Exact theory of two-dimensional self-focusing and one-dimensional self-modulation of waves in nonlinear media. *Sov. Phys. JETP* **34**(1): 62–69, 1972. Translated from *Zh. Eksp. Teor. Fiz.* **61**: 118–134, 1971.

[Zakharov, 1972] V. E. Zakharov. Collapse of Langmuir waves. *Sov. Phys. JETP* **35**(5): 908–914, 1972. Translated from *Zh. Eksp. Teor. Fiz.* **62**: 1745–1759, 1972.

Chapter 3

Waves on finite background

3.1 Introduction

As mentioned earlier in Chapter 1, the mathematical problem that is considered in this thesis is motivated by the following problem from the Maritime Research Institute Netherlands (MARIN). We want to be able to generate large and non-breaking waves, known as extreme waves, in the wave basins of MARIN. However, we do not know what kind of waves to generate. The wave generator, or wavemaker, has only limited capacity to make high waves directly. These high waves are already considered 'extreme' if the ratio of the highest amplitude and the initial amplitude reaches maximum value of three. Therefore, we let the 'nature' to produce extreme waves in the laboratory with input of relatively small amplitude wave signals. There are two possibilities in generating extreme waves mechanism: either linear focusing or the nonlinear modulational instability, as we have discussed in Chapter 2.

We choose for modulational instability process, in which the complete wave evolution is described by the Soliton on Finite Background (SFB), one family of solutions of the nonlinear Schrödinger (NLS) equation. By providing sufficient space for the waves to develop, the nature gives an amplitude amplification to these waves, leading to the formation of extreme wave events. The position where these extreme waves should occur is at a specific position in the wave basin. Practically it is desired to position the most extreme waves 'halfway' of the basin, in order not to destroy the artificial beach at the end of the basin. But importantly, this extreme position should also be sufficiently far from the wavemaker so that the nature has enough space in building up the extreme waves.

Investigating extreme waves on a finite background of a uniform monochromatic waves is related to the modulational instability of the plane wave solution of the NLS equation. Therefore, an initial modulated wave signal will grow exponentially in space according to the linear modulational instability but the nonlinearity will bound the

growth and the wave becomes an extreme wave event. If we consider the space to be infinite, this extreme wave has as finite background the plane wave solution. Actually, there is a family of exact solutions of the NLS equation that describes extreme wave events. This family is known as the SFB [Akhmediev et al., 1987]. The SFB is not the only family of solutions with waves on finite background. There are two other solutions which belong to the type of waves on finite background, namely the Ma soliton [Ma, 1979] and the rational soliton [Peregrine, 1983]. These three solutions of the NLS equation are also called breather solutions.

The contents of this chapter is a combination of two papers [Andonowati et al., 2006; Van Groesen et al., 2006] and is organized as follows. Section 3.2 will describe waves on finite background from a variational formulation perspective and a new displaced phase-amplitude representation is introduced. Sections 3.3–3.5 are devoted to a special class of waves on finite background, the SFB. This extensive discussion on the SFB is the main contribution of the thesis. In Section 3.3, we present the specifications and properties of the SFB, including several explicit expressions, the asymptotic behaviour at far distance, the physical wave field and the amplitude amplification factor. Section 3.4 discusses the evolution of an SFB wave signal, the evolution in the Argand diagram and the phase-plane representation for the SFB envelope signal. Section 3.5 explains the SFB wave signal in the frequency domain and the evolution of the amplitude and phase spectrum. Section 3.6 deals with other families of waves on finite background, namely the Ma soliton and the rational soliton. The relationship among these solutions is also explained and derived. The final section gives remarks on the contents of this chapter.

3.2 Description of waves on finite background

Waves on finite background have different characteristics from soliton type of solutions of the NLS equation, as described in Chapter 2 (see Subsection 2.4.3 on page 25). While the single-soliton vanishes at infinity, the waves on finite background are in fact nontrivial at infinity. In the case we will deal with in this chapter, the behaviour at infinity will be the plane-wave solution, as defined in Chapter 2, see the expression (2.45). In this section, the variational formulation of the NLS equation will be used to describe such waves.

We will write the complex amplitude of the NLS equation in the form of displaced phase-amplitude variables, with a displacement that depends on the background; the governing equations for these variables are derived. In Subsection 3.2.2, we investigate a special case by restricting the phase to depend only on space and not on time. As a consequence, the dynamics at each position is given as the motion of a nonlinear autonomous oscillator in a potential energy. The potential energy depends on the phase as a parameter and on the change of the phase with position. This change of phase with position corresponds physically to a change of the wavelength of the carrier wave and turns out to be the only driving force responsible for the nonlinear amplification towards

an extreme wave. Remarkably, the assumption of time-independent phase necessarily leads to the three families of breather solutions of the NLS equation mentioned in the preceding section.

3.2.1 Displaced phase-amplitude representation

We are interested in solutions of the NLS equation (2.23) on page 17 that are associated with modulational instability. Modulational instability , with the Benjamin-Feir instability of wave trains in surface water waves as prime example, is commonly associated with finite amplitude wave trains that get amplified by self focussing processes due to modulations in the envelope amplitude. We will restrict in the following to this basic setting of a perturbation of a uniform wave train, although other 'backgrounds' deserve more attention too.

To define more precisely the class of waves we are interested in, we take as background the plane-wave solution of the NLS equation (2.45), and will look for solutions of the form

$$A(\xi,\tau) = A_0(\xi)\, F(\xi,\tau), \tag{3.1}$$

where the asymptotic properties for F will be specified further. For this asymptotics we will require that except for a possible phase factor, the asymptotic value is the plane-wave solution, i.e. we require that

$$|F(\xi,\tau)| \longrightarrow 1 \qquad \text{for} \qquad \xi \longrightarrow \pm\infty \quad \text{or} \quad \tau \longrightarrow \pm\infty. \tag{3.2}$$

This asymptotic behaviour motivates, without further restrictions, the introduction of a displaced phase $\phi(\xi,\tau)$ and a displaced amplitude $G(\xi,\tau)$ parameter as follows

$$F(\xi,\tau) = G(\xi,\tau)e^{i\phi(\xi,\tau)} - 1, \qquad G \text{ and } \phi \in \mathbb{R}. \tag{3.3}$$

Since $|F| \longrightarrow 1$ at infinity, this means that $(G\cos\phi - 1)^2 + G^2\sin^2\phi = G(G - \cos 2\phi) + 1 \longrightarrow 1$. This implies that either $G \longrightarrow 0$ or $G - 2\cos\phi \longrightarrow 0$. Since we are not interested in a trivial solution, the asymptotic requirement implies that $G - 2\cos\phi \longrightarrow 0$. In the cases below we will deal with solutions for which G_τ and $\phi_\tau \longrightarrow 0$. Then for some limiting phases $\phi_\pm$ one finds

$$\phi(\xi) \longrightarrow \phi_\pm \qquad \text{and} \qquad G(\xi,\tau) \longrightarrow 2\cos(\phi_\pm) \qquad \text{asymptotically.} \tag{3.4}$$

In the complex plane, or Argand diagram, these parameters are depicted in Figure 3.1.

We are interested in solutions periodic in time τ with period T and an infinite range in space ξ. Therefore the integration boundaries of the corresponding action functional, Hamiltonian or other functions will be adjusted accordingly. Consider again the action functional corresponding to the NLS equation, namely equation (2.57) on page 28:

$$\mathcal{A}(A) = \int_{-\infty}^{\infty} \left(\int_{-T/2}^{T/2} \frac{1}{4} i \left(A^* \partial_\xi A - A \partial_\xi A^* \right) d\tau - H(A) \right) d\xi, \tag{3.5}$$

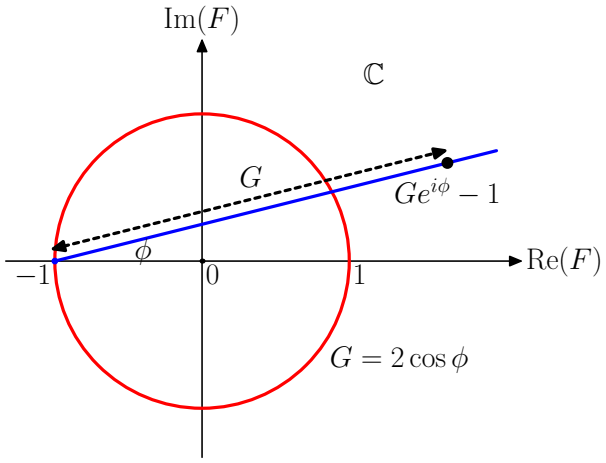

Figure 3.1: Indicated are the displaced phase-amplitude parameters in the Argand diagram for the amplitude of waves on finite background; the unit sphere corresponds to the set $G = 2\cos\phi$.

where the Hamiltonian H is a functional of functions in τ given by equation (2.61) on page 28:

$$H(A) = \int_{-T/2}^{T/2} \left(-\frac{1}{2}\beta \left|\partial_\tau A\right|^2 + \frac{1}{4}\gamma |A|^4 \right) \, d\tau. \tag{3.6}$$

To arrive at the governing phase-amplitude equations, we substitute

$$A(\xi,\tau) = A_0(\xi) \, \left[G(\xi,\tau) e^{i\phi(\xi,\tau)} - 1 \right] \tag{3.7}$$

into the action functional (3.5). Then we have the following expressions:

$$\begin{aligned}
\frac{1}{4} i \left(A^* \partial_\xi A - A \partial_\xi A^* \right) &= \frac{1}{2} r_0^2 \left[-G^2 \partial_\xi \phi + \gamma r_0^2 (G[G - 2\cos\phi] + 1) + \partial_\xi (G \sin\phi) \right] \\
\frac{1}{2}\beta |\partial_\tau A|^2 &= \frac{1}{2} r_0^2 \beta \left[(\partial_\tau G)^2 + G^2 (\partial_\tau \phi)^2 \right] \\
\frac{1}{4}\gamma |A|^4 &= \frac{1}{2} r_0^2 \, \frac{1}{2} \gamma r_0^2 (G[G - 2\cos\phi] + 1)^2 .
\end{aligned}$$

The action functional now depends on G and ϕ, and since the integration of the term $\partial_\xi (G \sin\phi)$ gives a constant difference, we neglect it and the action functional reads:

$$\mathcal{A}(G,\phi) = -\frac{1}{2} r_0^2 \int_{-\infty}^{\infty} \left(\int_{-T/2}^{T/2} (\partial_\xi \phi) G^2 \, d\tau + \bar{H}(G,\phi) \right) \, d\xi, \tag{3.8}$$

where the transformed Hamiltonian $\bar{H}$ reads

$$\bar{H}(G,\phi) = \int_{-T/2}^{T/2} \left[-\beta(\partial_\tau G)^2 - \beta(\partial_\tau \phi)^2 G^2 + W(G,\phi) \right] \, d\tau \tag{3.9}$$

and where we have introduced the normalized potential energy $W(G,\phi)$ as follows. The non normalized expression for W is given explicitly by $\frac{1}{2}\gamma r_0^2(G[G-2\cos\phi]+1)^2 - \gamma r_0^2(G[G-2\cos\phi]+1)^2 = \frac{1}{2}\gamma r_0^2\left(G^2[G-2\cos\phi]^2-1\right)$. In the following we will discard the uninteresting constant term which, moreover, gives rise to divergence of the action functional, and take

$$W(G,\phi) = \frac{1}{2}\gamma r_0^2 G^2 (G-2\cos\phi)^2. \tag{3.10}$$

It is to be noted that W has, besides the origin $G=0$, the unit circle in the complex plane as set of nontrivial critical points:

$$\frac{\partial W}{\partial G} = \frac{\partial W}{\partial \phi} = 0 \qquad \text{for } \; G = 2\cos\phi, \tag{3.11}$$

for which $W=0$ and $\left|Ge^{i\phi}-1\right| = 1$.

The governing equations follow from variations with respect to G and ϕ. Variation with respect to $\phi(\xi,\tau)$ gives the time integrated energy equation which takes the form

$$\partial_\xi(G^2) - 2\beta\partial_\tau(G^2\partial_\tau\phi) + \frac{\partial W}{\partial\phi} = 0, \tag{3.12}$$

this energy equation shows a forcing from the dependence of W on ϕ. Variation with respect to $G(\xi,\tau)$ gives the 'displaced' phase equation

$$\beta\partial_\tau^2 G + \left(\partial_\xi\phi - \beta(\partial_\tau\phi)^2\right) G - \frac{1}{2}\frac{\partial W}{\partial G} = 0, \tag{3.13}$$

which is the transformed nonlinear dispersion relation. This equation can be interpreted as a nonlinear oscillator equation for G, which now depends on ϕ through the dependence in W and on the combination of its derivatives $\partial_\xi\phi - \beta(\partial_\tau\phi)^2$ that contributes to the coefficient in front of the linear term. In general this is therefore a non-autonomous oscillator equation. Note that it has exactly the same form as the general phase equation (2.32), but now W depends essentially on the phase ϕ. The energy of each oscillator is not constant in general because of the dependence of the phase on τ in the expression. Indeed, if we denote the energy by E:

$$E(G,\phi) = \frac{1}{2}\beta\left(\frac{\partial G}{\partial\tau}\right)^2 + V(G,\phi), \tag{3.14}$$

where the potential function $V(G,\phi) = \frac{1}{2}\left[\partial_\xi\phi - \beta(\partial_\tau\phi)^2\right]G^2 - \frac{1}{2}W(G,\phi)$, the change of energy with respect to τ can be calculated explicitly:

$$\begin{aligned}\frac{\partial E}{\partial \tau} &= \underbrace{\left(\beta\frac{\partial^2 G}{\partial\tau^2} + \left[\partial_\xi\phi - \beta(\partial_\tau\phi)^2\right]G - \frac{1}{2}\frac{\partial W}{\partial G}\right)}_{=0}\frac{\partial G}{\partial\tau} \\ &\quad + \frac{1}{2}\frac{\partial}{\partial\tau}\left[\frac{\partial\phi}{\partial\xi} - \beta\left(\frac{\partial\phi}{\partial\tau}\right)^2\right]G^2 - \frac{1}{2}\frac{\partial W}{\partial\phi}\frac{\partial\phi}{\partial\tau}.\end{aligned} \tag{3.15}$$

Vanishing of the first term is a consequence of the displaced phase equation (3.13). For time periodic motions with period T, the time-integral over one period of $\partial_\tau E$ should vanish: $\int_{-T/2}^{T/2}\partial_\tau E(G,\phi)\,d\tau = 0$, so that there is no nett energy input or output. In the following section we will consider the case that the phase ϕ does not depend on τ; then the formula above shows that the energy is of each oscillator at each fixed ξ (hence fixed ϕ) is constant.

The conservation properties for the spatial evolution are now given by the wave energy (2.66):

$$\frac{\partial}{\partial\xi}\left(\int_{-T/2}^{T/2}(G^2 - 2G\cos\phi + 1)\,d\tau\right) = 0 \tag{3.16}$$

and the original Hamiltonian $H(A)$ (3.6):

$$\frac{\partial}{\partial\xi}\left(\int_{-T/2}^{T/2}\left(-\frac{1}{2}\beta r_0^2\left[(\partial_\tau G)^2 + (\partial_\tau\phi)^2G^2\right] + \frac{1}{4}\gamma r_0^4\left|Ge^{i\phi} - 1\right|^4\right)d\tau\right) = 0. \tag{3.17}$$

The transformed Hamiltonian $\bar{H}(G,\phi)$ is related to the Hamiltonian $H(A)$ and the wave energy by the following relation:

$$\frac{1}{2}r_0^2\bar{H}(G,\phi) = H(A) - \gamma\int_{-\infty}^{\infty}\left(|A|^2 - \frac{1}{2}r_0^2\right)d\tau. \tag{3.18}$$

As a consequence, the transformed Hamiltonian is also conserved: $\partial_\xi\bar{H}(G,\phi) = 0$. For solutions with the asymptotic behaviour as above, we have $W \longrightarrow 0$ for $\xi \longrightarrow \pm\infty$. Hence it follows that $\bar{H} = 0$ asymptotically, and then the constancy in ξ implies

$$\bar{H}(G,\phi) = 0 \qquad \text{for all } \xi\in\mathbb{R}. \tag{3.19}$$

Related to the non-autonomous character of the equation, in general, the dependence of ϕ on τ implies that at a fixed spatial position the motion in the Argand diagram is not on a straight line. In the next section we will consider special solutions for which the motion is at each position represented by a motion on a straight line, the line turning with position.

3.2.2 Pseudo-coherent wave solutions

We now consider special solutions for which the displaced phase ϕ does not depend on time τ but only depends on position ξ. We show that the spatial evolution is fully described by a family of constrained optimization problems for the time signals. Each optimization problem is only parameterized by the phase, and the spatial dynamics comes in from the change of a multiplier $\lambda(\phi)$ with phase. Remarkably, classes of solutions of these optimization problems can be found explicitly; the corresponding solutions found in this way will then be recognized as the well known soliton solutions of the NLS equation.

From the assumption that the phase does not depend on time,

$$F(\xi,\tau) = G(\xi,\tau)e^{i\phi(\xi)} - 1, \tag{3.20}$$

it follows that at each position the phase is constant, and the governing oscillator equation (3.13) for G is autonomous.

Note that although the displaced phase ϕ is assumed to depend on ξ only, if we write the complex amplitude $A = A_0(\xi)\,F(\xi,\tau)$ in the usual phase-amplitude form, $F(\xi,\tau) = b(\xi,\tau)e^{i\psi(\xi,\tau)}$, then the phase ψ will depend on ξ and τ. This phase $\psi(\xi,\tau)$ is related to the displaced phase $\phi(\xi)$ by the following relation:

$$\tan\psi(\xi,\tau) = \frac{G(\xi,\tau)\sin\phi(\xi)}{G(\xi,\tau)\cos\phi(\xi) - 1}. \tag{3.21}$$

Therefore, the wave signal of the NLS equation itself is not coherent; we will call this a 'pseudo-coherent' solution, since it is only coherent with respect to the displaced phase-amplitude variables.

The fact that the dependence on τ is missing in ϕ implies that the motions in the Argand plane are on straight lines through the point -1, with angle ϕ that depends on the position $\xi(=x)$: the solution is displaced over a distance -1 in the complex plane.

The equations for G and ϕ are a special case of the above, but it is illustrative to derive them directly from the action principle (3.8), where the Hamiltonian $\bar{H}(G,\phi)$ now becomes

$$\bar{H}(G,\phi) = \int_{-T/2}^{T/2} \left[-\beta(\partial_\tau G)^2 + W(G,\phi)\right]\, d\tau \tag{3.22}$$

with $W(G,\phi)$ as given in (3.10). To find the variation with respect to $\phi(\xi)$, we change the order of integration in the action functional (3.8). Consequently, we obtain the energy equation in the integral form:

$$\frac{1}{T}\int_{-T/2}^{T/2}\left(-\partial_\xi(G^2) + \frac{\partial W}{\partial\phi}\right)\, d\tau = 0. \tag{3.23}$$

This shows the presence of a forcing from the dependence of the potential energy on the phase. Variation with respect to $G(\xi,\tau)$ gives the displaced phase equation

$$(\partial_\xi\phi)\,G + \beta\partial_\tau^2 G - \frac{1}{2}\frac{\partial W}{\partial G} = 0. \tag{3.24}$$

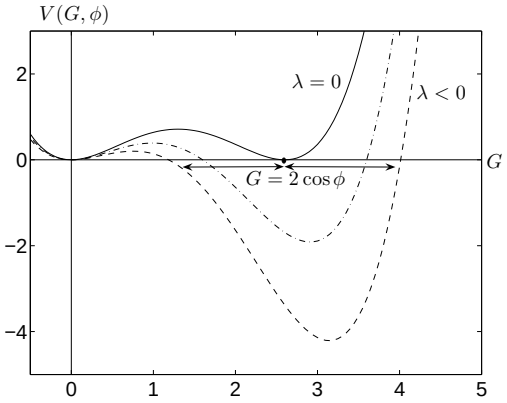

Figure 3.2: Plot of the effective potential for various values of $\lambda < 0$. The solid line is the plot for $\lambda = 0$.

This last equation shows that at fixed ξ the nonlinear oscillator equation for G depends on ϕ and $\partial_\xi \phi$ but not on τ, so that at each position the equation for G is autonomous. An effective potential energy defined by

$$V(G,\phi) = \frac{1}{2}\lambda G^2 - W(G,\phi) = \frac{1}{2}G^2\left(\lambda + \gamma r_0^2 (G - 2\cos\phi)^2\right), \tag{3.25}$$

is the oscillator potential for $\lambda = \partial_\xi \phi$. For negative λ the plots of the potential are depicted in Figure 3.2.

The conservation properties for the spatial evolution are as before the wave energy $\int |A|^2 d\tau$ and the Hamiltonian $H(A)$; in particular it holds that:

$$\bar{H}(G,\phi) = \int_{-T/2}^{T/2} \left(-\beta(\partial_\tau G)^2 + W(G,\phi)\right)\, d\tau = 0, \qquad \text{for all } \xi \in \mathbb{R}. \tag{3.26}$$

Inspection of the oscillator equation (3.24) shows that the solutions can be obtained in the following, somewhat surprising, variational way, the idea of which is motivated by the terms in the action functional.

Proposition 3.2.1 Consider for each ϕ the constrained variational problem*

$$\mathrm{Crit}_G \left\{ \int_{-T/2}^{T/2} \frac{1}{2} G^2 \, d\tau \;\middle|\; \bar{H}(G,\phi) = 0 \right\}. \tag{3.27}$$

*The notion 'Crit' denotes an optimization of the corresponding constrained problem, provided that the optimization exists and the functionals are differentiable. A critical point or stationary point of the functional $\mathcal{L} = \int \frac{1}{2}\lambda G^2 \, d\tau - \bar{H}(G,\phi)$ satisfies the condition that the first variation of $\mathcal{L}$ vanishes for all admissible variations near the critical point.

The nontrivial solutions $\tau \longrightarrow G(\phi)$ satisfy the Lagrange multiplier equation for some (reciprocal) multiplier $\lambda(\phi)$: $\lambda G = \delta_G \bar{H}(G, \phi)$. Then, if $\xi \longrightarrow \phi(\xi)$ is a solution of the equation $\partial_\xi \phi = \lambda(\phi)$, the spatial evolution $\xi \longrightarrow G(\phi(\xi))$ leads to a solution of the NLS equation given by

$$A(\xi, \tau) = A_0(\xi) \left[G(\xi, \tau) e^{i\phi(\xi)} - 1 \right]. \tag{3.28}$$

The multiplier equation reads in detail

$$\beta \partial_\tau^2 G + \lambda G + \gamma r_0^2 G(G - \cos\phi)(G - 2\cos\phi) = 0 \tag{3.29}$$

and has linear, quadratic and cubic nonlinear terms. It is interesting that various classes of solutions of the constrained variational problem can actually be given explicitly and simply. Now solutions of the NLS equation are of the form

$$G(\phi, \tau) = \frac{P(\phi)}{Q(\phi) - \zeta(\tau)} \tag{3.30}$$

where $\zeta(\tau)$ is one of three special functions, each of which corresponds to a well known special solution. For $\zeta(\tau) = \cos(\nu\tau)$, we will obtain the SFB solution [Akhmediev et al., 1987]; for $\zeta(\tau) = \cosh(\mu\tau)$, it corresponds to the Ma solution [Ma, 1979]; and for $\zeta(\tau) = 1 - \frac{1}{2}\nu\tau^2$, it is given by the rational solution [Peregrine, 1983]. We will specify the SFB solution in the following section and the Ma solution together with the rational solution in Section 3.6.

Remark 3.2.1 In the variational formulation above, it is possible to take another target functional to be optimized:*

$$\mathrm{Crit}_G \left\{ \frac{1}{T} \int_{-T/2}^{T/2} G \, d\tau \;\middle|\; \bar{H}(G, \phi) = 0 \right\}. \tag{3.31}$$

This is a consequence of the fact that the quadratic energy is conserved, implying that

$$\frac{1}{T} \int_{-T/2}^{T/2} (G^2 - 2G\cos\phi) \, d\tau = \text{constant}. \tag{3.32}$$

Of course the optimal solutions (and the multiplier) will be different, actually just a shift in G. This last formulation, for the signal at the extreme position only, was proposed in [Van Groesen et al., 2005; Andonowati et al., 2006].

*See the footnote of Proposition 3.2.1.

3.3 Specifications and properties of the SFB

3.3.1 An explicit expression

The Soliton on Finite Background (SFB) is derived in [Akhmediev et al., 1987]; the explicit expression already appeared earlier, see for instance [Akhmediev et al., 1985; Akhmediev and Korneev, 1986]. The authors suggested a method of obtaining exact solutions of the NLS equation by writing the complex amplitude A in the form $A(\xi,\tau) = [p(\xi,\tau) + iq(\xi)]\, e^{i\varrho(\xi)}$ and substituting it into the NLS equation. The method consists in constructing a certain system of ordinary differential equations in p, the solutions of which determine the solutions of the NLS equation. After an integration procedure, the system leads to a second order ordinary differential equation similar to (3.29), but it has a quartic term instead of the cubic term.

We derive an explicit expression of the SFB based on the variational formulation mentioned in the previous section, where the function P and Q depend on the displaced phase ϕ. We have the following proposition:

Proposition 3.3.1 For any value of a modulation frequency ν such that $0 < \tilde{\nu} < \sqrt{2}$, where $\tilde{\nu} = \nu / \left(r_0\sqrt{\gamma/\beta}\right)$ is the normalized modulation frequency, the solution is given by

$$G(\phi,\tau) = \frac{P(\phi)}{Q(\phi) - \cos(\nu\tau)} \tag{3.33}$$

where the coefficients are given by

$$P(\phi) = \frac{\tilde{\nu}^2 Q(\phi)}{\cos\phi}, \qquad Q^2(\phi) = \frac{2\cos^2\phi}{2\cos^2\phi - \tilde{\nu}^2}. \tag{3.34}$$

and the multiplier is given by $\lambda = \gamma r_0^2(\tilde{\nu}^2 - 2\cos^2\phi)$.

The result can easily be verified by considering the function (3.30) with $\zeta(\tau) = \cos(\nu\tau)$. Direct differentiation and algebraic manipulations show that this function satisfies an equation with linear, quadratic and cubic terms, which reads:

$$\frac{\partial^2 G}{\partial\tau^2} + \nu^2 G - 3\nu^2\frac{Q}{P}G^2 + 2\nu^2\frac{Q^2-1}{P^2}G^3 = 0. \tag{3.35}$$

Now we compare to the multiplier equation (3.29) as the governing equation for G that can be written as:

$$\beta\partial_\tau^2 G + (\lambda + 2\gamma r_0^2\cos^2\phi)G - 3\gamma r_0^2 G^2 + \gamma r_0^2 G^3 = 0. \tag{3.36}$$

Comparing coefficients of G^2 term, we have $Q/P = \cos\phi/\tilde{\nu}^2$ and from comparing coefficients G^3 term, we obtain $2\tilde{\nu}^2(Q^2-1) = P^2$. Using algebraic manipulation, we arrive at the proposition above. The explicit spatial evolution for ϕ as function of ξ is then found by solving

$$\partial_\xi\phi = \lambda = \gamma r_0^2(\tilde{\nu}^2 - 2\cos^2\phi), \qquad 0 < \tilde{\nu}^2 < 2. \tag{3.37}$$

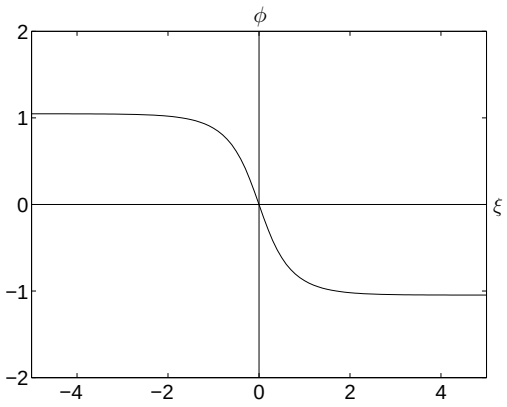

Figure 3.3: The plot of the displaced phase of the SFB for $\tilde{\nu} = \sqrt{1/2}$.

The result can be written in elementary functions, as will be given in (3.42). Note that the value of $\tilde{\nu}$ determines the asymptotic values of the phase: $\tilde{\nu} = \pm\sqrt{2}\cos\phi_{\pm}$ with $\phi_+ > \phi_-$ to assure that ϕ is decreasing. A characteristic plot of this function is given in Figure 3.3.

We write the explicit expression of the SFB in the displaced phase-amplitude representation given by (3.1) and the function F with time independent displaced phase, as in (3.20). Now, expressions for the displaced phase and amplitude are given as follows:

$$A_0(\xi) = r_0 e^{-i\gamma r_0^2 \xi} \tag{3.38}$$

$$G(\xi,\tau) = \frac{P(\xi)}{Q(\xi) - \cos[\nu(\tau-\tau_0)]} \tag{3.39}$$

$$P(\xi) = \tilde{\nu}\sqrt{\left(\tilde{\nu}^2 + \sinh^2[\sigma(\xi-\xi_0)]\right)/(1-\tilde{\nu}^2/2)} \tag{3.40}$$

$$Q(\xi) = \cosh[\sigma(\xi-\xi_0)]/\sqrt{1-\tilde{\nu}^2/2} \tag{3.41}$$

$$\phi(\xi) = \arctan\left(-(\tilde{\sigma}/\tilde{\nu}^2)\tanh[\sigma(\xi-\xi_0)]\right). \tag{3.42}$$

In this expressions, $(\xi_0,\tau_0) \in \mathbb{R}^2$ corresponds to the point where the SFB reaches a maximum value. For simplicity, we will make a shift in position and time so that the maximum value is at $(0,0)$, so that $\xi_0 = 0 = \tau_0$. The quantities ν and σ characterize the SFB and they are precisely the parameters that have been introduced in Chapter 2 in the context of the Benjamin-Feir instability. See Subsection 2.4.2 on pages 22–25 for more detail.

This solution describes the modulational instability process in the whole space from $\xi = -\infty$ to $\xi = \infty$. At the far distance $\xi \to \pm\infty$, the SFB is described by the linear theory of modulational instability. For ξ in the nonlinear regime, the SFB connects an exponential behaviour from two sides and bounds it by large, extreme envelope waves.

Note that this SFB depends on two parameters: the plane-wave amplitude r_0 and the (normalized) modulation frequency $\tilde{\nu}$. In order to assure that the SFB exists, $\tilde{\nu}$ has to be in the modulational instability interval $0 < \tilde{\nu} < \sqrt{2}$. The corresponding physical wave field has as additional parameter the carrier wave frequency ω_0. The physical space and time variables are scaled in a moving frame of reference by the relation $\xi = x$ and $\tau = t - x/\Omega'(k_0)$.

We have seen an expression for the SFB, but in fact there are several different ways to present the explicit expression. The SFB expression (3.38–3.42) can also be written as

$$A(\xi,\tau) = A_0(\xi)\left(\frac{\tilde{\nu}^2\cosh(\sigma\xi) - i\tilde{\sigma}\sinh(\sigma\xi)}{\cosh(\sigma\xi) - \sqrt{1-\frac{1}{2}\tilde{\nu}^2}\cos(\nu\tau)} - 1\right). \tag{3.43}$$

This expression is similar with the expression on page 51 of [Akhmediev and Ankiewicz, 1997], with different notations $p \mapsto \nu$, $\beta \mapsto \sigma$, $a_1 \mapsto (2-\nu^2)/4$ and $\psi'(\xi,\tau) \mapsto A(\xi,\tau) = \sqrt{2}\psi'(-2\xi,\tau)$.

An alternative description of the SFB is given in [Dysthe and Trulsen, 1999] and [Grimshaw et al., 2001] using the transformations $\nu = \sqrt{2}\sin\varphi$, $\sigma = \sin 2\varphi$, $t \mapsto -\frac{1}{2}\xi$, $x \mapsto \frac{1}{\sqrt{2}}\tau$:

$$A(\xi,\tau) = A_0(\xi)\frac{\cos\varphi\cos(\nu\tau) - \cosh(\sigma\xi + 2i\varphi)}{\cosh(\sigma\xi) - \cos\varphi\cos(\nu\tau)}. \tag{3.44}$$

Another representation of the SFB is given in [Ablowitz and Herbst, 1990] where the authors derived it using the Hirota's method. Prescribing $\beta = -1$, $\gamma = -2$, $\nu \mapsto p$, $r_0 \mapsto a$, and transforming the variables $\xi \mapsto t$, $\tau \mapsto x$, $A \mapsto u$ the SFB with a phase factor $-e^{2i\phi}$ can be written as:

$$u(x,t) = ae^{2ia^2t}\left(\frac{1 + 2\cos(px)e^{\sigma t+\gamma_1+2i\phi} + A_{12}e^{2(\sigma t+\gamma_1+2i\phi)}}{1 + 2\cos(px)e^{\sigma t+\gamma_1} + A_{12}e^{2(\sigma t+\gamma_1)}}\right) \tag{3.45}$$

where $\sin\phi = \frac{p}{2a}$, $A_{12} = \frac{1}{\cos^2\phi}$, $\sigma = \pm p\sqrt{4a^2 - p^2}$, and $e^{\gamma_1} = \pm\sqrt{1 - \frac{1}{2}\frac{p^2}{2a^2}}$.

Another explicit expression is given in [Osborne et al., 2000; Osborne, 2001] where the authors derived it using the inverse scattering technique. By prescribing $\tilde{\nu} = 1$, $\beta = -1$, $\gamma = -1$, $r_0 \mapsto a$, changing the variables $\xi \mapsto T$, $\tau \mapsto X$, $A \mapsto u$ and dividing by the term $\cos(2a^2t)$, the SFB now becomes:

$$u(X,T) = ae^{2ia^2T}\left(\frac{\cos(a\sqrt{2}X)\,\mathrm{sech}(2a^2T) + i\sqrt{2}\tanh(2a^2T)}{\sqrt{2} - \cos(a\sqrt{2}X)\,\mathrm{sech}(2a^2T)}\right). \tag{3.46}$$

This expression is the equation (4) of [Osborne et al., 2000] with a typographical error that has been corrected since it was written there $\mathrm{sech}(a^2\sqrt{2}T)$ instead of $\mathrm{sech}(2a^2T)$.

The name SFB itself comes from the characteristics of its complex amplitude plot. At a fixed time, in particular the times when it reaches maxima, the SFB has a soliton-like form with a finite background for $\xi \to \pm\infty$ instead of the standard soliton (2.51)

which has vanishing amplitude for the same limiting variable. The value of the background is always positive since it describes the envelope of the plane-wave solution in the far distance. At a fixed position, the SFB is periodic in the time variable, with the periodicity depending on the modulation frequency ν. We denote the period of the SFB as $T = 2\pi/\nu$. A plot of the absolute value of the SFB for $r_0 = 1$ is given in Figure 3.4.

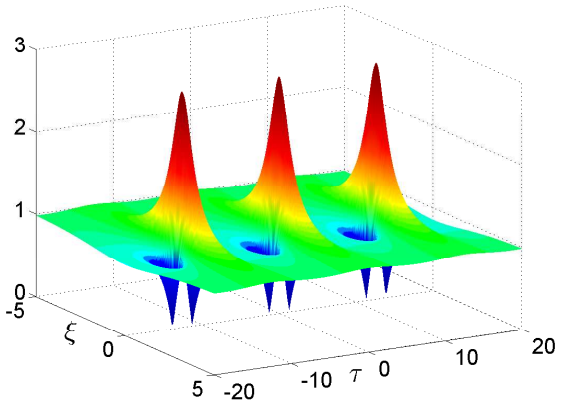

Figure 3.4: Plot of the absolute value of the SFB for $\tilde{\nu} = 1/2$. For illustration purposes, the axes are scaled corresponding to $\beta = 1 = \gamma$.

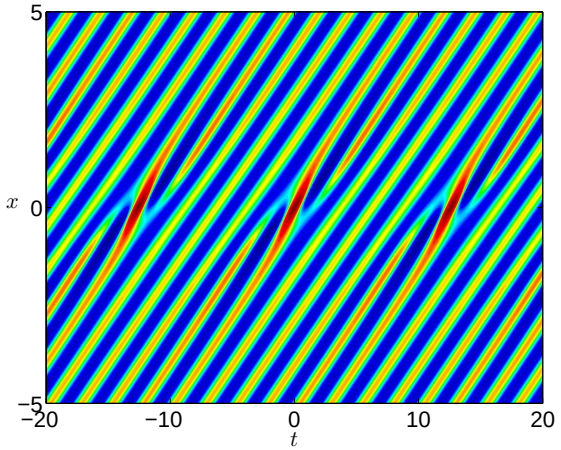

Figure 3.5: A density plot of the physical wave field $\eta(x,t)$ of the SFB for $\tilde{\nu} = 1/2$ corresponding to Figure 3.4 for $k_0 = 2\pi$. The plot is shown in a moving frame of reference with suitable chosen velocity.

3.3.2 The asymptotic behaviour

The asymptotic behaviour of the SFB is given at the far distance for $\xi \to \pm\infty$. It becomes the plane-wave solution $A_0(\xi)$, with a phase difference of $2\phi_0$ from $\xi = -\infty$ to $\xi = \infty$, as we will see in this subsection. However, we want to know the linear term after the lowest order that specifies the asymptotic behaviour of SFB. Thus, for the asymptotic behaviour, we include both the lowest order term and the linear term.

We only derive the result for $\xi \to -\infty$ since a similar procedure can be applied for $\xi \to \infty$. In order to find the asymptotic behaviour of the SFB, we introduce a new variable $y = e^{\sigma\xi}$. (For $\xi \to \infty$, a new variable $y = e^{-\sigma\xi}$ is chosen.) The SFB that we will concentrate on is the complex function F in (3.1). We do not take into account the plane-wave contribution since it will give fast oscillations and distracts our analysis. The function F now is given by:

$$F(y,\tau) = \left(\frac{(\tilde{\nu}^2 - i\tilde{\sigma})y^2 + \tilde{\nu}^2 + i\tilde{\sigma}}{y^2 + 1 - \sqrt{4 - 2\tilde{\nu}^2}\, y\, \cos(\nu\tau)} - 1 \right). \tag{3.47}$$

Since for $\xi \to -\infty$, $y \to 0$, we develop the function $F(y,\tau)$ in a Taylor expansion around $y = 0$:

$$F(y,\tau) = F(0,\tau) + \partial_y F(0,\tau) y + \frac{1}{2}\partial_y^2 F(0,\tau) y^2 + \dots . \tag{3.48}$$

After some simple manipulations we arrive at

$$F(0,\tau) = \tilde{\nu}^2 - 1 + i\tilde{\sigma}, \tag{3.49}$$

$$\partial_y F(0,\tau) = \sqrt{4 - 2\tilde{\nu}^2}(\tilde{\nu}^2 + i\tilde{\sigma})\cos(\nu\tau). \tag{3.50}$$

Therefore, the asymptotic behaviour for the SFB at $\xi \to \mp\infty$ is given by

$$A(\xi,\tau) \approx A_0(\xi) \left[e^{i\phi_0} + \sqrt{4 - 2\tilde{\nu}^2} e^{i\phi_1} e^{\pm\sigma\xi} \cos(\nu\tau) \right], \tag{3.51}$$

where

$$\tan\phi_0 = \mp \frac{\tilde{\sigma}}{\tilde{\nu}^2 - 1} \qquad \text{and} \qquad \tan\phi_1 = \mp \frac{\tilde{\sigma}}{\tilde{\nu}^2}. \tag{3.52}$$

Notice that $\tan 2\phi_1 = \tan\phi_0$ and the phases corresponding to the central frequency and the first sideband experience phase shifts of $2\phi_0$ and $2\phi_1$, respectively. The former one describes precisely the phase shift of the SFB.

This asymptotic behaviour of the SFB corresponds to the linear modulational (Benjamin-Feir) instability as mentioned already in Subsection 2.4.2 of the previous chapter. A similar relation between the phases θ_1 and θ_2 is also obtained (2.48) that $\tan(\theta_1 + \theta_2) = \tan\phi_0$ by the transformation in the time variable $\tau \mapsto \tau - \phi_0$. This instability is based on the linear theory but the SFB describes a complete nonlinear evolution of a modulated wave signal. The relation between modulational instability and the asymptotic behaviour of the SFB is known and given in [Akhmediev and Korneev, 1986].

3.3.3 Physical wave field

The SFB family, just like all solutions of the NLS equation, describe the envelopes of physical wave fields, in our case, the surface water waves. In order to study the corresponding physical wave field, we use the notion of the physical wave field $\eta(x,t)$ as a wave group with the complex amplitude A and the wave group frequency ω_0, as introduced in Section 2.2 and also Section 2.3. We consider only the lowest order contribution and we rewrite again the physical wave field η as follows:

$$\eta(x,t) = A(\xi,\tau)\, e^{i(k_0 x - \omega_0 t)} + \text{c c}. \tag{3.53}$$

The corresponding physical wave field of the SFB now depends on three essential parameters, namely the wave group frequency ω_0, the (normalized) modulation frequency $\tilde{\nu}$ and the plane-wave amplitude r_0. We called 'essential' since we do not consider two other parameters (ξ_0, τ_0). By shifting these parameters we can always obtain the maximum amplitude at the desired location and time, as we did earlier by prescribing $\xi_0 = 0 = \tau_0$. Both the dispersion coefficient β and the nonlinear transfer coefficient γ in the NLS equation depend on ω_0. The SFB physical wave field is periodic in time with the modulation period of $T = 2\pi/\nu$. During the downstream evolution, it experiences a phase shift of $2\phi_0$, where ϕ_0 is given by (3.52).

We often write the complex amplitude A in its polar form: $A = ae^{i\phi}$, where a and ϕ are the real-valued amplitude and the real-valued phase, respectively. The SFB physical wave field then becomes:

$$\eta(x,t) = 2a(x,t)\, \cos\Phi(x,t), \qquad \text{where} \qquad \Phi(x,t) = k_0 x - \omega_0 t + \phi(x,t). \tag{3.54}$$

We use this expression to give a graphical illustration of the SFB wave field. Using the shifting mentioned above, the SFB reaches the highest amplitude at $x = \xi = 0$ and we call it the 'extreme position'. By taking only the lowest order contribution, we neglect the Stokes effect from higher order terms. Consequently, the wave elevation from (3.54) is not completely realistic. Figure 3.5 shows the corresponding physical wave field of the SFB in scaled parameters $\beta = \gamma = r_0 = 1$. Notice that the wave field shows 'wavefront dislocation' at the extreme position for the interval $0 < \tilde{\nu} < \sqrt{3/2}$, where waves are merging or splitting [Nye and Berry, 1974]. This phenomenon will be explained in more detail in Chapter 4.

For both the theory and the experiment of extreme wave generation, we are interested in the ratio of the maximum amplitude and the value of the background. So, we have the following definition.

Definition 3.3.1 (Amplitude amplification factor, AAF) The AAF of a wave field is the ratio of the maximum amplitude and the value of its background.

For the SFB, the AAF depends only on the modulation frequency, and does not depend on the two other essential parameters. Explicitly it is given by [Onorato et al., 2000]:

$$\text{AAF}(\tilde{\nu}) = 1 + \sqrt{4 - 2\tilde{\nu}^2}, \qquad 0 < \tilde{\nu} < \sqrt{2}. \tag{3.55}$$

This result is easily obtained from substituting the point where the SFB amplitude reaches its maximum $(x,t) = (0,0)$ and taking the ratio of the background. In [Onorato et al., 2000], the AAF for the SFB is given as a function of the wave steepness and the number of waves under the modulation.

For a very long modulated wave signal, i.e. when the modulation frequency $\nu \to 0$, the AAF reaches a limiting value of 3. For $\tilde{\nu} \geq \sqrt{2}$, the SFB does not exist anymore and the AAF $= 1$ since the wave signal is just the stable plane-wave signal. The AAF decreases monotonically for increasing modulation frequency. Figure 3.6 shows the AAF plot of the SFB.

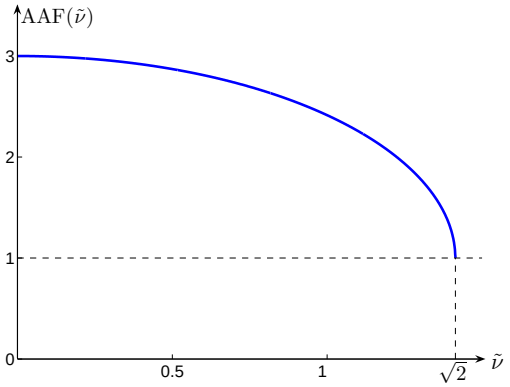

Figure 3.6: The plot of the amplitude amplification factor of the SFB as function of the modulation frequency $\tilde{\nu}$.

3.3.4 Maximum temporal amplitude

In this subsection, we introduce the concept of maximum temporal amplitude (MTA) which turns out to be a useful tool in the process to generate extreme wave events at a specific position in a wave basin. We begin with a formal definition of the maximum temporal amplitude.

Definition 3.3.2 (Maximum temporal amplitude, MTA) The MTA is defined as the maximum over time of a physical wave field $\eta(x,t)$:

$$\mathrm{MTA}(x) = \max_t \ \eta(x,t). \tag{3.56}$$

This concept of MTA is introduced in [Andonowati and Van Groesen, 2003] when discussing optical pulse deformation in nonlinear media. However, this quantity has also applications in water wave theory, in particular it is useful in the process of wave generation. From the definition above, the MTA describes the largest wave amplitude that

can appear at a certain position. It can also be interpreted as a stationary envelope of the wave groups envelope. Since we have an explicit expression for the SFB, we can find an explicit formulation for the MTA, given as follows [Andonowati et al., 2006]:

$$\mathrm{MTA}(x) = 2r_0\sqrt{1+\frac{\tilde{\nu}^2\sqrt{4-2\tilde{\nu}^2}}{\cosh(\sigma x)-\sqrt{1-\frac{1}{2}\tilde{\nu}^2}}}. \tag{3.57}$$

This explicit expression is found from the real amplitude of the SFB physical wave field, given by:

$$a^2(x,t) = 4r_0^2\frac{\left((\tilde{\nu}^2-1)\cosh(\sigma x)-\sqrt{1-\frac{1}{2}\tilde{\nu}^2}\cos\left[\nu\left(t-x/V_0\right)\right]\right)^2+\tilde{\sigma}^2\sinh^2(\sigma x)}{\left(\cosh(\sigma x)-\sqrt{1-\frac{1}{2}\tilde{\nu}^2}\cos\left[\nu\left(t-x/V_0\right)\right]\right)^2}. \tag{3.58}$$

We observe that $\cos\left[\nu\left(t-x/V_0\right)\right]=1$ for maximum over time. The rest is a simple algebraic calculation to arrive at the MTA expression for the SFB (3.57). In general, however, an explicit expression for the MTA is not easy to find.

In our application, the MTA is a very useful tool for designing a strategy of extreme wave generation. Using the MTA, we are able to determine the signal input to give to the wavemaker in order to produce an extreme wave signal at a specific desired position. We assume that the wave will not break during its downstream evolution. An MTA plot gives information about the extreme position, namely the position where the envelope of a wave signal is at its largest value. If we desire to produce this extreme wave signal at a particular position, to be denoted as $x=0$, taking the signal at $x=-x_0<0$ as initial signal will then produce this maximal wave at $x=0$. Hence, the signal at $x=-x_{wm}$, where x_{wm} is the distance to the wavemaker from the extreme position, will be the signal to be fed to the wavemaker. This given signal as input to the wavemaker will lead to become the extreme wave signal at the desired location, assuming that the NLS equation is an accurate description of the reality, there is no reflection and the domain is infinite. A plot of the MTA together with the spatial evolution and its envelope of the SFB is given in Figure 3.7.

3.4 Spatial evolution of the SFB wave signal

In the preceding section, we have seen in Figure 3.7 a snapshot of the SFB wave profile and see the downstream evolution of a small amplitude modulated wave into a large one during propagation over a sufficiently large distance. In this section, we will illustrate in more detail the spatial evolution of the signal. Additionally, a dynamic evolution of the envelope signal in the Argand diagram gives an illustration of the properties of the SFB. Particularly interesting is the wave signal at the extreme position $\xi=x=0$. Only at this position, the SFB is a real-valued function, while at $x\neq 0$, the SFB is a

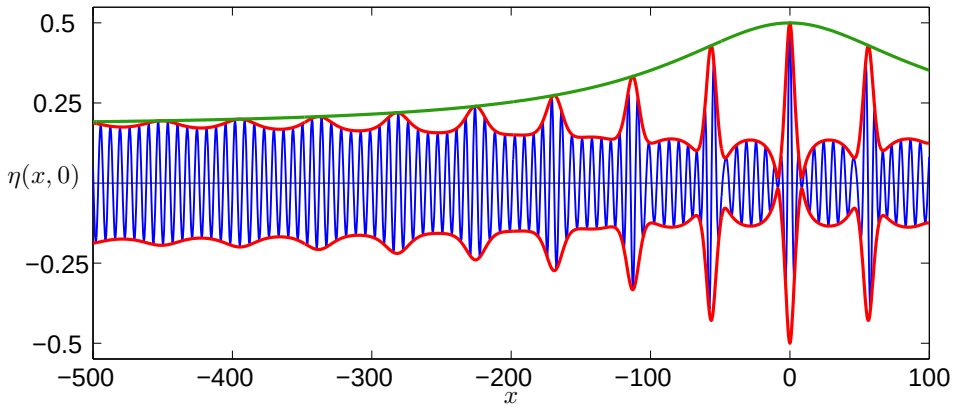

Figure 3.7: A plot of individual waves, the corresponding wave envelope and the time-independent MTA of the SFB. The horizontal axis is the distance from the extreme position and the vertical axis is the surface elevation. Units along the axes are in meters and the water depth of layer is 5 m. See also Figure 1.2 in Chapter 1.

complex-valued function. Furthermore, only at this position the amplitude will vanish, namely for the interval $0 < \tilde{\nu} < \sqrt{3/2}$ and leads to phase singularity. More properties of the signal at this position will be described in this section, where we will discuss the SFB wave signal evolution, the evolution in the Argand diagram and the phase plane representation of the SFB envelope signal at the extreme position.

3.4.1 Wave signal evolution

We have seen that the SFB solution behaves asymptotically as a plane-wave solution. The corresponding wave signal is a monochromatic wave with constant envelope $2r_0$, frequency ω_0 and travels with the phase velocity $\omega_0/(k_0-\gamma r_0^2)$. However, the modulated wave signal will grow in space during its evolution according the linear modulational (Benjamin-Feir) instability. The SFB describes the complete nonlinear evolution of the modulated wave signal for all x. The SFB wave signal reaches an extreme amplitude at the extreme position, after which it returns to its initial state. The modulation period T is maintained during its evolution and depends on the modulation frequency ν, $T = 2\pi/\nu$.

Figure 3.8 shows the spatial evolution of the SFB wave signal from a modulated wave signal into the extreme signal at the extreme position. In this figure, we see that parts of a wave group signal grow but other parts decrease in amplitude as the signal propagates toward the extreme position. At this extreme position, a pair of 'phase singularities' may occur in one modulation period. More explanation about 'phase singularity' will be given in Chapter 4.

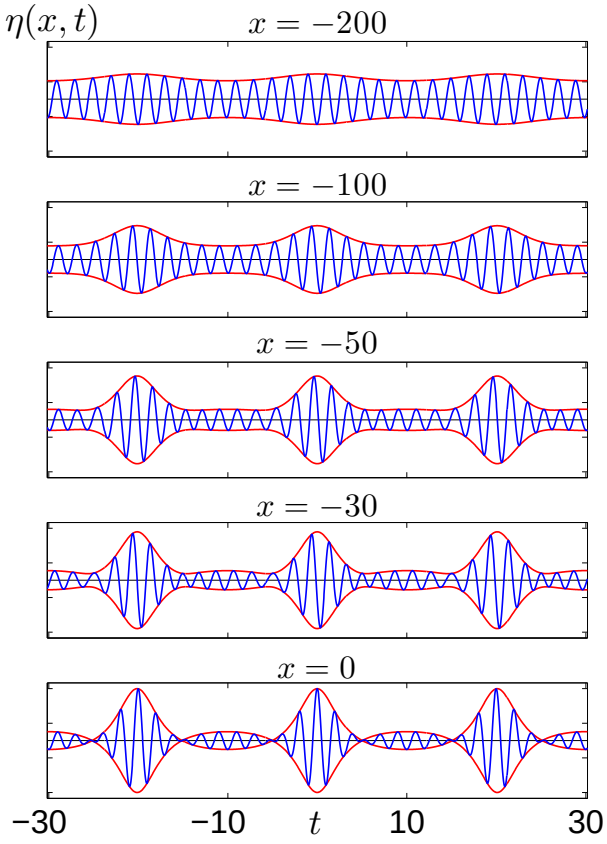

Figure 3.8: The downstream evolution of the SFB for $\tilde{\nu} = 1$ from a modulated wave signal into the extreme wave signal. The signals are taken at different positions: $x = -200$, $x = -100$, $x = -50$, $x = -30$ and $x = 0$, respectively. The time axis is in second and the position is in meter.

3.4.2 Evolution in the Argand diagram

In Subsection 3.2, we have introduced waves on finite background using the displaced phase-amplitude representation. Particularly, in Subsection 3.2.2, we restricted the displaced phase to be time independent and remarkably the SFB can be written in this representation. In this subsection, we will see that all evolution curves of the SFB in the Argand diagram are centered in $(-1, 0)$ and the angle with the real axis depends on the value of the displaced phase, i.e. on the position ξ.

Since the SFB is a complex-valued function, we can depict its evolution in the complex plane, the Argand diagram, with axes the real and the imaginary parts of the complex-amplitude A. This complex-amplitude A itself depends on the two variables

space ξ and time τ. Hence, the representation of the SFB will be a four-dimensional manifold. Here, we will fix one variable and use the other one to plot the evolution for different values in the Argand diagram. The dynamic evolution of the SFB for different τ parameterized in ξ is given in [Akhmediev and Ankiewicz, 1997], and for different ξ parameterized in τ in [Van Groesen et al., 2006]. We are more interested in the latter case since it is a significant help to understand the experimental results to be presented in Chapter 6.

In the Argand diagram, the time trajectories lie on straight lines. These lines have an angle that depends on the 'background' and the angle decreases as the position increases. At a fixed position, for one modulation period, a specific part of the lines is passed twice. All lines are centered in $(-1, 0)$ due to the displaced phase-amplitude representation. The angle that each line makes with the real axis is determined by the time-independent displaced phase $\phi(\xi)$. For $\xi < 0$, the evolution curves are above the real axis and below it for $\xi > 0$. For $\xi \to \pm\infty$, the trajectory reduces to a point. For $\xi = 0$, the curve is the longest and lies on the real axis. For the interval $0 < \tilde{\nu} < \sqrt{3/2}$, it also passes the origin twice for one modulation period. Therefore, this is the only position where we have (one pair of) phase singularities in each modulation period. Figure 3.9 shows the dynamic evolution of the SFB for different positions ξ and parameterized in time τ.

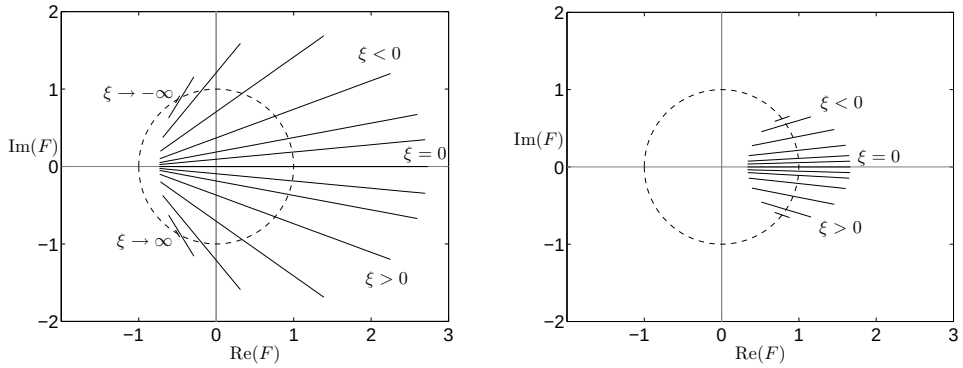

Figure 3.9: The dynamic evolution of the SFB parameterized in τ at different ξ for $\tilde{\nu} = \sqrt{1/2}$ (left) and $\tilde{\nu} = 4/3$ (right).

3.4.3 Phase plane representation of envelope signal

We want to investigate a dynamic property of the SFB envelope signal in the phase plane. Since the dynamic evolution of the displaced amplitude G is described by a second order differential equation (3.29), we can study its dynamics by investigating 'phase curves' in the phase plane. The SFB envelope signal is given by twice the magnitude

of its complex-valued amplitude $2|A|$. Phase curves for this quantity remain positive due to the absolute value. A better representation would be a four-dimensional manifold, presenting the real and the imaginary parts of the complex amplitude separately. However, such a representation is rather difficult to interpret the dynamics.

Nevertheless, the SFB envelope signal is particulary interesting at the extreme position $x = 0$ since there A is a real-valued function. At this position, the physical time coincides with the time in the moving frame of reference, $\tau = t$, so there is no effect of spatial displacement. The 'extreme signal' mentioned here refers to the SFB wave signal at the extreme position. We write the extreme signal as a function that depends on the parameter $\tilde{\nu}$. The parameter r_0 is less interesting and therefore we take the normalized value $r_0 = 1$. The SFB extreme signal is given as follows:

$$\eta(0, t; \tilde{\nu}) = 2|F(t; \tilde{\nu})| \cos\left[\omega_0 t + \frac{1}{2}\pi(1 - \text{sign}[F(t; \tilde{\nu})])\right], \tag{3.59}$$

where $\text{sign}[F(t; \tilde{\nu})]$ is given by 1 when $F(t; \tilde{\nu}) > 0$ and -1 when $F(t; \tilde{\nu}) < 0$; and $F(t; \tilde{\nu})$ is the envelope of the extreme signal, the 'extreme signal envelope'. Note that generally, the term 'envelope' always refer to a nonnegative quantity. In our context, however, we allow the envelope to be negative too. We know that since the wave signal itself depends on the modulation frequency ν, then certainly the extreme envelope does too. The smaller the modulation frequency, the larger the period will be, and the longer the time needed to repeat that periodic pattern.

We examine this extreme signal envelope by studying the phase curves of the envelope signal in a phase plane. The horizontal axis of the phase plane denotes twice extreme envelope $2F(t; \tilde{\nu})$ and the vertical axis denotes twice the derivative of the extreme envelope $2F'(t; \tilde{\nu})$. The motion along the phase curve as a function of time is clockwise as time increases. The closed curve is transferred precisely once in one modulation period. Pairs of phase singularities are visible if the phase curve crosses the vertical axis, which is the case for $0 < \tilde{\nu} < \sqrt{3/2}$. Figure 3.10 shows phase plots for different values of the modulation frequency $\tilde{\nu}$.

In Section 3.2, the displaced amplitude G was represented by the second order differential equation for all x (3.29). Yet, it is difficult to write such representation for the complex amplitude without the plane wave contribution F for $x \neq 0$. However, thanks to the fact that F is a real function at $x = 0$, we can write a second order differential equation for F as follows:

$$\frac{d^2F}{dt^2} + \frac{dV}{dF} = 0. \tag{3.60}$$

This equation describes a particle moving in a nonlinear oscillator with potential function $V(F)$. It has a mechanical analogy with Newton's second law of motion in classical mechanics. The potential function is given explicitly by:

$$V(F) = \alpha_1 F + \frac{1}{2}\alpha_2 F^2 + \frac{1}{3}\alpha_3 F^3 + \frac{1}{4}\alpha_4 F^4, \tag{3.61}$$

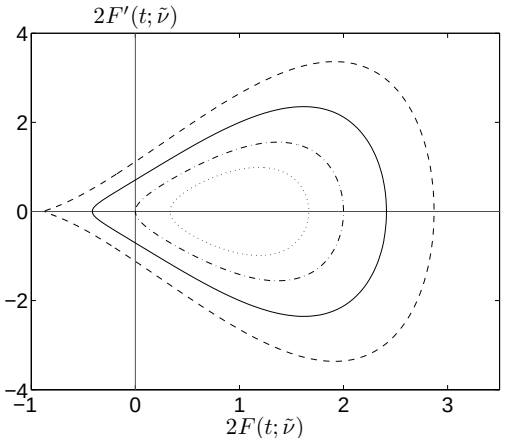

Figure 3.10: Phase curves in the phase plane of the corresponding SFB wave envelope at the extreme position. The curves are taken for different values of $\tilde{\nu}$: $\tilde{\nu} = 1/2$ (dash-dot curve), $\tilde{\nu} = 1$ (solid curve), $\tilde{\nu} = \sqrt{3/2}$ (dash curve) and $\tilde{\nu} = 4/3$ (dotted curve).

where $\alpha_1 = \frac{\gamma}{\beta} r_0^2(\tilde{\nu}^2 - 2)$, $\alpha_2 = \frac{\gamma}{\beta} r_0^2(\tilde{\nu}^2 - 3)$, $\alpha_3 = 0$ and $\alpha_4 = \frac{\gamma}{\beta} r_0^2$. Furthermore, the energy conservation equation for F is given by:

$$E(F) = \frac{1}{2}\left(\frac{dF}{dt}\right)^2 + V(F) = \frac{1}{4}\frac{\gamma}{\beta} r_0^2(3 - 2\tilde{\nu}^2). \tag{3.62}$$

The dynamic evolution for the displaced amplitude G at each position is governed by (3.35). At $x = 0$, we can also write a nonlinear oscillator equation for G similar to (3.60):

$$\frac{d^2G}{dt^2} + \frac{dV}{dG} = 0, \tag{3.63}$$

with the potential function $V(G)$ is given explicitly by:

$$V(G) = \frac{1}{2}\tilde{\alpha}_2 G^2 + \frac{1}{3}\tilde{\alpha}_3 G^3 + \frac{1}{4}\tilde{\alpha}_4 G^4, \tag{3.64}$$

where $\tilde{\alpha}_2 = \frac{\gamma}{\beta} r_0^2 \tilde{\nu}^2$, $\tilde{\alpha}_3 = -3\frac{\gamma}{\beta} r_0^2$ and $\tilde{\alpha}_4 = \frac{\gamma}{\beta} r_0^2$. At $x = 0$, the relation between F and G becomes $G = F + 1$. Substituting this into the potential function of G (3.64), we obtain the relation of the potential functions $V(G) = V(F) + E(F)$. Using these both relations, we confirm the fact that if G satisfies the oscillator equation (3.63), then F satisfies the oscillator equation (3.60). Moreover, the energy conservation equation for the displaced amplitude G at all position vanishes:

$$E(G) = \frac{1}{2}\left(\frac{dG}{d\tau}\right)^2 + V(G) = 0. \tag{3.65}$$

3.5 Amplitude spectrum evolution

So far we have considered the properties of the SFB in the time domain by studying the signal and its propagation. There are interesting properties that we can explore if we study this solution in the frequency domain. To accomplish this, we need the Fourier transform that maps the time domain into the frequency domain. Using this transformation, we obtain the corresponding 'spectrum evolution' of a wave signal. Furthermore, we can extract from this spectrum the 'absolute amplitude spectrum evolution' and a 'phase spectrum evolution'.

Since the complex-valued amplitude $A(\xi,\tau)$ is a periodic function in τ with period of $T = 2\pi/\nu$, we write it in the Fourier series representation:

$$A(\xi,\tau) = \sum_{n=-\infty}^{\infty} a_n(\xi) e^{in\nu\tau}. \tag{3.66}$$

Now, the spatial-dependent complex-valued Fourier coefficient is given by

$$a_n(\xi) = \frac{1}{T}\int_{-\frac{T}{2}}^{\frac{T}{2}} A(\xi,\tau) e^{-in\nu\tau} d\tau, \quad n \in \mathbb{Z}. \tag{3.67}$$

We introduce a dummy variable $\tilde{\tau} = \nu\tau$ and we apply the fact that $A(\xi,\tau)$ is an even function with respect to variable τ, and therefore $\int_{-T/2}^{T/2} A(\xi,\tau)\sin(n\nu\tau)\, d\tau = 0$. After dropping the tilde, the expression (3.67) becomes

$$a_n(\xi) = \frac{1}{2\pi}\int_{-\pi}^{\pi} A\left(\xi, \frac{\tau}{\nu}\right)\cos(n\tau)\, d\tau, \qquad n \in \mathbb{Z}. \tag{3.68}$$

From this it follows that $a_n = a_{-n}$ and that $|a_n| = |a_{-n}|$.

The complex Fourier coefficients $a_n(\xi)$ form an infinite sequence $\{a_n(\xi)\}_{n=-\infty}^{\infty}$, which is called the 'spectrum' of the complex function $A(\xi,\tau)$. By expressing a_n in polar form with its magnitude and argument, namely, $a_n(\xi) = |a_n(\xi)|e^{i\varphi_n(\xi)}$, the sequence of the real-valued absolute amplitude $\{|a_n(\xi)|\}_{n=-\infty}^{\infty}$ is called the 'absolute amplitude spectrum' and the sequence of real-valued phases $\{\varphi_n(\xi)\}_{n=-\infty}^{\infty}$ is called the 'phase spectrum' of the function $A(\xi,\tau)$. The coefficient a_n, $n \in \mathbb{Z}$ corresponds to the frequency $\omega_0 + n\nu$, $n \in \mathbb{Z}$ of the n^{th} complex Fourier mode of the physical wave field $\eta = Ae^{i(k_0 x - \omega_0 t)} + \text{c c}$. The carrier wave frequency ω_0 is called the central frequency and $\omega_0 \pm n\nu$ is called the n^{th} 'sideband'.

The explicit expression for a_n, $n \in \mathbb{Z}$ is given without derivation in the book of [Akhmediev and Ankiewicz, 1997]; we write their result again here according to our notation. For $n = 0$:

$$a_0(\xi) = A_0(\xi)\left(\frac{\tilde{\nu}^2\cosh(\sigma\xi) - i\tilde{\sigma}\sinh(\sigma\xi)}{\sqrt{\cosh^2(\sigma\xi) - \left(1 - \frac{1}{2}\tilde{\nu}^2\right)}} - 1\right), \tag{3.69}$$

and for $n \in \mathbb{Z}$, $n \neq 0$:

$$a_n(\xi) = A_0(\xi)\frac{\tilde{\nu}^2\cosh(\sigma\xi) - i\tilde{\sigma}\sinh(\sigma\xi)}{\sqrt{\cosh^2(\sigma\xi) - \left(1-\frac{1}{2}\tilde{\nu}^2\right)}}\left(\frac{\cosh(\sigma\xi) - \sqrt{\cosh^2(\sigma\xi) - \left(1-\frac{1}{2}\tilde{\nu}^2\right)}}{\sqrt{1-\frac{1}{2}\tilde{\nu}^2}}\right)^n. \tag{3.70}$$

The proof of this result is given in Appendix B on page 127.

For $\xi = \mp\infty$, the absolute of all amplitudes $|a_n(\xi)|$ vanish, except for $|a_0(\xi)|$ which approaches r_0. The asymptotic behaviour of the amplitude spectrum for $\xi \to \mp\infty$ is given in more detail by:

$$|a_0(\xi)| = r_0\left[1 - \tilde{\nu}^2(2-\tilde{\nu}^2)e^{\pm 2\sigma\xi}\right], \tag{3.71}$$

$$|a_n(\xi)| = r_0\tilde{\nu}\sqrt{2}\left(\sqrt{1-\frac{1}{2}\tilde{\nu}^2}e^{\pm\sigma\xi}\right)^{|n|},\ n \in \mathbb{Z},\ n \neq 0. \tag{3.72}$$

Conservation of energy, i.e., $1/T\int_{-T/2}^{T/2}|A|^2\,d\tau = \text{constant} = r_0^2$, using the property that $|a_n| = |a_{-n}|$, results into the fact that for the spectrum we have:

$$E = |a_0(\xi)|^2 + 2\sum_{n=1}^{\infty}|a_n(\xi)|^2 = r_0^2. \tag{3.73}$$

Figure 3.11 shows plots of the amplitude spectrum corresponding to the central frequency, the first sideband, the second sideband, and the remaining energy in the higher order sidebands. For all $\tilde{\nu}$ in the instability interval, we observe that the first sideband dominates the second sideband during the whole evolution. That is due to the fact that the term $|a_n|$ in (3.70) decreases in amplitude as n increases. There is a special case when the central frequency vanishes at the extreme position, namely for $\tilde{\nu} = \sqrt{1/2}$. This means that at the extreme position, the energy from the central frequency has been transferred during the spatial evolution completely to its sidebands. In other cases, the energy from the central frequency is only partly distributed to its sidebands.

By writing the spectrum in the polar from, we can obtain information about the phase spectrum evolution $\phi_n(\xi)$, $n \in \mathbb{Z}$:

$$\tan\phi_n(\xi) = \begin{cases} \dfrac{-\tilde{\sigma}\sinh(\sigma\xi)}{\tilde{\nu}^2\cosh(\sigma\xi) - \sqrt{\cosh^2(\sigma\xi) - \left(1-\frac{1}{2}\tilde{\nu}^2\right)}}, & \text{for } n = 0; \\ -\dfrac{\tilde{\sigma}}{\tilde{\nu}^2}\tanh(\sigma\xi), & \text{for } n \in \mathbb{Z},\ n \neq 0. \end{cases} \tag{3.74}$$

The asymptotic behavior of the phase for $\xi \to \mp\infty$ is given by:

$$\tan\phi_n^{\mp} = \begin{cases} \pm\dfrac{\tilde{\sigma}}{\tilde{\nu}^2 - 1}, & \text{for } n = 0; \\ \pm\dfrac{\tilde{\sigma}}{\tilde{\nu}^2}, & \text{for } n \in \mathbb{Z},\ n \neq 0. \end{cases} \tag{3.75}$$

Since not all Fourier components have the same phase, the SFB is not coherent, which is different from the plane wave solution (2.45) and the single soliton solution (2.51), as has been discussed in Subsection 2.4.3 on page 25. The result above agrees with the phase information when we look at the asymptotic behavior of the SFB (3.51). It is remarkable that the phases for all sidebands are equal since they do not depend on n.

The phase shift experienced by the central frequency is equal to the phase shift of the physical wave packet profile.

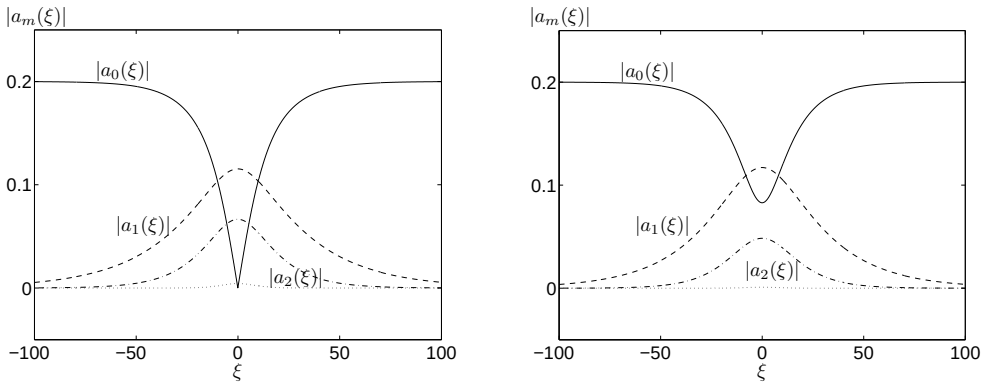

Figure 3.11: Plots of the absolute amplitude spectrum of the SFB corresponding to the central frequency (solid curve), the first sideband (dashed curve), the second sideband (dash-dotted curve) and the remaining energy in the higher order sidebands, defined as $2\sum_{n=3}^{\infty}|a_n(\xi)|^2$, (dotted curve) for two values of the modulation frequency $\tilde{\nu}$: $\tilde{\nu} = \sqrt{1/2}$ (left), and $\tilde{\nu} = 1$ (right). For $\tilde{\nu} = \sqrt{1/2}$ the central amplitude vanishes at the extreme position, which means that all energy is transferred to the sidebands.

3.6 Other soliton waves on finite background

In this section we derive two other exact solutions of the NLS equation. These exact solutions are known in the literature, together with the SFB treated above, as 'breather' solutions of the NLS equation [Dysthe and Trulsen, 1999; Dysthe, 2000; Grimshaw et al., 2001]. The name 'breather' reflects the behavior of the profile which is periodic in time or space and localized in space or time. The breather concept was introduced by [Ablowitz et al., 1974] in the context of the sine-Gordon partial differential equation. Breather solutions are also found in other equations, for instance in the Davey-Stewartson (DS) equation [Tajiri and Arai, 2000] and modified Korteweg-de Vries (mKdV) equation [Drazin and Johnson, 1989].

The breather solutions are found from our analysis in Subsection 3.2.2 in the form (3.30):

$$G(\phi,\tau) = \frac{P(\phi)}{Q(\phi) - \zeta(\tau)} \tag{3.76}$$

where P and Q depend on phase. We will see that different functions $\zeta(\tau)$ will lead to different breather solutions of the NLS equation.

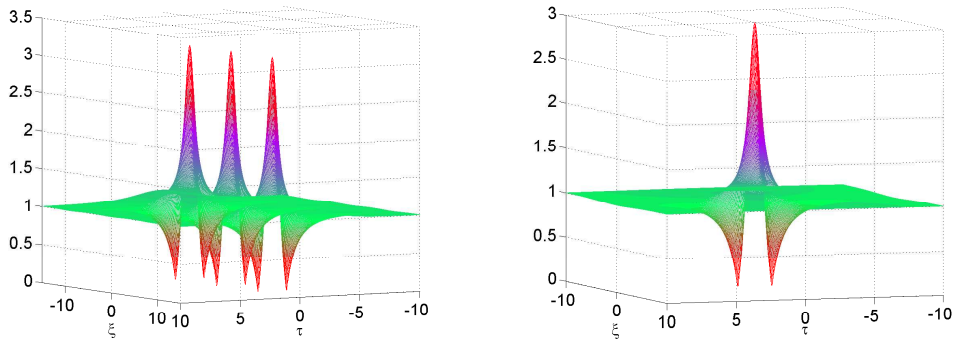

Figure 3.12: Plots of the absolute value of the Ma breather for $\tilde{\mu} = 0.4713$ (left) and the rational breather (right), for $r_0 = 1$ in all cases. For illustration purposes, the axis are scaled corresponding to $\beta = 1 = \gamma$.

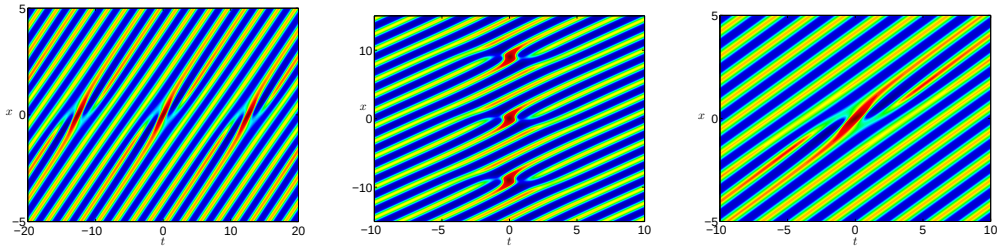

(a) (b) (c)

Figure 3.13: Density plot of the SFB for $\tilde{\nu} = 1/2$ (a), the Ma breather for $\tilde{\mu} = 0.4713$ (b) and the rational breather (c). For all cases $r_0 = 1$ and $k_0 = 2\pi$. The plots are shown in a moving frame of reference with suitable chosen velocity.

3.6.1 Breather solutions of the NLS equation

Firstly, for $\zeta(\tau) = \cos(\nu\tau)$, we obtain the SFB which we have discussed in the preceding sections. Secondly, we take $\zeta(\tau) = \cosh(\mu\tau)$, where $\mu = r_0\sqrt{\gamma/\beta}\tilde{\mu}$. The function G satisfies the following differential equation:

$$\partial_\tau^2 G = \mu^2 G - 3\mu^2 \frac{Q}{P} G^2 - 2\mu^2 \frac{1-Q^2}{P^2} G^3. \tag{3.77}$$

Comparing with (3.29), the solution (3.30) is obtained with $P(\phi) = -\tilde{\mu}^2 Q(\phi)/\cos\phi$, $Q^2(\phi) = 2\cos^2\phi/(2\cos^2\phi + \tilde{\mu}^2)$ and the displaced phase satisfies $\tan\phi(\xi) = -\frac{\tilde{\rho}}{\tilde{\mu}^2}\tan(\rho\xi)$, where $\tilde{\rho} = \tilde{\mu}\sqrt{2+\tilde{\mu}^2}$ and $\rho = \gamma r_0^2\tilde{\rho}$. The corresponding solution of the NLS equation (3.28) can then be written after some manipulations as

$$A(\xi,\tau) \quad = \quad A_0(\xi)\left(\frac{-\tilde{\mu}^2\cos(\rho\xi) + i\tilde{\rho}\sin(\rho\xi)}{\cos(\rho\xi) \pm \sqrt{1+\frac{1}{2}\tilde{\mu}^2}\cosh(\mu\tau)} - 1\right). \tag{3.78}$$

This is the Ma solution or the Ma breather [Ma, 1979].

Thirdly, we take $\zeta(\tau) = 1 - \frac{1}{2}\nu^2\tau^2$. (The same solution can also be obtained by substituting $\zeta(\tau) = 1 + \frac{1}{2}\mu^2\tau^2$.) Then, the function G satisfies the differential equation:

$$\partial_\tau^2 G = \frac{3\nu^2}{P} G^2 - 4\nu^2 \frac{Q-1}{P^2} G^3. \tag{3.79}$$

Comparing with (3.29), we have $P(\phi) = \tilde{\nu}^2/\cos\phi$, $Q(\phi) = 1 + P^2/(4\tilde{\nu}^2)$ and the displaced phase satisfies $\tan\phi(\xi) = -2\gamma r_0^2\xi$. Substituting into the Ansatz (3.30), we obtain

$$A(\xi,\tau) \quad = \quad A_0(\xi)\left(\frac{4(1-2i\gamma r_0^2)\xi}{1+4(\gamma r_0^2\xi)^2 - 2\frac{\gamma}{\beta}r_0^2\tau^2} - 1\right). \tag{3.80}$$

This is the rational solution or the rational breather, also called the algebraic solution [Peregrine, 1983]. Plots of the absolute value of the Ma soliton and the rational soliton for $r_0 = 1$ are given in Figure 3.12.

3.6.2 Relation between the breather solutions

As shown in [Dysthe and Trulsen, 1999], there is a relationship among the breather solutions of the NLS equation. Different parameters are used for explicit expressions of the SFB and the Ma breather in [Dysthe and Trulsen, 1999] as well as in [Grimshaw et al., 2001]. Introducing new parameters φ and $\vartheta \in \mathbb{R}$ by the following relations: $\tilde{\nu} = \sqrt{2}\sin\varphi$, $\tilde{\sigma} = \sin 2\varphi$, $\tilde{\mu} = \sqrt{2}\sinh\vartheta$ and $\tilde{\rho} = \sinh 2\vartheta$, we can write our expressions similar to the ones in these papers.

For the expressions given above for these solutions, we observe that the SFB becomes the Ma breather if we substitute $\nu = i\mu$ and it becomes the rational breather if $\nu \to 0$. Similarly, the Ma breather becomes the rational breather for $\mu \to 0$. The Ma breather becomes the single soliton solution for $\mu \to \infty$ [Akhmediev and Ankiewicz, 1997]. Figure 3.14 explains the schematic diagram of these relations. These relations can also be seen from the expression in the previous section. For the SFB, we take $\zeta(\tau) = \cos(\nu\tau)$, which leads to the Ma breather if we substitute $\nu = i\mu$, so that $\zeta(\tau) = \cos(i\mu\tau) = \cosh(\mu\tau)$. Taking the Taylor expansion either around $\nu = 0$ or $\mu = 0$, we get $\zeta(\tau) = 1 - \frac{1}{2}\nu^2\tau^2$ or $\zeta(\tau) = 1 + \frac{1}{2}\mu^2\tau^2$, and both cases will lead to the rational breather.

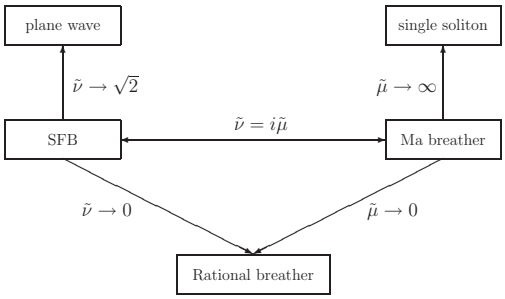

Figure 3.14: The schematic diagram for the derivation of the Ma breather and the rational breather from the SFB.

The relations have also consequences for the amplitude amplification factor (AAF), defined as the ratio between the maximum amplitude and the value of its background. The expressions for the breather solutions as given above were shifted such that the maximum amplitude is at $(\xi, \tau) = (0, 0)$ and the value of the background is r_0.

For the SFB, the amplification is given by $\mathrm{AAF}_{\mathrm{S}}(\tilde{\nu}) = 1 + \sqrt{4 - 2\tilde{\nu}^2}$. For $0 < \tilde{\nu} < \sqrt{2}$, the amplification is bounded and $1 < \mathrm{AAF}_{\mathrm{S}}(\tilde{\nu}) < 3$. The AAF for the Ma breather is given by $\mathrm{AAF}_{\mathrm{Ma}}(\tilde{\mu}) = 1 + \sqrt{4 + 2\tilde{\mu}^2}$. Hence, for $\tilde{\mu} > 0$, we have $\mathrm{AAF}_{\mathrm{Ma}} > 3$. The AAF for the rational breather is exactly 3, which follows by letting either $\tilde{\nu}$ or $\tilde{\mu}$ go to zero

$$\mathrm{AAF}_{\mathrm{Ra}} = \lim_{\tilde{\nu}\to 0} \mathrm{AAF}_{\mathrm{S}} = 3 = \lim_{\tilde{\mu}\to 0} \mathrm{AAF}_{\mathrm{Ma}}. \tag{3.81}$$

The plot of the AAF for all the three breather solutions is given in Figure 3.15. For $\tilde{\mu} \to \infty$ in the Ma breather, the single-soliton solution (2.51) is obtained, see page 61–64 of [Akhmediev and Ankiewicz, 1997].

3.6.3 Physical wave fields

The corresponding physical wave fields of the waves on finite background are particularly interesting to investigate. Considering only the first order contribution, the

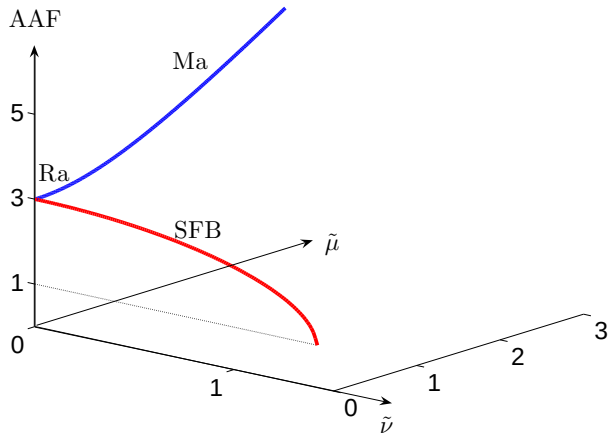

Figure 3.15: Plot of the amplitude amplification factor for the SFB and the Ma breather. The meeting point of the two curves is the AAF of the rational breather.

physical wave field η is given by (3.53). We apply the same moving frame of reference as in the case of SFB. Density plots for three breather solutions are given in Figure 3.13. For illustration, we choose $r_0 = 1$, $k_0 = 2\pi$ in all cases, modulation frequency $\tilde{\nu} = 1/2$ for the SFB and $\tilde{\mu} = 0.4713$ for the Ma breather. For better representation, the physical wave fields are shown in a moving frame of reference with suitable chosen velocity.

The SFB has extreme values at $x = \xi = 0$ and is periodic in time. The Ma breather has extreme values at $\tau = 0$ and is periodic in space. The rational breather is neither periodic in time nor in space, but decaying asymptotically in space and time to the plane wave solution (2.45) with its maximum at $(x, t) = (0, 0)$. Despite some differences, the breather solutions show 'wavefront dislocation', when splitting or merging of waves occurs [Nye and Berry, 1974]. For the SFB, it occurs at the interval $0 < \tilde{\nu} < \sqrt{3/2}$, for the Ma soliton for all $\mu > 0$ and also for the rational soliton.

3.7 Conclusions

In this chapter we have discussed the description of waves on finite background and its application to extreme water wave generation in the hydrodynamic laboratory. We introduced a transformation to displaced phase-amplitude variables with respect to a background of monochromatic waves and viewed it from the variational formulation perspective. The dynamical evolution of these waves is governed by a nonlinear oscillator equation for the displaced amplitude with a potential energy that depends on the displaced phase. The displaced phase-amplitude transformation and its physical interpretation are new contributions of this thesis.

Furthermore, by restricting to a special case that the displaced phase is time independent, the nonlinear oscillator equation for the wave signal at each position becomes autonomous. We observe that the change of the displaced phase with respect to the position is the only driving force for a spatial evolution toward extreme wave events. The restriction led to three exact solutions of the NLS equation for waves on finite background, also known as the breather solutions: the SFB solution, the Ma solution and the rational solution.

We studied extensively many properties of the SFB since this solution describes the spatial evolution of the envelope wave signal from a slightly modulated wave into a large extreme wave and returns again into the initial signal with a different phase. The asymptotic behaviour of the SFB in the far distances is described by the linear modulational (Benjamin-Feir) instability. The SFB bounds the exponential growth of this instability, is the extension in the nonlinear regime and therefore describes a complete evolution of the modulational instability process.

Particularly interesting is that we use the SFB in a real-life application for a model of extreme wave generation in the wave basin of a hydrodynamic laboratory. We use the concept of MTA to quantify the spatial evolution from a moderate amplitude into a large wave. This knowledge of MTA is used for the design of the wave generation. Since the initial SFB wave signal has a moderate amplitude, it is possible to generate it by the wavemaker. This is not the case for the initial wave signal that corresponds to the Ma solution which requires the highest amplitude waves at the wavemaker. Theoretically, the limiting case of the SFB for infinitely long modulation can reach an amplitude amplification of factor three, provided that the wave basin has enough space. This limiting case is precisely the wave signal that corresponds to the rational solution in which the wave signal has infinite periodicity and an exponentially confined extreme wave.

We also observed that the corresponding physical wave field of the SFB solution (for $0 < \tilde{\nu} < \sqrt{3/2}$), the Ma solution (for $\mu > 0$) and the rational solution show splitting and merging waves. The following chapter will discuss these phenomena in more detail.

References

[Ablowitz et al., 1974] M. J. Ablowitz, D. J. Kaup, A. C. Newell, and H. Segur. The inverse scattering transform-Fourier analysis for nonlinear problems. *Stud. Appl. Math.* **53**(4): 249–315, 1974.

[Ablowitz and Herbst, 1990] M. J. Ablowitz and B. M. Herbst. On homoclinic structure and numerically induced chaos for the nonlinear Schrödinger equation. *SIAM J. Appl. Math.* **50**(2): 339–351, 1990.

[Akhmediev et al., 1985] N. N. Akhmediev, V. M. Eleonskiĭ, and N. E. Kulagin. Generation of periodic trains of picosecond pulses in an optical fiber: exact solutions. *Sov. Phys. JETP* **62**(5): 894–899, 1985.

[Akhmediev and Korneev, 1986] N. N. Akhmediev and V. I. Korneev. Modulation instability and periodic solutions of the nonlinear Schrödinger equation. *Teoret. Mat. Fiz.* **62**(2): 189–194, 1986. English translation: *Theoret. Math. Phys.* **69**: 1089–1092, 1986.

[Akhmediev et al., 1987] N. N. Akhmediev, V. M. Eleonskiĭ, and N. E. Kulagin. First-order exact solutions of the nonlinear Schrödinger equation. *Teoret. Mat. Fiz.* **72**(2): 183–196, 1987. English translation: *Theoret. Math. Phys.* **72**(2): 809–818, 1987.

[Akhmediev and Ankiewicz, 1997] N. N. Akhmediev and A. Ankiewicz. *Solitons—Nonlinear Pulses and Beams*, volume **5** of *Optical and Quantum Electronic Series*. Chapman & Hall, first edition, 1997.

[Andonowati and Van Groesen, 2003] Andonowati and E. van Groesen. Optical pulse deformation in second order nonlinear media. *J. Nonlinear Opt. Phys.* **12**(2): 221–234, 2003.

[Andonowati et al., 2006] Andonowati, N. Karjanto, and E. van Groesen. Extreme wave phenomena in down-stream running modulated waves. *Appl. Math. Modelling*, article in press, corrected proof, available online 27 June 2006.

[Drazin and Johnson, 1989] P. G. Drazin and R. S. Johnson. *Solitons: an Introduction*. Cambridge University Press, 1989.

[Dysthe and Trulsen, 1999] K. B. Dysthe and K. Trulsen. Note on breather type solutions of the NLS as models for freak-waves. *Phys. Scripta* **T82**: 48–52, 1999.

[Dysthe, 2000] K. B. Dysthe. Modelling a "rogue wave"–speculations or a realistic possibility? In M. Olagnon and G. A. Athanassoulis, editors, *Proceedings of the Rogue Waves 2000*, Ifremeer, Brest, France, November 2000.

[Grimshaw et al., 2001] R. Grimshaw, D. Pelinovsky, E. Pelinovsky, and T. Talipova. Wave group dynamics in weakly nonlinear long-wave models. *Physica D* **159**: 35–37, 2001.

[Ma, 1979] Y.-C. Ma. The perturbed plane-wave solutions of the cubic Schrödinger equation. *Stud. Appl. Math.* **60**(1): 43–58, 1979.

[Nye and Berry, 1974] J.F. Nye and M.V. Berry. Dislocation in wave trains. *Proc. R. Soc. Lond. A* **336**: 165–190, 1974.

[Onorato et al., 2000] M. Onorato, A. Osborne, M. Serio and T. Damiani. Occurrence of freak waves from envelope equations in random ocean wave simulations. In M. Olagnon, editor, *Proceedings Rogue Waves 2000*, Brest, France, 2000.

[Osborne et al., 2000] A. R. Osborne, M. Onorato, and M. Serio. The nonlinear dynamics of rogue waves and holes in deep-water gravity wave trains. *Phys. Lett. A* **275**: 386–393, 2000.

References

[Osborne, 2001] A. R. Osborne. The random and deterministic dynamics of 'rogue waves' in unidirectional, deep-water wave trains. *Mar. Struct.* **14**: 275–293, 2001.

[Peregrine, 1983] D. H. Peregrine. Water waves, nonlinear Schrödinger equations and their solutions. *J. Austral. Math. Soc. Ser. B* **25**(1): 16–43, 1983.

[Tajiri and Arai, 2000] M. Tajiri and T. Arai. Periodic soliton solutions to the Davey-Stewartson equation. *Proc. Inst. Math. Natl. Acad. Sci. Ukr.* **30**(1): 210–217, 2000.

[Van Groesen et al., 2005] E. van Groesen, Andonowati and N. Karjanto. Deterministic aspect of nonlinear modulation instability. In M. Olagnon and M. Prevosto, editors, *Rogue Waves 2004*. Proceedings of a workshop in Brest, France (October 20-22, 2004), 12 pp, 2005.

[Van Groesen et al., 2006] E. van Groesen, Andonowati and N. Karjanto. Displaced phase-amplitude variables for waves on finite background. *Phys. Lett. A* **354**: 312–319, 2006.

Chapter 4

Wavefront dislocation in surface water waves

4.1 Introduction

We have seen in the previous chapter that the physical wave field of the Soliton on Finite Background (SFB) shows wavefront dislocation which happens for modulation frequency $\tilde{\nu} < \sqrt{3/2}$. This phenomenon occurs when the real amplitude of the SFB vanishes and then the phase is undefined, which is often called a phase singularity. In this chapter we will investigate in more detail the phenomena of wavefront dislocation and phase singularity in the field of water waves. Many studies in the literature are dedicated to phenomena related to 'phase singularity' and 'wavefront dislocation'. Since generally both phenomena occur simultaneously, the term phase singularity is more often used in physical optics to describe what we will refer to as wavefront dislocation, for instance in [Balistreri et al., 2000]. Phase singularities are also called 'intensity zeros', 'topological charges', or 'optical vortices' [Coullet et al., 1989; Nye, 1999; Berry and Dennis, 2000, 2001; Soskin and Vasnetsov, 2001]. In water waves, the 'disappearance of waves' in a modulated train of surface gravity waves was described in [Tanaka, 1995].

'Dislocation' is known for a long time in the field of material science. There it is used to describe an irregularity within a crystal structure, often responsible for the plastic deformation of metals and other crystalline solids. The concept was introduced as early as 1934 and proposed independently by several authors [Orowan, 1934; Polanyi, 1934; Taylor, 1934]. Other references to dislocation in crystals are [Read, 1953; Honeycombe, 1984; Dieter, 1988; Hull and Bacon, 2001]. The above phenomena are also found in several other branches of physics. A simple example of phase singularity is the singular time zone at the north pole [Dennis, 2001]. See Figure 4.2(b) for a visualization. In [Soskin and Vasnetsov, 2001], 'singular optics' is discussed as a new branch of modern

physical optics that deals with a wide class of effects associated with phase singularities in wave fields and with the topology of wavefronts. An introduction and a summary of a workshop on singular optics about recent progress in the field is given in [Berry et al., 2004].

Extensive references to many topics related to dislocations from theoretical to experimental observations and applications can be found in [Nabarro, 1979-2004]. Experimental observations in a neon discharge in two-dimensional space-time are reported by Krása [Krása, 1981]. A study of it in the Aharonov-Bohm effect is done by Berry [Berry et al., 1980]. An analysis for constructing a theory of wavefront dislocation using catastrophe theory is developed by Wright [Wright, 1979]. A study of the phenomenon in optics, particularly in monochromatic light waves is reported in [Basistiy et al., 1995]. Line singularities in vector and electromagnetic waves, including the paraxial case, when waves propagate in a certain direction and the general case, when waves propagate in all directions, is discussed in [Nye, 1997]. A theoretical framework for understanding the local phase structure and the motion of the most general type of dislocation in a scalar wave, how this dislocation may be categorized and how its structure in space and time is related, has been studied by Nye [Nye, 1981]. Statistical calculations associated with dislocations for isotropically random Gaussian ensembles, that is, superpositions of plane waves equidistributed in direction but with random phases, are given in [Berry and Dennis, 2000]. Knotted and linked phase singularities in monochromatic waves by constructing exact solutions of the Helmholtz equation are given in [Berry and Dennis, 2001].

Apparently, the same phenomenon is also observed in 3D surfaces of constant phase (wavefronts) of a wave field. A new concept of 'wavefront dislocation' was introduced in 1974 by Nye and Berry [Nye and Berry, 1974] and is used to explain the experimentally observed appearance and disappearance of crest or trough pairs in a wave field. The authors show that wavefront dislocation appears as a result of partial spatial overlapping of two quasi-monochromatic pulses. In their paper, the examples are given in two and three space dimensions plus time. They also predict the gliding and climbing of wavefront dislocation on the pulse envelope. Other terminologies that are also often used to describe the phenomenon are death and birth of waves, and annihilation and creation of waves. When dealing with waves, Nye and Berry [Nye and Berry, 1974] showed that dispersion is not really involved when wavefront dislocation occurs, while, on the other hand, Trulsen [Trulsen, 1998] explained that wavefront dislocation is a consequence of linear dispersion alone and predicted by the linear Schrödinger equation, an example of paramount importance of a linear dispersive wave equation.

In $(1+1)$D, dislocation happens at a set of points in (x,t) space. In higher dimensions however, for example in $(2+1)$D or $(3+1)$D, dislocation is a set of lines in (x,y,t) space or a set of planes in (x,y,z,t) space. There are several types of dislocation lines in higher order dimensions. But before that, let us introduce the analogue of the 'Burgers vector' in the crystal according to [Read, 1953]. It is a vector perpendicular to the wavefronts of length equal to the wavelength. If the Burgers vector is perpendicular

to the dislocation line, it is called 'pure edge' type. If the Burgers vector is parallel or antiparallel to the dislocation line, it is called 'pure screw' type. If both types are observed, it is called 'mixed edge-screw' dislocation. In this thesis, since we consider $(1+1)$D case, we observe only the pure edge type of dislocation point. Dislocations in crystals are shown in Figure 4.1.

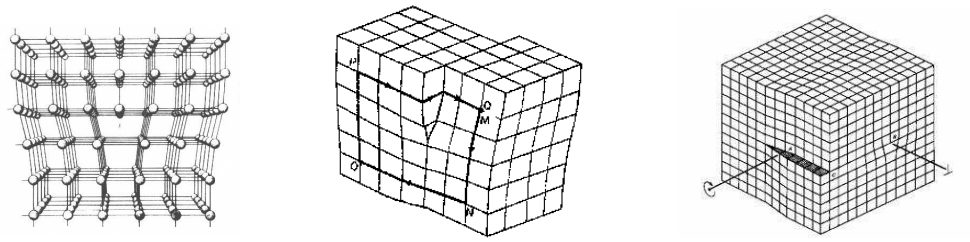

(a) (b) (c)

Figure 4.1: Schematic diagrams showing several type of dislocation lines: pure edge dislocation (a), pure screw dislocation (b) and mixed edge-screw dislocation (c).

In this chapter we restrict to wave fields with one spatial and one temporal variable. Even for this simplest case we sensed some confusion in the cited references above about the equivalence of the possibly different phenomena of phase singularity and wavefront dislocation. Moreover, it was not very clear if these phenomena are exceptional, rare events or should be expected at any point of vanishing amplitude. From a more practical point of view, we wanted to use the appearance of wavefront dislocations that we had found in the theoretical expression of the SFB as a check in measured signals of waves that were generated in a hydrodynamic laboratory. Robustness of such a phenomenon for perturbations of various kind is then required, a result that was not found in the cited references.

This chapter is organized as follows. In Section 4.2, we present the basic notions of phase singularity, wavefront dislocation and introduce the Chu-Mei quotient that will be used in this chapter. Further, we give the most trivial examples of surface wave fields, namely superpositions of two and three monochromatic waves. With these examples we will show that already for trichromatic waves phase singularity and wavefront dislocation will be generic properties, but also that phase singularity is not necessarily accompanied with wavefront dislocation. In Section 4.3 we study these aspects for wave groups. We will show that unboundedness of the Chu-Mei quotient is a necessary condition for the occurrence of wavefront dislocation. A perturbation analysis is done to show that boundedness of the Chu-Mei quotient is an exceptional case. Although all these phenomena are essentially linear, in Subsection 4.3.3 we investigate these phenomena for the special solution of the NLS equation, the SFB. We give a novel contribution to the theory of wave dislocation by introducing the Chu-Mei quotient and

relating it with wavefront dislocation. The final section concludes the chapter with some conclusions and remarks.

4.2 Preliminaries

This section is devoted to collect preliminary definitions that will be used in this chapter to study wavefront dislocation. We also illustrate degenerate and generic cases of the phenomena by using simple wave fields that consist of a superposition of a few harmonic modes.

4.2.1 Basic Notions

Let $\eta(x,t)$ be a real-valued function that describes a surface wave field in one space variable x and time t. The complexification of η is defined with the Hilbert transform $\mathcal{H}[\eta]$, given by $\eta_c(x,t) = \eta(x,t) + i\mathcal{H}[\eta(x,t)]$. The Hilbert transform of a function f is denoted as $\mathcal{H}[f(t)]$ and is given by an improper integral:

$$\mathcal{H}[f(t)] = \frac{1}{\pi}\mathrm{PV}\int_{-\infty}^{\infty}\frac{f(\tau)d\tau}{\tau - t} \tag{4.1}$$

where PV denotes the Cauchy principal value of the corresponding integral. Note that our wave field η depends on x and t and the Hilbert transform is applied with respect to the time variable t. Nonetheless, we can also apply the Hilbert transformation with respect to the space variable x. Written in polar form with real-valued phase and amplitude variables we get $\eta_c(x,t) = a(x,t)e^{i\Phi(x,t)}$. The *local wavenumber* and *local frequency* are defined respectively as $k(x,t) = \partial_x\Phi$ and $\omega(x,t) = -\partial_t\Phi$.

The phase Φ is uniquely defined for smooth functions η for all $(x,t) \in \mathbb{R}^2$ for which the amplitude does not vanish. When the wave field has *vanishing amplitude*, i.e. if $a(\hat{x},\hat{t}) = 0$, we call $(\hat{x},\hat{t}) \in \mathbb{R}^2$ a *singular point*. In the Argand diagram (the complex plane), the time signal at a fixed position corresponds to an evolution curve $t \mapsto \eta_c(x,t)$; a singular point $(\hat{x},\hat{t})$ lies on an evolution curve that is at the origin of the complex plane. Figure 4.2(a) shows a sketch of a complex-amplitude A that passes the origin and thus experiences singularity.

For nonzero amplitude, the phase of η_c has a well defined value, but at a singular point the phase Φ is undetermined or may even becomes singular. We will say that the wave field $\eta(x,t)$ has a *phase singularity* at the singular point $(\hat{x},\hat{t})$ if $\Phi(x,t)$ is not continuous. As is clear from the interpretation in the Argand diagram, in most cases the trajectory will cross the origin and the phase will be discontinuous and have a π-jump. Only in case the origin acts as a reflection point, the phase will be continuous. Examples are easily constructed for both cases by superposition of just a few waves, as we will show further on in Subsection 4.2.2 and Subsection 4.2.3.

Wavefront dislocation is observed when waves at a certain point and time merge or split. Necessarily this can happen only at a singular point, as we will see. Formally we

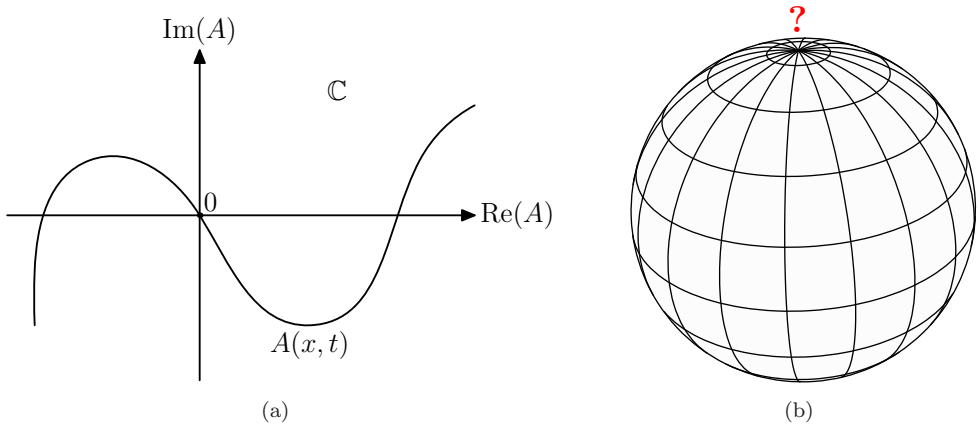

(a) (b)

Figure 4.2: (a) A sketch of a trajectory of the complex amplitude in the Argand diagram when a singularity appears where the trajectory crosses the origin. Typically the phase will experience a $\pi/2$ jump. (b) An example of singularity is the singular time zone at the North Pole.

will define that the wave field $\eta(x,t)$ has *wavefront dislocation* of strength $n \neq 0$ in the area of the (x,t) plane that is enclosed by a contour if the following contour integral has the given integer multiple of 2π [Nye and Berry, 1974; Berry, 1981, 1998]:

$$\oint d\Phi = \oint (k\,dx - \omega\,dt) = \iint \left(\frac{\partial \omega}{\partial x} + \frac{\partial k}{\partial t} \right) dx\,dt = 2n\pi, \qquad n \neq 0. \tag{4.2}$$

Instead of taking an arbitrary closed curve, it is also possible to investigate the property of a given singular point. Then, by taking a circle of radius ϵ, and allowing the radius to shrink to zero, the strength of the singular point is found from

$$I = \lim_{\epsilon \to 0} \oint_{C(\epsilon)} d\Phi = \lim_{\epsilon \to 0} \int_0^{2\pi} \frac{d\Phi}{d\theta} d\theta \tag{4.3}$$

where θ is the angle variable describing the circle. If $I = 0$ there is no wavefront dislocation, while if $I = \pm 2\pi$ there is wavefront dislocation. More specifically, splitting of waves for progressing time will occur if for increasing x the value of $I = -2\pi$; for $I = 2\pi$, merging of waves will happen for increasing x. Indeed, the formula to measure the number of waves of a signal in a certain time interval $(0,T)$ at a fixed position x is given by

$$N(x) = \frac{1}{2\pi} \int_0^T \omega(x,t) dt. \tag{4.4}$$

This shows that when crossing the singular position $\hat{x}$, the number of waves may change if the time interval contains singular times. When the time interval is just around one

singular time instant, we get that the change is equal to the strength of the singular point as defined above.

For a full description of the appearance of wavefront dislocation it turns out to be useful to introduce another quantity. This is the so-called 'Chu-Mei quotient'* defined for signalling problems by

$$\mathrm{CMq} = \frac{\partial_t^2 a}{a}; \tag{4.5}$$

for initial value problems the derivative with respect to x is used instead of to t. See equations (2.32) and (2.42) on page 19 and 20, respectively. This quotient appears in the dispersion relation for both linear and nonlinear dispersive wave equations and has a clear interpretation in this context, as we will show in Section 4.3.

In the remainder of this chapter we will show the following inclusive relations between the concepts introduced above. In Section 4.3 we will show that unboundedness of the Chu-Mei quotient is a necessary condition for wavefront dislocation to occur in wave groups. Further, wavefront dislocation at a point implies that there is phase singularity and phase singularity can only occur at singular points. Although we give examples that the reversed implications are not valid, this will only happen for degenerate cases. *Generically* it will be the case that at a singular point there is phase singularity, wavefront dislocation and unboundedness of the Chu-Mei quotient.

A monochromatic wave will not have any singular point, and therefore it is not interesting for our investigations. A bichromatic wave can have singular points, which may have phase singularity. In that last case, there will be no wavefront dislocation and the Chu-Mei quotient will be finite. A combination of three monochromatic waves can show all the phenomena; we will briefly describe these illustrative cases in the following subsections.

4.2.2 Bichromatic wave field

Consider the superposition of two monochromatic waves, known as the bichromatic waves. A complexified form is

$$\eta_{\mathrm{c}}(x,t) = |A_+| \exp(i\theta_+) + |A_-| \exp(i\theta_-) \tag{4.6}$$

where $A_\pm = |A_\pm| e^{i\phi_\pm}$ are the complex-valued amplitudes and where $\theta_\pm = k_\pm x - \omega_\pm t + \phi_\pm$ are the phases of the constituent monochromatic waves. Assume that the waves have different phase velocities. Inspection of the real amplitude of the superposition, shows that singular points can only, and will, happen for $|A_+| = |A_-|$ and then for

*Some authors call this quotient the 'Fornberg-Whitham term' [Infeld and Rowlands, 1990], referring to [Fornberg and Whitham, 1978]. However, throughout this chapter we call it the 'Chu-Mei quotient', since they introduced it for the first time [Chu and Mei, 1970, 1971] when they derived the modulation equations of Whitham's theory [Whitham, 1967] for slowly varying Stokes waves. However, the quotient already appeared earlier in [Karpman, 1967; Karpman and Krushkal', 1969] when they consider modulated waves in nonlinear media.

$\theta_+ - \theta_- = \frac{1}{2}n\pi$, $n \in \mathbb{Z}$. We consider the bichromatic with constituent waves of the same amplitude (taken to be unity for simplicity). Hence we consider

$$\begin{aligned} \eta(x,t) &= \sin[(k_0+\kappa)x - (\omega_0+\nu)t] - \sin[(k_0-\kappa)x - (\omega_0-\nu)t] \\ &= \frac{1}{2}\sin(\kappa x - \nu t)e^{i(k_0 x - \omega_0 t)} + \text{c.c.} \end{aligned} \tag{4.7}$$

where both κ and ν are small quantities, denote the modulation wavenumber and the modulation frequency, respectively. Indeed, the spatial period is given by $\lambda_s = 2\pi/\kappa$ and the temporal period is $T = 2\pi/\nu$. This wave field has a degeneracy of singular points: the amplitude vanishes on straight lines in the (x,t) plane that satisfy $\kappa\hat{x} - \nu\hat{t} = n\pi$, $n \in \mathbb{Z}$. At each point on such a line there is a jump of π in the phase, a phase singularity.

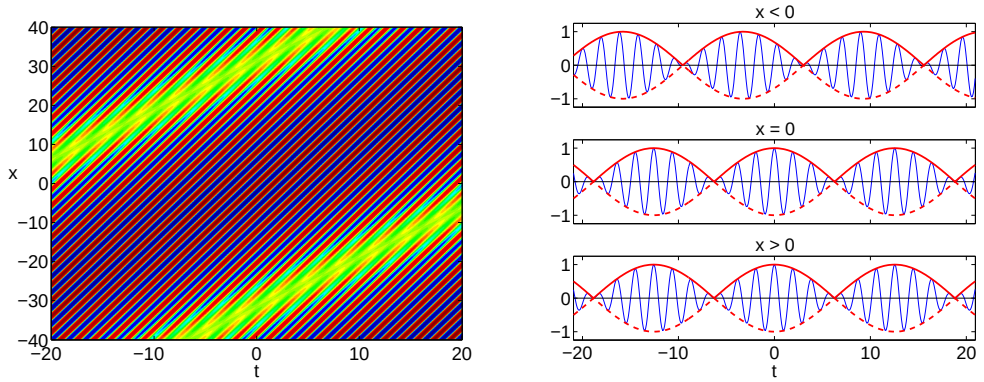

(a) (b)

Figure 4.3: A density plot of the bichromatic wave field (a) and the corresponding wave signals for three different positions (b). The number of waves near the singular points does not change, there is no wavefront dislocation in this wave field.

The Chu-Mei quotient can be calculated explicitly and is bounded at a singular point: $\text{CMq} = \lim_{t\to\hat{t}} \frac{\partial_t^2 a}{a}(x = \hat{x}, t) = -\nu^2$. Using Proposition 4.3.1 below, this implies that this wave field does not have wavefront dislocation. Without using that result, this can also be shown in a direct way by calculating the strength at each point. Calculating the contour integral (4.3) around any singular point $(\hat{x}, \hat{t})$ it is found that indeed $I(\hat{x}, \hat{t}) = 0$. Figure 4.3 shows the density plot of the bichromatic wave field. No wavefront dislocation is visible but the waves do show phase singularity: the crests become troughs and vice versa. The evolution in the Argand diagram for this simple solution is on the real axis, crossing the origin twice in each period.

4.2.3 Trichromatic wave field

Consider the superposition of three monochromatic waves. Already in this case, generically phase singularity and wavefront dislocation will occur whenever the amplitude vanishes. An example is a solution of the linear version of the NLS equation (4.15):

$$\partial_\xi A + i\beta\partial_\tau^2 A = 0. \tag{4.8}$$

Actually, almost any combination of three monochromatic waves can be used as example. This solution is expressed as $\eta(x,t) = A_{\rm TC}(\xi,\tau)e^{i(k_0x-\omega_0t)}+$ c.c., where

$$A_{\rm TC}(\xi,\tau) = \sum_{n=-1}^{1} b_n e^{i(\kappa_n\xi-\nu_n\tau)}, \tag{4.9}$$

with $b_n \neq 0$, $\kappa_0 = 0 = \nu_0$, $\nu_1 = \nu = -\nu_{-1}$ and $\kappa_1 = \nu^2 = \kappa_{-1}$.

This wave field is periodic in both spatial and temporal variables (ξ,τ). If the coefficients are such that there are singular points, the phenomena described above can be investigated. To start with, a simple example of a degenerate case is $\eta_{\rm DEGENERATE} = \frac{1}{2}[1+\sin(\kappa x-\nu t)]e^{i(k_0x-\omega_0t)}$. Clearly there is a singular point, but there is no phase singularity and wavefront dislocation: the evolution in the Argand diagram is a straight line on the nonnegative real axis with the origin as reflection point.

Phase singularity occurs when the coefficients of the trichromatic wave satisfy the following condition:

$$(b_1-b_{-1})^2 \leq b_0^2 \leq (b_1+b_{-1})^2, \qquad \text{if} \quad b_1b_{-1} > 0, \tag{4.10}$$

$$(b_1+b_{-1})^2 \leq b_0^2 \leq (b_1-b_{-1})^2, \qquad \text{if} \quad b_1b_{-1} < 0. \tag{4.11}$$

If the coefficients do not satisfy this condition, the real-valued amplitude remains positive definite and therefore there is no phase singularity. The singular points are the set of points (ξ,τ) that satisfy the following conditions:

$$\cos(2\nu^2\xi) = \frac{(b_1+b_{-1})^2[b_0^2-(b_1-b_{-1})^2]}{2b_0^2b_1b_{-1}} - 1 \tag{4.12}$$

$$\cos(2\nu\tau) = \frac{b_0^2-(b_1-b_{-1})^2}{2b_1b_{-1}} - 1. \tag{4.13}$$

There are four singular points within one spatial period and one singular point within one temporal period.

In general, as said before, at each singular point there will be a phase singularity and wavefront dislocation, and an unbounded Chu-Mei quotient. We illustrate some aspects for the case studied in [Trulsen, 1998], for which $b_0 = 2$, $b_1 = -2$, and $b_2 = 1$, $\nu = 1/13$ and $\omega_0 = 1$. The motion of the amplitude in the complex plane, shown in Figure 4.4(a), makes it clear that there are singular points with phase singularity. The appearance of wavefront dislocation is shown in the density plot in Figure 4.4(b),

and can be investigated in detail by counting the number of waves in one period. The Chu-Mei quotient is unbounded at the singular points. This is related to the fact that the local frequency and local wavenumber become unbounded, as shown in Figure 4.5.

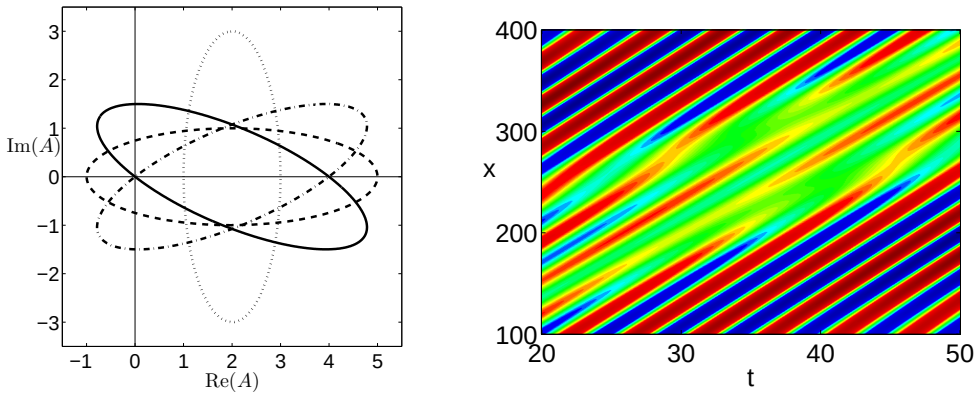

(a) (b)

Figure 4.4: (a) The evolution in the Argand diagram is shown for the trichromatic wave parameterized by τ and plots are given for different values of ξ: $\xi = 0$ (dotted); $\xi = \hat{\xi}_1$ (solid); $\xi = \pi/(2\nu^2)$ (dashed); $\xi = \hat{\xi}_2$ (dash-dot). The evolution curves are counterclockwise ellipses and follow a clockwise direction for increasing τ. When the ellipse crosses the origin, a phase singularity and wavefront dislocation occurs. (b) The density plot is shown of the trichromatic wave near a phase singularity where splitting and merging of waves can be seen.

4.3 Wavefront dislocations in wave groups

In the previous section, we showed that already a superposition of three monochromatic waves can show wavefront dislocation at singular points. In this section, we will consider linear and nonlinear dispersive wave equations and show that a necessary condition for a wave group to have a wavefront dislocation is that the Chu-Mei quotient is unbounded. Moreover, we will also show that the unboundedness of this term is a generic property: if it is bounded at a singular point for an exceptional case, any perturbation of the waves will result into an unbounded Chu-Mei quotient.

4.3.1 Linear and nonlinear dispersive wave equations

We consider a linear or nonlinear dispersive wave equation. As a model for mainly unidirectional propagation, we can take an evolution equation of KdV type:

$$\partial_t \eta + i\Omega(-i\partial_x)\eta + \partial_x N(\eta) = 0. \tag{4.14}$$

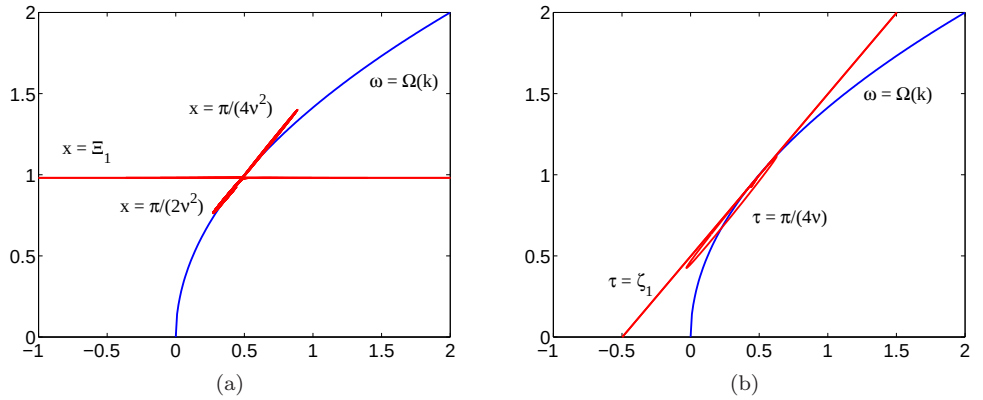

Figure 4.5: Plots of the local wavenumber k (horizontal axis) and the local frequency ω (vertical axis) in the dispersion plane of the considered trichromatic wave. (a) For fixed position some trajectories are shown parameterized by the time, showing that the local wavenumber becomes unbounded at the instance of singularity; similarly, (b) for a fixed time with trajectories parameterized by position, showing the local frequency becoming unbounded at the singular position.

Here $k \mapsto \Omega(k)$ determines the dispersion relation and the inverse will be denoted by K: $K = \Omega^{-1}$. The weak nonlinearity is given by $N(\eta) = a\eta^2 + b\eta^3$, but is of little relevance for the following discussion about wavefront dislocation as we shall see, so taking a linear equation for which $a = 0 = b$ is possible.

When looking for a wave group with carrier frequency ω_0, the evolution is described with a complex amplitude A, and is then given in lowest order by

$$\eta(x,t) = \epsilon A(\xi,\tau)e^{i\theta_0} + \text{c.c.}$$

where $\theta_0 = k_0 x - \omega_0 t$, with $k_0 = K(\omega_0)$ and c.c. denotes the complex conjugate of the preceding term. The amplitude is described in a time delayed coordinate system: $\xi = x$ and $\tau = t - x/V_0$ where $V_0 = \Omega'(k_0) = 1/K'(\omega_0)$. This transformation is suitable for studying the evolution in space, for the signalling problem. The resulting equation for A is then the spatial nonlinear Schrödinger (NLS) equation, given by

$$\partial_\xi A + i\beta\partial_\tau^2 A + i\gamma|A|^2 A = 0. \tag{4.15}$$

Here $\beta = -\Omega''(k_0)/(2[\Omega'(k_0)]^3)$ is related to the group velocity dispersion, while γ is a transfer coefficient from the nonlinearity ($\gamma = 0$ for the linear equation).

By writing A in its polar form with the real-valued amplitude a and the real-valued phase ϕ, $A = a(x,t)e^{i\phi(x,t)}$, and substituting into (4.15), we obtain the coupled phase-amplitude equations. In the original physical variables, the amplitude equation is known as the 'energy equation' (2.30) on page 18, and the phase equation can be written as the 'nonlinear dispersion relation' (2.32) on page 19. Even for a linear

equation, this phase equation contains an additional nonlinear term which results from the fact that the transformation $A \mapsto (a, \phi)$, $A = ae^{i\phi}$ itself is nonlinear.

At vanishing amplitude, the term from nonlinearity of the equation vanishes, $\gamma a^2 = 0$, which shows that the nonlinearity does not play an important role at vanishing amplitude and hence for the phenomena to follow. Only the Chu-Mei quotient plays a significant role in understanding phase singularity and wavefront dislocation phenomena. Unboundedness of the Chu-Mei quotient implies that $K(\omega) - k$ becomes unbounded, and hence that the local wavenumber or the local frequency become unbounded.

Now we will show that the Chu-Mei quotient is unbounded if the wavefront dislocation occurs. The following proposition and its proof have not been mentioned in the literature before.

Proposition 4.3.1 A necessary condition for a wave field to have a wavefront dislocation is that the Chu-Mei quotient is unbounded at a singular point.

Proof. The proposition means that if the contour integral $d\phi$ is nonzero, then the Chu-Mei quotient is unbounded at the singular points. We will show its contraposition, namely if the Chu-Mei quotient is bounded at singular points, then the contour integral vanishes and there is no wavefront dislocation. The Chu-Mei quotient being bounded at a singular point means that either both local wavenumber and local frequency are bounded at the singular point or that the local wavenumber or local frequency is unbounded, but $|K(\omega(x,t)) - k(x,t)| < \infty$. For the first case, since both quantities are bounded, the integrand in the contour integral (4.2) is bounded, and hence vanishes in the limit for vanishing contour around the point. For the latter case, it means that there exists a positive constant M such that $K(\omega(x,t)) - M \leq k(x,t) \leq K(\omega(x,t)) + M$. Hence, since $K(\omega) \to \pm\infty$ if and only if $\omega(x,t) \to \pm\infty$, both wavenumber and frequency have to be unbounded. For evaluating the contour integral (4.2), observe that

$$\oint (K(\omega)dx - \omega dt) - \oint M dx \leq \oint (kdx - \omega dt) \leq \oint (K(\omega)dx - \omega dt) + \oint M dx.$$

The contribution $\oint M dx$ vanishes in the limit for shrinking contour, and the same holds for the integral $\oint (K(\omega)dx - \omega dt)$ by selecting a limiting contour such as a rectangle for which the length of the sides are chosen appropriately, for instance $dx = \mathcal{O}(\omega/K(\omega))dt$. Thus, also in this case the contour integral (4.2) vanishes, and there is no wavefront dislocation. ■

4.3.2 The Chu-Mei quotient under perturbation

We will now show that the boundedness of the Chu-Mei quotient at a singular point is exceptional: almost any perturbation of the wave field will make the quotient to become unbounded. This is intuitively clear by looking at the trajectory in the Argand diagram: at a singular point, the trajectory crosses the origin, $a = 0$, and it will be exceptional if it does this with vanishing 'acceleration' $\partial_t^2 a = 0$.

The translation of this result to complex valued functions will give the required statement. Indeed, let $F : \mathbb{R}^2 \to \mathbb{C}$, and denote by F' and F'' respectively the first and second derivative with respect to the parameter t or, actually, in any direction. Then defining the amplitude a as $a^2 = |F|^2$, after some manipulations we get

$$\frac{\partial_t^2 a}{a} = \frac{\mathrm{Re}\,(F'' \cdot F^*)}{|F|^2} + \frac{[\mathrm{Im}\,(F' \cdot F^*)]^2}{|F|^4},$$

where all quantities at the right-hand side should be evaluated at a singular point for which $a = |F| = 0$. Boundedness of this expression is highly exceptional, and a generic perturbation of a function for which it is bounded, will lead to unboundedness.

4.3.3 SFB wave field

The NLS equation has many interesting special solutions. One family is the so-called SFB that has been studied extensively in the previous chapter. The SFB physical wave field depends on three parameters: the carrier wave frequency ω_0, the plane-wave amplitude r_0 and the normalized modulation frequency $\tilde{\nu}$, where $0 < \tilde{\nu} < \sqrt{2}$. Singular points of the SFB can be found by requiring the real-amplitude to vanish. This implies that both the real and the imaginary parts of the SFB complex amplitude vanish. Alternatively, we can also derive this using an argument of the displaced phase-amplitude representation (3.28).

The fact that ϕ is independent of τ means that at each position the trajectory in the Argand diagram is on a straight line through the point -1 under an angle ϕ. Hence, only when $\phi = 0$, which means at $\xi = 0$, there can be a singular point. At that position, singular points will occur if

$$\cos(\nu\tau) = \frac{2(1-\tilde{\nu}^2)}{\sqrt{4-2\tilde{\nu}^2}}. \tag{4.16}$$

Vanishing amplitude occurs for $0 < \tilde{\nu} \leq \sqrt{3/2}$ for which there is phase singularity. For $\sqrt{3/2} < \tilde{\nu} < \sqrt{2}$, the amplitude remains positive definite and there is no phase singularity. Such phase singularity occurs at $\xi = 0$ for two instants in each temporal period. At the phase singularities, the local wavenumber and local frequency become unbounded, as shown in Figure 4.6; this confirms the fact that the Chu-Mei quotient is unbounded at the singular points.

At the singular points there are wavefront dislocations. Let $(0, \zeta_1)$ and $(0, \zeta_2)$ be singular points of the SFB in one modulation period. We use the contour integral (4.3) to calculate the strength of the singular points. The contour integral around the first singular point is given by:

$$I(0,\zeta_1) = \lim_{\epsilon \to 0} \left(\phi(2\pi) - \lim_{\theta \to \pi/2^+} \phi(\theta) + \lim_{\theta \to \pi/2^-} \phi(\theta) - \phi(0) \right) = -2\pi. \tag{4.17}$$

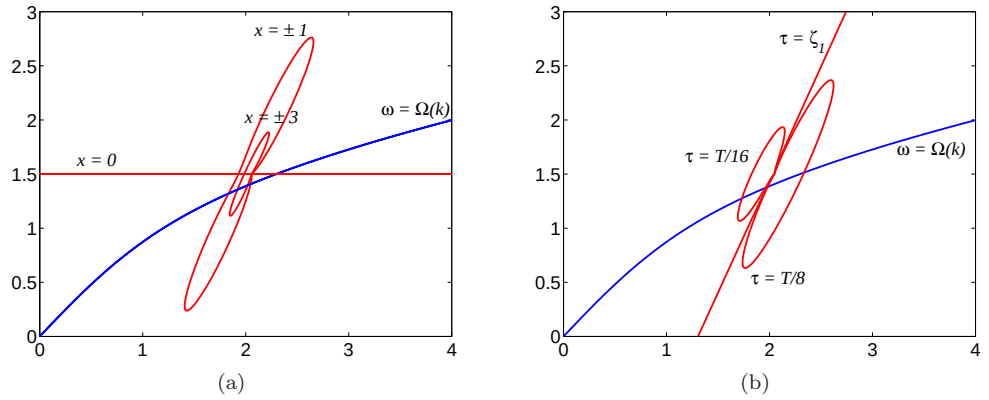

(a) (b)

Figure 4.6: Plots of the local wavenumber k (horizontal axis) and the local frequency ω (vertical axis) in the dispersion plane for $\nu = \frac{1}{2}$. At $x = 0$, the local wavenumber becomes unbounded (a), and at $\tau = \zeta_1$, the local frequency becomes unbounded (b).

Similarly, the contour integral around the second singular point is found to be $I(0, \zeta_2) = 2\pi$. These calculations show that during each modulation period, splitting of waves occur at $(0, \zeta_1)$ and merging of waves occur at $(0, \zeta_2)$ for increasing space.

Figure 4.7 shows a density plot of the SFB wave field around two phase singularities. We observe the splitting and merging waves in pairs. In plots of the time signal at different positions, we see the splitting and merging in more detail. In this example, for a half modulation period $t \in \left[-\frac{1}{2}T, 0\right]$, the number of waves decreases from 8 to 7, indicating that waves are merging when passing the singularity. At another half modulation period $t \in \left[0, \frac{1}{2}T\right]$, it increases from 7 to 8, which indicates that waves are splitting when passing the singularity. However, the number of waves in one modulation period for $x \to \pm\infty$ remains the same before and after undergoing the singularity, namely ω_0/ν.

An observation and investigation of wavefront dislocation in modulated surface water waves has been done by Tanaka [Tanaka, 1995]. His investigation is based on the modulated gravity waves corresponding to Benjamin-Feir instability and is done numerically. By taking an analogy to our signalling problem, the corresponding envelope function experiences vanishing amplitude at two different positions. He observed that between these two vanishing amplitudes, the wave crests 'disappear', as is confirmed by the decrease in number of waves.

4.4 Conclusions

We discussed the phenomena of phase singularity and wavefront dislocation that can happen at singular points of a wave field where the amplitude vanishes. We investi-

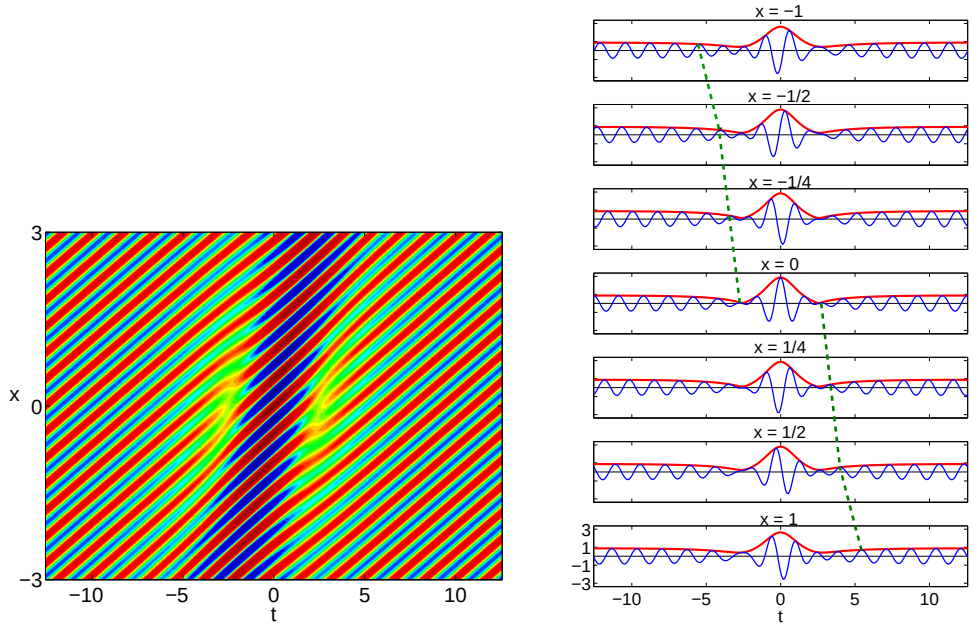

(a) (b)

Figure 4.7: Density plot of the SFB wave field with wavefront dislocations (a), and the corresponding wave signals for different positions in a moving frame of reference (b) for $\nu = \frac{1}{2}$. The number of waves decreases from 8 to 7 for the half period $t \in \left[-\frac{1}{2}T, 0\right]$ and it increases from 7 to 8 for the next half period $t \in \left[0, \frac{1}{2}T\right]$.

gated for wave fields in one spatial dimension the appearance of these essentially linear phenomena. We used simple examples of trichromatic waves to see the relation between these concepts. We introduced the Chu-Mei quotient as it is known to appear in the 'nonlinear dispersion relation' for wave groups as a consequence of the nonlinear transformation of the complex amplitude to real phase-amplitude variables. We also linked the unboudedness of this quotient to the unboundedness of the local wavenumber and frequency at singular points. This unboundedness is a generic property and is necessary for the occurrence of phase singularity and wavefront dislocation. Viewing the phenomena from this angle is novel and never been considered in the literature. It is important to stress again that the phenomena are essentially linear since nonlinear terms in the equation are of higher order at a singular point. We showed that for an interesting class of solutions of the NLS equation, the Solitons on Finite Background, wavefront dislocations occur there too.

References

[Balistreri et al., 2000] M. L. M. Balistreri, J. P. Korterik, L. Kuipers and N. F. van Hulst. Local observation of phase singularities in optical fields in waveguide structures. *Phys. Rev. Lett.* **85**: 294-297, 2000.

[Basistiy et al., 1995] I. V. Basistiy, M. S. Soskin, and M. V. Vasnetsov. Optical wavefront dislocations and their properties. *Opt. Comm.* **119**: 604-612, 1995.

[Berry et al., 1980] M. V. Berry, R. G. Chambers, M. D. Large, C. Upstill and J. C. Walmsley. Wavefront dislocations in the Aharonov-Bohm effect and its water wave analogue. *Eur. J. Phys.* **1**: 154–162, 1980.

[Berry, 1981] M. V. Berry. Singularities in waves and rays. In R. Balian, M. Kléman, and J.-P. Poirier, editors, *Les Houches 1980, Session XXXV, Physics of Defects*, North-Holland, Amsterdam, p 453–459, 1981.

[Berry, 1998] M. V. Berry. Much ado about nothing: optical dislocation lines (phase singularities, zeros, vortices...). In M. S. Soskin, editor, *Proceedings of International Conference on Singular Optics*, The International Society of Optical Engineering (SPIE), p 1–10, 1998.

[Berry and Dennis, 2000] M. V. Berry and M. R. Dennis. Phase singularities in isotropic random waves. *Proc. R. Soc. Lond. A* **456**: 2059–2079, 2000.

[Berry and Dennis, 2001] M. V. Berry and M. R. Dennis. Knotted and linked phase singularities in monochromatic waves. *Proc. R. Soc. Lond. A* **457**: 2251–2263, 2001.

[Berry et al., 2004] M. V. Berry, M. R. Dennis and M. S. Soskin. The plurarity of optical singularities. *J. Opt. A: Pure Appl. Opt.* **6**: S155–S156, 2004.

[Chu and Mei, 1970] V. H. Chu and C. C. Mei. On slowly-varying Stokes waves. *J. Fluid Mech.* **41**: 873–887, 1970.

[Chu and Mei, 1971] V. H. Chu and C. C. Mei. The nonlinear evolution of Stokes waves in deep water. *J. Fluid Mech.* **42**: 337–351, 1971.

[Coullet et al., 1989] P. Coullet, L. Gil and F. Rocca. Optical vortices. *Opt. Comm.* **73**: 403–408, 1989.

[Dennis, 2001] M. R. Dennis, *Topological Singularities in Wave Fields*. PhD thesis, University of Bristol, H. H. Wills Physics Laboratory, November 2001.

[Dieter, 1988] G. E. Dieter. *Mechanical Metallurgy*. McGraw-Hill, London, SI Metric edition, 1988.

[Fornberg and Whitham, 1978] V. Fornberg and G. B. Whitham. A numerical and theoretical study of certain nonlinear wave phenomena. *Phil. Trans. R. Soc. Lond. A* **289**: 373–404, 1978.

[Honeycombe, 1984] R. W. K. Honeycombe. *The Plastic Deformation of Metals*. Edward Arnold, London, second edition, 1984.

[Hull and Bacon, 2001] D. Hull and D. J. Bacon. *Introduction to Dislocations*. Butterworth Heinemann, Oxford, fourth edition, 2001.

[Infeld and Rowlands, 1990] E. Infeld and G. Rowlands. *Nonlinear waves, solitons and chaos*. Cambridge University Press, Cambridge, pp 117–119, 1990.

[Karpman, 1967] V. I. Karpman. Self-modulation of nonlinear plane waves in dispersive media, *JETP Lett.* **6**: 277–279, 1967.

[Karpman and Krushkal', 1969] V. I. Karpman and E. M. Krushkal'. Modulated waves in nonlinear dispersive media. *Sov. Phys. JETP* **28**: 277–281, 1969.

[Krása, 1981] J. Krása. Dislocation in turbulent ionisation waves. *J. Phys. D: Appl. Phys.* **14**: 1241–1246, 1981.

[Nabarro, 1979-2004] F. R. N. Nabarro, editor, *Dislocations in Solids* **1–12**, 1979–2004.

[Nye and Berry, 1974] J. F. Nye and M. V. Berry. Dislocation in wave trains. *Proc. R. Soc. Lond. A* **336**: 165–190, 1974.

[Nye, 1981] J. F. Nye. The motion and structure of dislocations in wavefronts. *Proc. R. Soc. Lond. A* **378**: 219–239, 1981.

[Nye, 1997] J. F. Nye. Line singularities in wave fields. *Proc. R. Soc. Lond. A* **355**: 2065–2069, 1997.

[Nye, 1999] J. F. Nye. *Natural Focussing and Fine Structure of Light: Caustics and Wave Dislocations*. IOP, Bristol, 1999.

[Orowan, 1934] E. Orowan. Zur Kristallplastizität. I: Tieftemperaturplastizität und Beckersche Formel. II: Die dynamische Auffassung der Kristallplastizifät. III: Über die Mechanismus des Gleitvorganges. *Zeitschrift für Physik (Z. Phys.)* **89**: 605–659, 1934.

[Polanyi, 1934] M. Polanyi. Über eine Art Gitterstörung die einen Kristall plastich machen könnte. *Z. Phys.* **89**: 660–664, 1934.

[Read, 1953] W. T. Read Jr. *Dislocations in Crystals*. McGraw-Hill, New York, 1953.

[Soskin and Vasnetsov, 2001] M. S. Soskin and M. V. Vasnetsov. Singular optics. *Prog. Opt.* **42**: 219-276, 2001.

[Tanaka, 1995] M. Tanaka. Dissapearance of waves in modulated train of surface gravity waves. *Structure and Dynamics of Nonlinear Waves in Fluids*. In A. Mielke and K. Kirchgässner, editors, Proceedings of the IUTAM/ISIMM Symposium held in Hannover August 1994, volume **7** of *Advanced Series in Nonlinear Dynamics*, World Scientific, Singapore, pp 392-398, 1995.

[Taylor, 1934] G. I. Taylor. The mechanism of plastic deformation of crystals. Part I: Theoretical. Part II: Comparison with observations. *Proc. R. Soc. London* **145A**: 362–404, 1934.

[Trulsen, 1998] K. Trulsen. Crest pairing predicted by modulation theory. *J. Geophys. Res.* **103**(C2): 3143–3147, 1998.

[Whitham, 1967] G. B. Whitham. Nonlinear dispersion of water waves. *J. Fluid Mech.* **27**: 399–412, 1967.

[Whitham, 1974] G. B. Whitham. *Linear and Nonlinear Waves*. John Wiley & Sons, New York, 1974.

[Wright, 1979] F. J. Wright. Wavefront dislocations and their analysis using catastrophe theory. In W. Güttinger and H. Eikemeier, editors *Structural Stability in Physics*, pp 141–156, 1979.

Chapter 5

Higher order waves on finite background

5.1 Introduction

This chapter deals with one of the special solutions of the NLS equation, but a different class than has been studied in Chapter 3. We will study a family of higher order solutions of the NLS equation that also describe modulational instability and this study can also seen as being motivated by the problem of extreme wave generation in the wave basin of a hydrodynamic laboratory. To distinguish from the previous Soliton on Finite Background (SFB), we give an index to the special classes of solutions that is based on the number of pairs of initial sidebands. In the context of this chapter, the SFB that we have discussed extensively in Chapter 3 is denoted as SFB_1 and its modulation frequency as ν_1. The higher order SFBs are denoted as SFB_2, SFB_3 and so on. In this chapter, we only concentrate on SFB_2.

In the spectral domain, the initial Benjamin-Feir spectrum is represented by one central frequency and one pair of sidebands inside the instability interval. However, if there is more than one pair of sidebands as the initial condition of modulation, and all these are inside the instability interval, then, due to the four-wave mixing process, all will be amplified. However, since this process is a nonlinear superposition of the elementary processes of the Benjamin-Feir instability with one pair of initial sidebands, the total effect can no longer be described by the SFB_1. Higher order solutions of the NLS equation can then be constructed using a Darboux transformation. Readers who are interested in the topic of Darboux transformation may consult [Matveev and Salle, 1991; Rogers and Schief, 2002].

Similar to SFB_1, also SFB_2 describes waves on finite background and these solutions were found by [Akhmediev et al., 1985]. SFB_2 in this thesis refers to the dynamic evolution in which the modulation frequencies are ν_2 and $2\nu_2$, where $\nu_2 = \frac{1}{2}\nu_1$. Note

that this choice of modulation frequencies is a special case, which is chosen since then the explicit expressions are less complicated than arbitrary combination of modulation frequencies. For a special choice of parameters, solutions from SFB_2 can have an amplitude amplification up to a factor of 5. Therefore, by providing sufficient space for waves to propagate downstream, extreme wave events with even larger amplitude than waves from SFB_1 can be generated. Another similarity with SFB_1 is that SFB_2 solutions also show wavefront dislocation and phase singularity.

The aim of this chapter is to present some aspects of the SFB_2 which have not been discussed in the literature; the chapter is organized as follows. After this introduction, Section 5.2 discusses specifications and properties of SFB_2, including the explicit expression, asymptotic behaviour, physical wave field and maximum temporal amplitude. Section 5.3 explains the spatial evolution of the SFB_2 signal. We will also see phase singularity and give phase plane representation of the solutions. Section 5.4 presents the SFB_2 spectrum and its evolution. Finally, Section 5.5 gives conclusions and remarks about this chapter.

5.2 Specifications and properties of SFB_2

5.2.1 An explicit expression

We have seen in Subsection 3.2.2 on page 41 that SFB_1 can be written in a displaced phase amplitude expression as given by $A(\xi,\tau) = A_0(\xi)\,F(\xi,\tau)$, where $F(\xi,\tau)$ is given by (3.20). SFB_2 cannot be expressed in a similar way with these displaced phase amplitude variables, since the evolution in the Argand diagram is not a set of straight lines, as we will see in Subsection 5.3.3.

An explicit expression for SFB_2 can be found in [Akhmediev and Ankiewicz, 1997]. Another expression can also be found in [Ablowitz and Herbst, 1990; Calini and Schober, 2002]. The authors derived it using the Hirota's method and associated it with the dark-hole soliton solutions of the defocusing NLS equation. Explicitly, both SFB_1 and SFB_2 can be given by the following expression:

$$A_j(\xi,\tau;\tilde{\nu}_j) = A_0(\xi)\left(\frac{P_j(\xi,\tau)+iQ_j(\xi,\tau)}{H_j(\xi,\tau)} - 1\right), \qquad j = 1,2, \tag{5.1}$$

where the indices $j = 1,2$ corresponds to SFB_1 and SFB_2, respectively. For both SFBs, $A_0(\xi)$ denotes the plane wave solution of the NLS equation, as given by (2.45) on page 24. Expressions for P_j, Q_j and H_j are given as follows:

$$P_1(\xi,\tau) = \tilde{\nu}_1^2\cosh[\sigma(\xi-\xi_0)] \tag{5.2}$$

$$Q_1(\xi,\tau) = -\tilde{\sigma}\sinh[\sigma(\xi-\xi_0)] \tag{5.3}$$

$$H_1(\xi,\tau) = \cosh[\sigma(\xi-\xi_0)] - \sqrt{1-\frac{1}{2}\tilde{\nu}_1^2}\cos[\nu_1(\tau-\tau_0)] \tag{5.4}$$

$$P_2(\xi,\tau) = \frac{3}{2\tilde{\nu}_2\sqrt{2}}\left[\cos\nu_2(\tau+\tau_{01}-2\tau_{02}) + \frac{1}{9}\cos\nu_2(3\tau-2\tau_{02}-\tau_{01})\right] + \frac{1}{2\tilde{\sigma}_1}(2-\tilde{\nu_2}^2)\cosh\sigma_1(\xi-\xi_{01})\cos 2\nu_2(\tau-\tau_{02}) + \frac{2}{\tilde{\sigma}_2}(1-2\tilde{\nu}_2^2)\cosh\sigma_2(\xi-\xi_{02})\cos\nu_2(\tau-\tau_{01}) - \frac{4}{3\tilde{\nu}_2\sqrt{2}}\left[\frac{\tilde{\nu}_2^2(17\tilde{\nu}_2^2-10)}{2\tilde{\sigma}_1\,\tilde{\sigma}_2}\cosh\sigma_1(\xi-\xi_{01})\,\cosh\sigma_2(\xi-\xi_{02}) + \sinh\sigma_1(\xi-\xi_{01})\,\sinh\sigma_2(\xi-\xi_{02})\right] \tag{5.5}$$

$$Q_2(\xi,\tau) = \frac{1}{2}\sinh\sigma_1(\xi-\xi_{01})\,\cos 2\nu_2(\tau-\tau_{02}) + \sinh\sigma_2(\xi-\xi_{02})\,\cos\nu_2(\tau-\tau_{01}) + \frac{\tilde{\nu}_2\sqrt{2}}{\tilde{\sigma}_1\,\tilde{\sigma}_2}\left[\tilde{\sigma}_2\cosh\sigma_1(\xi-\xi_{01})\,\sinh\sigma_2(\xi-\xi_{02}) - \tilde{\sigma}_1\sinh\sigma_1(\xi-\xi_{01})\,\cosh\sigma_2(\xi-\xi_{02})\right] \tag{5.6}$$

$$H_2(\xi,\tau) = \frac{3}{4\tilde{\nu}_2\sqrt{2}}\left[\cos\nu_2(\tau+\tau_{01}-2\tau_{02}) + \frac{1}{9}\cos\nu_2(3\tau-2\tau_{02}-\tau_{01})\right] + \frac{1}{2\tilde{\sigma}_1}\cosh\sigma_1(\xi-\xi_{01})\,\cos 2\nu_2(\tau-\tau_{02}) + \frac{1}{\tilde{\sigma}_2}\cosh\sigma_2(\xi-\xi_{02})\,\cos\nu_2(\tau-\tau_{01}) - \frac{2}{3\tilde{\nu}_2\sqrt{2}}\left[\frac{\tilde{\nu}_2^2(4\tilde{\nu}_2^2-5)}{\tilde{\sigma}_1\,\tilde{\sigma}_2}\cosh\sigma_1(\xi-\xi_{01})\,\cosh\sigma_2(\xi-\xi_{02}) + \sinh\sigma_1(\xi-\xi_{01})\,\sinh\sigma_2(\xi-\xi_{02})\right]. \tag{5.7}$$

To guarantee the existence of the SFBs, the modulation frequencies ν_j, $j=1,2$ have to be in the instability interval, $0<\tilde{\nu}_1<\sqrt{2}$ and $0<\tilde{\nu}_2<\sqrt{1/2}$, where $\tilde{\nu}_j = \nu_j/\left(r_0\sqrt{\gamma/\beta}\right)$. For SFB$_1$, σ is the growth rate that corresponds to the Benjamin-Feir instability, given as $\sigma = \gamma r_0^2\tilde{\sigma}$, where $\tilde{\sigma} = \tilde{\nu}_1\sqrt{2-\tilde{\nu}_1^2}$. For simplicity, we take $(\xi_0,\tau_0)=(0,0)$, so that SFB$_1$ reaches its maximum at $(\xi,\tau)=(0,2n\pi/\nu_1)$, $n\in\mathbb{Z}$.

For SFB$_2$, σ_1 and σ_2 are two growth rates in the modulational instability process that correspond to the first and the second side band, respectively. They are given as $\sigma_1=\sigma(\tilde{\nu}_2)=\gamma r_0^2\tilde{\sigma}_1$, where $\tilde{\sigma}_1=\tilde{\nu}_2\sqrt{2-\tilde{\nu}_2^2}$ and $\sigma_2=\sigma(2\tilde{\nu}_2)=\gamma r_0^2\tilde{\sigma}_2$, where $\tilde{\sigma}_2 = 2\tilde{\nu}_2\sqrt{2-4\tilde{\nu}_2^2}$. In the following subsection, we will see that the asymptotic behaviour of SFB$_2$ depends on these growth rates. The parameters ξ_{01}, ξ_{02}, τ_{01} and τ_{02} are arbitrary real and determine the position and time lag of SFB$_2$. Let us now define $\Delta\xi := |\xi_{01}-\xi_{02}|$ and $\Delta\tau := |\tau_{01}-\tau_{02}|$ as parameters related to space and time variables, respectively. For definiteness, we will consider SFB$_2$ with maxima at $(\xi,\tau)=(0,2n\pi/\nu_2)$, $n\in\mathbb{Z}$. This is obtained by choosing $\Delta\xi=0=\Delta\tau$ or by taking $\xi_{01}=0=\xi_{02}$ and $\tau_{01}=\pi/\nu_2=\tau_{02}$. With this choice of parameters, SFB$_2$ reduces to SFB$_1$ for $\tilde{\nu}_2\to\sqrt{1/2}$:

$$\lim_{\tilde{\nu}_2\to\sqrt{1/2}} A_2(\xi,\tau;\tilde{\nu}_2) = A_1\left(\xi,\tau;\tilde{\nu}_1=\sqrt{1/2}\right). \tag{5.8}$$

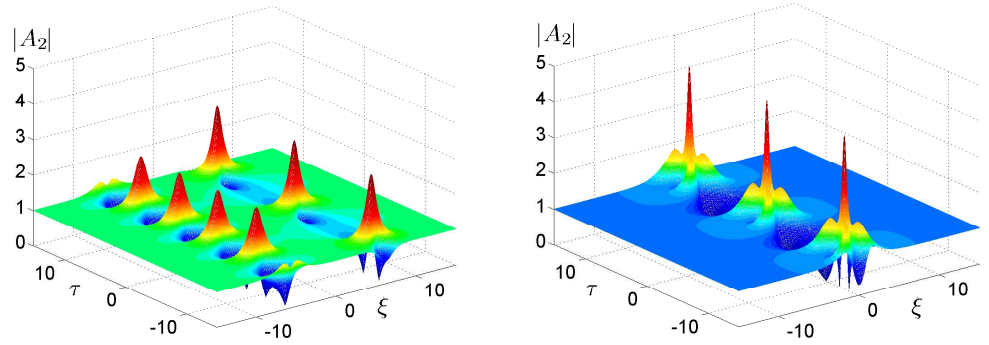

Figure 5.1: Three-dimensional plots of the absolute value of SFB_2 for $\tilde{\nu}_2 = \frac{1}{2}$, $\Delta\tau = 0$, $\Delta\xi = 10$ (left), and $\Delta\xi = 0$ (right), which show an interaction of two SFB_1s. For illustration purposes, the axes are scaled corresponding to $\beta = 1 = \gamma$ in the NLS equation.

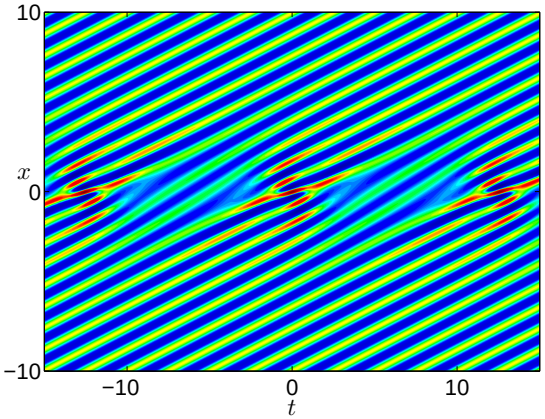

Figure 5.2: A density plot of SFB_2 physical wave field for $\tilde{\nu}_2 = \frac{1}{2}$.

The plots of the absolute value of SFB_2 for different values of parameters show that there are interactions between two SFB_1s with different modulation period. Figure 5.1 shows the plots of SFB_2 for both $\Delta\xi \neq 0$ and $\Delta\xi = 0$. For nonzero $\Delta\xi$, the plot shows two SFB_1s which are separated by a peak distance of approximately $\Delta\xi$. They have modulation frequencies of $\frac{1}{2}\nu_1$ and ν_1 and modulation period of $4\pi/\nu_1$ and $2\pi/\nu_1$, respectively. By allowing $\Delta\xi$ to decrease to zero, an interaction occurs between these two SFB_1s and a change in the modulation period takes place. For $\Delta\xi = 0$, we see the result of the SFB_1 interaction, which has higher maximum amplitude than the individual SFB_1s. The modulation period of this SFB now becomes $4\pi/\nu_1 = 2\pi/\nu_2$.

5.2.2 The asymptotic behaviour

Similar as SFB$_1$, the asymptotic behaviour of SFB$_2$ at the far distance $\xi \to \pm\infty$ is given by the plane wave solution $A_0(\xi)$ of the NLS equation with a phase difference of $2\phi_{20}$ from $\xi = -\infty$ to $\xi = \infty$, where ϕ_{20} is given in Appendix C on page 131. However, we can apply the same procedure as in Subsection 3.3.2 on page 48 to find the asymptotic behaviour that includes the lowest order term and the linear terms. Since SFB$_2$ has two growth rates, the asymptotic behavior will then depend on the value of its modulation frequency $\tilde{\nu}_2$. Different values of $\tilde{\nu}_2$ gives different growth rate ratio. Here we present some selected asymptotic expressions of SFB$_2$ based on different growth rate ratio for $\xi \to \mp\infty$:

- $\sigma_2/\sigma_1 \ll 1$:

$$A_2(\xi,\tau) \approx A_0(\xi)\left[e^{i\phi_{20}} + (e^{\sigma_1\xi})^2\, w_{23} + e^{\sigma_1\xi}\,\tilde{w}_{21}\,\cos(\nu_2\tau) + (e^{\sigma_1\xi})^2\,\tilde{w}_{22}\,\cos(2\nu_2\tau)\right] \tag{5.9}$$

- $\sigma_2/\sigma_1 \approx 1$:

$$A_2(\xi,\tau) \approx A_0(\xi)\left[e^{i\phi_{20}} + e^{\sigma_1\xi}\,w_{21}\,\cos(\nu_2\tau) + e^{\sigma_2\xi}\,w_{22}\,\cos(2\nu_2\tau)\right] \tag{5.10}$$

- $\sigma_2/\sigma_1 \approx 2$:

$$A_2(\xi,\tau) \approx A(\xi)\left[e^{i\phi_{20}} + e^{\sigma_2\xi}\,w_{23} + e^{\sigma_1\xi}\,w_{21}\,\cos(\nu_2\tau) + e^{\sigma_2\xi}\bar{w}_{22}\,\cos(2\nu_2\tau)\right]. \tag{5.11}$$

The quantities w_{2l}, $l = 1,2,3$, $\bar{w}_{22}$, $\tilde{w}_{22} \in \mathbb{C}$ and are given in Appendix C on page 131. From the above expressions, we can see that each side band carries different phase information due to different growth rate ratio.

5.2.3 Physical wave field

We also use the expression (3.54) on page 49 to give an illustration of the physical wave field corresponding to SFB$_2$. Again in this case, we consider only the lowest order contribution of the physical wave field. Figure 5.2 shows a density plot of SFB$_2$ physical wave field for scaled parameters $\beta = 1 = \gamma = r_0$. We observe a similar phenomenon of wavefront dislocation in SFB$_2$ as we have in SFB$_1$, but now with a varied pattern. In SFB$_1$, wavefront dislocation occurs at $x = 0$ and periodically in time but only for $0 < \tilde{\nu}_1 \leq \sqrt{3/2}$. In SFB$_2$, wavefront dislocation also occurs at $x = 0$ and is periodic in time but now for all $0 < \tilde{\nu}_2 < \sqrt{1/2}$. Depending on the value of ν_2, there can be either one or two pair of wavefront dislocations during one modulation period. For $0 < \tilde{\nu}_2 < \tilde{\nu}_2^*$, SFB$_2$ has two pairs of wavefront dislocations and for $\tilde{\nu}_2^* < \tilde{\nu}_2 < \sqrt{1/2}$, it has only one pair during one modulation period, where $\tilde{\nu}_2^* = \frac{1}{6}\sqrt{8\sqrt{10}-10}$. Like SFB$_1$, in between one such pair of wavefront dislocations, the real-valued amplitude reaches its extreme value.

For both theory and experiment on extreme wave generation of SFB$_2$ wave field, we are also interested in the amplitude amplification factor, denoted as AAF and defined

in Definition 3.3.1 on page 49. The AAF of SFB_1 and SFB_2 are denoted as AAF_1 and AAF_2, respectively. We know that the AAF of SFB_1 is given by:

$$\mathrm{AAF}_1(\tilde{\nu}_1) = 1 + \sqrt{4 - 2\tilde{\nu}_1^2} \tag{5.12}$$

for $0 < \tilde{\nu}_1 < \sqrt{2}$. For a very long modulation, when the (normalized) modulation frequency $\tilde{\nu}_1 \to 0$, it can reach up to a maximum value of 3. It decreases monotonically for increasing values of modulation frequency. The AAF of SFB_2 is given by

$$\mathrm{AAF}_2(\tilde{\nu}_2) = 1 + \sqrt{4 - 2\tilde{\nu}_2^2} + 2\sqrt{1 - 2\tilde{\nu}_2^2}. \tag{5.13}$$

Interestingly, there exists a relationship between AAF_1 and AAF_2 and it can be written explicitly as a simple linear relation:

$$\mathrm{AAF}_2(\tilde{\nu}_2) = 1 + (\mathrm{AAF}_1(\tilde{\nu}_2) - 1) + (\mathrm{AAF}_1(2\tilde{\nu}_2) - 1)\,. \tag{5.14}$$

For a very long modulation, AAF_2 can reach up to a maximum value of 5 for $\nu_2 \to 0$. For the whole range of frequencies $0 < \tilde{\nu}_2 < \sqrt{1/2}$, the boundary values are $1 + \sqrt{3} < \mathrm{AAF}_2 < 5$. Figure 5.3 shows the plot of the amplification amplitude factors.

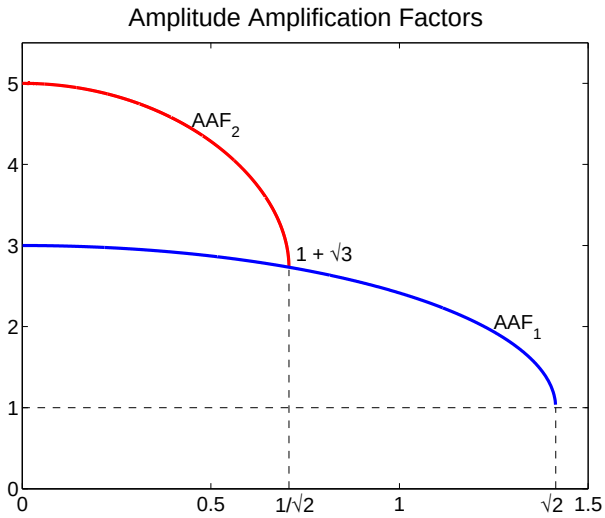

Figure 5.3: Plots of amplification amplitude factors of SFB_1 and SFB_2. Both AAF plots are monotonically decreasing for increasing modulation frequency. The same value of $\mathrm{AAF} = 1 + \sqrt{3}$ is reached when $\tilde{\nu}_2 = \sqrt{1/2}$ and $\tilde{\nu}_1 = \sqrt{1/2}$, because the limiting value of $\tilde{\nu}_2 \to \sqrt{1/2}$ leads SFB_2 to SFB_1 with $\tilde{\nu}_1 = \sqrt{1/2}$.

5.2.4 Maximum temporal amplitude

The concept of the maximum temporal amplitude (MTA) is introduced in Subsection 3.3.4 and the definition is given in Definition 3.3.2 on page 50. The MTA is useful for the generation of extreme waves in the wave basin, particularly to determine a signal input for the wavemaker so that the extreme wave signal is produced at a certain location.

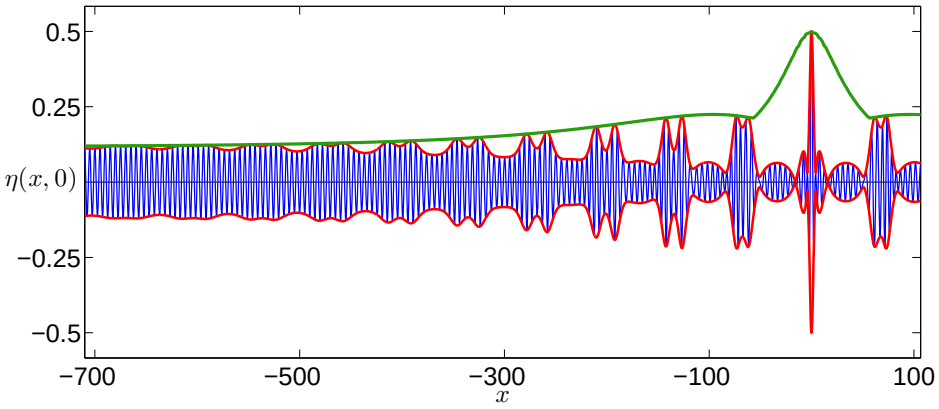

Figure 5.4: A plot of individual waves, the corresponding wave envelope and the time-independent MTA of SFB_2 for $\tilde{\nu}_2 = \frac{1}{2}$. The horizontal axis is the distance from the extreme position and the vertical axis is the surface elevation. Both axes are measured in meter.

The MTA plot of SFB_2 is illustrated in Figure 5.4. This figure shows the propagation of waves of varying amplitude after they are being generated by the wavemaker at the left-hand side. In this example, the water depth is 3.55 m, the wavelength is approximately 6.2 m and both horizontal and vertical distances are in meter. The wave signal is generated on the left-hand side, and waves propagate to the right and reach an extreme condition at $x = 0$. The shown SFB_2 wave field has initial signal of 15 cm amplitude and it reaches an extreme amplitude of 45 cm, an amplitude amplification of factor three. The MTA plot for SFB_2 shows a somewhat different gradual pattern evolution than MTA for SFB_1, see Figure 3.7 on page 52 for a comparison. For SFB_2 the MTA increases monotonically and very slowly until 200 m from the extreme position, then decreases slightly, and after that it starts to grow significantly faster than before it reaches the area of the extreme position. Afterwards, it returns to the initial behavior in the reverse order.

The double modulated wave train envelope travels downstream with an increasing amplitude for SFB_2. Wave groups are deformed and increase in amplitude until they reach the extreme position. For SFB_2, the visible pattern is a result of wave packet interaction and the effect becomes more significant and tangible as the wave profile approaches the extreme position. This focussing of the two constituent wave packages

is the explanation of the fast growth from a certain position relatively close to the extreme position. It is also very significant that close to the extreme position, the amplitude can grow to very large values within a short distance.

5.3 Spatial evolution of SFB_2 wave signal

We have observed in the previous section that double modulated wave groups with small amplitude evolve into large amplitude waves over sufficiently long distance. These wave groups interact during the downstream evolution toward the extreme position. In this section, we will illustrate in more detail the spatial evolution of the signal. We pay more attention to the wave signal at $x = 0$ since at this position the complex amplitude SFB_2 becomes a real-valued function. Also at this position, the amplitude vanishes and leads to phase singularity. Illustrations in the dispersion plane are presented to see that indeed the Chu-Mei quotient is unbounded at such instances. We also present the dynamic evolution of the envelope signal of SFB_2 in the Argand diagram and the phase plane at the extreme position.

5.3.1 Wave signal evolution

We have understood that SFBs behaves asymptotically as a plane-wave solution. Similar with the case of SFB_1, a modulated wave signal with two different modulation frequencies from SFB_2 will grow in space during its evolution according to the modulational instability. SFB_2 describes the complete nonlinear evolution of this modulated wave signal. The modulation period T_2 is preserved during the evolution and is determined by the modulation frequency ν_2, $T_2 = 2\pi/\nu_2$. Figure 5.5 shows the evolution of SFB_2 from a modulated monochromatic wave signal into an extreme condition. We see in this figure that in one modulation period, two parts of a wave group signal grow and interact as the wave signal evolve in space toward the extreme signal. The signal at the extreme position, or the extreme signal, of SFB_2 shows a different pattern from the SFB_1 extreme signal. It has two pairs of phase singularities for $0 < \tilde{\nu}_2 < \tilde{\nu}_2^*$ and one pairs of singularities for $\tilde{\nu}_2^* < \tilde{\nu}_2 < \sqrt{1/2}$, as we shall see in the next subsection.

5.3.2 Phase singularity

We have understood in Chapter 4 that phase singularity and wavefront dislocation is generically a result of vanishing amplitude. We have also understood that the unboundedness of the Chu-Mei quotient is responsible for the occurrence of these phenomena. In this subsection, we explain that the same phenomena also occur in the SFB_2 physical wave field. We have shown that for SFB_1, phase singularity occurs for a certain value of modulation frequency ν_1, namely $0 < \tilde{\nu}_1 \leq \sqrt{3/2}$. However, SFB_2 always shows phase singularity and wavefront dislocation for any $\tilde{\nu}_2$ with $0 < \tilde{\nu}_2 < \sqrt{1/2}$.

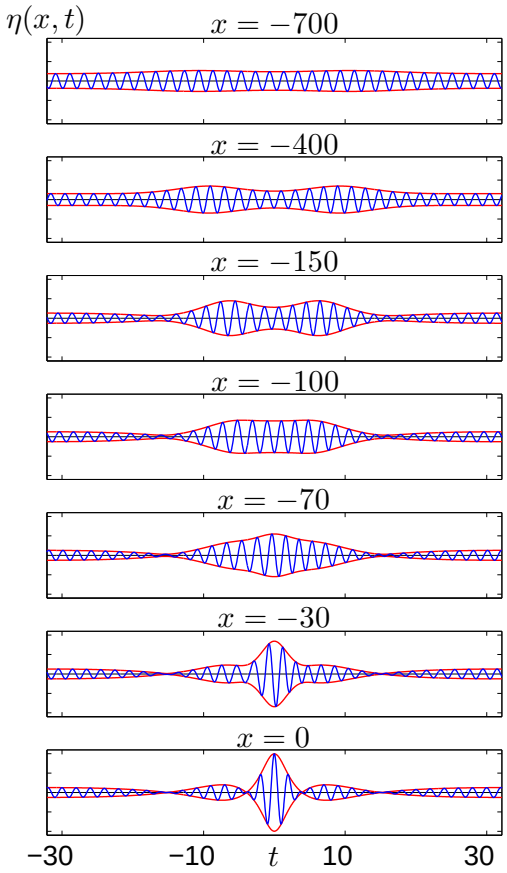

Figure 5.5: The evolution of time signal of SFB$_2$ for $\tilde{\nu}_2 = \frac{1}{2}$ from a modulated wave signal into an extreme signal.

Different with SFB$_1$ which has only one pair of singularities, SFB$_2$ can have two pairs of singularities for $0 < \tilde{\nu}_2 < \tilde{\nu}_2^*$, where $\tilde{\nu}_2^* = \frac{1}{6}\sqrt{8\sqrt{10} - 10}$.

For SFB$_2$, a phase singularity occurs when $\cos(\nu_2\zeta_2)$ satisfies the following cubic equation:

$$\cos^3(\nu_2\zeta_2) + C_2\cos^2(\nu_2\zeta_2) + C_1\cos(\nu_2\zeta_2) + C_0 = 0, \tag{5.15}$$

where C_0, C_1, and C_2 are coefficients depending on $\tilde{\nu}_2$. Explicit expressions of these coefficients are given in Appendix C on page 133. By defining the intermediate variables $Q = \frac{1}{9}(3C_1 - C_2^2)$ and $R = \frac{1}{54}(9C_1C_2 - 27C_0 - 2C_2^3)$, as well as the discriminant of the cubic equation $D = Q^3 + R^2$, we find that for normalized quantities r_0, β, and γ for each $\tilde{\nu}_2$ with $0 < \tilde{\nu}_2 < \sqrt{1/2}$, the discriminant is negative $D < 0$. Therefore, all

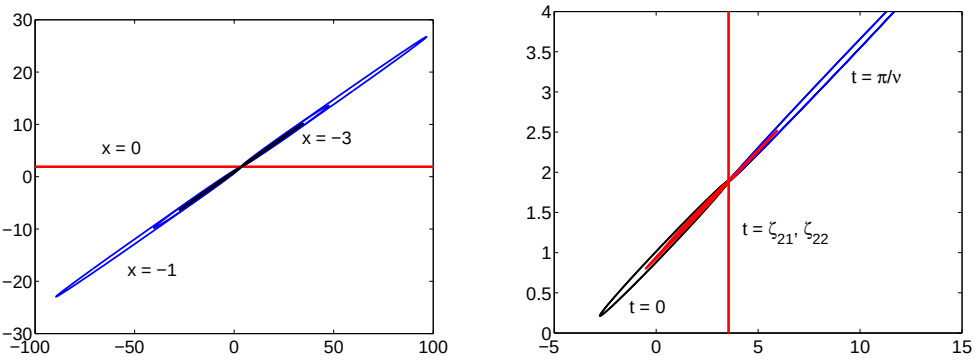

(a) (b)

Figure 5.6: Plots of local wavenumber k (horizontal axis) and local frequency ω (vertical axis) in the dispersion plane for $\tilde{\nu}_2 = \frac{1}{2}$. At $x = 0$, the local wavenumber is unbounded (a) and at $\tau = \zeta_{21}$ or ζ_{22}, the local frequency is unbounded (b).

roots of the cubic equation (5.15) are all real and unequal. However, when solving for ζ_2, not all solutions are real. Two real solutions that correspond to the time when the envelope vanishes are given by:

$$\zeta_{21} = \frac{\sqrt{\beta/\gamma}}{r_0\tilde{\nu}_2} \arccos\left[-\frac{C_2}{3} + 2\sqrt{-Q}\cos\left(\frac{\theta}{3} + \frac{4\pi}{3}\right)\right], \quad 0 < \tilde{\nu}_2 < \sqrt{\frac{1}{2}}, \tag{5.16}$$

$$\zeta_{22} = \frac{\sqrt{\beta/\gamma}}{r_0\tilde{\nu}_2} \arccos\left[-\frac{C_2}{3} + 2\sqrt{-Q}\cos\left(\frac{\theta}{3} + \frac{2\pi}{3}\right)\right], \quad 0 < \tilde{\nu}_2 < \tilde{\nu}_2^*, \tag{5.17}$$

where $\cos\theta = R/\sqrt{-Q^3}$.

Another way to confirm the occurrence of phase singularity is by showing that the Chu-Mei quotient is unbounded at the singular points. This can be shown by plotting the local wavenumber and local frequency, as we also have shown for SFB_1 in Subsection 4.3.3 on page 78. Figure 5.6 shows the plot of trajectories in the dispersion plane when local wavenumber and local frequency are unbounded.

5.3.3 Argand diagram

The evolution in the Argand diagram for SFB_2 is a collection of curves in a complex plane parameterized in time or in space. The horizontal and the vertical axes are the real and the imaginary parts of SFB_2 after removing the plane wave solution, respectively. The space trajectories of the evolution in the Argand diagram for SFB_2 can be found in [Akhmediev and Ankiewicz, 1997]. For time trajectories, the evolution in the Argand diagram for SFB_2 shows a different pattern than for SFB_1. Instead of

a collection of straight lines, it is a collection of curves. Figure 5.7 shows the time trajectories in the Argand diagram of SFB_2 for $\tilde{\nu}_2 = \frac{1}{2}$.

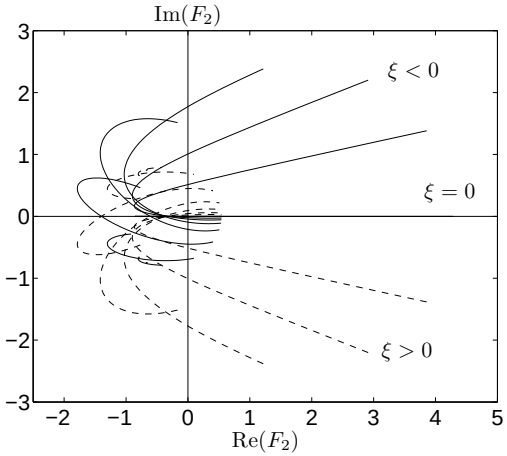

Figure 5.7: The dynamic evolution of SFB_2 parameterized in time at different positions for $\tilde{\nu}_2 = \frac{1}{2}$. At $\xi = 0$, the curve lies on the real axis; solid curves indicate $\xi < 0$; and dashed curves indicate $\xi > 0$.

5.3.4 Phase plane representation

In this subsection, we investigate a dynamic property of SFB_2, namely the envelope signal in the phase plane. At the extreme position SFB_2 is a real-valued function. We study the extreme envelope by plotting the corresponding phase curves in a phase plane. Figure 5.8 shows phase plots of SFB_2 extreme envelope for different values of $\tilde{\nu}_2$. The horizontal axis denotes twice the extreme envelope $2F_2(t;\nu_2)$ and the vertical axis denotes twice the derivative of the extreme envelope $2F'(t;\nu_2)$. For increasing time, the motion along the phase curve is in clockwise direction.

5.4 Amplitude spectrum evolution

In the preceding sections we have considered the characteristics and properties of SFB_2 in the time domain. In this section, we study the corresponding characteristics in the frequency domain. The changes of the spectrum of a wave signal during the evolution reflects the changes of the signal itself during downstream evolution. The SFB_2 spectrum has two pairs of sidebands at the initial state. During the evolution, the spectrum develops into more pairs of sidebands and eventually returns again to the initial state. This energy distribution and recollection from and to the central frequency is caused by the nonlinear effects of the modulational instability, which is also observed in SFB_1.

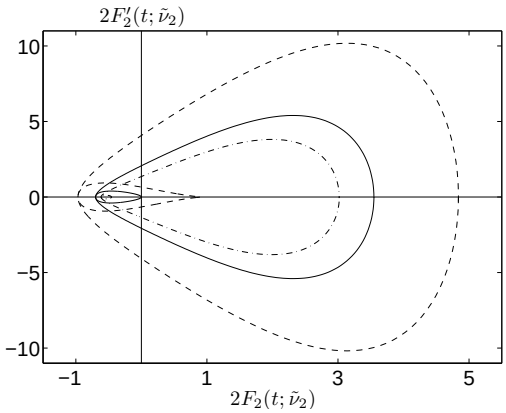

Figure 5.8: Plots of phase curves in the phase plane SFB_2 at the extreme position. The curves correspond to different values of $\tilde{\nu}_2$: $\tilde{\nu}_2 = \frac{1}{4}$ (dashed), $\tilde{\nu}_2 = \tilde{\nu}_2^*$ (solid) and $\tilde{\nu}_2 = 0.7$ (dash-dotted). Note that for each value of $\tilde{\nu}_2$, the phase plot crosses $F_2 = 0$, and for $\tilde{\nu}_2 < \tilde{\nu}_2^*$ it crosses this axis twice, corresponding to one and two pairs of phase singularities.

For SFB_1, the amplitude spectrum corresponding to the first sideband always decays more slowly than the second sideband for $\xi \to \pm\infty$. However, for SFB_2, this is not always the case due to the two growth rates. Depending on the modulation frequency $\tilde{\nu}_2$, which in turns gives different growth rate ratio, the first sideband decays faster for $\xi \to \pm\infty$ if $\tilde{\nu}_2^* < \tilde{\nu}_2 < \sqrt{1/2}$.

We have been able to derive the spectrum corresponding of SFB_1 as presented in Appendix B on page 127. Deriving an exact expression for the spectrum of SFB_2 is complicated. However, the corresponding absolute amplitude spectrum can be calculated numerically. This spectrum contains an integral expression and the numerical approximation to this integral is calculated by applying the trapezoidal rule. Figure 5.9 shows the plots of this absolute amplitude spectrum for four different values of the modulation frequency $\tilde{\nu}_2$. The different behaviour between the first sideband and the second sideband is caused by the different ratio of the growth rates.

For $0 < \tilde{\nu}_2 < \sqrt{2/5}$, the first growth rate has a lower value than the second one, $\sigma_1 < \sigma_2$. Consequently, the first sideband dominates the second sideband if the position far enough from the extreme position. For $\tilde{\nu}_2 = \sqrt{2/5}$, both growth rates have the same value, $\sigma_1 = \sigma_2$, and therefore both amplitude spectra have the same growth and decay rates when $\xi \to \pm\infty$. But for $\sqrt{2/5} < \tilde{\nu}_2 < \sqrt{1/2}$, the first growth rate is larger than the second one, $\sigma_1 > \sigma_2$. Consequently, the first sideband is dominated by the second sideband for $\xi \to \pm\infty$, but as they evolve toward the extreme position, the first sideband takes over and starts to dominate the second sideband.

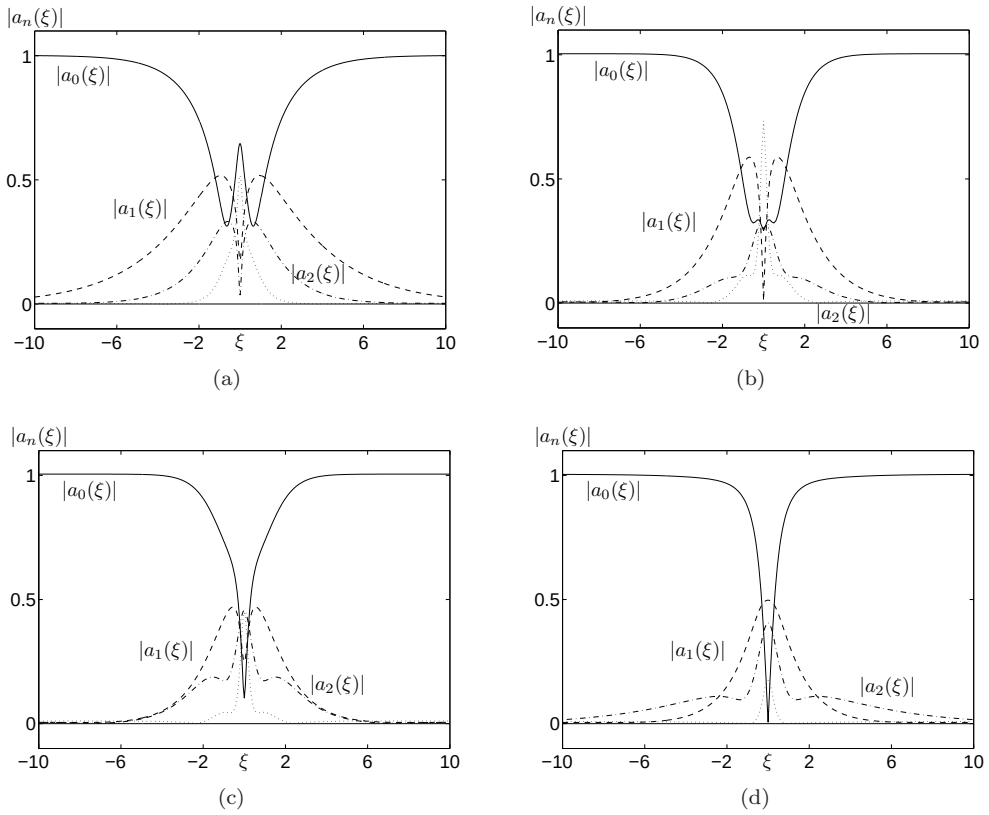

Figure 5.9: Plots of the absolute amplitude spectrum SFB_2 corresponding to the central frequency, the first sideband, and the second sideband. The plots are given for different values of modulation frequency $\tilde{\nu}_2$: (a) $\tilde{\nu}_2 = 1/4$, (b) $\tilde{\nu}_2 = 1/2$, (c) $\tilde{\nu}_2 = \sqrt{2/5}$, and (d) $\tilde{\nu}_2 = 0.7$.

5.5 Conclusions and remarks

In this chapter we studied some characteristics of higher order waves on finite background, particularly the SFB_2 solution of the NLS equation that describes the modulational instability with two pairs of initial sidebands. We also made some comparison with SFB_1 that has been discussed extensively in Chapter 3. Since the initial evolution of SFB_2 has two different modulation wavelengths, an interaction of two wave groups takes place as they propagate downstream, see Figure 5.4. Due to this wave group interaction, we observed that SFB_2 can have a higher amplitude amplification than SFB_1, up to a maximum factor of 5. This factor depends strongly on the modulation frequency and an explicit expression between amplitude amplification factors of SFB_1 and SFB_2 has been presented.

The corresponding physical wave field of SFB_2 shows an interesting pattern of wavefront dislocation. Depending on the value of modulation frequency, either one pair or two pairs of wavefront dislocations in one modulation period are observed. For $0 < \tilde{\nu}_2 < \tilde{\nu}_2^*$, we have two pairs of wavefront dislocations, while for $\tilde{\nu}_2^* < \tilde{\nu}_2 < \sqrt{1/2}$, only one pair of wavefront dislocations is observed, where $\tilde{\nu}_2^* = \frac{1}{6}\sqrt{8\sqrt{10} - 10}$. Wavefront dislocation occurs at the extreme position $x = 0$ and periodically in time. In fact at these instances, the corresponding amplitude of the SFB_2 wave field vanishes and the corresponding phase becomes singular, the phase singularity. Additionally, the Chu-Mei quotient becomes unbounded, as shown by the dispersion plot in Figure 5.6, when the local wavenumber and the local frequency become unbounded.

We also mentioned that the asymptotic behaviour for $\xi \to \pm\infty$ and the amplitude spectrum evolution of SFB_2 depend on the growth rate ratio, which is determined by the modulation frequency ν_2. Some illustrative plots are presented in Figure 5.9. We also observed that during the spectrum evolution, the energy from the central frequency is distributed into its sidebands and collected again to the initial state. This process is similar as the extreme wave formation from a single modulated wave and how that returns to its initial condition.

References

[Ablowitz and Herbst, 1990] M. J. Ablowitz and B. M. Herbst. On homoclinic structure and numerically induced chaos for the nonlinear Schrödinger equation. *SIAM J. Appl. Math.* **50**(2): 339–351, 1990.

[Akhmediev et al., 1985] N. N. Akhmediev, V. M. Eleonskiĭ, and N. E. Kulagin. Generation of periodic trains of picosecond pulses in an optical fiber: exact solutions. *Sov. Phys. JETP* **62**(5): 894–899, 1985.

[Akhmediev et al., 1987] N. N. Akhmediev, V. M. Eleonskiĭ, and N. E. Kulagin. First-order exact solutions of the nonlinear Schrödinger equation. *Teoret. Mat. Fiz.* **72**(2): 183–196, 1987. English translation: *Theoret. Math. Phys.* **72**(2): 809–818, 1987.

[Akhmediev and Ankiewicz, 1997] N. N. Akhmediev and A. Ankiewicz. *Solitons—Nonlinear Pulses and Beams*, volume **5** of *Optical and Quantum Electronic Series*. Chapman & Hall, first edition, 1997.

[Calini and Schober, 2002] A. Calini and C. M. Schober. Homoclinic chaos increases the likelihood of rogue wave formation. *Phys. Lett. A* **298**: 335–349, 2002.

[Matveev and Salle, 1991] V.B. Matveev and M.A. Salle. *Darboux Transformations and Solitons*. Springer-Verlag, 1991.

[Rogers and Schief, 2002] C. Rogers and W. K. Schief. *Bäcklund and Darboux Transformations: Geometry and Modern Applications in Soliton Theory*. Cambridge University Press, 2002.

Chapter 6

Experimental results on extreme wave generation

6.1 Introduction

In the previous chapters, we have discussed the theoretical aspects of extreme wave generation. As explained in the introductory chapter, the original aim of this investigation is the wish of MARIN (Maritime Research Institute Netherlands) to generate large amplitude, non-breaking waves in its wave basin. These large waves will be used for testing model ships and offshore constructions in extreme wave conditions as occur in the open oceans. In this chapter, we will discuss some results from the experiments on extreme waves that have been conducted at MARIN during the summer period of 2004.

Based on the modulational instability of a modulated wave signal that has been discussed in Chapter 2, we know theoretically that the SFB family studied in Chapter 3 (and 5) is a potentially good class of extreme waves. This chapter describes to what extent our aim to generate large waves has been achieved. We present comparisons between the experimental results from MARIN and our theoretical analysis based on the SFB. Another comparison of the experimental results and wave signals calculated by the nonlinear wave model *HUBRIS* has been presented in *Rogue Waves 2004* conference held by IFREMER in Brest, France [Huijsmans et al., 2005].

Choosing the SFB as family for generating extreme waves implies that we want to exploit modulational instability as the process to make extreme waves with the aid of natural processes. This is a highly nonlinear process, very different from pseudo-linear dispersive wave focussing, as in the linear frequency focusing wave [Longuet-Higgins, 1974; Chaplin, 1996]. From the start, it is not clear whether the asymptotic description using the NLS equation is robust enough to describe the complicated dynamic reality. In principle, higher order nonlinear effects, combined with dispersion, could

counterbalance the nonlinear amplification predicted by SFB. Robustness of the process would mean that the SFB modulational instability would survive these and other effects which are not accounted for by the NLS model. In the literature, except for our paper [Huijsmans et al., 2005], no experiments are described that relate in detail observed waves with the SFB solution. It was mentioned in [Onorato, 2004] that SFB waves were generated in a laboratory, but a precise account of the results has not been published. Personal contacts with [Onorato, 2004] revealed that only the development into large waves was observed, but that no detailed analysis was performed. It is our aim to provide such a detailed analysis of the MARIN experiments, and the description here serves as an initiation thereof.

6.2 Experimental setting

6.2.1 Wave basin aspects

The experiment is conducted at the 'high speed basin' of MARIN. This basin has dimension of 200 m long, 4 m wide and the water depth is 3.55 m. It is used for wave generation of regular and irregular waves in the longitudinal direction. The main application of this basin is for resistance, propulsion and seakeeping tests for high speed vessels. See the website of MARIN for more information about the facilities. Unidirectional waves are generated by a flap-type wavemaker at one side and the waves are absorbed at the other side by an artificial beach. The hinge of the flap-type wavemaker is at 1.27 m above the basin floor. A predefined wave board signal was given to the hydraulic wavemaker and for each experiment the stroke of the wave flap is measured. Figure 6.1 shows a simple sketch of the wave basin and the position of wave gauges that were used during the experiments.

The electronic wave gauges measure the wave signal in the vertical (z) direction. It is important to note that only point measurements at discrete positions can be obtained. There are 14 gauges in total. Except for one, all gauges are installed in the middle of the lateral (y) direction. To check the unidirectionality of the waves, one gauge is placed 1 m from the flume center line, as indicated in Figure 6.1. Two gauges are installed close to the wavemaker at $x = 10$ m in order to compare the initial stage of the wave signal evolution. Two gauges are installed around $x = 40$ m, $x = 150$ m and $x = 160$ m. Six gauges are installed around $x = 100$ m since in the initial design of the experiment this is the extreme position. However, another set of designs are proposed, to avoid initial breaking, for which the extreme position is at $x = 150$ m from the wavemaker. Because of technical reasons, the wave gauges were not replaced and the positioning of Figure 6.1 was kept. With two measurements at around both 150 m and 160 m, we expected to catch sufficient useful information on extreme wave characteristics including large non-breaking waves and phase singularities.

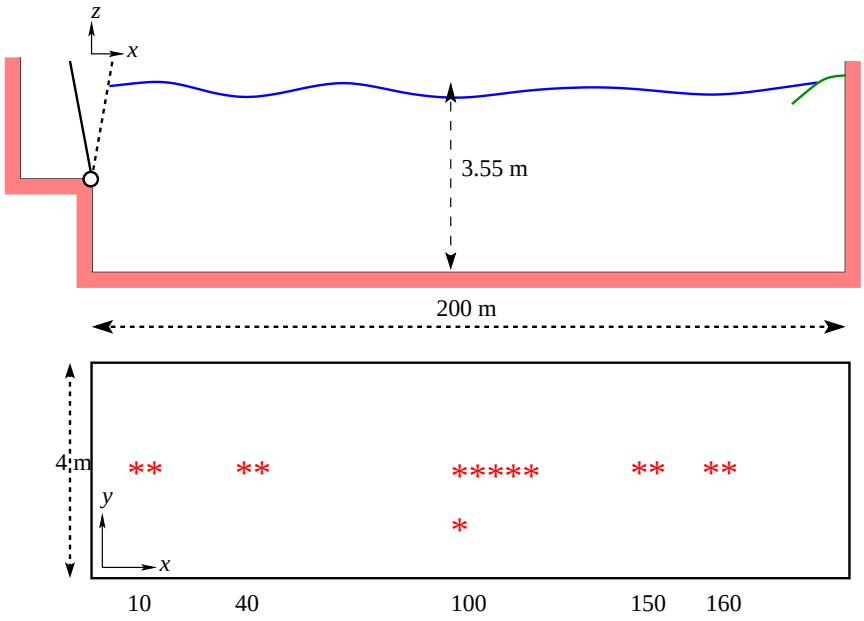

Figure 6.1: Sketch of the wave basin and the positions of the wave gauge.

6.2.2 Removing second-order effects

At each wave gauge, the actual wave height is measured with respect to time. Therefore we obtain a time signal of the measured wave height. This measured wave signal contains higher order effects. We know that the first order physical wave field constructed with the theoretical SFB wave signal that we have discussed in Chapter 3 does not possess these higher order contributions. Since we want to make both qualitative and quantitative comparison with this theoretical signal, we would like to remove the higher order effects from the measured wave signal. In the following, we describe how to remove the second order contributions, since the high frequency components of this contribution perturb the signal with rapid oscillations without essentially changing its behaviour at the carrier frequency or the modulation frequency of the wave groups. Furthermore, in order to prevent that the second-order free waves are generated by the wavemaker, we have applied second-order steering of the wavemaker. The theory of wave generation based on the fully nonlinear water wave equation with its boundary conditions including the second-order steering is presented in Appendix D.

Now we discuss in some detail the effect of second-order contributions that are generated by nature from the primary, first order waves. Let η_1 denote a measured wave signal at the position $x = x_1$ m, where x_1 is one of the positions of the wave

gauges. We assume that the measured wave signal η_1 consists of first-order (linear) harmonic waves, second-order double harmonic waves and second-order non-harmonic long waves, given as follows:

$$\eta_1(t) = A_1(t)e^{-i\omega_0 t} + \epsilon[B_1(t)e^{-2i\omega_0 t} + C_1(t)] + \text{c c}. \tag{6.1}$$

Note that A_1 in this expression is at the order of ϵ compared to A in expression (2.11). The second-order terms from the above expression appear from a generation through the nonlinear mode. This means that for a linear wave with frequency ω_0 and complex amplitude A_1, the nonlinear effect will generate frequency $2\omega_0$ and zero frequency, with complex amplitudes B_1 and C_1, respectively. These complex amplitudes will be of the order of A_1^2.

We now want to remove the second-order terms from the measured wave signal η_1 using an iteration method. After N number of iterations, we obtain a reduced signal without the second-order contribution, denoted as η_{N+1}. So, we write $\eta_{N+1}(t) = A_{N+1}(t)e^{-i\omega_0 t} + \text{c c}$. In the following, we will call the measured signal in which the second-order contribution has been removed the 'experimental signal'.

The first step is to find the complexification of the measured wave signal η_1 by applying the Hilbert transform $\mathcal{H}$ as given in (4.1) on page 70. Initially, we assume that the measured signal has only the first order harmonic contribution and therefore we can extract the complex amplitude A_1 as in (2.11) on page 16 but now with additional factor $e^{ik_0 x_1}$. Then with this A_1, the complex amplitudes of the second-order double harmonic B_1 and the second-order non-harmonic C_1 are calculated. We obtain the complexified signal η_2 by subtracting the second-order contribution from η_1. By adding the complex conjugate, we obtain the wave signal η_2. By repeating the same procedure again for N times, we now obtain the measured wave signal without the second-order contribution η_{N+1}. An illustration for removing the second-order contribution is given in Algorithm 6.2.1.

Algorithm 6.2.1 [Removing the second-order contribution from a measured signal]

$\omega_0 =$ `3.7834 rad/s`
$\eta_1 \equiv$ `measured wave signal`
`For` $j = 1$ to N

$\mathcal{H}[\eta_j]$	`the Hilbert transform of` η_j
$(\eta_j)_{\mathbb{C}} = (\eta_j + i\mathcal{H}[\eta_j])$	`the complexification of` η_j
$A_j = (\eta_j)_{\mathbb{C}}/(2e^{-i\omega_0 t})$	`the complex amplitude` A
$B_j = k_0 c A_j^2/[2\omega_0 - \Omega(2k_0)]$	`the complex amplitude` B
$C_j = c\lvert A_j\rvert^2/[\Omega'(k_0) - \Omega'(0)]$	`the complex amplitude` C
$(\eta_{j+1})_{\mathbb{C}} = (\eta_j)_{\mathbb{C}} - \epsilon(B_j e^{-2i\omega_0 t} + C_j)$	`the complexification of` η_{j+1}
$\eta_{j+1} = (\eta_{j+1})_{\mathbb{C}} + \text{c c}$	`wave signal \ 2nd order effect`

`end`

For the convergence criterium, we calculated the L^2-norm of the difference $\eta_{N+1} - \eta_N$. The iteration stops for $\|\eta_{N+1} - \eta_N\| < \delta_0$, where $\delta_0 > 0$ is a small parameter. Choosing $\delta_0 = 10^{-6}$ gives the minimum number of iterations $N = 2$. In Figure 6.2, we choose $\delta_0 = 10^{-15}$, so that the number of iterations $N = 5$ is needed to remove the second order terms and to call the resulting signal the experimental signal.

We remark that a second-order contribution gives the Stokes effect, which makes the crest steeper and the trough flatter: the second-order effect has a tendency to increase the crest and to decrease the trough. Therefore, the experimental signal which has the second order terms removed, has a lower crest and higher trough than the measured signal, see Figure 6.2.

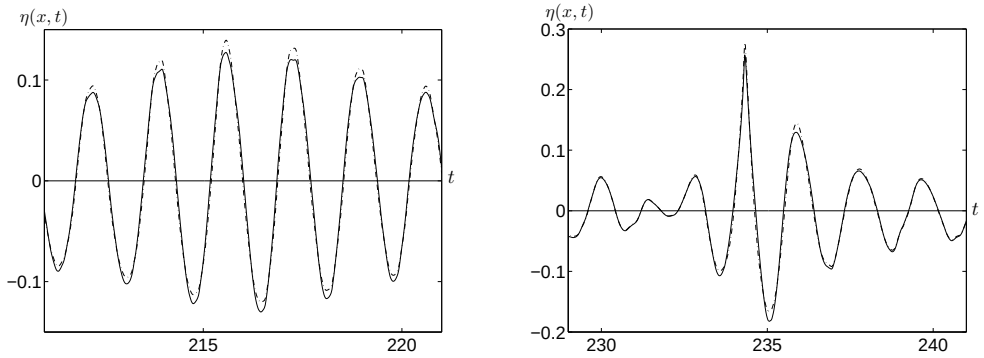

Figure 6.2: A comparison of a measured wave signal (dashed-dot) and the experimental signal (solid), that is the same wave signal without the second-order effect at 10 m (left) and at 150 m (right) from the wavemaker. In this example, the norm of the difference between two final iterations is chosen less than 10^{-15}, so it is sufficient to take the number of iteration as $N = 5$.

6.2.3 Experimental wave parameters

Once we have chosen the extreme position, we have to select a wave signal as input for the wavemaker. The selection of input is done using the information from the maximum temporal amplitude (MTA) of the SFB that has been discussed in Subsection 3.3.4. A snapshot showing the SFB wave profile, its envelope and its MTA is given in Figure 3.7 of Section 3.3. The MTA tells where the wave signal reaches an extreme condition. By taking the SFB solution backward to the wavemaker position, theoretically we know the initial wave signal that, when fed to the wavemaker, will eventually become an extreme signal at the desired position. So, the movement of the wavemaker is specified according to this theoretical SFB signal. We say 'theoretically' since we use the NLS equation as a model for wave evolution. In practice and in reality, however, the nature guides the wave evolution in a more complicated way, and many factors such as noise, generated currents and reflected waves can cause deviations from the theoretical findings.

Table 6.1: Basic parameter values for the experiments

carrier wave frequency ω_0 (rad/s)	3.7284
carrier wave period $T_c = 2\pi/\omega_0$ (sec)	1.6852
carrier wavenumber $k_0 = K(\omega_0)$ (m^{-1})	1.4171
carrier wavelength $\lambda_0 = 2\pi/k_0$ (m)	4.4337
extremal position x_{max} (m)	150
dispersive coefficient of the NLS equation β	1.013
nonlinear coefficient of the NLS equation $\gamma = \gamma_{des}$	230.2496

Table 6.1 shows the basic parameters of the carrier wave and the coefficients of the NLS equation with which the SFB solutions will be calculated. These parameters belong to one experiment that we will consider in more detail below. We designed a number of experiments with different modulation frequencies $\tilde{\nu}$ and different maximum amplitude M. Although experiments were also performed with $\tilde{\nu} = 1/\sqrt{2}$ and $\tilde{\nu} = \sqrt{3/2}$, better results were obtained for $\tilde{\nu} = 1$. Table 6.2 gives additional values of the parameters that determine the SFB solution; we will refer to this set of parameters as test A. Knowledge of the steepness at the extreme position can be used as a breaking criterium. Using breaking criteria based on the crest particle velocity exceeding the phase speed, the breaking limit of the two-dimensional Stokes wave is known to occur at a wave steepness $s = ak = 0.443$ and crest angle 120°, where a is wave amplitude and k is wavenumber [Stokes, 1880; Michell, 1893; Havelock, 1918]. Hence, based on this information from the design, it is expected that the resulting waves will not break.

Table 6.2: Design parameters for test A

maximum amplitude M (cm)	21.3000
asymptotic amplitude $2r_0$ (cm)	8.8227
initial steepness $s_0 = (2r_0)k_0$	0.1250
extremal steepness s_M	0.3019
normalized modulation frequency $\tilde{\nu}$	1.0000
modulation frequency ν (sec^{-1})	0.3114
modulation period $T = 2\pi/\nu$ (sec)	20.1800
number of waves in one modulation period N	11.9747

6.3 Qualitative comparisons

The first observations after analyzing all experimental signals can be formulated as follows: *All experimental signals show the typical development of the modulational instability as described by the SFB solution of the NLS equation. Moreover, it is observed that the carrier wave frequency and the modulation frequency are conserved very accurately during downstream evolution, keeping the same values as determined by the wavemaker motion.*

Recall again the MTA plot of the theoretical SFB as given in Figure 3.7. Although we do not have continuous data from the experiments, the experimental signals show the amplitude amplification in the first part of the downstream running waves. After that, a monotone decrease is observed. Therefore, the qualitative characteristic shape of the MTA is a robust phenomenon. Figure 6.3 shows the experimental signals from test A at several positions from the wavemaker.

6.3.1 Symmetry property

In Figure 3.8 of Section 3.4, we have seen that an SFB wave signal maintains a symmetric structure within one modulation period as it propagates toward the extreme position. This is not surprising since from the theoretical SFB expression (3.43) on page 46, the complex amplitude A is symmetric with respect to $\tau = 0$, namely $A(\xi, -\tau) = A(\xi, \tau)$. Furthermore, if we move with respect to the group velocity V_0, the real amplitude a of expression (3.54) on page 49 is also symmetric with respect to $t = 0$, i.e., $a(x, -t) = a(x, t)$. The term symmetry in this context refers to the envelope, which is symmetric around the middle of the modulation period. Since the ratio of ν/ω_0 generally is not an integer, the carrier wave shifts a little bit from one modulation to the other. Consequently, the maximum amplitude will differ from one wave group to another and thus the signal is not really symmetric.

In contrast, however, the symmetry is lost in the experiments. We observe that the experimental wave signals show a deformed wave group structure with a steep front and a flat rear within one modulation period. This asymmetric structure is observed when the waves propagate sufficiently far from the wavemaker but before reaching the extreme position. This occurs in the region where waves experience amplitude amplification and an increase of the MTA. After the extreme position, the asymmetry becomes reversed: the experimental wave signals flatten at the front and steepen at the rear within one modulation period. Figure 6.4 shows an example of wave signal plots from test B at two different positions with asymmetric structure. Test B has design characteristics of maximum amplitude of $M = 21.30$ m and the normalized modulation frequency $\tilde{\nu} = \sqrt{3/2}$.

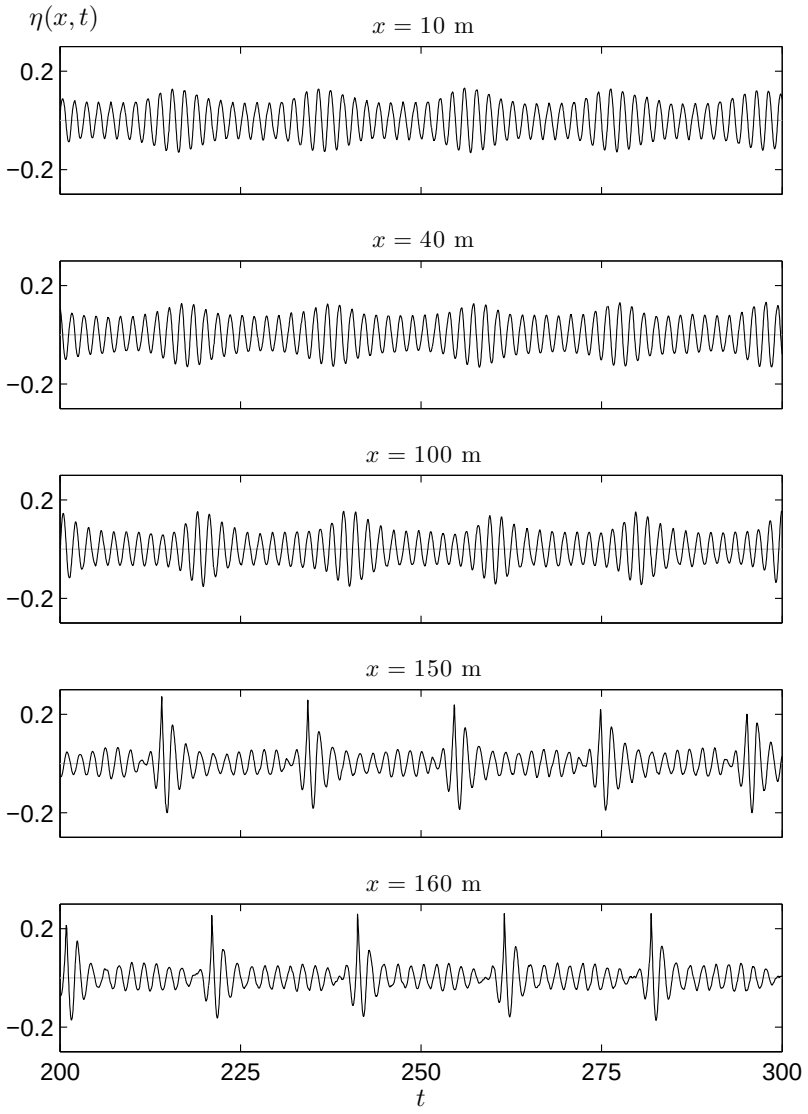

Figure 6.3: Plot of the experimental wave signal at different positions. Wave amplitude increase is observed as the waves propagate further from the wavemaker towards the extremal position which is near 160 m.

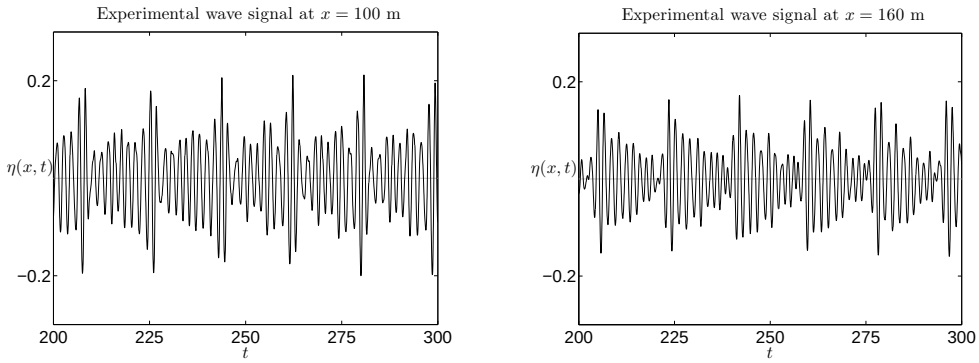

Figure 6.4: Plot of experimental wave signals from test B at two different positions $x = 100$ m and $x = 160$ m. This plot shows two important characteristics of experimental signals: the waves in between the extremal waves are not symmetric; before the wave group has passed the extreme position, the waves in one wave group are higher immediately after the highest wave, and smaller at the rear. When the wave group has passed the extreme position the waves after the largest wave are small and larger waves are found at the rear of the wave group.

6.3.2 Argand diagram representation

We have remarked and shown in Subsection 6.3.1 above that the symmetry within one modulation period of the envelope of the experimental wave signals is lost and that asymmetry is reversed when passing the extreme position. In this subsection we describe the evolution of both theoretical and experimental wave signals in the Argand diagram (complex plane). This comparison is new and gives better understanding of the experimental signals. We have discussed in Subsection 3.4.2 that the evolution of the SFB wave signal in the Argand diagram is a set of straight lines. In fact, returning back and forth in one period along the same curve is not a robust property. Any arbitrary perturbation will deform the path from a straight line into an elliptical curve, possibly even a twisted elliptical curve. This change will disturb the symmetry of the envelope wave signals. Figure 6.5 shows a schematic perturbation of the straight lines in the Argand diagram. In this figure, the depicted plots are given near the extreme position. The clockwise rotation of the curves corresponds with increasing position. For SFB, one pair of phase singularities occur at the extreme position, when the curve lies on the real axis. For the perturbed SFB, phase singularities occur before and after the extreme position.

We now compare the complex-valued amplitudes of the SFB and the experiments without the oscillating part from the plane wave solution of the NLS equation. By writing the complex-valued amplitude of the SFB signal as in (3.1), $A(\xi,\tau) = A_0(\xi)F(\xi,\tau)$, we make plots of $F \in \mathbb{C}$ for the theoretical result in the Argand diagram. For the experimental signal, the plots are parameterized in time at several positions. For this, we take its Hilbert transform and then multiply with a complex exponential (different

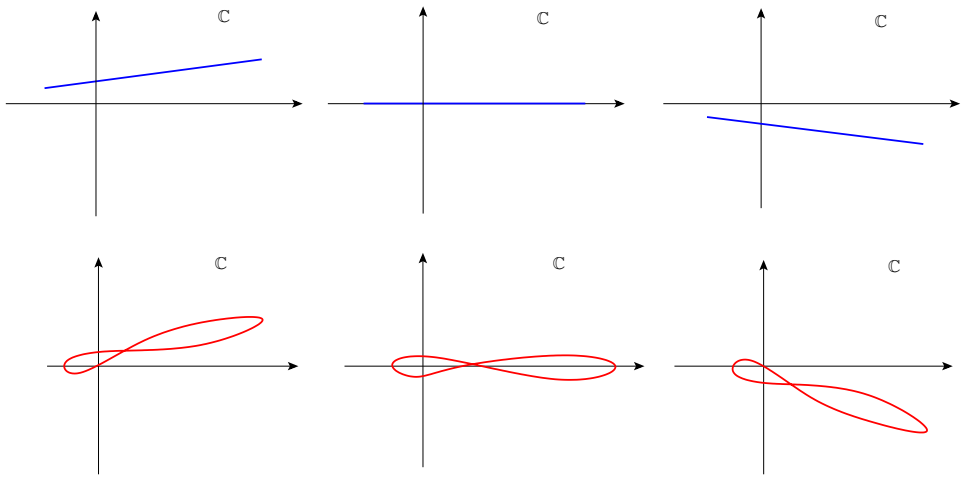

Figure 6.5: (Top) Plots of the evolution corresponding to the SFB solution in the Argand diagram before, at and after the extreme position. (Below) Qualitative sketches of a perturbed SFB around the extreme position showing twisted elliptical curves.

at different positions) with a phase to account for the increase in position. Figure 6.6 shows the evolution in the Argand diagram for both the SFB and the experiment.

For the SFB, the evolution curves are a set of straight lines. At the extreme position, the line lies exactly on the real axes and crosses the origin twice. This is the reason why we have a pair of phase singularities in one modulation period only at the extreme position. The experimental results show different behaviour of the evolution in the Argand diagram. They are not straight lines, but a set of twisted ellipse-like curves. This can be interpreted as a small perturbation of the straight lines of the SFB. As a consequence, the experiments do not show two phase singularities at one position, but rather one singularity at one position before the extreme position and one singularity at a place after the extreme position. This property is clearly related to the fact that the experimental signals are asymmetric. At one position, the singularity is immediately behind a large amplitude wave while at another position the singularity is in front of that large amplitude wave. Magnification plots of the experimental signal that show phase singularity are given in Figure 6.7.

We discuss the special wave signals of both the theoretical SFB and the experimental results at or near the extreme position, the so-called extreme signals. It should be noted that we do not know precisely the experimental extreme signal due to limitations of measurement positions. Nevertheless, since the experiments show that the waves reach high amplitude and show extreme characteristics near 150–160 m from the wavemaker, we can use the wave signals at these positions for comparison with the theoretical SFB.

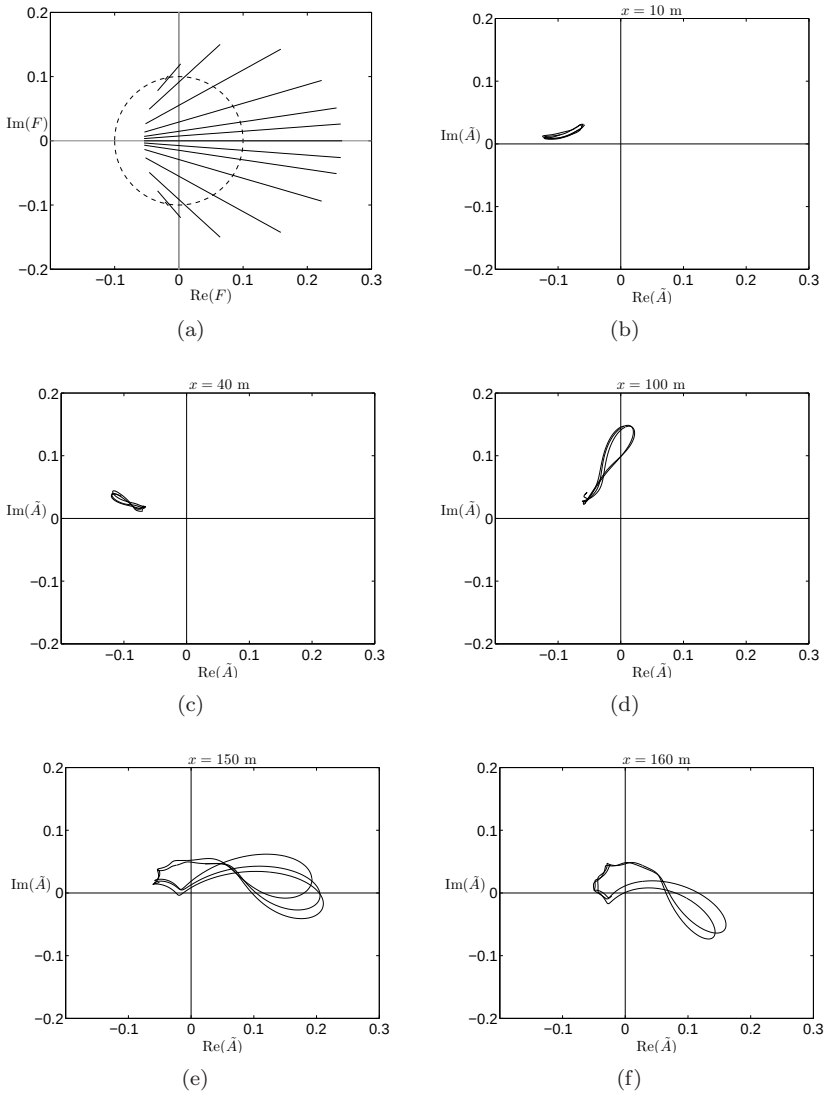

Figure 6.6: Plots of the SFB (a) and experimental complex-valued amplitudes for test A (b)–(f) in the Argand diagram after removing an oscillating part. The plots are parameterized in time at several positions. For the experiment, the following positions are the distance from the wavemaker (b) 10 m, (c) 40 m, (d) 100 m, (e) 150 m and (f) 160 m.

We have discussed in Section 3.4 the spatial evolution of the SFB to become the extreme signal. This extreme signal shows phase singularity when the amplitude van-

ishes, which occurs for $0 < \tilde{\nu} < \sqrt{3/2}$. In Section 4.3, we have seen that the physical wave field shows wavefront dislocation, where waves merge and split. We have also showed that the Chu-Mei quotient is unbounded at a singular point and this is a generic property. Therefore we expect that phase singularity also occurs in reality. With measurements at discrete positions only, we are not able to show completely that the experiments also show wavefront dislocation. However, the (almost) vanishing of the experimental signal at positions near 150 m, as in Figure 6.7, may be a strong indication of the appearance of these singularities.

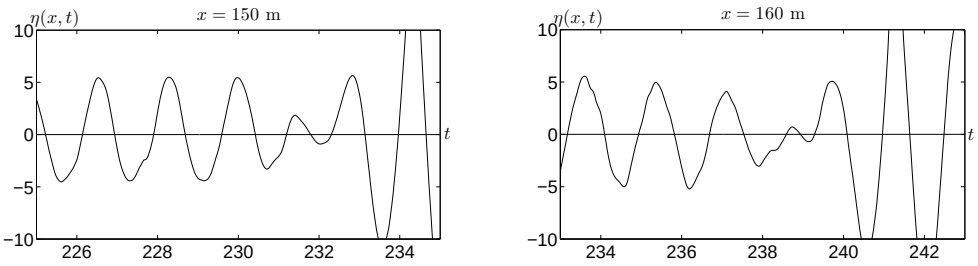

Figure 6.7: Magnification plots of the experimental signal at 150 m and 160 m from the wavemaker. The distance difference of 10 m and the group velocity of 1.32 m/s give the time difference of 7.8 sec in the occurrence of phase singularity. We observe that at certain time the wave period becomes as twice larger, indicating that we are at a phase singularity at which the local frequency is very large.

For the theoretical SFB at the extreme position there is one pair of phase singularities in each modulation period. Due to the symmetry breaking in the experiments as described above, this property is lost in the experiments. As discussed earlier in this subsection, in the Argand diagram straight lines are deformed into elliptical curves under a small perturbation. This seems to describe what can be observed in the experiments. Indeed, phase singularities are observed in the sense of vanishingly small wave amplitudes at certain instants, one singularity before and another one after the experimental extreme position. This interpretation of the experiments is a strong indication that the generated wave fields indeed follow an evolution according to the theoretical SFB solution, albeit a bit perturbed.

6.3.3 Phase plane representation

We now present phase plane representations for both the theoretical SFB and the experimental results. A phase plot is a plot of the complex-valued amplitude and its derivative parameterized by time. Since the complex-valued amplitude has real and imaginary parts, the phase plot will be a four-dimensional manifold. At the extreme position, the SFB is a real-valued function and therefore the phase plot can be shown in a plane. The experimental results, however, leads to a complexified signal that always contains a non vanishing real and imaginary part. Since we do not know precisely

the position where a phase singularity occurs in the experiments, it is rather difficult to make a comparison. However, we can still use the experimental signals close to or around the expected extreme position, which is near 150–160 m from the wavemaker. To compare the theoretical and the experimental signals, we took the absolute value of the complexified experimental signal. As a consequence, the phase plots are in the non-negative region right of the horizontal axis. As shown by the evolution curves in the Argand diagram, the experimental signals at these positions show that phase singularities are close by, since at some instant the amplitude almost vanishes.

Figure 6.8 shows the phase plane plots of the SFB and the experimental result. When looking at this plot of the experimental signal, it has to be kept in mind that calculation of the derivative of the absolute amplitude of the complexified experimental signal introduces additional inaccuracies when compared to the signal itself. Furthermore, the plot clearly shows the asymmetry within one modulation period. Despite the limited equivalence with the exact SFB representation, we like to remark that this kind of sensitive comparisons of properties of theoretical and experimental signals appears to be novel.

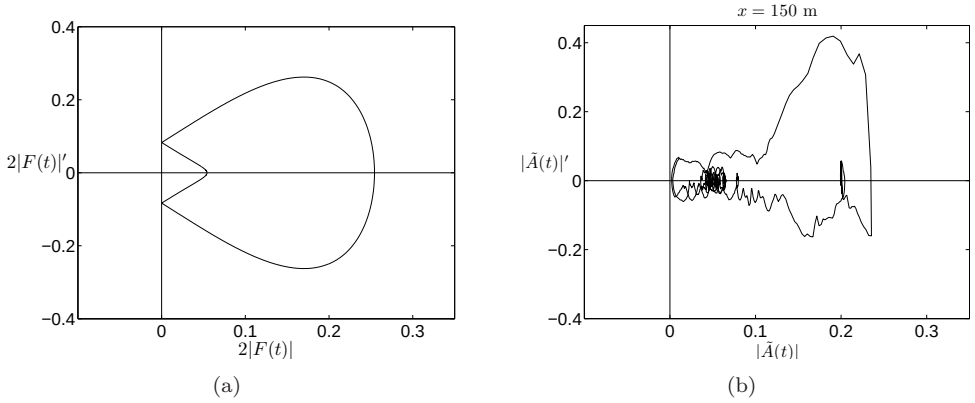

Figure 6.8: Phase plane plots of the SFB and the experimental envelope signals at and close by the extreme position. Observe that the SFB phase plot (a) is symmetric while the experimental signal phase plot (b) is asymmetric with respect to the horizontal axis.

6.4 Quantitative comparisons

In the previous section we have described that some detailed characteristic properties of the SFB solutions are observable in the experimental signals. This is a clear evidence that waves belonging to the SFB family were generated in the wave basin. Even though small perturbations developed during the propagation, most visibly the symmetry breaking, it can be concluded that the SFB family composes a robust class of surface

wave fields when it concerns the gradual formation of wave groups that increase in amplitude when running towards the extreme position, and decrease afterwards. Above we made mainly qualitative comparisons between the theoretical SFB and the experimental signals. In this section, we will give some quantitative comparisons between these two signals.

Since the theoretical SFB family possesses several parameters, it is not an obvious task to connect between the two wave signals. Indeed, in reality these parameters could change during downstream propagation in the wave basin, while for the theoretical model, these parameters are constant. Apart from this, differences between the model assumption and reality have to be taken into account. For instance, the theoretical model of the NLS equation deals with waves that propagate unidirectionally. In reality however, there is an effect that waves reflect at the artificial beach. We assume that the effect of wave reflection is small and negligible. To make a quantitative comparison between the theoretical SFB and the experimental results, we have to find an SFB wave signal that resembles the experimental signal for the whole evolution.

The comparisons presented in this section are based on choosing reasonable parameters which give a good agreement between the theoretical and the experimental signals. As mentioned already in the introduction of this chapter, we observed that the experimental signals maintain within experimental accuracy the values of the carrier wave frequency ω_0 and the modulation frequency ν. Then there remain three basic parameters corresponding to the SFB family: the asymptotic amplitude $2r_0$, the maximum amplitude M and the extreme position $x_{\max}$. By taking the origin of the wavemaker position as the origin of the x-axis, the physical wave field is denoted to be dependent on those parameters as $\eta_{SFB}(r_0, M, x_{\max})(x,t)$. The MTA turns out to be a very useful and simple way to obtain a good view about the dependence on these parameters. This investigation is novel and contributes in understanding when choosing parameters for the experiments.

6.4.1 Sensitivity of MTA for parameter changes

We consider the SFB solutions with parameter values close to these of the experimental result and design. In this subsection, we investigate the sensitivity of the MTA by allowing one parameter to change but fixing the others. The wavemaker position is at $x = 0$ and since the closest measurement is at 10 m from the wavemaker, we will consider the MTA at this position. As an MTA0 reference, we take the SFB wave signal with $M = 25$ cm, $\tilde{\nu} \approx 0.9$ and the extreme position $x_{\max} = 150$ m from the wavemaker. The corresponding parameter related to the asymptotic amplitude is $r_0 = 4.9118$ cm and we denote this parameter as $r_{0\text{ref}}$. Earlier, test A has design characteristics of $M = 21.3$ cm and $\tilde{\nu} = 1$. Since we want to keep the modulation frequency ν fixed, increase in M means decrease in $\tilde{\nu}$. The corresponding parameter related to the asymptotic amplitude for test A is given by $r_0 = 4.4114$ cm, see Table 6.2.

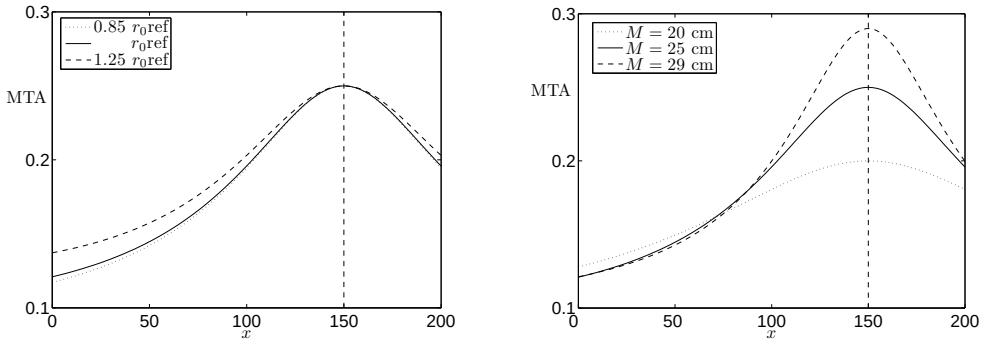

(a) For fixed M (b) For fixed r_0

Figure 6.9: Plots of the MTA of the SFB wave signal by allowing one parameter to change and fixing the others. In all cases the extreme position is kept at 150 m. (a) MTA plots for different values of $r_0 = 0.85\, r_{0\text{ref}}$, $r_{0\text{ref}}$ and $1.25\, r_{0\text{ref}}$ for fixed $M = 25$ cm. (b) MTA plots for different values of M, $M = 20, 25$, and 29 cm for fixed $r_0 = r_{0\text{ref}} = 4.9118$ cm.

The MTA plots are presented for restricted values of the amplitude since we are interested in a normalized modulation frequency that lies within the interval where the SFB shows wavefront dislocation, $0 < \tilde{\nu} < \sqrt{3/2}$. In fact, the experimental design was also restricted to this interval of modulation frequencies. We investigate which parameters give a significant change to the wave evolution.

Figure 6.9 shows the MTA plots for different r_0 at given M and vice versa for the fixed extreme position $x_{\max} = 150$ m. The MTA that has parameters $M = 25$ cm and $r_{0\text{ref}}$ is now the MTA reference, denoted as MTA_{ref}. From Figure 6.9 we observe that for different parameters r_0 or M, the maximum amplitude at 10 m from the wavemaker has different values. From Figure 6.9(a), we observe that for fixed M, the maximum wave amplitude at 10 m from the wavemaker for different r_0 ranges from 12.08 cm (for $0.85\, r_{0\text{ref}}$) to almost 14 cm (for $1.25\, r_{0\text{ref}}$). Figure 6.9(b) shows MTA plots for different M with fixed r_0. In this plot, we present the lowest $M = 20$ cm, the MTA_{ref} with $M = 25$ cm and the highest $M = 29$ cm. The maximum wave amplitude at 10 m from the wavemaker ranges from 12.34 cm, which corresponds to $M = 27$ cm (not shown in the plot) to 13.14 cm, which corresponds to $M = 20$ cm. In this case, the highest $M = 29$ cm does not give the lowest initial amplitude but the lowest M gives the highest initial amplitude. If we require that all the MTA curves have the same maximum wave amplitude with MTA_{ref} at 10 m from the wavemaker, we have to shift either to the left or to the right. It should be noted that requiring the maximum wave amplitude at 10 m from the wavemaker to be equal does not mean that the amplitude at the wavemaker itself is equal. As a consequence, the extreme position that is initially at 150 m from the wavemaker will be shifted as well. Figure 6.10 shows the shifted MTA curves for different r_0 at given M and vice versa.

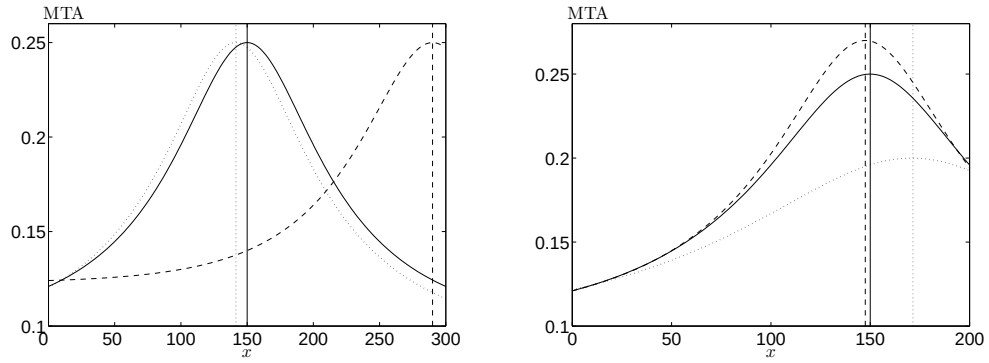

(a) For fixed M (b) For fixed r_0

Figure 6.10: Plots of the MTA after shifting the curves such that the maximum amplitude at 10 m from the wavemaker is equal: (a) for different values of r_0: $0.85\, r_{0\text{ref}}$ (dotted), $r_{0\text{ref}}$ (solid) and $1.25\, r_{0\text{ref}}$ (dashed) for given $M = 25$ cm. (b) for different values of M: 20 cm (dotted), 25 cm (solid) and 27 cm (dashed) for given $r_0 = r_{0\text{ref}}$.

From both cases, changing either r_0 or M, we observe that the extreme position is shifted from the initial reference at 150 m from the wavemaker. However, changes in r_0 give more significant shifts at the extreme position than changes in M. For changes in r_0, the range of possible extreme positions is almost 150 m. For changes in M, this range is less than 25 m. Therefore, this result indicates that the actual extreme position depends quite sensitive on the parameters, and in particular more sensitive on parameter r_0 than on the maximum amplitude M.

6.4.2 Comparisons of the SFB and experimental signals

Firstly, we compare the theoretical SFB signal based on the initial design with the corresponding result of experimental signal (test A). The design parameters read: carrier wave frequency $\omega_0 = 3.7284$ rad/s, normalized modulation frequency $\tilde{\nu} = 1$, modulation period $T = 20.18$ sec, maximum amplitude $M = 21.3$ cm, $r_0 = 4.4114$ cm and extreme position $x_{\max} = 150$ m. Figure 6.11 shows the comparison at two different positions: at 10 m and at 150 m from the wavemaker. The plots show that the initial signals do not have a good agreement since the experimental signal has larger amplitude between 0.5–1.5 cm. After downstream evolution, it is no surprise that there exists no good agreement at all between the theoretical SFB and the experimental signals. The experimental signal shows larger amplitude than the SFB signal with $M = 21.3$ cm. The initial maximum amplitude at 10 m from the wavemaker for the SFB signal is

12.41 m. Therefore the practical amplitude amplification factor for this SFB is 1.72.*

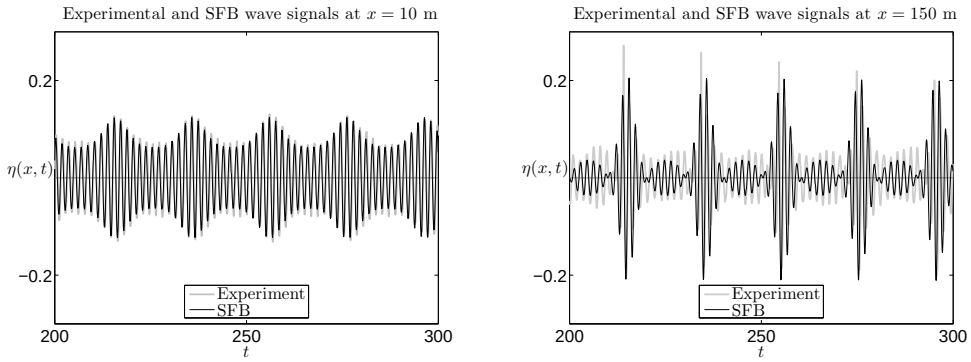

Figure 6.11: Plot of an SFB and the experimental signals at $x = 10$ m (a) and $x = 150$ m (b). The SFB signal plot is based on the design with maximum amplitude $M = 21.30$ cm and $x_{\max} = 150$ m.

We conclude that the experiment seems to produce waves with larger amplitude than the initial design. Therefore we will compare the experimental signal with another SFB signal with larger maximum amplitude M. We choose $M = 25$ cm with extreme position at 150 m from the wavemaker. Since we want to keep a fixed modulation period, choosing $M = 25$ cm gives a different normalized modulation frequency, now $\tilde{\nu} \approx 0.9$ and $r_0 = 4.9118$ cm. This SFB signal has a maximum amplitude at 10 m from the wavemaker of 12.44 cm. Therefore, the practical amplitude amplification factor for this SFB is around 2.01. Figure 6.12 shows the comparison of downstream evolution between the experimental signal from test A and the SFB signal with $M = 25$ cm and $x_{\max} = 150$ m from the wavemaker. This comparison shows much better agreement than the previous case, although at 100 m from the wavemaker the experimental signal has larger amplitude than the SFB signal at certain time interval and smaller amplitude than the SFB signal at another time interval. The choice of $M = 25$ cm (found by choosing various values in a small region around this value) is not a bad choice after all since the experimental signal has reasonable comparison in maximum amplitude to the SFB signal at both 150 m and 160 m from the wavemaker.

We already remarked earlier the fact that the experimental signal shows asymmetric structure after downstream evolution, while we know that the theoretical SFB signal always maintains the symmetry structure during the evolution. Despite this difference between the two signals, we can conclude the following facts. First, the experimental

*The practical amplitude amplification factor in this chapter is defined as the ratio of the maximum amplitude at the extreme position and the maximum amplitude at 10 m from the wavemaker.

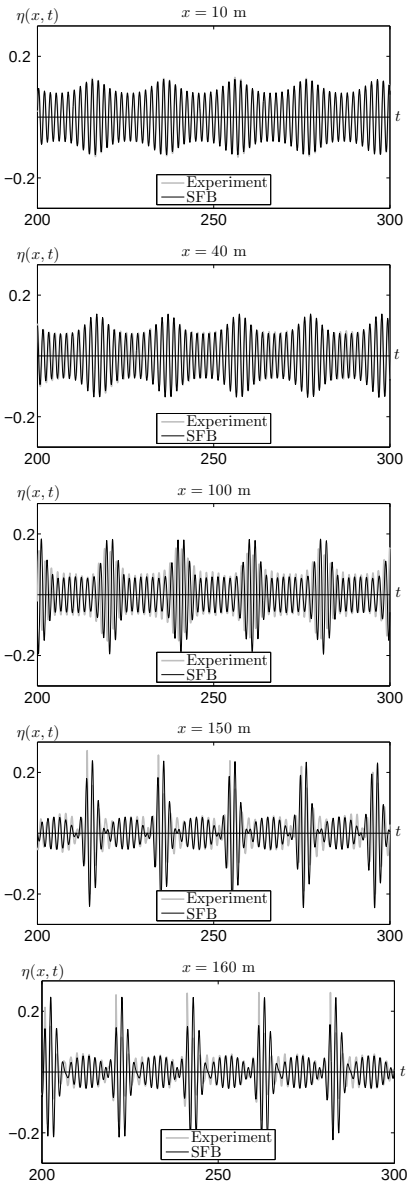

Figure 6.12: Plot of an SFB and the experimental signals (test A) at $x = 10$ m, $x = 40$ m, $x = 100$ m, $x = 150$ m and $x = 160$ m. The SFB wave signal has maximum amplitude $M = 25$ cm and $x_{\max} = 150$ m from the wavemaker.

signal still has good agreement with the theoretical SFB signal. The experimental design predicts very well where the experimental extreme position is. Although it is not precise, from the time signals we can conclude that this extreme position is not too far from 150 m or 160 m from the wavemaker. This can also be concluded from the experimental signal that shows clearly the occurrence of phase singularity close to these positions, which is according to the properties of the SFB family occurs for $0 < \tilde{\nu} < \sqrt{3/2}$. The fact that the experimental wave signal produces waves with slightly larger amplitude far away from the wavemaker may be due to higher order effects.

6.4.3 Variations in a model parameter

In the preceding subsections we have shown the sensitivity of the theoretical SFB signal for changes in the parameters of the SFB: r_0, M and $x_{\max}$, and we compared members of this family with the experimental signal.

Of course, the SFB family, consisting of solutions of the NLS equation, depends on the precise form of this equation, i.e. on the parameters in this equation. There are two essential parameters, the parameter β which is the group velocity parameter, and the coefficient γ, the nonlinear coefficient. The parameter β is well defined as group velocity dispersion, related to the change in group velocity with wavenumber. The nonlinear parameter, however, is less well-defined, and various expressions can be found in the literature. The reason is that in the derivation of the NLS equation in Subsection 2.3.2, a choice has to be made about the third order bound long wave contribution, for which only its derivative is given in (2.22). Making a choice influences the resulting value of γ. This is related to the validity of a 'zero mass flux' assumption of the water. Although we consider the unidirectional propagation of waves, there is a significant difference between the condition in the laboratory and the condition in the open sea or near the beach. An essentially different value appears when the NLS equation is derived for sea-waves, when there is no closed basin which introduces return current. See for instance [Mei, 1983; Janssen, 2006].

Another difficulty in finding the correct value of the nonlinear coefficient of the NLS equation that really describes the nonlinear effect in nature is as follows. We denote the nonlinear coefficient γ presented in (2.25) as γ_{KdV} in the context of this chapter since it was derived from a KdV type of equation. This coefficient is obtained after applying the gauge transformation on page 17. In fact, the original nonlinear coefficient γ is the one before the gauge transformation is applied to the NLS equation. This coefficient now depends on the position and the time, and is explicitly given by

$$\gamma(\xi,\tau) = \gamma_{\mathrm{KdV}} + \frac{2k_0 c}{\Omega'(k_0)} \frac{\mathrm{Re}[\alpha_S(\xi)]}{|A(\xi,\tau)|^2}. \tag{6.2}$$

It is inconvenient for designing the experiments that this nonlinear coefficient is not constant. That is why we take a constant value for the design value of this nonlinear coefficient, as we will see in the following paragraph. Although the value we used for

the design and comparison seems to be the correct one, as we shall indicate below, it seems worthwhile to investigate the dependence on this parameter also. This will be done in this subsection. We remark in addition that this coefficient, although it is in front of the nonlinear term in the NLS equation, depends strongly on dispersive contributions in the nonlinearity in the full (exact) equations, and therefore also on the nonlinear dispersion relation (2.32); the poor modelling of the dispersion in these nonlinear terms causes the problems and the different results that can be found in the literature.

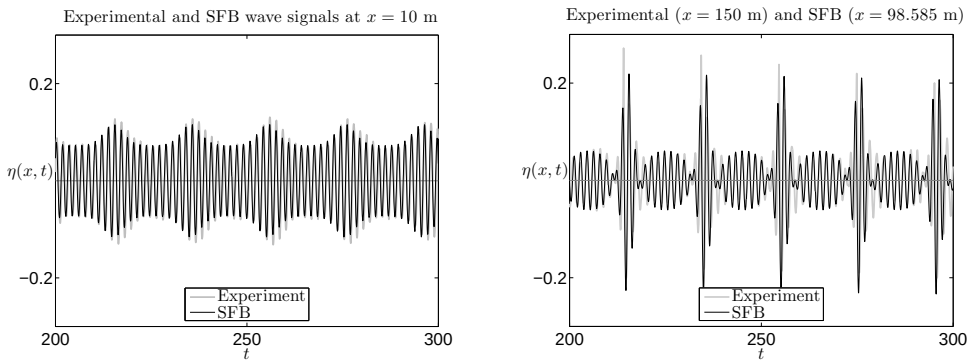

Figure 6.13: Plot of the SFB signal and the experimental signal at $x = 10$ m (a) and at the extreme position (b). With $\gamma = \gamma_{\text{DO}}$ and fixing the asymptotic amplitude $2r_0$, the SFB wave signal now reaches an extreme at $x_{\max} = 98.585$ m with maximum amplitude $M = 23.734$ cm.

Next, we discuss how changes of the nonlinear coefficient of the NLS equation γ influence the SFB signal, and in particular the extreme position $x_{\max}$. The SFB in the previous comparisons has the design value of γ, denoted as γ_{des} explicitly given by

$$\gamma_{\text{des}} = \gamma_{\text{KdV}} + \frac{2k_0^2}{\omega_0 V_0}, \tag{6.3}$$

where γ_{KdV} is the nonlinear coefficient based on derivation from the KdV equation with exact dispersion relation given in Section 2.3. An explicit expression of γ_{KdV} is given by (2.25). For $\omega_0 = 3.7284$ rad/s, $\gamma_{\text{des}} = 230.2496$.

Another value of this nonlinear coefficient has been proposed, and will be denoted here as γ_{DO}. This value of γ takes into account the presence of the current after wave generation. An explicit expression of this coefficient can be found in [Dingemans and Otta, 2001; Klopman, 2005; Huijsmans et al., 2005] and is given by:

$$\gamma_{\text{DO}} = \frac{\gamma_1(k_0) + k_0\alpha_U + \lambda(k_0)\alpha_\zeta}{V_0} \tag{6.4}$$

where

$$\gamma_1(k_0) = k_0^2\omega_0\frac{9\tanh^4 k_0 - 10\tanh^2 k_0 + 9}{4\tanh^4 k_0} \tag{6.5}$$

$$\lambda(k_0) = \frac{1}{2}k_0^2\frac{1-\tanh^2 k_0}{\omega_0} \tag{6.6}$$

$$\alpha_\zeta = -\frac{1}{\Omega(k_0)}\frac{4k_0V_0-\omega_0}{[\Omega'(0)]^2 - V_0^2} \tag{6.7}$$

$$\alpha_U = \alpha_\zeta V_0 - \frac{2k_0}{\omega_0}. \tag{6.8}$$

For given $\omega_0 = 3.7834$ rad/s, the value is found to be $\gamma_{\text{DO}} = 402.4946$ which, when compared to γ_{des}, leads to an almost two times larger value: $\gamma_{\text{DO}} \approx 1.75\gamma_{\text{des}}$.

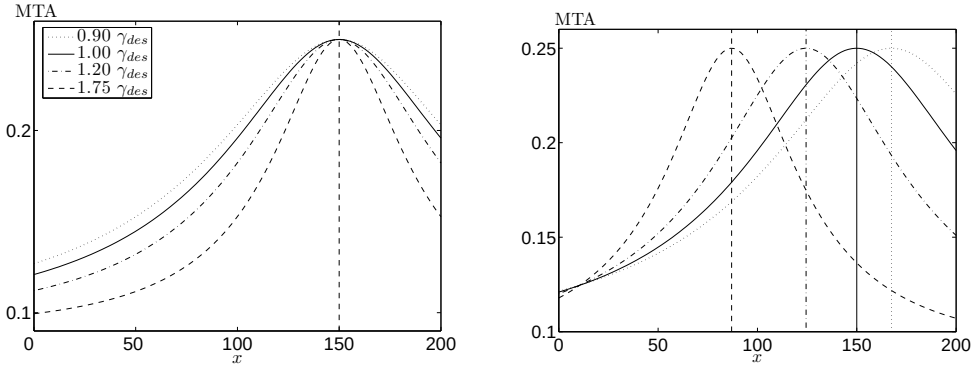

Figure 6.14: (a) Plot of the MTA corresponding to the theoretical SFB signal with $M = 25$ cm for different values of γ_{des}. (b) Plot of the shifted MTA curves such that the maximum amplitude at 10 m from the wavemaker is equal for different values of γ: $0.9\,\gamma_{\text{des}}$ (dotted), γ_{des} (solid), $1.2\,\gamma_{\text{des}}$ (dot-dashed) and $1.75\,\gamma_{\text{des}}$ (dashed).

We will now compare the experimental signal with the theoretical SFB signal for $\gamma = \gamma_{\text{DO}}$. We take the asymptotic amplitude $2r_0$ to be fixed, and allow the maximum amplitude M and the extreme position $x_{\max}$ to change. It is found that the normalized modulation frequency now becomes $\tilde{\nu} = 0.756$, the maximum amplitude $M = 23.734$ cm and the extreme position $x_{\max} = 98.585$ m from the wavemaker. The maximum amplitude of the initial SFB signal at 10 m from the wavemaker is 11.63 cm and therefore the practical amplitude amplification factor is around 2.04. Figure 6.13 shows the comparison between the theoretical SFB for $\gamma = \gamma_{\text{DO}}$ and the experimental signals at 10 m and at 150 m from the wavemaker for the experimental signal and at $x_{\max}$ for the SFB signal. The comparison at 10 m from the wavemaker

does not show a good agreement between the two signals since the experimental signal has larger amplitude up to 1.5 cm. After downstream evolution, both signals do not have a good agreement either, since the theoretical SFB signal reaches its extreme position at 98.585 m from the wavemaker, while the experimental signal reaches its largest amplitude at around 150 m or 160 m from the wavemaker. Based on the fact that the extreme position is shifted about 50 m to 60 m, it is unlikely that γ_{DO} is the correct nonlinear coefficient for the experiments since it does not describe accurately the experiments in the wave basin.

In order to get a better understanding how the nonlinear coefficient γ influences the extreme position, we look at the corresponding MTA plots for fixed parameters except the value of γ. Figure 6.14(a) shows the MTA plot corresponding to the SFB by allowing the nonlinear coefficient γ to change. The solid curve that corresponds with $\gamma = \gamma_{\text{des}}$ is regarded as MTA_{ref}. It can be observed that for a fixed maximum amplitude M, the maximum amplitude close to the wavemaker changes according to the value of γ. Figure 6.14(b) shows the plot of the same MTA after shifting such that the maximum wave amplitude at 10 m from the wavemaker is equal to MTA_{ref}. We observe that the extreme position is shifted significantly, particularly for a factor difference in γ of 75%. This indicates that the value of the nonlinear coefficient γ plays an important role in designing the experiments on extreme wave generation. Therefore, the correct value of γ deserves more attention in the future research especially to design experiments using the theoretical SFB family.

6.5 Conclusions and remarks

In this chapter, we presented experimental results on extreme wave generation based on the theoretical SFB that has been conducted at the high speed basin of MARIN. After removing the second-order contribution from the measured signal, we described both qualitative and quantitative comparisons between the theoretical and the experimental signals. It should be noted that all experimental results show amplitude increase according to the Benjamin-Feir instability of the SFB solution of the NLS equation. We also observed that both the carrier wave frequency and the modulation period are conserved during the propagation in the wave basin. A significant difference is that the experimental wave signal does not preserve the symmetry structure as the theoretical SFB does.

We also observed from the evolution in the Argand diagram that the experimental signal resembles qualitatively the perturbed SFB. The theoretical SFB signal has one pair of singularities within one modulation period at the extreme position. In the Argand diagram, this is indicated by the curve that lies on the real axis. The evolution curves for the experimental signal in the Argand diagram are no longer straight lines, but twisted elliptical-like curves. It implies that at the extreme position, there is no phase singularity. However, the experimental signal still has two singularities within

one modulation period, but now at two different positions close to the extreme position located between the singularity positions.

A quantitative comparison was made between the theoretical SFB and the experimental signals. We found that the MTA plot is sensitive to the changes in the parameters of the SFB. We also compared the experimental signal with a family of the theoretical SFB with chosen parameters. With the choice of $M = 25$ cm, we have reasonable comparison in maximum amplitude at both 150 and 160 m from the wavemaker.

We investigated variations in one of the two model parameters. For the NLS equation, these are the group velocity dispersion β and the nonlinear coefficient γ. The parameter β is well-defined but γ is less well-defined because we do not consider the gauge transformation in the derivation of the NLS equation carefully. Although another value of γ has been proposed in the literature, the signal comparison showed that it does not describe accurately the experiments in the wave basin: it leads to a large shift of the extreme position of more than 50 m.

Several experts in the field have suggested to implement the modified NLS equation since it contains higher order terms [Dysthe, 1979; Trulsen and Dysthe, 1996]. Further investigation on model equations, model parameters, design parameters and some qualitative aspects of extreme waves gives many opportunities for future research.

References

[Chaplin, 1996] J. R. Chaplin. On frequency-focusing unidirectional wave. *Int. J. Offshore Polar Eng.* **6**(2): 131–137, 1996.

[Dingemans and Otta, 2001] M. W. Dingemans and A. K. Otta. *Nonlinear Modulation of Water Waves*, volume **7** of *Advances in Coastal and Ocean Engineering*. World Scientific, Singapore, 2001.

[Dysthe, 1979] K. B. Dysthe. Note on a modification to the nonlinear Schrödinger equation for application to deep water waves. *Proc. Royal Soc. London A*, **369**: 105–114, 1979.

[Havelock, 1918] T. Havelock. Periodic, irrotational waves of finite height. *Proc. Roy. Soc. London*, **95A**: 38-56, 1918.

[Huijsmans et al., 2005] R. H. M. Huijsmans, G. Klopman, N. Karjanto and Andonowati. Experiments on extreme wave generation using the Soliton on Finite Background. In M. Olagnon and M. Prevosto, editors, *Rogue Waves 2004*. Proceedings of a workshop in Brest, France (October 20-22, 2004), 10 pp, 2005.

[Janssen, 2006] T. T. Janssen. *Nonlinear Surface Waves Over Topography*. PhD thesis, Department of Civil Engineering, Technical University of Delft, The Netherlands, 2006.

[Klopman, 2005] G. Klopman. Heuristic derivation of the spatial NLS equation for signalling problem in wave flumes. *Concept Report*, unpublished, University of Twente, 2005.

[Longuet-Higgins, 1974] M. S. Michell. Breaking waves–in deep and shallow water. *Proc. 10th Symp. on Naval Hydrodynamics*, pp. 597605, US Government Printing Office, Cambridge, Massachusetts, 1974.

[Mei, 1983] C. C. Mei. *The Applied Dynamics of Ocean Surface Waves*. John Wiley & Sons, New York, 1983.

[Michell, 1893] J. H. Michell. On the highest waves in water. *Philos. Mag.*, Ser. 5, **365**: 430-437, 1893.

[Onorato, 2004] M. Onorato, personal communication.

[Stokes, 1880] G. Stokes. Supplement to a paper on the theory of oscillatory waves. *Math. Phys. Papers*, **1**: 314-326, 1880.

[Trulsen and Dysthe, 1996] K. Trulsen and K. B. Dysthe. A modified nonlinear Schrödinger equation for broader bandwith gravity waves on deep water. *Wave Motion*, **24**: 281–289, 1996.

`http://www.marin.nl/`

Chapter 7

Conclusions and recommendations

We have mentioned in the introduction of this thesis that we want to contribute to understanding of the evolution and design of generation properties of large amplitude non-breaking waves, also known as extreme waves. In this thesis, we have presented both theoretical and experimental studies of modelling and generation of extreme waves. In the following, we compare our contributions to the existing knowledge on extreme water waves. In the final section, we present possible topics for future research on this subject.

7.1 Conclusions

In the literature, studies of extreme wave modelling and nonlinear wave phenomena in general, are more often based on the temporal NLS equation than on the spatial one. In this thesis we focused on the signalling problem in which the evolution of the surface wave envelope is more directly described by the spatial NLS equation than the temporal one. Both the spatial and the temporal NLS equations are derived under the assumption of a narrow-banded spectrum, and give a quadratic contribution to the linear dispersion relation. The spatial NLS equation has better dispersive properties than the temporal NLS equation. For these reasons the entire contents of this thesis is devoted to the spatial NLS equation, simply referred to as the NLS equation. Thus, the choice of the spatial NLS equation is especially relevant to extreme wave modelling in the wave basin of MARIN.

We considered several exact solutions of the NLS equation. In particular, we were interested in waves on finite background that do not vanish at infinity. The background is a plane wave, which is a uniform monochromatic wave, and an exact solution of the NLS equation. We have shown that the plane wave and the single soliton solutions are

coherent since the phases of the spectrum are constant for all frequencies. On the other hand, waves on finite background are not coherent, as we have shown in the case of the Soliton on Finite Background (SFB). Therefore, we conclude that the SFB and other non-coherent solutions are more interesting to be investigated in order to understand the dynamics of the spectrum evolution.

We presented the description of waves on finite background using the variational formulation of the displaced phase-amplitude representation. This representation seems to be novel and useful in understanding the dynamics that leads to extreme wave events. The dynamic evolution of the corresponding displaced amplitude has an analogy with the dynamics of an autonomous nonlinear oscillator in a certain effective potential energy. When the displaced-phase is restricted to be time independent, the changing of phase with position physically corresponds to a change of the wavelength of the carrier wave of the wave groups. This turns out to be the only driving force responsible for the nonlinear amplitude amplification toward extreme wave events. Remarkably, the assumption of time independent displaced phase leads to three (known) exact solutions of the NLS equation: the SFB, the Ma solution and the rational solution. Hence, the displaced phase-amplitude is a good representation for understanding the dynamics of waves on finite background.

We investigated the process that leads to amplitude amplification concerning waves with modulated initial evolution. This process is governed by the nonlinear modulational instability, also known as the Benjamin-Feir instability in the context of water waves. According to this instability, a slightly modulated wave signal with one pair of sidebands corresponding to sufficiently long modulation length will grow exponentially in space during its evolution but eventually the nonlinear effect will take over and bounds the growth. The complete evolution of the wave signal according to the NLS equation is given by the SFB. The asymptotic behaviour of the SFB wave signal is precisely the linearly modulated wave signal. In comparison to the Ma solution that has large amplitudes during its initial evolution, the SFB has moderate wave amplitudes during its initial evolution. Consequently, the SFB is a good candidate for extreme waves generation. SFB waves can reach a maximum amplification factor of three for a very long modulation wavelength (when the modulation frequency $\nu \to 0$).

We studied in detail the corresponding physical wave field of the SFB and observed interesting physical phenomena. For a sufficiently long modulation wavelength, the physical wave field shows wavefront dislocation, which is related to phase singularity and vanishing amplitude. To understand better these phenomena, we showed that unboundedness of the Chu-Mei quotient in the nonlinear dispersion relation is a generic property when the amplitude vanishes, which itself is a necessary condition for the occurrence of wavefront dislocation and phase singularity. This connection between Chu-Mei quotient and the physical phenomena of the SFB seems not been investigated in the literature. We used this observation to confirm that our experimental signals have similar properties with the theoretical SFB signal. Therefore, wavefront dislo-

cation and phase singularity are not only interesting theoretically but also important characteristics for confirming the experimental results.

We examined the evolution in the Argand diagram in order to understand the dynamics of the SFB complex amplitude and also the experimental signals. The evolution curves are straight lines centered at $(-1, 0)$ and the angle with real axis depends on the time independent displaced-phase. At the extreme position, the line lies at the real axis and crosses the origin twice during one sufficiently long modulation period. This explains why we have one pair of phase singularities/wavefront dislocations in one modulation period. A small perturbation to the SFB will deform the straight lines in the Argand diagram into twisted elliptical-like curves. As a consequence, the curves cross the origin at two different positions, and the extreme position is located in between. In addition, the symmetry structure of the SFB wave signal is not preserved anymore and the perturbed signal becomes asymmetric. Thus, the perturbed SFB signal has two phase singularities at two different positions with the extreme position is in between. So, we conclude that the occurrence of phase singularity in the SFB will always be related to the extreme position.

We performed some experimental tests on extreme wave generation using a theoretical model based on the SFB of the NLS equation. The comparisons using several mathematical concepts discussed in this thesis are new contributions to better understanding of extreme wave characteristics. From the experimental results, we conclude that all experimental signals show amplitude increases according to the modulational instability process of the SFB wave signal of the NLS equation. We observed that both the carrier wave frequency ω_0 and the modulation frequency ν are conserved very accurately during downstream evolution. This gives an indication that the SFB is a good model for extreme wave generation and the modulational instability of the NLS equation is a robust property.

Furthermore, we found out that the experimental signals have asymmetric structure, different from symmetric signals of the SFB. From the comparisons of the complex amplitudes evolution in the Argand diagram, we conclude that the experimental signals resembles qualitatively with the perturbed SFB signal mentioned earlier. This conclusion is also supported by the fact that the experimental signals have two phase singularities at two different positions and the extreme position is located in between. Therefore, although the SFB is indeed a good model, the evolution curves in the Argand diagram are not robust quantities.

We explored the concept and properties of maximum temporal amplitude (MTA), in order to know qualitatively the sensitivity of this MTA and its extreme position toward parameter changes. The MTA is very useful in experimental design for determining the exact location of the initial signal such that the extreme position occurs at the desired location. By allowing to shift several MTA curves accordingly, we found out that the corresponding extreme position is more sensitive toward changes in the asymptotic amplitude r_0 rather than in the maximum amplitude M. Similar sensitivity is also observed for the variations in the nonlinear coefficient of the NLS equation. Therefore,

if we want to have good accuracy in the precise location of the extreme position, we have to choose carefully the parameters in both the SFB and the NLS equation for the experimental design.

We also examined some theoretical aspects of higher order family of SFB solutions, in particular SFB_2. Since there is wave group interaction during downstream evolution, it is particularly interesting to investigate the dynamics of SFB_2. Several physical characteristics such as wavefront dislocation and phase singularity are also observed in SFB_2. Outstandingly, SFB_2 waves can reach a maximum amplification factor of five for a very long modulation wavelength. Therefore, SFB_2 is also a good candidate for extreme wave generation and indeed it deserves more further studies, as we will mention in the following section.

7.2 Recommendations

The following problems are recommended for future research in the field of nonlinear wave phenomena related to the work in this thesis.

- We have presented the SFB (or SFB_1 in the context of Chapter 5) in the displaced phase-amplitude representation. Using a restriction to time independent displaced-phase, the dynamics of SFB_1 at each position is given as the motion of a nonlinear autonomous oscillator in a potential energy. For SFB_2, the dynamics can possible be described as an interaction between two nonlinear oscillators. Further investigations are required to improve understanding of the characteristics of SFB_2.

- It is useful to improve the accuracy of model parameters in the NLS equation, particularly the nonlinear coefficient γ. This is important for a good comparison of other future experiments on extreme wave generation with solutions of the NLS equation. See Subsection 6.4.3 on page 115 for the variations in this nonlinear coefficient.

- Only unidirectional waves were considered here in a one dimensional physical domain. An extension to the two-dimensional domain for studying the mechanism of extreme wave generation in the context of multidirectional waves would be interesting.

Appendix A

Spectrum of the single soliton solution

In this appendix, we present the spectrum of the single soliton solution of the NLS equation as given by (2.54) on page 27. To find the spectrum evolution, we apply the Fourier transform to the solution by multiplying with $e^{-i\omega\tau}$ and integrating with respect to τ. Now it reads

$$\hat{A}(\xi,\omega) = \int_{-\infty}^{\infty} A_0(\xi)\sqrt{2}\frac{e^{-i\omega\tau}}{\cosh(\alpha\tau)}d\tau. \tag{A.1}$$

Using the fact that the integration of an odd function $\sin(\omega\tau)$ along a symmetric interval vanishes and the integration of an even function $\cos(\omega\tau)$ results twice of the integral with half-interval, we have:

$$\hat{A}(\xi,\omega) = 2\sqrt{2}A_0(\xi)\int_{-\infty}^{0} \frac{\cos(\omega\tau)}{\cosh(\alpha\tau)}d\tau. \tag{A.2}$$

The integration results to the following expression:

$$\hat{A}(\xi,\omega) = \frac{2\sqrt{2}A_0(\xi)}{\alpha^2+\omega^2}\left[(\alpha+i\omega)_2F_1\left(\frac{1}{2}\left(1-i\frac{\omega}{\alpha}\right),1;\frac{1}{2}\left(3-i\frac{\omega}{\alpha}\right);-1\right)+\mathrm{c\,c}\right], \tag{A.3}$$

where ${}_2F_1(a,b;c;z)$ is frequently known as 'the' hypergeometric function or Gauss' hypergeometric function since it is the first hypergeometric function to be studied back in the early 19$^{\text{th}}$ century [`http://mathworld.wolfram.com/HypergeometricFunction.html`]. The hypergeometric functions are solutions to the hypergeometric differential equation

$$z(1-z)\frac{d^2y}{dz^2}+[c-(a+b+1)z]\frac{dy}{dz}-aby=0. \tag{A.4}$$

Appendix A. Spectrum of the single soliton solution

A generalized hypergeometric function ${}_pF_q(a_1, a_2, \ldots, a_p; b_1, b_2, \ldots, b_q; z)$ is a function which can be defined in the form of a hypergeometric series, i.e. a series for which the ratio of successive terms can be written as

$$\frac{c_{k+1}}{c_k} = \frac{(k+a_1)(k+a_2)\ldots(k+a_p)}{(k+b_1)(k+b_2)\ldots(k+b_q)(k+1)}z. \tag{A.5}$$

For more information on this function, please consult "Hypergeometric Functions", Chapter 15 in *Handbook of Mathematical Functions with Formulas, Graphs, and Mathematical Tables*, edited by M. Abramowitz and I. A. Stegun, 9th printing. New York: Dover, pp. 555–566, 1972.

So, the spectrum of the single soliton now reads

$$\hat{A}(\xi,\omega) = \frac{2\sqrt{2}A_0(\xi)}{\alpha^2+\omega^2}\left[(\alpha+i\omega)\sum_{m=0}^{\infty}(-1)^m\frac{\alpha-i\omega}{\alpha(2m+1)-i\omega} + \mathrm{c\,c}\right]. \tag{A.6}$$

We can simplify this expression leading to (2.54), written as follows:

$$\hat{A}(\xi,\omega) = 4\alpha\sqrt{2}A_0(\xi)\sum_{m=0}^{\infty}(-1)^m\left(\frac{2m+1}{\alpha^2(2m+1)^2+\omega^2}\right). \tag{A.7}$$

Appendix B

Spectrum of the SFB

In this appendix, we will show the derivation of the spectrum corresponding to the SFB solution of the NLS equation as given by (3.69–3.70) on page 58. The expressions are presented but not derived in Chapter 3 of *Solitons–Nonlinear Pulses and Beams* by N. N. Akhmediev and A. Ankiewicz, Chapman & Hall, 1997. This appendix helps the readers who are curious with the derivation. To start with, we will show two useful trigonometric integrals and one useful trigonometric series. Later on, we will use these useful formulation to derive the spectrum formulation of the SFB.

B.1 Proof of a useful trigonometric integral

We show the first useful trigonometric integral is correct:

$$\int_0^{\pi} \frac{d\tau}{1 - a\,\cos\tau} = \frac{\pi}{\sqrt{1-a^2}}. \tag{B.1}$$

Substituting $z = \tan\left(\frac{1}{2}\tau\right)$, we now have $d\tau = 2\,\cos^2\left(\frac{1}{2}\tau\right)\,dz = 2/(1+z^2)dz$ and $\cos\tau = 2/(1+z^2) - 1$. The integral turns into

$$\int_0^{\pi} \frac{d\tau}{1 - a\,\cos\tau} = \int_0^{\infty} \frac{2\,dz}{(1-a) + (1+a)z^2}. \tag{B.2}$$

Substituting $(1+a)/(1-a)\,z^2 = \tan^2 w$, we have $\sqrt{(1+a)/(1-a)}\,dz = (1+\tan^2 w)\,dw$ and the integral becomes:

$$\int_0^{\pi} \frac{d\tau}{1 - a\,\cos\tau} = \frac{2}{\sqrt{1-a^2}} \int_0^{\pi/2} \frac{1+\tan^2 w}{1+\tan^2 w}\,dw. \tag{B.3}$$

The integral simplifies to $\pi/2$ and we obtain (B.1).

B.2 Proof of a useful trigonometric series

We show the following useful trigonometric series:

$$\sum_{n=0}^{\infty} r^n \cos(n\tau) = \frac{1}{2}\left(1 + \frac{\cos s}{1 - \sin s \cos x}\right). \tag{B.4}$$

For $|r| < 1$ and $n \in \mathbb{N}_0$, we have the following series identity:

$$\sum_{n=0}^{\infty} (re^{i\tau})^n = \frac{1}{1 - re^{i\tau}} = \frac{1 - re^{-i\tau}}{1 - 2r\cos\tau + r^2}. \tag{B.5}$$

Also, for $|r| < 1$ but $n \in \mathbb{Z} \setminus \mathbb{N}$, we have another series identity:

$$\sum_{n=-\infty}^{0} \left(\frac{1}{r}e^{i\tau}\right)^n = \frac{1}{1 - re^{-i\tau}} = \frac{1 - re^{i\tau}}{1 - 2r\cos\tau + r^2}. \tag{B.6}$$

Taking the real part of both series (B.5) and (B.6), we obtain:

$$\sum_{n=0}^{\infty} r^n \cos(n\tau) = \frac{1 - r\cos\tau}{1 - 2r\cos\tau + r^2} = \sum_{n=-\infty}^{0} \frac{1}{r^n}\cos(n\tau). \tag{B.7}$$

Now consider $n \in \mathbb{N}_0$ and substitute $r = \tan\left(\frac{1}{2}s\right)$. Multiple both the numerator and the denominator by $\cos^2\left(\frac{1}{2}s\right)$ the infinite series becomes

$$\sum_{n=0}^{\infty} r^n \cos(n\tau) = \frac{\cos^2\left(\frac{1}{2}s\right) - \frac{1}{2}\sin s \cos\tau}{1 - \sin s \cos\tau}. \tag{B.8}$$

Substituting $\cos^2\left(\frac{1}{2}s\right) = \frac{1}{2}(1 + \cos s)$, we obtain the desired useful trigonometric series (B.4).

B.3 Proof of another useful trigonometric integral

We show that the following trigonometric integral is correct:

$$\int_0^{\pi} \frac{\cos(n\tau)\,d\tau}{b - a\cos\tau} = \frac{\pi}{\sqrt{b^2 - a^2}}\left(\frac{b - \sqrt{b^2 - a^2}}{a}\right)^n, \qquad \text{for } n \in \mathbb{Z}. \tag{B.9}$$

Let

$$f_n = \int_0^{\pi} \frac{\cos(n\tau)\,dx}{b - a\cos\tau}, \tag{B.10}$$

then we have the following series

$$\sum_{n=0}^{\infty} r^n\, f_n = \int_0^{\pi} \left(\sum_{n=0}^{\infty} r^n\, \cos(n\tau) \right) \frac{d\tau}{b - a\, \cos\tau}. \tag{B.11}$$

By letting $a/b = \sin y$ and applying the trigonometric series (B.4), we obtain an integral series

$$\sum_{n=0}^{\infty} r^n\, f_n = \frac{1}{2b} \int_0^{\pi} \frac{d\tau}{1 - \sin y\, \cos\tau} + \frac{1}{2b} \int_0^{\pi} \frac{\cos s\, d\tau}{(1 - \sin y\, \cos\tau)(1 - \sin y\, \cos\tau)}. \tag{B.12}$$

The first integral of this expression can be evaluated using (B.1). After applying the partial fraction, we can also evaluate the second integral using (B.1). Thus the series (B.11) now becomes

$$\sum_{n=0}^{\infty} r^n\, f_n = \frac{\pi}{2b} \left(\frac{1}{\cos y} + \cos s \frac{\tan s - \tan y}{\sin s - \sin y} \right). \tag{B.13}$$

Let $r = \tan\left(\frac{1}{2}s\right)$, then $\sin s = 2r/(1+r^2)$, $\cos s = 1-r^2/(1+r^2)$, and $\tan s = 2r/(1-r^2)$. Substituting these relations into the series we now have

$$\sum_{n=0}^{\infty} r^n f_n = \sum_{n=0}^{\infty} r^n \frac{\pi}{b \cos y} \left(\frac{\sin y}{1 + \cos y} \right)^n. \tag{B.14}$$

For $n \in \mathbb{Z} \setminus \mathbb{N}$, the following relation holds:

$$\sum_{n=-\infty}^{0} \frac{1}{r^n}\, f_n = \sum_{n=-\infty}^{0} \frac{1}{r^n} \frac{\pi}{b} \frac{1}{\cos y} \left(\frac{1 + \cos y}{\sin y} \right)^n. \tag{B.15}$$

Therefore we have an expression for f_n

$$f_n = \frac{\pi}{b} \frac{1}{\cos y} \left(\frac{\sin y}{1 + \cos y} \right)^n, \quad \text{for } n \in \mathbb{N}_0, \tag{B.16}$$

and

$$f_n = \frac{\pi}{b} \frac{1}{\cos y} \left(\frac{1 + \cos y}{\sin y} \right)^n, \quad \text{for } n \in \mathbb{Z} \setminus \mathbb{N}. \tag{B.17}$$

Substituting back the relation $\sin y = a/b$ and $\cos y = \sqrt{b^2 - a^2}/b$, f_n then turns into:

$$f_n = \frac{\pi}{\sqrt{b^2 - a^2}} \left(\frac{b - \sqrt{b^2 - a^2}}{a} \right)^n, \quad \text{for } n \in \mathbb{N}_0 \tag{B.18}$$

and

$$f_n = \frac{\pi}{\sqrt{b^2 - a^2}} \left(\frac{b + \sqrt{b^2 - a^2}}{a} \right)^n, \quad \text{for } n \in \mathbb{Z} \setminus \mathbb{N}. \tag{B.19}$$

We can write these expressions into a single formula as follows:

$$f_n = \frac{\pi}{\sqrt{b^2 - a^2}} \left(\frac{b - \sqrt{b^2 - a^2}}{a} \right)^n, \qquad \text{for } n \in \mathbb{Z}. \tag{B.20}$$

Thus, we have showed that the second trigonometric integral is correct.

B.4 Derivation of the SFB spectrum

The spectrum is defined by the expression (3.68). Using the fact that the integrand is an even function with respect to τ, we can write the spectrum explicitly as follows:

$$a_n(\xi) = \frac{A_0(\xi)}{\pi} \left(\int_0^\pi \frac{f(\xi)\, \cos(n\tau)}{\cosh(\sigma\xi) - \sqrt{1 - \frac{1}{2}\tilde{\nu}^2}\cos\tau}\, d\tau - \int_0^\pi \cos(n\tau)\, d\tau \right), \qquad n \in \mathbb{Z}, \tag{B.21}$$

where $f(\xi) = \tilde{\nu}^2 \cosh(\sigma\xi) - \tilde{\sigma}\sinh(\sigma\xi)$. The expression $\int_0^\pi \cos(n\tau)\, d\tau$ vanishes for $n \neq 0$. Using the relation (B.9), we find the spectrum for $n \neq 0$ as given in (3.70):

$$a_n(\xi) = A_0(\xi) \frac{\tilde{\nu}^2 \cosh(\sigma\xi) - i\tilde{\sigma}\sinh(\sigma\xi)}{\sqrt{\cosh^2(\sigma\xi) - \left(1 - \frac{1}{2}\tilde{\nu}^2\right)}} \left(\frac{\cosh(\sigma\xi) - \sqrt{\cosh^2(\sigma\xi) - \left(1 - \frac{1}{2}\tilde{\nu}^2\right)}}{\sqrt{1 - \frac{1}{2}\tilde{\nu}^2}} \right)^n. \tag{B.22}$$

For $n = 0$, the integral $\int_0^\pi \cos(n\tau)\, d\tau = \pi$, and therefore the spectrum for $n = 0$ is given by

$$a_0(\xi) = A_0(\xi) \left(\frac{\tilde{\nu}^2 \cosh(\sigma\xi) - i\tilde{\sigma}\sinh(\sigma\xi)}{\sqrt{\cosh^2(\sigma\xi) - \left(1 - \frac{1}{2}\tilde{\nu}^2\right)}} - 1 \right). \tag{B.23}$$

Therefore, we have obtained the spectrum of the SFB.

Appendix C

Quantities related to SFB_2

This appendix presents explicit expressions which are related to SFB_2 discussed in Chapter 5.

C.1 Quantities related to the asymptotic behaviour

The phase difference ϕ_{20} mentioned in Subsection 5.2.2 on page 87 reads

$$\tan\phi_{20} = \frac{3\tilde{\nu}_2(2\sqrt{2-4\tilde{\nu}_2^2} - \sqrt{2-\tilde{\nu}_2^2})}{13\tilde{\nu}_2^2 - 5 + 2\sqrt{2-4\tilde{\nu}_2^2}\,\sqrt{2-\tilde{\nu}_2^2}}. \tag{C.1}$$

The complex quantities mentioned in the same subsection have rather lengthy expressions. The quantity w_{21} reads:

$$w_{21} = \rho_{21}\, e^{\,i\phi_{21}} \tag{C.2}$$

where

$$\rho_{21} = \frac{6\tilde{\nu}_2\sqrt{f_1(\tilde{\nu}_2) + f_2(\tilde{\nu}_2)\,2\sqrt{2-4\tilde{\nu}_2{}^2}\,\sqrt{2-\tilde{\nu}_2^2}}}{(4\tilde{\nu}_2^2 - 5 + 2\sqrt{2-4\tilde{\nu}_2^2}\,\sqrt{2-\tilde{\nu}_2^2})^2} \tag{C.3}$$

$$\tan\phi_{21} = \frac{4(2\tilde{\nu}_2^2-3)\sqrt{2-4\tilde{\nu}_2^2} + (9-16\tilde{\nu}_2^2)\sqrt{2-\tilde{\nu}_2^2}}{\tilde{\nu}_2(16\tilde{\nu}_2^2 - 11 + 2\sqrt{2-4\tilde{\nu}_2^2}\sqrt{2-\tilde{\nu}_2^2})} \tag{C.4}$$

and

$$f_1(\tilde{\nu}_2) = 4\tilde{\nu}_2^4(30\tilde{\nu}_2^4 - 233\tilde{\nu}_2^2 + 511) - 5(341\tilde{\nu}_2^2 - 90) \tag{C.5}$$

$$f_2(\tilde{\nu}_2) = 48\tilde{\nu}_2^6 - 217\tilde{\nu}_2^4 + 296\tilde{\nu}_2^2 - 108. \tag{C.6}$$

The quantity $\tilde{w}_{21}$ reads:

$$\tilde{w}_{21} = \tilde{\rho}_{21} e^{\,i\tilde{\phi}_{21}} \tag{C.7}$$

where

$$\tilde{\rho}_{21} = \frac{\sqrt{f_3(\tilde{\nu}_2) + f_4(\tilde{\nu}_2)\sqrt{2-\tilde{\nu}_2^2}\sqrt{2-4\tilde{\nu}_2^2}}}{3\tilde{\nu}_2^2(2-\tilde{\nu}_2^2)(1-2\tilde{\nu}_2^2)} \tag{C.8}$$

$$\tan\tilde{\phi}_{21} = \frac{3}{\tilde{\nu}_2}\frac{(2\tilde{\nu}_2^2-1)\sqrt{2-\tilde{\nu}_2^2}-(2\tilde{\nu}_2^2-5)\sqrt{2-4\tilde{\nu}_2^2}}{13-14\tilde{\nu}_2^2-7\sqrt{2-\tilde{\nu}_2^2}\sqrt{2-4\tilde{\nu}_2^2}} \tag{C.9}$$

and

$$f_3(\tilde{\nu}_2) = 106\tilde{\nu}_2^6 + 23\tilde{\nu}_2^4 - 488\tilde{\nu}_2^2 + 234, \tag{C.10}$$

$$f_4(\tilde{\nu}_2) = 62\tilde{\nu}_2^4 + 17\tilde{\nu}_2^2 - 45. \tag{C.11}$$

The quantity $\bar{w}_{21}$ reads:

$$\bar{w}_{21} = w_{21} + \tilde{w}_{21}. \tag{C.12}$$

The quantity w_{22} reads:

$$w_{22} = \rho_{22}e^{\,i\phi_{22}} \tag{C.13}$$

where

$$\rho_{22} = \frac{\sqrt{g_0(\tilde{\nu}_2)}}{(4\tilde{\nu}_2^2-5+2\sqrt{2-4\tilde{\nu}_2^2}\,\sqrt{2-\tilde{\nu}_2^2})^2} \tag{C.14}$$

$$\tan\phi_{22} = \frac{4\tilde{\nu}_2^2-5+2\sqrt{2-4\tilde{\nu}_2^2}\,\sqrt{2-\tilde{\nu}_2^2}-3\tilde{\nu}_2(\sqrt{2-4\tilde{\nu}_2^2}-\sqrt{2-\tilde{\nu}_2^2})}{\tilde{\nu}_2^2[4(\tilde{\nu}_2^2+1)+2\sqrt{2-4\tilde{\nu}_2^2}\sqrt{2-\tilde{\nu}_2^2}]} \tag{C.15}$$

and

$$g_0(\tilde{\nu}_2) = g_1(\tilde{\nu}_2) + g_2(\tilde{\nu}_2)\sqrt{2-4\tilde{\nu}_2^2}\sqrt{2-\tilde{\nu}_2^2} + g_3(\tilde{\nu}_2)\sqrt{2-4\tilde{\nu}_2^2} + g_4(\tilde{\nu}_2)\sqrt{2-\tilde{\nu}_2^2} \tag{C.16}$$

$$g_1(\tilde{\nu}_2) = -288\tilde{\nu}_2^6(8\tilde{\nu}_2^4-6\tilde{\nu}_2^2+9) + 1139\tilde{\nu}_2^4 - 44\tilde{\nu}_2^2 + 41 \tag{C.17}$$

$$g_2(\tilde{\nu}_2) = -576\tilde{\nu}_2^4(2\tilde{\nu}_2^2-1)(\tilde{\nu}_2^2+1) - (\tilde{\nu}_2^2+10) \tag{C.18}$$

$$g_3(\tilde{\nu}_2) = 18\tilde{\nu}_2(3-2\tilde{\nu}_2^2) \tag{C.19}$$

$$g_4(\tilde{\nu}_2) = 18\tilde{\nu}_2(4\tilde{\nu}_2^2-3). \tag{C.20}$$

The quantity $\tilde{w}_{22}$ reads:

$$\tilde{w}_{22} = \tilde{\rho}_{22}e^{\,i\tilde{\phi}_{22}} \tag{C.21}$$

where

$$\tilde{\rho}_{22} = \frac{9\tilde{\nu}_2^2(2-\tilde{\nu}_2^2)\sqrt{g_5(\tilde{\nu}_2)+g_6(\tilde{\nu}_2)\sqrt{2-\tilde{\nu}_2^2}\sqrt{2-4\tilde{\nu}_2^2}}}{(4\tilde{\nu}_2^2-5+2\sqrt{2-\tilde{\nu}_2^2}\sqrt{2-4\tilde{\nu}_2^2})^3} \tag{C.22}$$

$$\tan(\tilde{\phi}_{22}) = 2\tilde{\nu}_2\sqrt{2-4\tilde{\nu}_2^2}\frac{4\tilde{\nu}_2^2-5+2\sqrt{2-\tilde{\nu}_2^2}\sqrt{2-4\tilde{\nu}_2^2}}{16\tilde{\nu}_2^2-11+8\sqrt{2-\tilde{\nu}_2^2}\sqrt{2-4\tilde{\nu}_2^2}} \tag{C.23}$$

and

$$g_5(\tilde{\nu}_2) = 377 - 8\tilde{\nu}_2^2(83 + 98\tilde{\nu}_2^2 - 192\tilde{\nu}_2^4 + 64\tilde{\nu}_2^6) \quad \text{(C.24)}$$

$$g_6(\tilde{\nu}_2) = -16(16\tilde{\nu}_2^6 - 28\tilde{\nu}_2^4 - 6\tilde{\nu}_2^2 - 11). \quad \text{(C.25)}$$

The quantity $\bar{w}_{22}$ reads:

$$\bar{w}_{22} = w_{22} + \tilde{w}_{22}. \quad \text{(C.26)}$$

The quantity w_{23} reads:

$$w_{23} = \rho_{23} e^{\,i\phi_{23}} \quad \text{(C.27)}$$

where

$$\rho_{23} = \frac{3\sqrt{h_1(\tilde{\nu}_2) + h_2(\tilde{\nu}_2)\sqrt{2-\tilde{\nu}_2^2}\sqrt{2-4\tilde{\nu}_2^2}}}{(4\tilde{\nu}_2^2 - 5 + 2\sqrt{2-\tilde{\nu}_2^2}\sqrt{2-4\tilde{\nu}_2^2})^3} \quad \text{(C.28)}$$

$$\tan\phi_{23} = \frac{3\,h_3(\tilde{\nu}_2)\,\tilde{\nu}_2\sqrt{2-4\tilde{\nu}_2^2} - 2\,h_4(\tilde{\nu}_2)\,\tilde{\nu}_2\sqrt{2-\tilde{\nu}_2^2}}{3\tilde{\nu}_2^2[(2-\tilde{\nu}_2^2)(5-16\tilde{\nu}_2^2) + 4(2\tilde{\nu}_2^2-1)\sqrt{2-\tilde{\nu}_2^2}\sqrt{2-4\tilde{\nu}_2^2}]} \quad \text{(C.29)}$$

and

$$h_1(\tilde{\nu}_2) = -128\tilde{\nu}_2^{10}(290\tilde{\nu}_2^6 - 1614\tilde{\nu}_2^4 + 4487\tilde{\nu}_2^2 - 9286) - \tilde{\nu}_2^2(1693780\tilde{\nu}_2^6 - 1348157\tilde{\nu}_2^4 + 517080\tilde{\nu}_2^2 - 74492) \quad \text{(C.30)}$$

$$h_2(\tilde{\nu}_2) = -12\tilde{\nu}_2^2\left(256\tilde{\nu}_2^{12} - 6680\tilde{\nu}_2^{10} + 24904\tilde{\nu}_2^8 - 33084\tilde{\nu}_2^6 + 19788\tilde{\nu}_2^4 - 6291\tilde{\nu}_2^2 + 930\right) \quad \text{(C.31)}$$

$$h_3(\tilde{\nu}_2) = 32\tilde{\nu}_2^6 - 76\tilde{\nu}_2^4 + 35\tilde{\nu}_2^2 - 10 \quad \text{(C.32)}$$

$$h_4(\tilde{\nu}_2) = 8\tilde{\nu}_2^6 - 196\tilde{\nu}_2^4 + 304\tilde{\nu}_2^2 - 95. \quad \text{(C.33)}$$

C.2 Coefficients of the cubic equation related to phase singularity

In Subsection 5.3.2, we mention about coefficients of the cubic equations in $\cos(\nu_2\zeta_2)$. Explicit expressions of these coefficients are given as follows:

$$C_0(\tilde{\nu}_2) = \frac{2\tilde{\nu}_2^2}{\tilde{\sigma}_1\tilde{\sigma}_2}(13\tilde{\nu}_2^2 - 5) + \frac{3\sqrt{2}}{2\tilde{\sigma}_1}\tilde{\nu}_2(1-\tilde{\nu}_2^2), \quad \text{(C.34)}$$

$$C_1(\tilde{\nu}_2) = \frac{3}{2} + \frac{3\sqrt{2}}{\tilde{\sigma}_2}\tilde{\nu}_2(1-4\tilde{\nu}_2^2) \quad \text{(C.35)}$$

$$C_2(\tilde{\nu}_2) = \frac{3\sqrt{2}}{\tilde{\sigma}_1}\tilde{\nu}_2(\tilde{\nu}_2^2 - 1). \quad \text{(C.36)}$$

Appendix D

Wave generation theory

D.1 Introduction

In this section, we will consider the problem how to generate waves in a wave tank of a hydrodynamic laboratory. The wave tank in the context of this thesis is a facility with a wavemaker on one side and a wave absorbing beach on the other side. We consider a tank with flat bottom, and no water is flowing in or out of the tank. Typically, the situation is that waves are generated by a flap type wavemaker at one side of a long tank; the motion of the flap 'pushes' the waves to start propagating along the tank. This means that typically we are dealing with a signalling problem or a boundary value problem (BVP), which is different from an initial value problem (IVP) when one tries to find the evolution of waves from given surface elevation and velocities at an initial moment.

To illustrate this for the simplest possible case, consider the linear, non-dispersive second-order wave equation for waves in one spatial direction x and time t : $\partial_t^2\eta = c^2\partial_x^2\eta$. Here, $\eta(x,t)$ denotes the surface wave elevation, and $c > 0$ is the constant propagation speed. The general solution is given by $\eta(x,t) = f(x-ct) + g(x+ct)$, for arbitrary functions f and g. The term $f(x-ct)$ is the contribution of waves travelling to the right (in positive x-direction), and $g(x+ct)$ waves running to the left. For the IVP, specifying at an initial time (say at $t = 0$) the wave elevation $\eta(x,0)$ and the velocity $\partial_t\eta(x,0)$ determines the functions f and g uniquely. For the BVP, resembling the generation at $x = 0$, we prescribe the wave elevation at $x = 0$ for all positive time, assuming the initial elevation to be zero for positive x (in the tank this means a flat surface prior to the start of the generation). If the signal is given by $s(t)$, vanishing for $t < 0$, the corresponding solution running into the tank is $\eta(x,t) = f(x-ct)$ which should be equal to $s(t)$ at $x = 0$, leading to $\eta(x,t) = s(t-x/c)$. Reversely, for a desired wave field $f(x-ct)$ running in the tank, the required surface elevation at $x = 0$ is given

by $s(t) = f(-ct)$. This shows the characteristic property of the BVP for the signalling problem.

The actual equations for the water motion, and the precise incorporation of the flap motion, are much more difficult then shown in the simple example above. In particular for the free motion of waves there are two nontrivial effects: 'dispersion' and 'nonlinearity'. 'Dispersion' means the propagation speed of waves depend on their wavelength (or frequency), described explicitly in the linear theory (i.e. for small surface elevations) by the linear dispersion relation (LDR), see formula (D.5). In fact, for a given frequency there is one normal mode that travels to the right as a harmonic wave, the propagating mode, and there are solutions decaying exponentially for increasing distance (the evanescent modes). We will use the right propagating mode and the evanescent modes as building blocks to describe the generation of waves by the wavemaker. For each frequency in the spectrum, the Fourier amplitude of the flap motion is then related to the amplitude of the corresponding propagating and evanescent modes. If we assume these amplitudes to be sufficiently small, say of the 'first order' ϵ, with ϵ a small quantity, we will be able to deal with nonlinear effects in a sequential way. This is needed because the second effect is that in reality the equations are nonlinear. The quadratic nature of the 'nonlinearity' implies that each two wave components will generate other components with an amplitude that is proportional to the product of the two amplitudes, the so-called 'bound-wave' components which have amplitudes of the order ϵ^2. These are the so-called 'second-order effects'.

For instance, two harmonic waves of frequency ω_1, ω_2 and wavenumber k_1, k_2 (related by the LDR) will have a bound-wave with frequency $\omega_1 + \omega_2$ and wavenumber $k_1 + k_2$. Since the LDR is a concave function of the wavenumber, this last frequency–wavenumber combination does not satisfy the LDR, i.e. this is not a free-wave: it can only exist in the combination with the free-wave. 'Free-wave' components mean that frequency and wavenumber satisfy the LDR. This second-order bound-wave that comes with a first-order free-wave has also its consequence for the wave generation. If the first-order free-wave component is compatible with the flap motion, the presence of the bound-wave component will disturb the wave motion, such that the additional second-order free-wave will be generated as well. This is undesired, since the second-order free-wave component has a different propagation speed as the bound-wave component, thereby introducing a spatially inhomogeneous wave field. That is why we add to the flap motion the additional effects of second-order bound-waves, thereby preventing any second-order free-wave component to be generated. This process is called 'second-order steering' of the wavemaker motion.

This technique can be illustrated using a simple IVP for an ordinary differential equation as follows. Consider the nonlinear equation with a linear operator $\mathcal{L}$:

$$\mathcal{L}\eta := \partial_t^2 \eta + \omega_0^2 \eta = \eta^2,$$

for which we look for small solutions, say of order ϵ, a small quantity. The series expansion technique then looks for a solution in the form

$$\eta = \epsilon\eta^{(1)} + \epsilon^2\eta^{(2)} + \mathcal{O}(\epsilon^3).$$

Substitution in the equation and requiring each order of ϵ to vanish leads to a sequence of IVPs, the first two of which read:

$$\mathcal{L}\eta^{(1)} = 0; \qquad \mathcal{L}\eta^{(2)} = (\eta^{(1)})^2; \quad \dots .$$

Observe that the equations for $\eta^{(1)}$ and $\eta^{(2)}$ are linear equations, homogeneous for $\eta^{(1)}$ and nonhomogeneous (with known right hand side after $\eta^{(1)}$ has been found) for $\eta^{(2)}$.

Suppose that the first-order solution we are interested in is $\eta^{(1)} = ae^{-i\omega_0 t}$, already introducing the complex arithmetic that will be used in the sequel also. This solution is found for the initial values $\eta^{(1)}(0) = a$, $\partial_t\eta^{(1)}(0) = -i\omega_0 a$. Then the equation for $\eta^{(2)}$, i.e. $\mathcal{L}\eta^{(2)} = a^2e^{-2i\omega_0 t}$ has as particular solution: $\eta_{\mathrm{p}}^{(2)} = Ae^{-2i\omega_0 t}$ with $A = -a^2/(3\omega_0^2)$. This particular solution is the equivalent of a bound-wave component mentioned above: it comes inevitably with the first-order solution $\eta^{(1)}$. However, $\eta_{\mathrm{p}}^{(2)}$ will change the initial condition; forcing it to remain unchanged could be done by adding a solution $\eta_{\mathrm{h}}^{(2)}$ of the homogeneous equation: $\mathcal{L}\eta_{\mathrm{h}}^{(2)} = 0$ that cancels the particular solution at $t = 0$, explicitly: $\eta_{\mathrm{h}}^{(2)} = \frac{1}{2}A\left(e^{i\omega_0 t} - 3e^{i\omega_0 t}\right)$. This homogeneous solution corresponds to the second-order free-wave component mentioned above. To avoid this solution to be present, the initial value has to be taken like:

$$\eta(0) = \epsilon a + \epsilon^2 A; \qquad \partial_t\eta(0) = -i\epsilon\omega_0 a - 2i\epsilon^2\omega_0 A.$$

The second-order terms in ϵ in these initial conditions are similar to second steering of the flap motion for the signalling problem.*

Besides the two difficult aspects of nature, dispersion and nonlinearity, the precise description of the signal is also quite involved, since the signal has to be described on a moving boundary, the flap, which complicates matters also. In the rest of this chapter we will describe the major details of this procedure. The next section presents the BVP for the wave generation problem. Section D.3 and Section D.4 discus the first and the second-order wave generation theory, respectively.

The first-order wave generation theory for unidirectional regular waves corresponding to linearized Stokes theory has been known for almost a century and reference is made to the review in [Svendsen, 1985], Chapter 6 of [Dean and Dalrymple, 1991] and Chapter 7 of [Hughes, 1993]. Second-order wave generation theory has been studied since the 1960s, and many people have improved the theory thereafter. In this thesis,

*Just as in this example, the hierarchy of equations also continues for the BVP: there will also be third and higher order contributions, and bound and free-waves in each order. Higher order steering than second-order has not been done until now, since the effects are smaller, although there are some exceptions.

we only refer to relatively current publications by Schäffer for this theory. The full second-order wave generation theory for irregular waves is given by [Schäffer, 1996]. The complete second-order wave generation theory for multidirectional waves in a semi-infinite basin is given by [Schäffer and Steenberg, 2003]. Both papers include both superharmonic and subharmonic waves and cover wavemakers of the piston (translatory) and hinged (rotational) type.

D.2 Governing equation

Let $\mathbf{u} = (u, w) = (\partial_x\phi, \partial_z\phi)$ define the velocity potential function $\phi = \phi(x, z, t)$ in a Cartesian coordinate system (x, z). Let also $\eta = \eta(x, t)$ denotes the surface wave elevation, $\Xi = \Xi(z, t) = f(z)S(t)$ denotes the wavemaker position, g denotes the gravitational acceleration, h denotes the still water depth and t denotes the time. The governing equation for the velocity potential is the Laplace equation

$$\partial_x^2\phi + \partial_z^2\phi = 0, \qquad \text{for } x \geq \Xi(z,t), \;\; -h \leq z \leq \eta(x,t);$$

that results from the assumption that water (in a good approximation) is incompressible: $\nabla \cdot \mathbf{u} = 0$. The dynamic and kinematic free surface boundary conditions (DFSBC and KFSBC), the kinematic boundary condition at the wavemaker (KWMBC), and the bottom boundary condition (BBC) are given by

$$\begin{aligned}
\text{DFSBC}: &\quad \partial_t\phi + \tfrac{1}{2}|\nabla\phi|^2 + g\eta = 0 &&\text{at } z = \eta(x,t);\\
\text{KFSBC}: &\quad \partial_t\eta + \partial_x\eta\partial_x\phi - \partial_z\phi = 0 &&\text{at } z = \eta(x,t);\\
\text{KWMBC}: &\quad \partial_x\phi - f(z)S'(t) - f'(z)S(t)\partial_z\phi = 0 &&\text{at } x = \Xi(z,t);\\
\text{BBC}: &\quad \partial_z\phi = 0 &&\text{at } z = -h.
\end{aligned}$$

The DFSBC is obtained from Bernoulli's equation, the KFSBC and the KWMBC are derived by applying the material derivative to the surface elevation and wavemaker motion, respectively. The BBC is obtained from the fact that no water comes in nor goes out of the wave tank. Note that the DFSBC and KFSBC are nonlinear boundary conditions prescribed at a yet unknown and moving free surface $z = \eta(x, t)$. The elevation, potential and wavemaker position are given by the following series expansions

$$\begin{aligned}
\eta &= \epsilon\eta^{(1)} + \epsilon^2\eta^{(2)} + \ldots\\
\phi &= \epsilon\phi^{(1)} + \epsilon^2\phi^{(2)} + \ldots\\
S &= \epsilon S^{(1)} + \epsilon^2 S^{(2)} + \ldots,
\end{aligned}$$

where ϵ is a small parameter, a measure of the surface elevation nonlinearity.

The wavemaker we will consider is a rotating flap, see Figure D.1. It is given by $\Xi(z, t) = f(z)S(t)$, where $f(z)$ describes the geometry of the wavemaker:

$$f(z) = \begin{cases} 1 + \dfrac{z}{h+H}, & \text{for } -(h-d) \leq z \leq 0;\\ 0, & \text{for } -h \leq z < -(h-d). \end{cases} \tag{D.1}$$

Note that $f(z)$ is given by design, and $S(t)$ is the wavemaker motion that can be controlled externally to generate different types of waves. The center of rotation is at $z = -(h + H)$. If the center of rotation is at or below the bottom, then $d = 0$ and in fact we do not have the last case of (D.1). If the center of rotation is at a height d above the bottom, then $d = -H$.

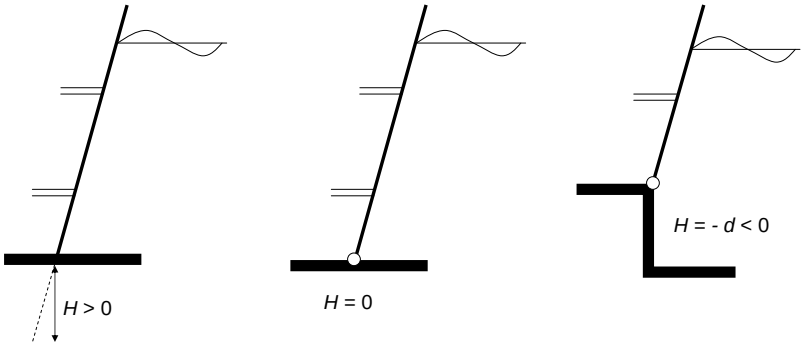

Figure D.1: The flap type of wavemaker with different center of rotations: below the bottom (left), at the bottom (middle), and above the bottom (right).

D.3 First-order wave generation theory

In this section we solve a homogeneous BVP for the first-order wave generation theory. By prescribing the first-order wavemaker motion as a linear superposition of monochromatic frequencies, we find the generated surface elevation also as a linear superposition of monochromatic modes. After applying the Taylor series expansion of the potential function ϕ around $x = 0$ and $z = 0$ as well as applying the series expansion method, the first-order potential function has to satisfy the Laplace equation

$$\partial_x^2\phi^{(1)} + \partial_z^2\phi^{(1)} = 0, \qquad \text{for } x \geq 0, \;\; -h \leq z \leq 0. \tag{D.2}$$

We also obtain the BVP for the first-order wave generation theory at the lowest expansion order. It reads

$$\begin{aligned} g\eta^{(1)} + \partial_t\phi^{(1)} &= 0, \qquad \text{at } z = 0; \\ \partial_t\eta^{(1)} - \partial_z\phi^{(1)} &= 0, \qquad \text{at } z = 0; \\ \partial_x\phi^{(1)} - f(z)\tfrac{dS^{(1)}}{dt} &= 0, \qquad \text{at } x = 0; \\ \partial_z\phi^{(1)} &= 0, \qquad \text{at } z = -h. \end{aligned} \tag{D.3}$$

By combining the DFSBC and the DFSBC at $z = 0$ (D.3), we obtain the first-order homogeneous free surface boundary condition

$$g\partial_z\phi^{(1)} + \partial_t^2\phi^{(1)} = 0, \qquad \text{at } z = 0. \tag{D.4}$$

We look for the so-called monochromatic waves:

$$\phi^{(1)}(x,z,t) = \psi(z)e^{-i\theta(x,t)},$$

where $\theta(x,t) = kx - \omega t$. Then from the Laplace equation (D.2), we have $\psi''(z) - k\psi(z) = 0$, for $-h \le z \le 0$. Applying the BBC leads to $\psi(z) = \alpha \cosh k(z+h)$, $\alpha \in \mathbb{C}$. From the combined free surface condition (D.4), we obtain a relation between the wavenumber k and frequency ω, known as the *linear dispersion relation* (LDR), explicitly given by

$$\omega^2 = gk \tanh kh. \tag{D.5}$$

Let us assume that the first-order wavemaker motion $S^{(1)}(t)$ is given by a harmonic function with frequency ω_n and maximum stroke $|S_n|$ from an equilibrium position, represented in complex notation as

$$S^{(1)}(t) = \sum_{n=1}^{\infty} -\frac{1}{2} i S_n e^{i\omega_n t} + \text{c.c.},$$

where c.c. denotes the complex conjugate of the preceding term. Since this 'first-order steering' contains an infinite number of discrete frequencies ω_n, it motivates us to write a general solution for the potential function by linear superposition of discrete spectrum. By choosing the arbitrary spectral coefficient $\alpha = \frac{ig}{2\omega_n} \frac{C_n}{\cosh k_n h}$, the first potential function is found to be

$$\phi^{(1)}(x,z,t) = \sum_{n=1}^{\infty} \frac{ig}{2\omega_n} C_n \frac{\cosh k_n(z+h)}{\cosh k_n h} e^{-i\theta_n(x,t)} + \text{c.c.},$$

where $\theta_n(x,t) = k_n x - \omega_n t$, with wavenumber-frequency pairs (k_n, ω_n), $n \in \mathbb{Z}$ satisfying the LDR (D.5). For a continuous spectrum, the summation is replaced by an integral. Allowing the wavenumber to be complex valued, the LDR becomes

$$\omega_n^2 = gk_{nj} \tanh k_{nj} h, \quad j \in \mathbb{N}_0.$$

For $j = 0$, the wavenumber is real and it corresponds to the propagating mode of the surface wave elevation. For $j \in \mathbb{N}$, the wavenumbers are purely imaginary, and thus $ik_{nj} \in \mathbb{R}$. Since we are interested to the decaying solution, we choose $ik_{nj} > 0$ and hence the modes of these wavenumbers are called the evanescent modes. As a consequence, the first-order potential function can now be written as

$$\phi^{(1)}(x,z,t) = \sum_{n=1}^{\infty} \sum_{j=0}^{\infty} \frac{ig}{2\omega_n} C_{nj} \frac{\cosh k_{nj}(z+h)}{\cosh k_{nj} h} e^{-i\theta_{nj}(x,t)} + \text{c.c.}, \tag{D.6}$$

where $\theta_{nj}(x,t) = k_{nj}x - \omega_n t$.

Furthermore, applying the KWMBC (D.3), integrating along the water depth, and using the property that $\left\{ \cosh k_{nj}(z+h), \cosh k_{nl}(z+h),\ j,l \in \mathbb{N}_0 \right\}$ is a set of orthogonal

functions for $j \neq l$, we can find the surface wave complex-valued amplitude C_{nj} as follows

$$\begin{aligned} C_{nj} &= \frac{\omega_n^2 S_n}{g k_{nj}} \cosh k_{nj} h \frac{\int_{-h}^{0} f(z) \cosh k_{nj}(z+h)\, dz}{\int_{-h}^{0} \cosh^2 k_{nj}(z+h)\, dz} \\ &= \frac{4 S_n \sinh k_{nj} h}{k_{nj}(h+H)} \frac{k_{nj}(h+H)\sinh k_{nj} h + \cosh k_{nj} d - \cosh k_{nj} h}{2 k_{nj} h + \sinh(2 k_{nj} h)},\ j \in \mathbb{N}_0. \end{aligned}$$

Finally, the first-order surface elevation can be found from the DFSBC (D.3), and is given as follows

$$\eta^{(1)}(x,t) = \sum_{n=-\infty}^{\infty} \sum_{j=0}^{\infty} \frac{1}{2} C_{nj} e^{-i\theta_{nj}(x,t)} + \text{c.c.}$$

This first-order theory can also be found in [Dean and Dalrymple, 1991].

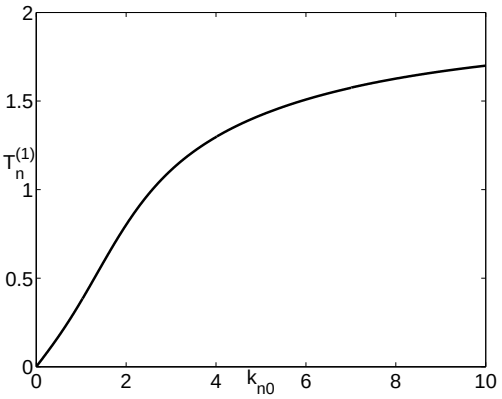

Figure D.2: The first-order transfer function plot as a function of wavenumber k_{n0}, for the case that the water depth is $h = 1$ and the center of rotation is at $d = \frac{1}{3}h$ above the tank floor.

REMARK 1.

For 'practical' purposes, it is useful to introduce the so-called *transfer function* or *frequency response* of a system. It is defined as the ratio of the output and the input of a system. In our wave generation problem, we have a system with a wavemaker motion as input and the surface wave amplitude as output. Therefore, the first-order transfer function $T_n^{(1)}$ is defined as the ratio between the surface wave amplitude of

the propagating mode C_{n0} as output and the maximum stroke $|S_n|$ as input, explicitly given by

$$T_n^{(1)} = 4\,\frac{\sinh k_{n0}h}{k_{n0}(h+H)}\,\frac{k_{n0}(h+H)\sinh k_{n0}h + \cosh k_{n0}d - \cosh k_{n0}h}{2k_{n0}h + \sinh 2k_{n0}h}.$$

Figure D.2 shows the first-order transfer function plot as function of wavenumber k_{n0} for a given water depth h and the center of rotation d. For increasing k_{n0}, which also means increasing frequency ω_n, the transfer function is monotonically increasing as well. It increases faster for smaller value of k_{n0} and slower for larger value of k_{n0}, approaching the asymptotic limit of $T_n^{(1)} = 2$ for $k_{n0}h \to \infty$.

D.4 Second-order wave generation theory

In this section we solve a nonhomogeneous BVP for the second-order wave generation theory. Due to the nonhomogeneous boundary condition at the free surface, which causes interactions between each possible pair of first-order wave components, the resulting surface wave elevation has a second-order effect, known as the bound-wave component. Furthermore, due to first-order wavemaker motion and the boundary condition at the wavemaker, the generated wave also has another second-order effect, namely the free-wave component. The latter component is undesired since it results in a spatially inhomogeneous wave field due to the different propagation velocities of bound-wave and free-wave components with the same frequency. Therefore, in order to prevent the free-wave component to be generated, we add an additional second-order bound-wave effect to the flap motion. This process is known as 'second-order steering' of the wavemaker motion. More details about this theory, including an experimental verification can be found in [Schäffer, 1996]. For the history of wave generation theory, see also references in this paper.

Taking terms of the second-order in the series expansion, we obtain the BVP for the second-order wave generation theory. The second-order potential function also satisfies the Laplace equation

$$\partial_x^2\phi^{(2)} + \partial_z^2\phi^{(2)} = 0, \qquad \text{for } x \geq 0,\ \ -h \leq z \leq 0.$$

Almost all the second-order boundary conditions now become nonhomogeneous:

$$\begin{aligned}
g\eta^{(2)} + \partial_t\phi^{(2)} &= -\Big(\eta^{(1)}\partial_{tz}^2\phi^{(1)} + \tfrac{1}{2}|\nabla\phi^{(1)}|^2\Big), && \text{at } z = 0;\\
\partial_t\eta^{(2)} - \partial_z\phi^{(2)} &= \eta^{(1)}\partial_z^2\phi^{(1)} - \partial_x\eta^{(1)}\partial_x\phi^{(1)}, && \text{at } z = 0;\\
\partial_x\phi^{(2)} - f(z)\tfrac{dS^{(2)}}{dt} &= S^{(1)}(t)\Big(f'(z)\partial_z\phi^{(1)} - f(z)\partial_x^2\phi^{(1)}\Big), && \text{at } x = 0;\\
\partial_z\phi^{(2)} &= 0, && \text{at } z = -h.
\end{aligned} \tag{D.7}$$

By combining the DFSBC and KFSBC of (D.7) at $z = 0$, we have the second-order nonhomogeneous free surface boundary condition

$$g\partial_z\phi^{(2)} + \partial_t^2\phi^{(2)} = \text{RHS}_1, \quad \text{at } z = 0. \tag{D.8}$$

Using the first-order potential function (D.6), RHS$_1$ is explicitly given by

$$\begin{aligned} \text{RHS}_1 &= -\left(\frac{\partial}{\partial t}|\nabla\phi^{(1)}|^2 + \eta^{(1)}\frac{\partial}{\partial z}\left[g\frac{\partial\phi^{(1)}}{\partial z} + \frac{\partial^2\phi^{(1)}}{\partial t^2}\right]\right)\Bigg|_{z=0} \\ &= \sum_{m,n=1}^{\infty}\sum_{l,j=0}^{\infty}\left(A^{+}_{mnlj}e^{-i(\theta_{ml}+\theta_{nj})} + A^{-}_{mnlj}e^{-i(\theta_{ml}-\theta^{*}_{nj})}\right) + \text{c.c.}, \end{aligned}$$

where

$$\begin{aligned} \frac{A^{+}_{mnlj}}{C_{ml}C_{nj}} &= \frac{1}{4i}\left[(\omega_m+\omega_n)\left(g^2\frac{k_{ml}k_{nj}}{\omega_m\omega_n} - \omega_m\omega_n\right) + \frac{g^2}{2}\left(\frac{k_{ml}^2}{\omega_m} + \frac{k_{nj}^2}{\omega_n}\right) - \frac{1}{2}(\omega_m^3+\omega_n^3)\right], \\ \frac{A^{-}_{mnlj}}{C_{ml}C^{*}_{nj}} &= \frac{1}{4i}\left[(\omega_m-\omega_n)\left(g^2\frac{k_{ml}k^{*}_{nj}}{\omega_m\omega_n} + \omega_m\omega_n\right) + \frac{g^2}{2}\left(\frac{k_{ml}^2}{\omega_m} - \frac{k_{nj}^2}{\omega_n}\right) - \frac{1}{2}(\omega_m^3-\omega_n^3)\right]. \end{aligned}$$

In order to find the bound-wave component, the free-wave component and to apply the second-order steering wavemaker motion, we split the second-order BVP (D.7) into three BVPs. For that purpose the second-order potential function is split into three components as follows

$$\phi^{(2)}(x,z,t) = \phi^{(21)}(x,z,t) + \phi^{(22)}(x,z,t) + \phi^{(23)}(x,z,t).$$

Now the corresponding BVP for the first component of the potential function $\phi^{(21)}$ reads

$$\begin{aligned} g\partial_z\phi^{(21)} + \partial_t^2\phi^{(21)} &= \text{RHS}_1, && \text{at } z=0; \\ \partial_z\phi^{(21)} &= 0, && \text{at } z=-h. \end{aligned} \tag{D.9}$$

The corresponding BVP for the second component of the potential function $\phi^{(22)}$ reads

$$\begin{aligned} g\partial_z\phi^{(22)} + \partial_t^2\phi^{(22)} &= 0, && \text{at } z=0; \\ \partial_x\phi^{(22)} &= S^{(1)}(t)\Big(f'(z)\partial_z\phi^{(1)} - f(z)\partial_x^2\phi^{(1)}\Big) - \partial_x\phi^{(21)}, && \text{at } x=0; \\ \partial_z\phi^{(22)} &= 0, && \text{at } z=-h. \end{aligned} \tag{D.10}$$

And the BVP for the third component of the potential function $\phi^{(23)}$ reads

$$\begin{aligned} g\partial_z\phi^{(23)} + \partial_t^2\phi^{(23)} &= 0, && \text{at } z=0; \\ \partial_x\phi^{(23)} &= f(z)\tfrac{dS^{(2)}}{dt}, && \text{at } x=0; \\ \partial_z\phi^{(23)} &= 0, && \text{at } z=-h. \end{aligned} \tag{D.11}$$

By taking the Ansatz for the first part of the second-order potential function $\phi^{(21)}$ as follows

$$\begin{aligned}\phi^{(21)}(x,z,t) &= \sum_{m,n=1}^{\infty}\sum_{l,j=0}^{\infty} B^{+}_{mnlj}\frac{\cosh(k_{ml}+k_{nj})(z+h)}{\cosh(k_{ml}+k_{nj})h}e^{-i(\theta_{ml}+\theta_{nj})} \\ &+ B^{-}_{mnlj}\frac{\cosh(k_{ml}-k^{*}_{nj})(z+h)}{\cosh(k_{ml}-k^{*}_{nj})h}e^{-i(\theta_{ml}-\theta^{*}_{nj})} + \text{c.c.},\end{aligned}$$

then we can derive the corresponding coefficients to be:

$$\begin{aligned}B^{+}_{mnlj} &= \frac{A^{+}_{mnlj}}{\Omega^{2}(k_{ml}+k_{nj})-(\omega_m+\omega_n)^{2}}, \\ B^{-}_{mnlj} &= \frac{A^{-}_{mnlj}}{\Omega^{2}(k_{ml}-k^{*}_{nj})-(\omega_m-\omega_n)^{2}}.\end{aligned}$$

This first component of the second-order potential function will contribute the bound-wave component to the second-order surface wave elevation $\eta^{(2)}$. For $j=0$, the wave component is a propagating mode and for $j\in\mathbb{N}$, it consists of evanescent modes. Since the wavenumbers $k_{mj}+k_{nj}$ and $k_{mj}+k^{*}_{nj}$, $j\in\mathbb{N}_0$ do not satisfy the LDR with frequencies $\omega_m\pm\omega_n$, then the denominator part of $B^{\pm}_{mnj}$ will never vanish and thus the potential function is a bounded function.

Let the right hand side of the boundary condition at the wavemaker for the second BVP (D.10) be denoted by RHS_2, which is expressed as

$$\text{RHS}_2 = \sum_{m,n=1}^{\infty}\sum_{l,j=0}^{\infty}\left(F^{+}_{mnlj}(z)e^{i(\omega_m+\omega_n)t}+F^{-}_{mnlj}(z)e^{i(\omega_m-\omega_n)t}\right)+\text{c.c.},$$

where

$$\begin{aligned}F^{+}_{mnlj}(z) &= \frac{g}{8\omega_n}\frac{S_m k_{nj}C_{nj}}{\cosh k_{nj}h}\left[f'(z)\sinh k_{nj}(z+h)+k_{nj}f(z)\cosh k_{nj}(z+h)\right] \\ &\quad + i(k_{ml}+k_{nj})B^{+}_{mnlj}\frac{\cosh(k_{ml}+k_{nj})(z+h)}{\cosh(k_{ml}+k_{nj})h}, \\ F^{-}_{mnlj}(z) &= -\frac{g}{8\omega_n}\frac{S_m k^{*}_{nj}C^{*}_{nj}}{\cosh k^{*}_{nj}h}\left[f'(z)\sinh k^{*}_{nj}(z+h)+k^{*}_{nj}f(z)\cosh k^{*}_{nj}(z+h)\right] \\ &\quad + i(k_{ml}-k^{*}_{nj})B^{-}_{mnlj}\frac{\cosh(k_{ml}-k^{*}_{nj})(z+h)}{\cosh(k_{ml}-k^{*}_{nj})h}.\end{aligned}$$

Let the Ansatz for the second component of the second-order potential function $\phi^{(22)}$ be

$$\begin{aligned}\phi^{(22)}(x,z,t) &= \sum_{m,n=1}^{\infty}\sum_{l,j=0}^{\infty}\left(\frac{i\,g\,P^{+}_{mnlj}}{2(\omega_m+\omega_n)}\frac{\cosh K^{+}_{mnlj}(z+h)}{\cosh K^{+}_{mnlj}h}e^{-i(K^{+}_{mnj}x-(\omega_m+\omega_n)t)}\right.\\ &+ \left.\frac{i\,g\,P^{-}_{mnlj}}{2(\omega_m-\omega_n)}\frac{\cosh K^{-}_{mnlj}(z+h)}{\cosh K^{-}_{mnlj}h}e^{-i(K^{-}_{mnlj}x-(\omega_m-\omega_n)t)}\right)+\text{c.c.},\end{aligned}$$

where the wavenumbers $K^{\pm}_{mnlj}$, $j\in\mathbb{N}_0$ and frequencies $\omega_m\pm\omega_n$ satisfy the LDR. Using the property that $\left\{\cosh K^{\pm}_{mnlj}(z+h),\cosh K^{\pm}_{mnl'j'}(z+h),\ l,l',j,j'\in\mathbb{N}_0\right\}$ is a set of orthogonal functions for $l\neq l'$ and $j\neq j'$, we find the coefficients $P^{\pm}_{mnlj}$ as follows

$$\begin{aligned}P^{\pm}_{mnlj} &= \frac{2(\omega_m\pm\omega_n)\cosh K^{\pm}_{mnlj}h}{gK^{\pm}_{mnlj}}\frac{\displaystyle\int_{-h}^{0}F^{\pm}_{mnlj}(z)\cosh K^{\pm}_{mnlj}(z+h)\,dz}{\displaystyle\int_{-h}^{0}\cosh^2 K^{\pm}_{mnlj}(z+h)\,dz}\\ &= 8\frac{K^{\pm}_{mnlj}\sinh K^{\pm}_{mnlj}h}{\omega_m\pm\omega_n}\frac{\displaystyle\int_{-h}^{0}F^{\pm}_{mnlj}(z)\cosh K^{\pm}_{mnlj}(z+h)\,dz}{2K^{\pm}_{mnlj}h+\sinh(2K^{\pm}_{mnlj}h)}.\end{aligned}\tag{D.12}$$

The second component of the second-order potential function $\phi^{(22)}$ will give contributions to the free-wave component of the second-order surface wave elevation $\eta^{(2)}$. This component arises due to the boundary condition at the wavemaker caused by the first-order wavemaker motion. Since the desired surface elevation is only the bound-wave component, we want to get rid this term, especially the propagating mode. The evanescent modes vanishes anyway after they evolve far away from the wavemaker. By prescribing the second-order wavemaker motion such that the propagating mode of the third component $\phi^{(23)}$ will cancel the same mode of the second one $\phi^{(22)}$, then far from the wavemaker we have the desired bound-wave component only.

Let the second-order wavemaker motion be given by

$$S^{(2)}(t)=\sum_{m,n=1}^{\infty}-\frac{1}{2}i\left(S^{+}_{mn}e^{i(\omega_m+\omega_n)t}+S^{-}_{mn}e^{i(\omega_m-\omega_n)t}\right)+\text{c.c.}$$

Let also the Ansatz for the third component of the second-order potential function $\phi^{(23)}$ be

$$\begin{aligned}\phi^{(23)}(x,z,t) &= \sum_{m,n=1}^{\infty}\sum_{l,j=0}^{\infty}\left(\frac{i\,g\,Q^{+}_{mnlj}}{2(\omega_m+\omega_n)}\frac{\cosh K^{+}_{mnlj}(z+h)}{\cosh K^{+}_{mnlj}h}e^{-i(K^{+}_{mnlj}x-(\omega_m+\omega_n)t)}\right.\\ &+ \left.\frac{i\,g\,Q^{-}_{mnlj}}{2(\omega_m-\omega_n)}\frac{\cosh K^{-}_{mnlj}(z+h)}{\cosh K^{-}_{mnlj}h}e^{-i(K^{-}_{mnlj}x-(\omega_m-\omega_n)t)}\right)+\text{c.c.},\end{aligned}$$

where $\Omega(K^{\pm}_{mnlj}) = \omega_m \pm \omega_n$. Using the orthogonality property again, we find the coefficients $Q^{\pm}_{mnlj}$ as follows

$$\begin{aligned} Q^{\pm}_{mnlj} &= S^{\pm}_{mn} \sinh K^{\pm}_{mnlj} h \frac{\displaystyle\int_{-h}^{0} f(z) \cosh K^{\pm}_{mnlj}(z+h)\, dz}{\displaystyle\int_{-h}^{0} \cosh^2 K^{\pm}_{mnlj}(z+h)\, dz} \\ &= \frac{4S^{\pm}_{mn} \sinh K^{\pm}_{mnlj} h}{K^{\pm}_{mnlj}(h+H)} \frac{K^{\pm}_{mnlj}(h+H) \sinh K^{\pm}_{mnlj} h + \cosh K^{\pm}_{mnlj} d - \cosh K^{\pm}_{mnlj} h}{2K^{\pm}_{mnlj} h + \sinh(2K^{\pm}_{mnlj} h)}. \end{aligned} \tag{D.13}$$

To have the propagating mode of the free-wave from the second $\big(\phi^{(22)}\big)$ and the third $\big(\phi^{(23)}\big)$ components cancel each other, we must require $P_{mn00} + Q_{mn00} = 0$, which leads to the following second-order wavemaker motion, known as 'second-order steering':

$$S^{\pm}_{mn} = \frac{2\big(K^{\pm}_{mn00}\big)^2 I^{\pm}_{mn00}(h+H)}{\big(\omega_m \pm \omega_n\big)\big(\cosh K^{\pm}_{mn00} h - \cosh K^{\pm}_{mn00} d - K^{\pm}_{mn00}(h+l)\sinh K^{\pm}_{mn00} h\big)},$$

where

$$I^{\pm}_{mn00} = \int_{-h}^{0} F^{\pm}_{mn00}(z) \cosh K^{\pm}_{mn00}(z+h)\, dz.$$

Therefore, with this choice of second-order wavemaker motion, the second-order potential function can be written as

$$\phi^{(2)}(x,z,t) = \phi^{(2)}_{\text{propagating}}(x,z,t) + \phi^{(2)}_{\text{evanescent}}(x,z,t),$$

where

$$\begin{aligned} \phi^{(2)}_{\text{propagating}} &= \phi^{(21)}_{\text{bound-wave, propagating}}, \\ \phi^{(2)}_{\text{evanescent}} &= (\phi^{(21)}_{\text{bound-wave}} + \phi^{(22)}_{\text{free-wave}} + \phi^{(23)}_{\text{free-wave}})_{\text{evanescent}}. \end{aligned}$$

Consequently, from the second-order DFSBC (D.7), we find the second-order surface wave elevation. It can be written as follows

$$\eta^{(2)}(x,t) = \eta^{(2)}_{\text{propagating}} + \phi^{(2)}_{\text{evanescent}},$$

where

$$\eta^{(2)}_{\text{propagating}} = \sum_{m,n=1}^{\infty} D^{+}_{mn00} e^{-i(\theta_{m0}+\theta_{n0})} + D^{-}_{mn00} e^{-i(\theta_{m0}-\theta_{n0})},$$

and

$$\begin{aligned}\eta^{(2)}_{\text{evanescent}} &= \sum_{m,n=1}^{\infty}\sum_{\substack{j=1,\\ l=0}}^{\infty}\Big(D^{+}_{mnlj}e^{-i(\theta_{ml}+\theta_{nj})}+D^{-}_{mnlj}e^{-i(\theta_{ml}-\theta^{*}_{nj})}\\ &+ \frac{1}{2}(P^{+}_{mnlj}+Q^{+}_{mnlj})e^{-i(K^{+}_{mnlj}x-(\omega_m+\omega_n)t)}\\ &+ \frac{1}{2}(P^{-}_{mnlj}+Q^{-}_{mnlj})e^{-i(K^{-}_{mnlj}x-(\omega_m-\omega_n)t)}\Big)+\text{c.c.},\end{aligned}$$

where for $l, j \in \mathbb{N}_0$:

$$\begin{aligned}D^{+}_{mnlj} &= -\frac{1}{g}\left[i(\omega_m+\omega_n)B^{+}_{mnlj}+\frac{1}{8}\left(g^2\frac{k_{ml}k_{nj}}{\omega_m\omega_n}-\omega_m\omega_n-(\omega_m^2+\omega_n^2)\right)C_{ml}C_{nj}\right],\\ D^{-}_{mnlj} &= -\frac{1}{g}\left[i(\omega_m-\omega_n)B^{-}_{mnlj}+\frac{1}{8}\left(g^2\frac{k_{ml}k^{*}_{nj}}{\omega_m\omega_n}+\omega_m\omega_n-(\omega_m^2+\omega_n^2)\right)C_{ml}C^{*}_{nj}\right].\end{aligned}$$

We have seen that the first-order surface wave elevation consists of a linear superposition of monochromatic frequencies. However, due to nonlinear effects, nonhomogeneous BVP, and interactions of the first-order wave components, the second-order surface elevation is composed by a superposition of bichromatic frequencies $\omega_m \pm \omega_n$. The components with frequency $\omega_m + \omega_n$ are called the 'superharmonics' and those with frequency $|\omega_m - \omega_n|$are called the 'subharmonics'.

REMARK 2.

Similar to the first-order wave generation theory, we can define a second-order transfer function as well. Detailed formula for this transfer function can be found in [Schäffer, 1996].

References

[Dean and Dalrymple, 1991] R. G. Dean and R. A. Dalrymple. *Water Wave Mechanics for Engineers and Scientists*, volume **2** of *Advanced Series of Ocean Engineering*. World Scientific, Singapore, 1991.

[Hughes, 1993] S. A. Hughes. *Physical Models and Laboratory Techniques in Coastal Engineering*, volume **7** of *Advanced Series of Ocean Engineering*. World Scientific, Singapore, 1993.

[Schäffer, 1996] H. A. Schäffer. Second-order wavemaker theory for irregular waves. *Ocean Engng.* **23**(1):47–88, 1996.

[Schäffer and Steenberg, 2003] H. A. Schäffer and C. M. Steenberg. Second-order wavemaker theory for multidirectional waves. *Ocean Engng.* **30**:1203–1231, 2003.

[Svendsen, 1985] I. A. Svendsen. Physical modelling of water waves. In R. A. Dalrymple, editor, *Physical Modelling in Ocean Engineering*, A. A. Balkema, Rotterdam, 1985.

Summary

In this thesis we discuss mathematical aspects of extreme water wave generation in a hydrodynamic laboratory. The original problem comes from the Maritime Research Institute Netherlands (MARIN) to generate large amplitude and non-breaking waves to test ship and offshore construction. We choose the spatial nonlinear Schrödinger (NLS) equation as a mathematical model for this problem and concentrate on the study of one family of exact solutions of this equation that describes extreme wave events in a wave basin.

We derive the NLS equation using the multiple scale method, derive the phase-amplitude equations and introduce the Chu-Mei quotient from the nonlinear dispersion relation. We are interested in the modulational instability of the nonlinear plane wave solution of the NLS equation. The physical wave field of a plane wave serves as the 'finite' background of the extreme wave model.

We discuss extensively the properties of waves on finite background which are exact solutions of the NLS equation. Three types of such waves are known in the literature: the Soliton on Finite Background (SFB), the Ma solution and the rational solution. In particular, the SFB solution receives special attention since the corresponding physical wave signal is a good candidate for extreme wave generation. The asymptotic behaviour of the SFB in the far distance corresponds to a modulated plane wave solution of the NLS equation. For a very long modulation, the SFB has amplitude amplification up to a maximal factor of three.

We introduce a transformation to displaced phase-amplitude variables with respect to a background of the monochromatic plane wave solution. The transformation of the displaced phase is restricted to be time independent. The change of phase with position physically corresponds to a change of the wavelength of the carrier wave of a wave group. This turns out to be the only driving force responsible for the nonlinear amplitude amplification toward extreme wave events. Remarkably, the assumption that the displaced-phase is time independent leads to the waves on finite background which are the three exact solutions of the NLS equation mentioned earlier.

We study the corresponding physical wave field of the SFB and observe that the interesting, purely linear, phenomena of vanishing amplitude, phase singularity and wavefront dislocation, occur simultaneously. We connect the unboudedness of the Chu-Mei quotient with the unboundedness of the local wavenumber and the local frequency at singular points. This unboundedness is a generic property and is responsible for the occurrence of phase singularity and wavefront dislocation.

We study some characteristics of higher order waves on finite background, particularly the SFB_2 solution.* The corresponding physical wave field shows an interaction of two wave groups as they propagate downstream . Theoretically, SFB_2 is also a good candidate for extreme wave generation since it has amplitude amplification up to maximal factor of five. We present an explicit relation of the amplitude amplification factors between SFB_2 and SFB. Vanishing amplitude, phase singularity and wavefront dislocation also occur simultaneously in the physical wave field of SFB_2.

We designed a set of experiments for extreme wave generation based on the theoretical prediction with SFB. These experiments were executed in the wave basin of MARIN. We compare the experimental results and the theoretical prediction qualitatively and quantitatively. All experimental signals show a pattern of modulational instability as described by SFB during the downstream evolution. We observe that both the carrier wave frequency and the modulation frequency are conserved accurately during the evolution. We explain several differences between the theoretical SFB and the experimental signals using the evolution curves in the Argand diagram and the maximum temporal amplitude plots. The experimental signals have phase singularities at two different positions, with the extreme position located in between. We describe that the extreme position is sensitive for parameter changes in the SFB family and also for the nonlinear coefficient of the NLS equation. We conclude that the SFB family provides suitable wave groups that can be used to generate extreme waves in the laboratory in a deterministic way.

*The index two now denotes the number of initial pairs of sidebands in the spectrum.

Samenvatting

In dit proefschrift behandelen we wiskundige modellen voor het opwekken (genereren) van extreme golven in een waterloopkundig laboratorium. Het Maritiem Onderzoeks Instituut MARIN gebruikt deze modellen om hoge, niet brekende golven te genereren voor het testen van schepen en offshore constructies. Als wiskundig model is gekozen voor de niet-lineaire Schrödinger (NLS) vergelijking. We hebben een groep van exacte oplossingen van de vergelijking bestudeerd die extreme golven in een laboratorium beschrijven.

Wij leiden de NLS vergelijking af met behulp van de meer-schalen methode. Vervolgens leiden we de fase-amplitude vergelijkingen af en introduceren het Chu-Mei quotiënt van de niet-lineaire dispersie relatie. Wij zijn geinteresseerd in de modulatie instabiliteit van de niet-lineaire vlakke golf oplossing van de NLS vergelijking. Het fysische golfveld van een vlakke golf dient als de 'eindige' achtergrond van het extreme golf model.

Wij bespreken uitgebreid de eigenschappen van golven op eindige achtergrond die nauwkeurige oplossingen van de NLS vergelijking zijn. Drie types van dergelijke golven zijn bekend in de literatuur: de Soliton op Eindige Achtergrond (*SFB*), de Ma oplossing en de rationele oplossing. In het bijzonder krijgt de SFB oplossing speciale aandacht aangezien het overeenkomstige fysische golfsignaal een goede kandidaat voor extreme golfgeneratie is. Het asymptotische gedrag van het SFB voor grote afstand is een gemoduleerde vlakke golfoplossing van de NLS vergelijking. Voor een zeer lange modulatie heeft SFB een amplitudevergroting tot een maximale factor van drie.

Wij introduceren een transformatie naar verschoven fase-amplitude variabelen met betrekking tot een achtergrond van de monochromatische vlakke golfoplossing. De transformatie van de verschoven fase wordt beperkt door deze tijdonafhankelijke te nemen. De verandering van fase met positie correspondeert fysisch met een verandering van de golflengte van de draaggolf van een golfgroep. Dit blijkt de enige drijvende kracht te zijn verantwoordelijk is voor de niet-lineaire amplitudetoename naar extreme golven. Opmerkelijk is dat de veronderstelde tijdonafhankelijkheid leidt tot de drie exacte oplossingen die bekend zijn van de eerder vermelde NLS vergelijking.

Wij bestuderen het bijbehorend fysisch golfveld van de SFB en constateren een gelijktijdig optreden van drie zuiver lineaire verschijnselen: verdwijnende amplitude, fase singulariteit en golffront vertakking. In de singuliere punten leggen we een verband tussen de onbegrensdheid van het Chu-Mei quotiënt met die van het locale golfgetal

en de locale frequentie. Dit onbegrensd zijn is een generieke eigenschap die verantwoordelijk is voor het optreden van fase singulariteit en golffront vertakking.

Wij onderzoeken eigenschappen van golven van hogere orde op eindige achtergrond, vooral de SFB_2 oplossing.* Het bijhorende fysische golfpatroon toont een wisselwerking van twee golfgroepen die in de stromingsrichting voortbewegen. Theoretisch is de SFB_2 ook een goede kandidaat voor het opwekken van extreme golven omdat hij een amplitudegroei tot op het vijfvoudige veroorzaken kan. Wij geven een expliciete relatie voor het groei van de amplitude van SFB_2 en SFB. Verdwijnende amplitude, fase singulariteit en golffront vertakking kunnen ook simultaan in het fysische golfveld van de SFB_2 voorkomen.

We hebben een aantal experimenten ontworpen voor het genereren van extreme golven gebaseerd op de theoretische voorspellingen met SFB. Deze experimenten werden uitgevoerd in het golfbasin van MARIN. Wij vergelijken de experimentele resultaten met theoretische voorspellingen, zowel kwalitatief als kwantitatief. Alle experimentele signalen tonen een patroon van modulatie instabiliteit zoals omschreven door de SFB tijdens een stroomafwaartse evolutie. Wij nemen waar dat zowel de frequentie van de draaggolf als die van de modulatie nauwkering behouden blijven tijdens de evolutie. Wij verklaren een aantal verschillen tussen de theoretische SFB en de experimentele signalen door gebruik te maken van evolutiekrommen in het Argand diagram en de informatie over de maximale tijdsafhankelijke amplitude (*MTA*). De experimentele signalen hebben fasesingulariteiten op twee verschillende posities, met de extreme positie hier tussen. Wij beschrijven dat de extreme positie gevoelig is voor parameter veranderingen in de SFB familie en ook voor de niet-lineaire coefficient van de NLS vergelijking. Wij concluderen dat de SFB familie geschikte golfgroepen beschrijven die gebruikt kunnen worden om extreme golven in het laboratorium te genereren op een deterministische weijze.

*Index twee geeft nu het aantal initiële paren *sidebands* in het spectrum aan.

Ringkasan

Tesis ini membahas pembangkitan gelombang air ekstrim pada laboratorium hidrodinamika ditinjau dari segi matematis. Permasalahan asalnya diajukan oleh Institut Penelitian Kelautan Belanda (*MARIN*) yang bermaksud membangkitkan gelombang dengan amplitudo tinggi namun tak pecah guna menguji konstruksi kapal dan bangunan lepas pantai. Persamaan Schrödinger tak linear tipe ruang (*spatial NLS*) dipilih untuk memodelkan permasalahan ini dan penelitian dalam tesis ini dipusatkan pada satu kelas penyelesaian eksak dari persamaan tersebut, yang sekaligus menggambarkan kejadian gelombang ekstrim di suatu kolam pengujian gelombang.

Persamaan NLS diturunkan dengan menggunakan metode skala kelipatan (*multiple-scale*), diturunkan juga persamaan fasa-amplitudo (*phase-amplitude equations*) dan diperkenalkan suku Chu-Mei dari hubungan dispersi tak linear (*nonlinear dispersion relation*). Ketidakstabilan modulasi (*modulational instability*) dari penyelesaian gelombang datar (*plane wave*) tak linear yang berkaitan dengan persamaan NLS dipelajari dalam tesis ini. Medan gelombang fisik dari gelombang datar (*plane wave*) berperan sebagai latar terbatas dari model gelombang ekstrim tersebut.

Sifat-sifat gelombang pada latar terbatas (*waves on finite background*) yang merupakan penyelesaian eksak dari persamaan NLS dibahas secara mendalam. Tiga jenis gelombang tersebut dapat ditemukan dalam kepustakaan: Soliton pada Latar Terbatas (*SFB*), penyelesaian Ma dan penyelesaian rasional. Dari ketiga penyelesaian ini, penyelesaian SFB mendapatkan perhatian khusus karena sinyal gelombang fisiknya merupakan kandidat yang cocok untuk pembangkitan gelombang ekstrim. Perilaku asimptotik dari SFB di kejauhan berkaitan dengan penyelesaian gelombang datar dari persamaan NLS yang termodulasi. Untuk modulasi gelombang yang sangat panjang, SFB mempunyai faktor kelipatan amplitudo (*amplitude amplification*) sampai maksimal tiga kali.

Suatu transformasi pada peubah-peubah fase-amplitudo tergeser (*displaced phase-amplitude*) terhadap suatu latar berupa penyelesaian gelombang datar dengan frekuensi tunggal diperkenalkan dalam tesis ini. Transformasi terhadap fase tergeser dibatasi sehingga tidak bergantung pada waktu. Perubahan fase terhadap posisi secara fisik berkaitan dengan perubahan panjang gelombang dari gelombang pembawa suatu kelompok gelombang. Hal ini ternyata menjadi satu-satunya gaya pemicu yang mengakibatkan kelipatan amplitudo tak linear pada peristiwa gelombang ekstrim. Sungguh menakjubkan bahwa fase tergeser yang diasumsikan tidak bergantung pada waktu me-

nuntun pada gelombang-gelombang dengan latar terbatas yang tidak lain adalah ketiga penyelesaian pasti dari persamaan NLS di atas.

Sifat-sifat medan gelombang fisik dari SFB telah dipelajari dan terdapat fenomena linear yang menarik, yaitu terjadinya secara bersamaan lenyapnya amplitudo (*vanishing amplitude*), singularitas fase (*phase singularity*) dan dislokasi muka gelombang (*wavefront dislocation*). Ketidakterbatasan suku Chu-Mei dikaitkan dengan ketidakterbatasan dari bilangan gelombang lokal (*local wavenumber*) dan frekuensi lokal (*local frequency*) pada titik-titik singular (*singular points*). Ketidakterbatasan ini adalah sifat umum yang menentukan terjadinya singularitas fase serta dislokasi muka gelombang.

Beberapa sifat gelombang pada latar terbatas tingkat tinggi juga telah dipelajari, khususnya penyelesaian SFB_2.* Medan gelombang fisiknya menunjukan interaksi dua kelompok gelombang pada saat merambat ke arah hilir (*downstream*). Secara teori, SFB_2 juga calon yang baik untuk pembangkitan gelombang ekstrim karena ia memiliki faktor kelipatan amplitudo sampai maksimal lima kali. Hubungan eksplisit dari faktor-faktor kelipatan amplitudo antara SFB_2 dan SFB juga disajikan dalam tesis ini. Lenyapnya amplitudo, singularitas fase dan dislokasi gelombang muka juga terjadi secara bersamaan di medan gelombang fisik SFB_2.

Sejumlah percobaan telah dilaksanakan untuk membangkitkan gelombang ekstrim berdasarkan perkiraan teoretis dengan menggunakan SFB. Percobaan ini dilakukan pada kolam pengujian gelombang di MARIN. Hasil percobaan di laboratorium dan perkiraan teori telah dibandingkan baik dari segi kualitas maupun kuantitas. Semua sinyal percobaan menunjukan pola ketidakstabilan modulasi sebagaimana digambarkan oleh SFB selama perambatan ke arah hilir. Pada percobaan ini, dapat diamati bahwa frekuensi gelombang pembawa (*carrier frequency*) dan frekuensi modulasi (*modulation frequency*) dipertahankan dengan tepat selama perambatan gelombang. Beberapa perbedaan antara SFB teoretis dan sinyal percobaan dijelaskan dengan menggunakan kurva evolusi di diagram Argand dan grafik amplitudo maksimum terhadap waktu (*MTA*). Sinyal percobaan mempunyai singularitas fase pada dua posisi yang berbeda, dengan posisi ekstrim terletak di antaranya. Posisi ekstrim ini ternyata cukup peka terhadap perubahan parameter pada kelas SFB dan terhadap koefisien tak linear dari persamaan NLS. Dari pembahasan dalam tesis ini, dapat disimpulkan bahwa kelas SFB memberikan kelompok gelombang yang cocok untuk digunakan pada pembangkitkan gelombang ekstrim di laboratorium secara deterministik.

*Indeks dua sekarang menyatakan jumlah pasangan awal pita samping (*sidebands*) pada spektrum.

Index

About the author

I was born in Bandung, West Java, Indonesia, on April 1, 1979 and also grew up there. I attended a senior high school at SMU/SMA Negeri 4 Bandung and finished the natural sciences program in 1997. From August 1997 until February 2001, I enrolled as an undergraduate student at Department of Mathematics, Bandung Institute of Technology, also known as ITB. During my final project period, Dr. Andonowati was my undergraduate supervisor, resulting to a bachelor thesis entitled 'A two-dimensional flap type wavemaker theory'. After that, I came to the Netherlands in August 2001 to pursue graduate studies at Department of Applied Mathematics, University of Twente. Meanwhile, I also participated in the combined MSc–PhD program in the Applied Analysis and Mathematical Physics chair within the same department. I obtained my master degree in June 2003 with the thesis entitled 'Wave group evolution and interaction' and my PhD degree in December 2006, both under the supervision of Professor E. (Brenny) van Groesen. The result of my doctoral research entitled 'Mathematical aspects of extreme water waves' is presented in this thesis.